

---

# An experiment apparatus for the production of ultracold bosonic dipolar ground state $^{23}\text{Na}^{39}\text{K}$ molecules and Feshbach spectroscopy in a cold mixture of $^{23}\text{Na}$ and $^{39}\text{K}$

---

Von der Fakultät für Mathematik und Physik der  
Gottfried Wilhelm Leibniz Universität Hannover

zur Erlangung des Grades

**Doktor der Naturwissenschaften**  
- Dr. rer. nat. -

genehmigte Dissertation von

M. Sc. Torsten Hartmann,  
geboren am 19.02.1985 in Neustadt a. Rbge.

2019



**Referentin:** Prof. Dr. Silke Ospelkaus,  
Institut für Quantenoptik, Leibniz Universität Hannover

**Korreferent:** apl. Prof. Dr. Milutin Kovacev,  
Institut für Quantenoptik, Leibniz Universität Hannover

**Tag der Promotion:** 28.11.2018



"Hofstadter's Law: It always takes longer than you expect, even when you take into account Hofstadter's Law." - D. R. Hofstadter, 1979

"More power!" - Tim Taylor, Home Improvement

"Never give up, never surrender!" - Commander Peter Quincy Taggart, Galaxy Quest



# ABSTRACT

---

The field of ultracold matter has developed rapidly over the course of the past twenty to thirty years. One outstanding achievement has been the realisation of Bose-Einstein condensation (BEC) only 23 years ago. Many other fascinating observations of quantum phenomena have been made at an incredibly fast pace using ultracold atomic samples with contact force interactions as a testbed. Due to the rapid successes of all these experiments on atomic ensembles, researchers began to aim for more elaborate inter-particle interactions.

A possible additional one is the dipole-dipole interaction (DDI), the long-range character of which stands out in comparison to the contact interactions. Moreover, DDI is anisotropic and the possibility to tune the direction of the dipoles in the experiment as well as the interaction strength promises the possibility to study a plethora of new quantum phenomena.

In recent years, several experiments using different combinations of alkali atoms to create ground-state hetero-nuclear molecules in the ultracold regime have been set up, following the pioneering work on KRb molecules. Of all possible combinations of two alkali atoms, NaK combines the advantages of a high induced electric dipole moment of 2.72 Debye, chemical stability of the ground-state molecules, the possibility to realise bosonic as well as fermionic molecules and a large knowledge base for cooling and trapping of the two atomic species.

This thesis reports on the development and construction of an experiment apparatus for the production of ultracold bosonic dipolar ground state  $^{23}\text{Na}^{39}\text{K}$  molecules. This includes the setup of an ultra-high vacuum (UHV) system, several laser light sources, microwave (MW) and radio frequency (RF) antennas and electronics to control the various components of the experiment. The system pre-cools the atomic samples of  $^{23}\text{Na}$  and  $^{39}\text{K}$  and loads them into a dual-species three-dimensional magneto-optical trap (3D MOT). After a transfer to a magnetic quadrupole trap, the mixture is cooled by forced MW evaporation until three-body losses limit dual-species operation at high densities and zero magnetic field. Using the pure optical trapping potential of a crossed optical dipole trap (cODT) and RF-state-transfer, the scattering properties of the bosonic mixture of  $^{23}\text{Na}+^{39}\text{K}$  are investigated in extensive atom loss measurements for a magnetic field range from 0 to 750 G. Several Feshbach resonances, zero crossings of the interspecies scattering length and inelastic loss features in many different scattering channels are identified. The results of this study are used to refine the molecular potentials of NaK and to produce a dual-species quantum-degenerate mixture of two BECs in the state  $|f=1, m_f = -1\rangle_{^{23}\text{Na}} + |f=1, m_f = -1\rangle_{^{39}\text{K}}$ . The measurements and refined molecular potentials will considerably aid in the future realisation of  $^{23}\text{Na}^{39}\text{K}$  molecules in their absolute ground state.

**Key words:** Dipolar systems, Feshbach resonances, quantum degenerate mixtures



# ZUSAMMENFASSUNG

---

Das Forschungsgebiet ultrakalter Materie hat in den letzten 20 bis 30 Jahren eine massive Entwicklung durchlaufen. Ein herausstechendes Forschungsergebnis ist die erste experimentelle Realisation eines Bose-Einstein-Kondensates (BEK), welches vor nur 23 Jahren publiziert wurde. Weitere faszinierende Entdeckungen folgten in kurzem zeitlichen Abstand und verdeutlichen die Eignung ultrakalter Atome zur Untersuchung quantenmechanischer Phänomene. Zunächst wurden ausschließlich interatomare Kontaktwechselwirkungen genutzt, doch mit zunehmendem Erfolg der Experimente begannen die Experimentatoren komplexere Wechselwirkungsprozesse in ihre Überlegungen einzubeziehen.

Die Dipol-Dipol-Wechselwirkung (DDW) ist ein möglicher Kandidat hierfür und insbesondere aufgrund ihrer langen Reichweite und Anisotropie interessant. Des Weiteren ist es möglich, Richtung und Stärke der DDW im Experiment zu verändern. Dies verspricht die Erforschung einer Fülle von neuen quantenmechanischen Phänomenen.

Den bahnbrechenden Arbeiten an KRb folgend, wurden in den vergangenen Jahren diverse Experimente aufgebaut, welche verschiedene Kombinationen von Alkaliatomen nutzen, um ultrakalte, heteronuklare Grundzustandsmoleküle herzustellen. NaK kombiniert dabei die Vorteile eines großen, induzierten Dipolmoments von 2,72 Debye mit einer hohen chemischen Stabilität im Grundzustand, der Möglichkeit sowohl bosonische als auch fermionische Moleküle zu erzeugen und einem großen Vorwissen, hinsichtlich des Kühlens und Fangens der beiden Atomsorten.

Diese Doktorarbeit beschreibt die Entwicklung und die Konstruktion eines Versuchsaufbaus zur Erzeugung ultrakalter, dipolarer  $^{23}\text{Na}^{39}\text{K}$ -Moleküle. Dazu gehören eine Vakuumapparatur, diverse Lasersysteme, Antennen zur Abstrahlung von Radiofrequenzen und Mikrowellen und elektronische Komponenten zur Steuerung des Experiments. Im Versuchsablauf werden  $^{23}\text{Na}$  und  $^{39}\text{K}$  Atome gekühlt und in einer dreidimensionalen, magneto-optischen Falle gespeichert. Nach der Transferierung in eine magnetische Quadrupolfalle wird eine Mikrowellenevaporation durchgeführt, bis deren Effizienz durch das Auftreten von Dreikörperstößen eingeschränkt wird. Ein Umladen der kalten Atome in ein rein optisches Fallenpotential macht die Manipulation der internen Atomzustände mittels Radiofrequenzübergängen und damit die Untersuchung von Streueigenschaften in einer ultrakalten Mischung aus  $^{23}\text{Na}$  und  $^{39}\text{K}$  möglich.

Diverse Feshbachresonanzen, inelastische Verlustsignale und Nulldurchgänge der Streulänge in verschiedenen Streukanälen und in einem Magnetfeldbereich von 0 bis 750 G werden vermessen und identifiziert. Die Ergebnisse dieser Messungen werden genutzt, um die Darstellung der Molekülpotentiale von NaK zu optimieren und um eine quantenentartete Mischung aus zwei BEKen im  $|f = 1, m_f = -1\rangle_{^{23}\text{Na}} + |f = 1, m_f = -1\rangle_{^{39}\text{K}}$  Zustand zu erzeugen. Die vorgestellten Messungen und die verbesserten Molekülpotentiale liefern einen wichtigen Beitrag für die Produktion ultrakalter  $^{23}\text{Na}^{39}\text{K}$  Grundzustandsmoleküle.

**Schlagwörter:** Dipolare Systeme, Feshbachresonanzen, quantenentartete Mischungen



## LIST OF PUBLICATIONS

---

Contents presented in this thesis have partly been published in the following research publications:

- T. Hartmann, T. A. Schulze, K. K. Voges, P. Gersema, M. W. Gempel, A. Zenesini, S. Ospelkaus and E. Tiemann,  
*Feshbach resonances in  $^{23}\text{Na} + ^{39}\text{K}$  mixtures and refined molecular potentials for the NaK molecule*  
Physical Review A **99**, 032711 (2019), [1]
- T. A. Schulze, T. Hartmann, K. K. Voges, M. W. Gempel, E. Tiemann, A. Zenesini and S. Ospelkaus,  
*Feshbach spectroscopy and dual-species Bose-Einstein condensation of  $^{23}\text{Na} - ^{39}\text{K}$  mixtures*  
Physical Review A **97**, 023623 (2018), [2]
- M. W. Gempel, T. Hartmann, T. A. Schulze, K. K. Voges, A. Zenesini and S. Ospelkaus,  
*Versatile electric fields for the manipulation of ultracold NaK molecules*  
New Journal of Physics **18**, 045017 (2016), [3]
- T. A. Schulze, I. I. Temelkov, M. W. Gempel, T. Hartmann, H. Knöckel, S. Ospelkaus and E. Tiemann,  
*Multichannel modeling and two-photon coherent transfer paths in NaK*  
Physical Review A **88**, 023401 (2013), [4]



# Contents

<b>List of publications</b>	<b>v</b>
<b>1 Introduction</b>	<b>1</b>
1.1 Long-range interactions . . . . .	1
1.2 Dipolar molecules . . . . .	2
1.3 State of the art for NaK . . . . .	3
1.4 The scope of this thesis . . . . .	3
<b>I Theory</b>	<b>7</b>
<b>2 Molecular potentials</b>	<b>11</b>
2.1 Quantum-mechanical treatment of atoms . . . . .	11
2.1.1 Interaction with an external magnetic field . . . . .	14
2.2 Molecular potentials . . . . .	16
2.2.1 Electronic part of the potentials . . . . .	18
2.2.2 Vibrational and rotational part of the potentials . . . . .	24
2.2.3 Hund's cases . . . . .	28
<b>3 Scattering theory</b>	<b>31</b>
3.1 Classical scattering theory . . . . .	31
3.2 Quantum-mechanical treatment of scattering . . . . .	37
3.2.1 The method of partial waves . . . . .	40
3.2.2 Calculation of the scattering phase . . . . .	45
3.2.3 Scattering on a square potential . . . . .	46
3.2.4 Shape resonances . . . . .	48
3.2.5 Scattering of identical particles . . . . .	48
<b>4 Feshbach resonances</b>	<b>51</b>
4.1 Phenomenological description of Feshbach resonances . . . . .	51
4.1.1 Derivation of the scattering length in the low-energy limit . . . . .	52
4.1.2 Coupling mechanisms . . . . .	55
4.1.3 Inelastic scattering . . . . .	58
4.2 Modelling of molecular potentials and Feshbach resonances . . . . .	59
<b>5 Theory of Bose-Einstein condensation</b>	<b>65</b>
5.1 Theoretical description of BEC . . . . .	65
5.1.1 Non-interacting indistinguishable particles . . . . .	65
5.1.2 Interacting bosons . . . . .	67
Two-component Bose gases . . . . .	68
5.2 Experimental signatures of BEC . . . . .	69
5.2.1 Bimodal distribution . . . . .	69

5.2.2 Turning of aspect ratio . . . . .	70
<b>II Experiment</b>	<b>73</b>
<b>6 Experiment setup</b>	<b>75</b>
6.1 Experiment setup in the laboratory . . . . .	76
6.2 Vacuum apparatus . . . . .	76
6.2.1 General theory of vacuum . . . . .	77
Differential pumping . . . . .	81
Measuring UHV conditions . . . . .	82
6.2.2 Main chamber . . . . .	82
Investigated subjects . . . . .	83
Main chamber modifications and vacuum testing . . . . .	85
Vacuum windows . . . . .	88
6.2.3 2D MOT and Zeeman slower . . . . .	88
Zeeman slower . . . . .	88
Two-dimensional magneto-optical trap . . . . .	91
Important details on ultra-high vacuum . . . . .	92
6.3 Experiment control . . . . .	94
6.4 Laser systems . . . . .	96
6.4.1 Sodium laser system . . . . .	96
6.4.2 Potassium laser system . . . . .	98
6.4.3 Blue-plug and cODT laser systems . . . . .	100
Blue-plug laser system . . . . .	101
Laser system for the cODT . . . . .	102
6.5 Magnetic field coils and current switching . . . . .	103
6.5.1 Feshbach coils and compensation cage . . . . .	103
6.5.2 IGBTs and current control system . . . . .	105
6.6 Atom sources . . . . .	107
6.6.1 Zeeman slower . . . . .	108
Alignment of the Zeeman slower laser beam . . . . .	109
6.6.2 Two-dimensional magneto-optical trap . . . . .	109
Alignment of the 2D MOT . . . . .	110
6.7 3D magneto-optical trap . . . . .	111
6.7.1 Two-species 3D MOT . . . . .	113
6.7.2 Dark-SPOT MOT vs. bright MOT . . . . .	114
6.8 Optical pumping, molasses and magnetic trap . . . . .	115
6.8.1 Optical pumping and optical molasses . . . . .	115
6.8.2 Magnetic trap . . . . .	117
6.9 Imaging setup . . . . .	117
6.9.1 Theory of imaging atoms . . . . .	118
Fluorescence imaging . . . . .	118
Absorption imaging . . . . .	119
6.9.2 Imaging on horizontal axes . . . . .	120
Determining the temperature of an ensemble . . . . .	122
<i>In-situ</i> and TOF imaging . . . . .	122
High-field imaging . . . . .	123
6.9.3 Imaging on the vertical axis . . . . .	123
6.10 Evaporation in the magnetic trap and blue plug . . . . .	124
6.10.1 RF and MW evaporation . . . . .	125
RF evaporation . . . . .	126

MW evaporation . . . . .	126
Evaporation ramp optimisation . . . . .	127
6.10.2 Majorana spin flip losses . . . . .	129
6.10.3 Blue plug . . . . .	130
6.10.4 Sympathetic cooling of $^{39}\text{K}$ . . . . .	134
6.11 Crossed optical dipole trap . . . . .	135
6.11.1 Theoretical description . . . . .	136
Gravitational sag . . . . .	137
6.11.2 Experimental implementation . . . . .	138
Alignment procedure . . . . .	138
Trap frequencies . . . . .	139
Loading efficiency . . . . .	141
6.11.3 Evaporation in the cODT . . . . .	142
6.12 RF transfer in the cODT . . . . .	143
6.12.1 Theory of RF transfers . . . . .	143
Adiabatic rapid passage . . . . .	143
Polarization of the RF field . . . . .	144
Cut-off frequencies of waveguides . . . . .	145
Dipole antenna . . . . .	145
6.12.2 Antenna design, characterisation and placement . . . . .	146
6.12.3 Transfer efficiencies . . . . .	149
<b>7 Feshbach resonance measurements</b>	<b>153</b>
7.1 Methods to measure Feshbach resonances . . . . .	153
Elastic and inelastic collisions . . . . .	155
7.2 Known Feshbach resonances . . . . .	155
7.3 Three-body losses in $(1, -1)_{\text{Na}} + (1, -1)_K$ mixtures . . . . .	155
7.4 Sequence for Feshbach measurements . . . . .	157
7.4.1 Magnetic field calibration . . . . .	157
7.4.2 Preparation of a cold mixture in the cODT . . . . .	158
7.4.3 Adjusting the initial atom numbers . . . . .	159
7.4.4 Atom loss measurements . . . . .	160
7.4.5 Image post-processing . . . . .	161
7.5 Results . . . . .	162
7.5.1 Experiment results . . . . .	162
Special features . . . . .	165
7.5.2 Theoretical calculations . . . . .	166
Predictions of Feshbach resonance positions . . . . .	166
Calculation of molecular potentials . . . . .	168
Refined molecular potentials and resonance positions . . . . .	168
<b>8 Bose-Einstein condensation</b>	<b>171</b>
8.1 Single-species BECs in $ f = 1, m_f = -1\rangle_{\text{Na/K}}$ . . . . .	171
8.2 Dual-species BEC using Feshbach resonances . . . . .	173
8.3 BEC of $^{23}\text{Na}$ in $ f = 1, m_f = 1\rangle$ . . . . .	176
8.3.1 Levitating a BEC of $^{23}\text{Na}$ in $ f = 1, m_f = 1\rangle$ . . . . .	176

<b>9 Conclusion and Outlook</b>	<b>179</b>
9.1 Feshbach molecules . . . . .	179
9.2 Ground-state molecule production via STIRAP . . . . .	180
9.3 Optical lattice and single-site imaging . . . . .	181
9.3.1 Inducing electric dipoles . . . . .	182
9.4 Polarized $^{23}\text{Na}^{39}\text{K}$ molecules in an optical lattice . . . . .	182





# Chapter 1

## Introduction

In the past 25 years, the research field of cold atoms has achieved tremendous results at an incredibly fast pace. This ranges from the first trapping of atoms in an optical lattice [5–7] to the realisation of various new quantum phenomena. For example, the first Bose-Einstein condensates (BECs) were generated in a laboratory [8–10] only 23 years ago.

While experiments with ultracold atoms in a bulk have enabled e.g. the investigation of entanglement phenomena [11], interaction-free measurements [12] and the observation of the BCS-BEC crossover [13, 14], trapping atoms in an optical lattice has led e.g. to the observation of the superfluid to Mott insulator transition [15]. In 2010, these experiments have first been performed with  $^{87}\text{Rb}$  under a microscope with single-atom resolution [16] and thereby the direct observation of a Mott insulator [17, 18] has been made possible. Single-site resolution of atoms has nowadays been achieved for bosonic as well as fermionic species [19–21].

### 1.1 Long-range interactions

While the speed with which all these experiments have been successful is astounding, it also entailed that researchers began to aim for interactions additional to the short-range contact forces present in the used ultracold atomic samples. A possible additional interaction term would be the DDI which can be described by the formula

$$V_{dd}(r) = \frac{C_{dd}}{4\pi} \frac{1 - 3\cos^2(\theta)}{r^3} , \quad (1.1)$$

where  $C_{dd}$  is a constant that contains the interaction strength,  $\theta$  is the angle between the two interacting dipole moments and  $r$  is the distance in between them. As can be seen, the DDI is both long-range due to the  $r^{-3}$  dependency and anisotropic due to  $\theta$ . It has been proposed that a dipole-dipole interaction would lead to interesting new phenomena [22, 23] both in a bulk sample (as BEC of chromium, see [24] and references therein) as well as in a lattice (for example new states of matter like super-solidity [25–27]).

A permanent dipole moment can be found as a magnetic dipole in atoms with open shell electrons like  $^{52}\text{Cr}$ ,  $^{164}\text{Dy}$  and  $^{168}\text{Er}$ . In the past years, experiments have been successful to control several of these atoms and achieve quantum degenerate states [28–30] as well as to trap them in an optical lattice [31]. First observations of dipole-dipole interaction-induced phenomena were reported, such as quantum magnetism [32] and self-stabilizing quantum droplets [33]. However, the dipole-dipole interaction originating from the internal magnetic moment of the atoms is relatively weak compared to contact interaction forces (which is relevant in bulk systems) and to the normal spacing of an optical lattice (which is often on the order of 500 nm). A possibility is to use smaller lattice spacings which on the other hand makes other experiment techniques more challenging, especially high-resolution imaging.

## 1.2 Dipolar molecules

The search for larger dipole strength leads to hetero-nuclear molecules. The electric dipole of such molecules is not permanent as it is the case for the magnetic dipoles in atoms, but needs to be induced by an external electric field [3]. This means that the electric dipole-dipole interaction strength can be freely tuned. Moreover, for maximally polarized hetero-nuclear molecules, the induced electric dipoles surpass even the largest possible magnetic moments. In fig. 1.1, a comparison of DDI strength in units of the Bohr radius  $a_0$  is given.

The molecules listed in fig. 1.1 are mainly formed from alkali atoms. To investigate physics in the ultracold regime, the preparation of molecules in an oven [37], in a heat pipe [38] or by ablation [39] as it is done e.g. in spectroscopic experiments is not feasible. The methods mentioned above produce molecules in their electronic ground state. However, the ro-vibrational states, unique to molecules in comparison with atoms, are thermally populated. Cooling techniques are necessary to produce a sample of ultracold molecules in the absolute ro-vibrational ground state. Direct cooling techniques have made considerable progress in the last years (three laser-cooled molecules are included in fig. 1.1), including centrifuge [40], Stark [41] and Zeeman deceleration [42]. Additionally, trapping of such molecules has been realised in magnetic [43], magneto-optical [44] and pure optical traps [45]. However, the achieved ensemble temperatures are still in the  $\mu\text{K}$  range [46], far away from the  $\text{nK}$  regime aimed for. Furthermore, the number of molecules finally trapped in MOTs [47] or magnetic traps [48] are only a fraction of the numbers in ensembles achieved in atomic experiments.

The standard procedure for producing ultracold molecules in the absolute ground state was first realised in the group of Deborah Jin and Jun Ye at JILA. It follows the path of first cooling two atomic species to or close to quantum degeneracy, then associating them using a Feshbach resonance [49] and transferring them to the absolute ground state by stimulated Raman adiabatic passage (STIRAP) [50, 51].

Because this method benefits from knowledge about handling and cooling atomic species, the first choice for an experimental realisation have been alkali atoms which have been well known from the many ultracold atom experiments in which they have been chosen because of their similarity to hydrogen and thus the relatively simple structure of their inner states. Many different combinations of alkalis are used to produce ground state molecules [52–59]. Shortly after the first alkali hetero-nuclear molecules were assembled, attempts have been started to create ground state molecules with alkaline earth and lanthanide atoms [60–62].

Already the first choice for a molecule of alkali atoms,  $^{40}\text{K}^{87}\text{Rb}$ , showed an unexpectedly short lifetime in the bulk system of 10 to 100 ms [63]. This is due to the fact that the reaction  $\text{KRb} + \text{KRb} \rightarrow \text{K}_2 + \text{Rb}_2$  is exothermic, thereby leading to strong losses from the trap. While establishing a new research field of ultra-cold chemistry [64–66], the process hindered other

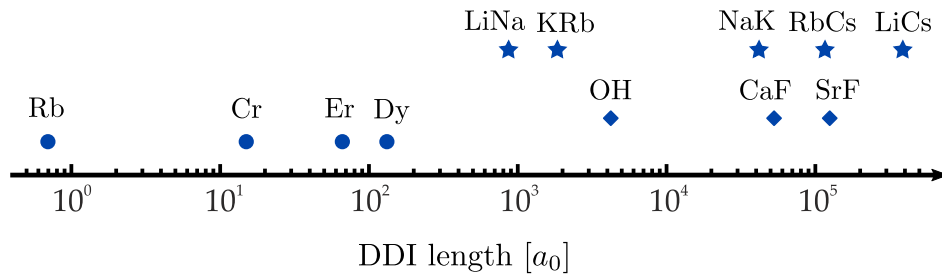


**Figure 1.1: Dipole-dipole interaction.** For different magnetic atoms (dots), molecules which are laser cooled to date (diamonds) and heteronuclear molecules which have been produced in their absolute ground state (stars), the DDI is given in units of the Bohr radius  $a_0$ . Data taken from [34–36].

applications which require long lifetimes in the bulk system. For  $^{40}\text{K}^{87}\text{Rb}$ , the problem could be mitigated by producing the molecules in an optical lattice [67]. Recently, indications have been found that reaching quantum degeneracy with  $^{40}\text{K}^{87}\text{Rb}$  stabilizes the sample in a bulk system against the described loss mechanism due to the fermionic nature of the molecule [68]. Directly after the observation of the chemical reactivity in  $^{40}\text{K}^{87}\text{Rb}$ , investigations have been performed to identify combinations of alkali atoms for which the formed molecules do not experience exothermic reactions in their absolute ground state [69]. It was predicted that only NaK, NaRb, NaCs, KCs and RbCs will have chemically stable ground-state molecules, which is why those combinations are in the focus of recent experiments.

Nevertheless, the added complexity in a gas of ultracold molecules also showed some still not completely understood effects. For instance, even molecules which do not have an exothermic reaction path suffer from short lifetimes of around 25 ms in a bulk sample [57, 70]. This may be an effect of so-called *sticky collisions* [71, 72] in which the molecules are believed to form long-lived tetramers which can lead to losses from the trap when they scatter with another molecule. This process has, however, not yet been experimentally observed in a distinct way.

### 1.3 State of the art for NaK

Of all stable combinations, NaK features a high induced electric dipole moment of 2.72 Debye [73] as well as the possibility to switch between bosonic and fermionic molecules by associating either  $^{23}\text{Na}^{39}\text{K}$  (and  $^{23}\text{Na}^{41}\text{K}$ ) or  $^{23}\text{Na}^{40}\text{K}$ . Several current experiments work with the fermionic molecule (see [58, 74, 75]). Its Feshbach resonance spectrum has been mapped out in detail ([76] and [74]). Additionally, theoretical investigations on a possible two-photon STIRAP pathway to the ground state were performed [4]. Recently, fermionic ground-state molecules have successfully been produced using two different STIRAP pathways ([58] and [75]).

The bosonic species, however, have so far not been experimentally investigated. All knowledge about their internal structure is limited to spectroscopic data of the potential energies gathered in heat pipe experiments [37] and predictions obtained by isotope-mass rescaling.

To follow the outlined path of Feshbach association and STIRAP transfer to finally achieve bosonic ground-state  $^{23}\text{Na}^{39}\text{K}$  molecules is therefore a task which will enrich the understanding of this molecule further. Additionally, with the ground state molecules at hand, further fascinating experiments can be performed.

### 1.4 The scope of this thesis

The scope of this thesis is to design and set up an experiment apparatus capable to trap  $^{23}\text{Na}$  and  $^{39}\text{K}$  and to cool the mixture to the quantum degenerate state from which ground-state molecules can be produced via Feshbach association and two-photon ground-state transfer.

With the working experiment apparatus at hand, an in depth investigation of the Feshbach spectrum of  $^{23}\text{Na}^{39}\text{K}$  is performed which gives the possibility to expand the existing knowledge about the potential energy curves (PECs) of the bosonic molecule. Moreover, achieving quantum degeneracy in a mixture of  $^{23}\text{Na}+^{39}\text{K}$  is an important step towards ground-state molecules and is tackled in this work.

The thesis is separated into two main parts. The first part introduces the theoretical concepts which are the basis for understanding and interpreting the experiments performed and results achieved in this work. It is organized as follows:

- In chap. 2, the description of molecular PECs is derived, starting with a recapitulation of important quantum-mechanical principles in atoms.
- Chapter 3 introduces the concepts of scattering theory, first for classical and then for quantum-mechanical scattering processes. Together with the methods derived in the previous chapter, the foundations for the following chapter are thereby laid.
- In chap. 4, the theory behind the phenomenon of Feshbach resonances is presented. A phenomenological description is followed by an overview over several methods to model molecular potentials and to predict the positions of Feshbach resonances.
- The last chapter of the first part, chap. 5, deals with the concepts of BEC.

In the second part of this thesis, the experiment setup and the performed experiments are presented.

- Chapter 6 gives a detailed overview over the experiment as it has been set up during the course of this thesis. It starts with the description of the vacuum apparatus and subsequently covers the laser systems, the atom sources, the different types of traps to confine and cool the atomic samples and the methods to manipulate their internal states. Such an experiment apparatus is quite complex and beyond what a single person can set up in a reasonable time, which is why it has been built from scratch together with M. W. Gempel and T. A. Schulze, later modifications have been also implemented by A. Zenesini, K. K. Voges and P. Gersema.
- The main findings of this thesis are presented in chap. 7. The chapter is based on results published in [1] and discusses the measurements of various resonant structures in a mixture of ultracold bosonic  $^{23}\text{Na}+^{39}\text{K}$ .
- Chapter 8 describes the experiment procedure to achieve dual-species degeneracy in  $^{23}\text{Na}+^{39}\text{K}$  mixtures. Additionally, further measurements on the produced BECs are discussed, such as the magnetic levitation of a BEC of  $^{23}\text{Na}$  in the  $|f=1, m_f=1\rangle$  hyperfine state. Parts of this chapter have been published in [2].
- The achieved results are summarised in chap. 9. Furthermore, an outlook is given on the next steps which will be performed with the experiment apparatus presented in this thesis.





# **Part I**

# **Theory**



# Introduction to the theory part

Feshbach resonances are a phenomenon that occurs when two atoms interact at close range. They can also be used to drive the formation of a molecular bond. Therefore, they are described with the tools of molecular physics. The first contact with this field of physics can be daunting because adding a second atom also adds a lot of complexity to the methods known from atomic physics. The Schrödinger equation for a hydrogen atom is well solvable but already atoms with more electrons require approximations and numerical solutions. Combining two atoms increases the complexity further. Theoretical and experimental results in this thesis will be discussed on the basis of molecular PECs. An example is given in fig. 1.2 which shows the potentials of the ground state and first excited state of the NaK molecule together with their spectroscopic notation, the molecular wave functions of some of the states and a possible two-photon pathway to the absolute ground state of the molecule. To fully understand the figure, different concepts have to be introduced and combined.

The goal of the theory part is to prepare the reader to understand the experiments performed and results achieved in this thesis, assuming a basic knowledge of the quantum-mechanical description of the hydrogen atom.

The discussion starts with chap. 2 with an introduction of the concepts behind the representation of molecular potentials. In chap. 3, a description of scattering processes is given. Combining the knowledge of molecular potential energy curves and quantum-mechanical scattering theory, the theory of Feshbach resonances is introduced in chap. 4. This is done first on a phenomenological level and then a short overview over the theoretical calculation methods is given which are the basis for the results obtained in chap. 7.

Finally, chap. 5 discusses the ideas behind the theory of BEC to support the experimental findings which are presented in chap. 8.

Theoretical concepts of the techniques used in the experiment apparatus will not be introduced in this part of the thesis but are instead incorporated in the respective chapters in the second part of this work.

The theory of molecules and BECs is presented in a certain depth and a reader already familiar with these fields of physics might find that a more compacted presentation would be sufficient for her or him. In that case, it is possible to skip the theory part of this thesis and instead read the theory discussion e.g. in [77] and [36].

Theoretical descriptions in this part of the thesis are mainly oriented along [78, 79] and [80, 81]. Chapter 8 mainly follows [80, 82, 83].

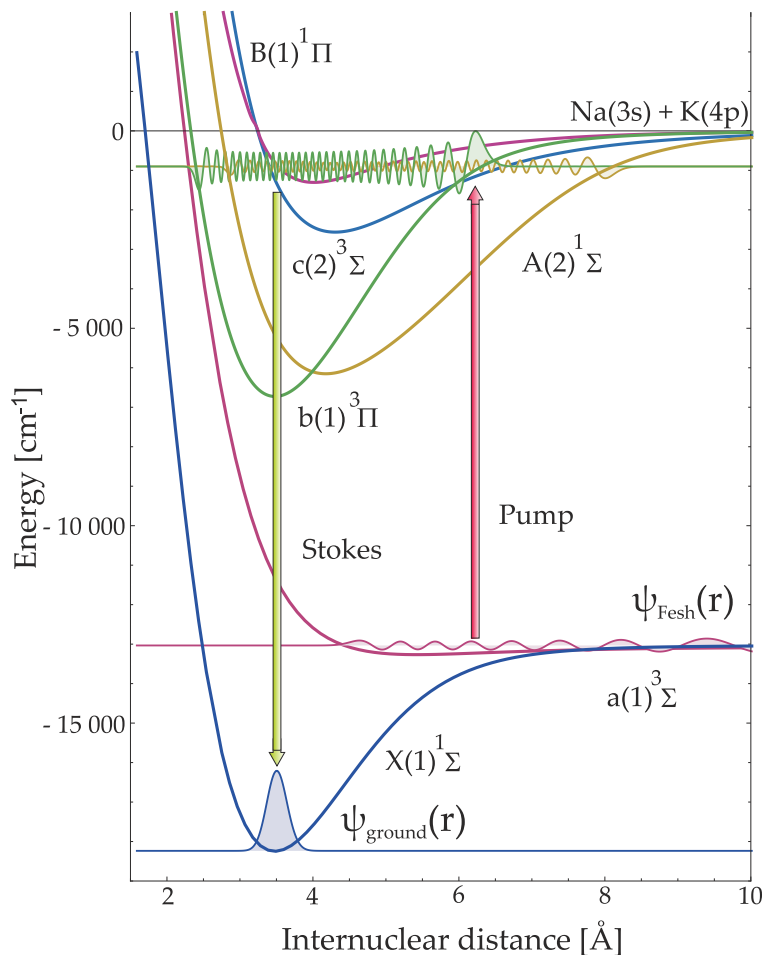


**Figure 1.2: Molecular potentials and two-photon transfer scheme of  $^{23}\text{Na}^{40}\text{K}$ .** The scheme shows the coherent transfer sequence from a Feshbach state to the absolute ground state of the molecule, indicated by the two arrows. In this example, the intermediate level is of the resonant  $A^1\Sigma \sim b^3\Pi$  type. The amplitudes of the wave-function reflect the singlet or triplet components. Taken from [4].

# Chapter 2

## Molecular potentials

Graphical representations of molecular potentials in textbooks are only at first glance similar to the representation of atomic potentials. Figure 2.1 shows a schematic graphic representation of hydrogen-like atomic potentials as well as a schematic representation of molecular potentials of a heteronuclear diatomic molecule. The goal of this chapter is to summarise the theory necessary to understand the differences between the two representations originating from the much higher internal complexity of diatomic molecules.

### 2.1 Quantum-mechanical treatment of atoms

First, it is helpful to give a short revision of the quantum-mechanical treatment of atoms, because many used methods can also be found in the treatment of more complex systems such as atom-atom collisions and molecules.

The Schrödinger equation describing a hydrogen-like atom with only one electron reads:

$$H\Psi(\vec{r}) = \left[ -\frac{\hbar^2}{2\mu} \nabla^2 - \frac{Ze^2}{(4\pi\epsilon_0)r} \right] \Psi(\vec{r}) = E\Psi(\vec{r}) \quad . \quad (2.1)$$

Here, the centre of mass motion of the nucleus together with the electron has been separated and only the part describing the relative motion between the particles is presented. For more details on the separation of the centre of mass motion and internal energy, see e.g. chapter 2.7 of [78]. In eq. 2.1,  $r$  is the distance between nucleus and electron,  $\mu$  is the reduced

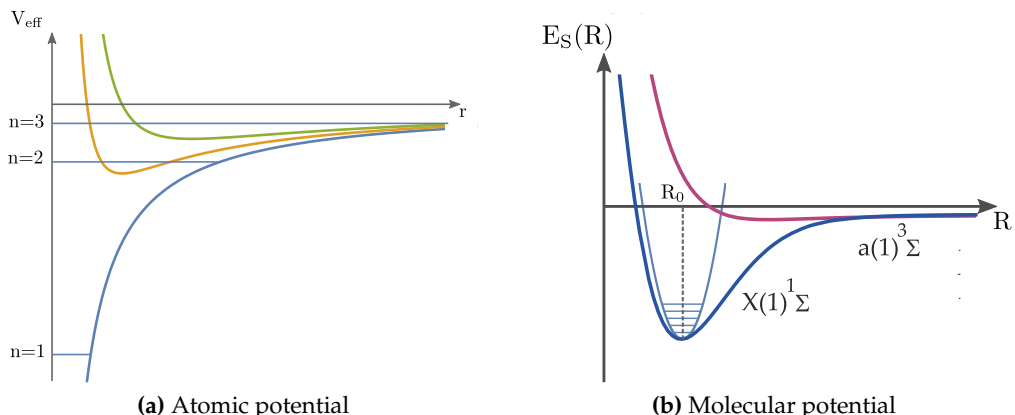


**Figure 2.1: Schematic representation of atomic (a) and molecular (b) potentials.** For details see text.

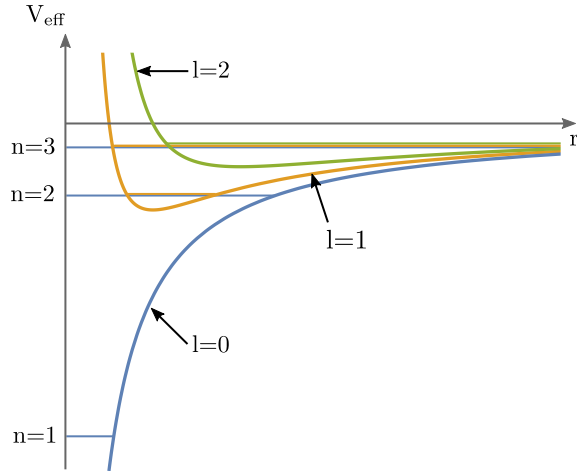


**Figure 2.2: Schematic of atomic potentials for different angular momentum quantum numbers.** For increasing angular momentum quantum number  $l$ , the centrifugal barrier of the potential increases, altering the form of a pure Coulomb potential, thereby massively reducing the probability for an electron in a potential with  $l > 0$  to come close to the nucleus.

mass of nucleus and electron,  $Z$  is the number of protons in the nucleus and  $\epsilon_0$  is the vacuum permittivity.

Because the Coulomb interaction potential in equation 2.1 is a central potential, it is best treated in spherical polar coordinates and with the ansatz of the wave function that is a product of two functions, one of which depending only on the radial coordinate  $r$  and the other one only on the angles  $\theta$  and  $\phi$ :

$$\Psi_{E,l,m}(r, \theta, \phi) = R_{E,l}(r) \cdot Y_{lm}(\theta, \phi) . \quad (2.2)$$

This leads to the well known spherical harmonics  $Y_{lm}(\Theta, \phi)$  for the angular part, depending on the angular momentum quantum number  $l$  and the magnetic quantum number  $m$ . The radial Schrödinger equation then reads:

$$\frac{d^2 u_{E,l}}{dr^2} + \frac{2\mu}{\hbar^2} [E - V_{\text{eff}}(r)] u_{E,l}(r) = 0 , \quad (2.3)$$

where

$$u_{E,l}(r) = r R_{E,l}(r) \quad (2.4)$$

with  $R_{E,l}(r)$  being the radial wave function.

An important point is that in eq. 2.3 the effective potential has the form

$$V_{\text{eff}}(r) = -\frac{Ze^2}{(4\pi\epsilon_0)r} + \frac{l(l+1)\hbar^2}{2\mu r^2} . \quad (2.5)$$

That means that the Coulomb potential is altered by a term which is dependent on the angular momentum quantum number  $l$  that is often called the *centrifugal barrier*. The effective potentials for different  $l$  are depicted in fig. 2.2. It can be seen that the centrifugal barrier increases for increasing  $l$ , thereby altering the form of a pure Coulomb potential in a way that the probability for an electron to come close to the nucleus massively decreases.

Solving the radial Schrödinger equation leads to the well known energy eigenvalues (see e.g. chapter 3.2 of [78])

$$E_n = -\frac{e^2}{(4\pi\epsilon_0)a_\mu} \frac{Z^2}{2n^2} , \quad (2.6)$$

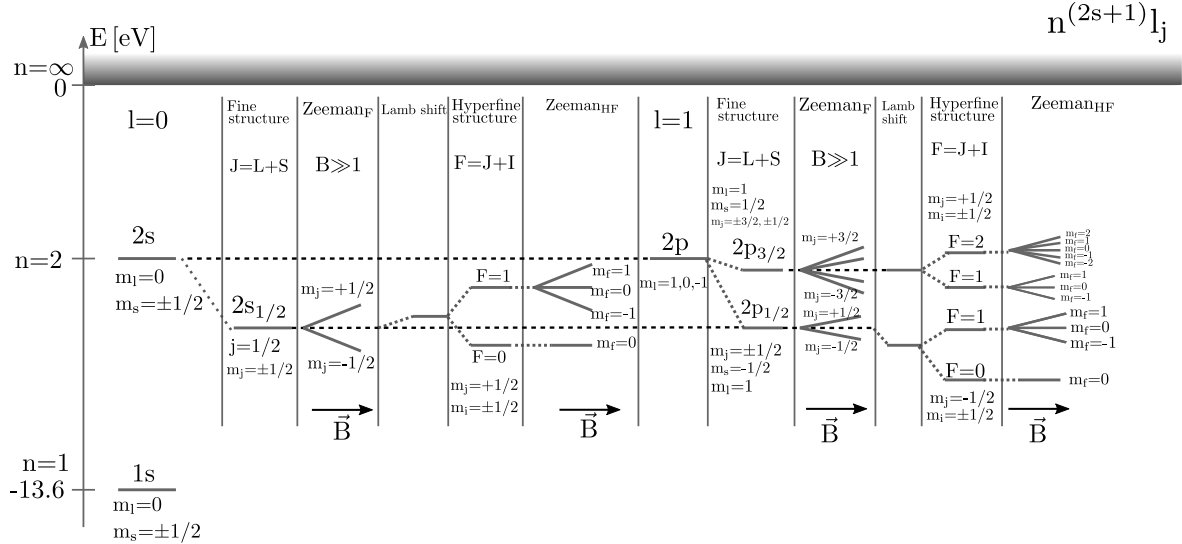


**Figure 2.3:** Schematic overview over all energy shifts present in an atom. The shifts are given exemplarily for  $n = 2$  of the hydrogen atom. Note that additionally to the Lamb shift also relativistic corrections of the kinetic energy and the Darwin term contribute to the shift of the levels. The term symbol of the spectroscopic notation is given in the top right corner. The Zeeman effect is given for the two cases of large external magnetic field strength in which case it acts on the fine structure (Zeeman<sub>F</sub>) and for smaller external magnetic field strength in which case it acts on the hyperfine structure (Zeeman<sub>HF</sub>).

where  $n$  is the principle quantum number and  $a_\mu = 4\pi\epsilon_0\hbar^2/(\mu e^2)$  is the modified Bohr radius with the reduced mass  $\mu$ . The principle quantum number has the values  $n = 1, 2, \dots$

The  $E_n$  are  $n^2$  times degenerate in  $l$ , with values  $l = 0, \dots, (n - 1)$ . This leads to the spectroscopic notation of atomic levels as:

$$n^{(2s+1)}l \quad , \quad (2.7)$$

where  $s$  is the spin of the electron and  $l$  is replaced by s, p, d, f, ... for  $l = 0, 1, 2, 3, \dots$

With  $E_n$  still  $l$  times degenerate, many effects occurring in atoms are not yet included in the investigation. A full treatment of hydrogen-like atoms would be above the scope of this chapter and can be found in many textbooks like e.g. [78, 84]. The additional effects include relativistic corrections to the eigenenergies such as the Lamb shift and the effects of spin couplings. The fine structure partially lifts the degeneracy in  $l$  by coupling the (total) electron spin  $\vec{S}$  to the angular momentum  $\vec{L}$  of the electron precession around the nucleus. This leads to the total angular momentum  $\vec{J} = \vec{S} + \vec{L}$  of the electron. The hyperfine coupling adds further structure to the energies by coupling the total angular momentum of the electron to the spin of the nucleus  $\vec{I}$ . Without an external magnetic field, the hyperfine structure is still degenerate in the magnetic quantum number of the hyperfine structure  $m_f$ . Figure 2.3 shows a qualitative overview over the different energy shifts in hydrogen for the principle quantum number  $n = 2$ . It is important to notice that if relating the different energy levels and eigenstate wave functions to the effective potentials in fig. 2.1a, care has to be taken which potential curve belongs to which eigenenergy since the effective potentials are different for different angular momentum quantum numbers  $l$ . In fig. 2.4, this assignment is done by colours, giving also an idea why electrons with higher  $l$  quantum number have zero probability to be located at the position of the nucleus: The centrifugal barrier of the potential makes it impossible for the electron to come close to  $r = 0$ . To summarise, the curves depicted in fig. 2.4 show the electronic potentials as a function of the distance between the

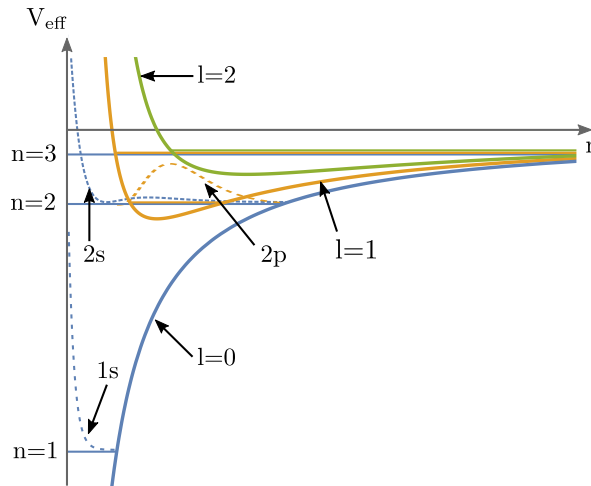


**Figure 2.4: Schematic of atomic potential energy curves and electron wave functions.** The assignment of the electron wave function to the correct atomic potential is given by the colour coding.

nucleus and the (valence) electron  $r$  as well as the eigenenergies. The energies are modified by smaller effects inside the atom (as shown in fig. 2.3), leading to the final energies in the atom.

### 2.1.1 Interaction with an external magnetic field

For the understanding of Feshbach resonances, a recapitulation of the effect of an external magnetic field on the energies of atoms is helpful. A brief overview of it shall be given in this section.

The Zeeman effect describes the behaviour of atoms (and molecules) in a static homogeneous external magnetic field. This magnetic field interacts with the different magnetic moments present inside the atom. For simplicity, the theory of the Zeeman effect will be illustrated for the atoms of the first column of the periodic table: the alkali atoms. For the magnetic field strengths used in this thesis, the Zeeman effect is dominant only on the energy scale of the hyperfine structure. This means that the coupling between angular momentum  $\vec{L}$  and spin  $\vec{S}$  of the valence electron is stronger than the coupling of the individual momenta with the external magnetic field, leaving  $J$  and  $m_J$  to be good quantum numbers<sup>1</sup>. Each hyperfine state is  $2F + 1$  times degenerate in  $m_f$  and this degeneracy is broken due to the external magnetic field.

The Hamilton operator for a hydrogen-like atom inside an external magnetic field reads:

$$H = T + V(r) + V_{LS} + H_{ZeeHf} \quad , \quad (2.8)$$

where  $T$  is the operator of the kinetic energy,  $V(r)$  the Coulomb potential,  $V_{LS} = \xi(\vec{r})\vec{L} \cdot \vec{S}$  the potential energy coming from the LS-coupling and  $H_{ZeeHf}$  the operator describing the interaction of the external magnetic field with the hyperfine structure. The operator reads:

$$H_{ZeeHf} = A \cdot \vec{I} \cdot \vec{J} + \vec{B}_0 \cdot \vec{M}_J + \vec{B}_0 \cdot \vec{M}_I \quad , \quad (2.9)$$

with  $A \cdot \vec{I} \cdot \vec{J}$  being the hyperfine interaction term, where  $A$  is the hyperfine structure constant,  $\vec{B}_0$  is the static homogeneous external magnetic field and  $\vec{M}_J = g_J \frac{\mu_B}{\hbar} \vec{J}$  and  $\vec{M}_I = g_I \frac{\mu_B}{\hbar} \vec{I}$

<sup>1</sup>Good quantum numbers correspond to conserved quantities and are associated with operators which commute with the Hamiltonian of the system. Therefore, they can be used to unambiguously describe any state of the system at any time.

are the magnetic moments induced by the total angular momentum  $\vec{J}$  and spin of the nucleus  $\vec{I}$ , respectively. The  $g_{J/I}$  can be found e.g. in [85] for sodium and in [86] for potassium. By taking the magnetic field along the z-axis in the laboratory frame, the Hamiltonian 2.9 is given by

$$H_{ZeeHf} = A \cdot \vec{I} \cdot \vec{J} + \frac{\mu_B}{\hbar} (g_J J_z + g_I I_z) B_z . \quad (2.10)$$

At zero magnetic field up to very low external magnetic fields, the coupling between  $J$  and  $I$  is stronger than the coupling of each of the magnetic moments onto the magnetic field axis, leaving  $F$  and  $m_f$  to be good quantum numbers. Thereby the states of the atom can be described in the basis of the hyperfine interaction term  $A \cdot \vec{I} \cdot \vec{J}$ . The states can be labelled by  $F, m_f$ . The splitting of the hyperfine states due to their different energetic behaviour in the external magnetic field is called the *Zeeman effect of the hyperfine structure*.

For very strong magnetic fields (in terms of hyperfine energy spacing, still being much smaller than the fine structure energy thus leaving the LS-coupling still active), the  $JI$ -coupling is broken as the total angular momentum  $\vec{J}$  and spin of the nucleus  $\vec{I}$  start precessing about the external magnetic field axis. The states must be described in a new set of good quantum numbers, being  $J, m_j, I, m_i$ . The energy splitting for high fields is said to show the *Paschen-Back effect of the hyperfine structure*.

The behaviour for the two extreme cases of very low and very high external magnetic field can be expressed analytically (see e.g. [85]), but the intermediate region is more difficult to describe. The Hamiltonian (eq. 2.10) has to be diagonalized for every magnetic field strength  $B$  to access the energies of each state at the given magnetic field. For the ground state, the full behaviour of the hyperfine states can be expressed by the *Breit-Rabi formula* [85, 87]:

$$E_{|J=1/2, m_j; I, m_i\rangle} = -\frac{\Delta E_{hfs}}{2(2I+1)} + g_I \mu_B m B \pm \frac{\Delta E_{hfs}}{2} \left(1 + \frac{4mx}{2I+1} + x^2\right)^{1/2}, \quad (2.11)$$

where  $\Delta E_{hfs} = A_{hfs}(I + 1/2)$  is the hyperfine splitting with  $A_{hfs}$  being the hyperfine structure constant,  $m = m_i \pm m_j = m_i \pm 1/2$  and the  $\pm$  sign in eq. 2.11 has to be chosen according to the sign in the equation for  $m$ ,  $x$  is given by

$$x = \frac{(g_J - g_I)\mu_B B}{\Delta E_{hfs}} . \quad (2.12)$$

For the two states with  $m = \pm(I + 1/2)$ , a sign ambiguity occurs in eq. 2.11 which can be

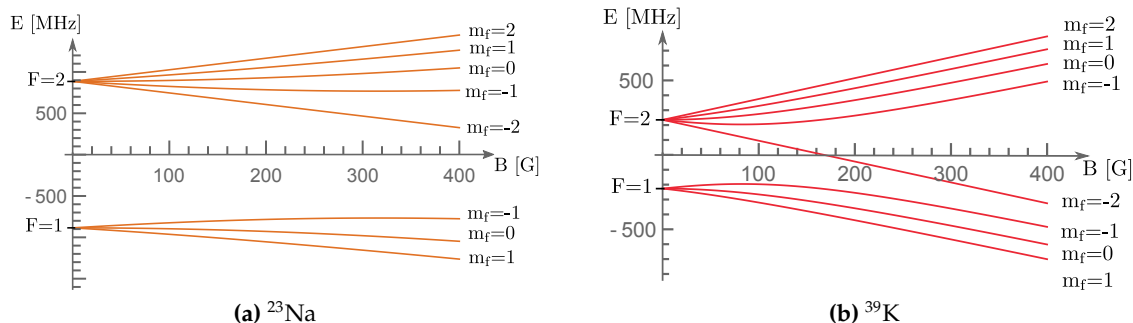


**Figure 2.5: Dependence of the hyperfine energies of (a)  $^{23}\text{Na}$  and (b)  $^{39}\text{K}$  ground states on the strength of an external magnetic field.** The Zeeman hyperfine states are labelled by their  $m_f$  quantum numbers. Note that for high magnetic field these are no longer good quantum numbers. The assignment of  $m_j$  and  $m_i$  is not shown for lucidity.

circumvented by using for those two states the formula:

$$E_{|J=1/2, m=\pm(I+1/2)\rangle} = \Delta E_{hfs} \frac{I}{2I+1} \pm \frac{1}{2}(g_J + 2Ig_I)\mu_B B . \quad (2.13)$$

The Breit-Rabi formula is a very useful tool and will be used in chap. 4 for the investigation of channel crossings in atom-atom scattering processes. In fig. 2.5, the ground-state hyperfine energies are plotted for sodium and potassium up to a magnetic field strength of 400 G.

## 2.2 Molecular potentials

For molecules, the system under investigation becomes more complicated. This is (among other reasons) because there are now two nuclei and with this the spherical symmetry of the potential is lost. With this, symmetry properties of the wave functions become important, which is not the case in an atom. Figure 2.6 shows a schematic drawing of a heteronuclear diatomic molecule in the centre of mass system. The coordinates are given in the body-fixed frame where the origin is set to the position of the centre of mass of the molecule and the internuclear position vector  $\vec{R}$  is given by  $\vec{R} = \vec{R}_B - \vec{R}_A$ . The core includes the nucleus and all completely filled shells of the atom since only the valence electrons will contribute to the molecular energies. To write down the Hamiltonian which describes this system, it is helpful to question which energies should be taken into account:

1. The kinetic energy of the cores  $T_N$ . They can move in space and also with respect to each other, leading to translational, rotational and vibrational motions.
2. The kinetic energy of the electrons,  $T_e$ .
3. The total potential energy of the system  $V$ , which includes the interactions of the cores with the valence electrons, the interactions of the cores with each other and the interactions of the electrons with each other, all this by the means of Coulomb and also spin-dependent interactions.

Neglecting the mass of an electron with respect to the reduced mass of the nuclei

$$\mu = \frac{M_A M_B}{M_A + M_B} , \quad (2.14)$$

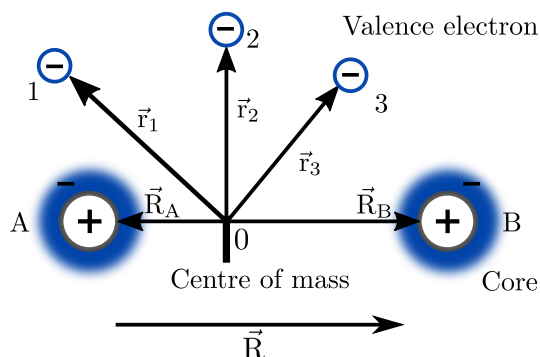


**Figure 2.6: Schematic of a two-atomic molecule in the centre of mass system.** The coordinates are given in the body-fixed frame where the origin is set to be equal to the centre of mass of the molecule. The core includes the nucleus and all completely filled shells of the atom since only the valence electrons will contribute to the molecular energies. The internuclear position vector  $\vec{R}$  is given by  $\vec{R} = \vec{R}_B - \vec{R}_A$ .

the kinetic energy of the cores can be written as:

$$T_N = -\frac{\hbar^2}{2\mu} \nabla_{\vec{R}}^2 . \quad (2.15)$$

The kinetic energy of the N valence electrons can be written as

$$T_e = \sum_{i=1}^N \left( -\frac{\hbar^2}{2m_e} \nabla_{\vec{r}_i}^2 \right) , \quad (2.16)$$

where  $m_e$  is the mass of an electron.

For the beginning, all spin-dependent interactions are excluded. The potential energy then only contains the Coulomb interactions between the particles of the molecule:

$$\begin{aligned} V(\vec{R}; \vec{r}_1, \vec{r}_2, \dots, \vec{r}_N) = & - \sum_{i=1}^N \left[ \frac{Z_A e^2}{(4\pi\epsilon_0)|\vec{r}_i - \vec{R}_A|} + \frac{Z_B e^2}{(4\pi\epsilon_0)|\vec{r}_i - \vec{R}_B|} \right] \\ & + \sum_{i < j=1}^N \frac{e^2}{(4\pi\epsilon_0)|\vec{r}_i - \vec{r}_j|} + \frac{Z_A Z_B e^2}{(4\pi\epsilon_0)R} , \end{aligned} \quad (2.17)$$

where the first sum describes the interaction of the cores A and B (with charges  $Z_A$  and  $Z_B$ ) with the valence electrons, the second sum the interaction of the valence electrons with each other and the last term accounts for the Coulomb interaction between the two cores. The position vectors are in the centre of mass system as shown in fig. 2.6.

The time-independent Schrödinger equation now reads:

$$[T_N + T_e + V] \Psi(Q_A, Q_B; q_1, q_2, \dots, q_N) = E \Psi(Q_A, Q_B; q_1, q_2, \dots, q_N) , \quad (2.18)$$

where  $Q_A$ ,  $Q_B$  and the  $q_i$  represent the space and spin coordinates of the cores and the valence electrons, respectively. At this point, it is important to point out that the total wave function  $\Psi$  has to be totally antisymmetric for the interchange of any pair of electrons due to the *Pauli exclusion principle*. In the following description, the spin dependence will not be shown for simplicity reasons but symmetry properties always have to be taken into account when finally constructing the molecular wave functions.

To find an appropriate way of approaching the Schrödinger equation, it is helpful to consider the energy scale of the different contributions to the potential energy. First and foremost, it is important to notice that the forces which act on the electrons and the forces which act on the nuclei are of comparable magnitude since they all are originated in the Coulomb interaction. But since the nuclei are much heavier than the electrons, their motion is much slower than the motion of the electrons. This directly translates into an energy scaling of the different contributions to the Hamiltonian.

As can be shown (see e.g. chapter 10.1 of [78]), the kinetic energy of the (valence) electrons and thereby the magnitude of the electronic energies is roughly given by

$$E_e \approx \frac{\hbar^2}{m_e a^2} , \quad (2.19)$$

where  $m_e$  is the electron mass and  $a$  the average distance of the nuclei in a molecule. Since  $a \approx 1 \text{ \AA}$ ,  $E_e$  is on the order of a few eV. This is also roughly the separation between two low-lying electronic molecular states.

For the kinetic energy of the cores, the translational, rotational and vibrational motion of the nuclei has to be taken into account. In the centre of mass system one can separate the

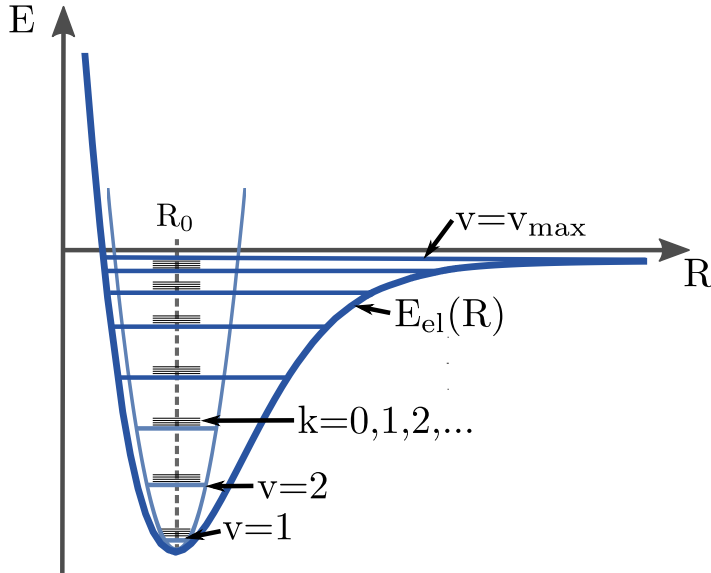


**Figure 2.7: Schematic of a molecular potential.** The molecular potential contains the electronic energy curve  $E_{el}(R)$  and the vibrational ( $v = 1, 2, \dots$ ) and rotational ( $k = 0, 1, 2, \dots$ ) energy levels.

translational energy and treat it as for a free moving particle. It can be shown [78] that the vibrational energy scales like:

$$E_v \simeq \left( \frac{m_e}{M} \right)^{1/2} E_e , \quad (2.20)$$

where  $M$  is on the order of a typical nuclear mass and therefore  $E_v$  is smaller than  $E_e$  by a factor of  $10^{-3}$  to  $10^{-5}$ . Finally, the rotational motion of the nuclei is on the order of

$$E_r \simeq \frac{m_e}{M} E_e , \quad (2.21)$$

which means that the rotational energy is again one to three orders of magnitude smaller than the vibrational energy.

### 2.2.1 Electronic part of the potentials

The basic survey of the different energy scales alone gives a first idea to understand typical molecular potential pictures as shown in fig. 2.7, where on top of each electronic state there are several vibrational and on top of them rotational levels. Moreover, the argument of the different energy scales shall be the starting point for a more thorough approach to the energy spectrum of molecules which will be sketched in the following. Keeping the different energy contributions in mind, it is best to start with solving the Schrödinger equation of  $N$  electrons moving in the Coulomb potential of the two cores with a fixed distance  $R$ . Then the so-called *electronic Hamiltonian* reads:

$$H_e = T_e + V \quad (2.22)$$

and the electronic wave equation is:

$$H_e \Phi_q(\vec{R}; \vec{r}_1, \vec{r}_2, \dots, \vec{r}_N) = E_q(R) \Phi_q(\vec{R}; \vec{r}_1, \vec{r}_2, \dots, \vec{r}_N) , \quad (2.23)$$

where the wave function  $\Phi_q(\vec{R}, \vec{r}_1, \vec{r}_2, \dots, \vec{r}_N)$  and the eigenenergy  $E_q(R)$  for a specific electronic state  $q$  (leading to one specific potential energy curve of that state) depend on

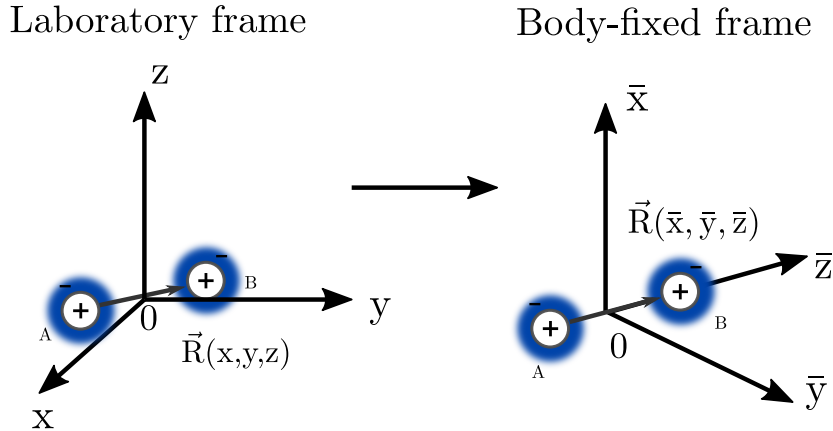


**Figure 2.8: Laboratory and body-fixed frame.** In the laboratory frame the molecule has no distinct orientation with respect to the coordinate axes. Setting the centre of mass of the molecule equal to the origin of the coordinate frame, the molecule is described in the centre of mass system (left figure). In the body-fixed frame the origin is set at the centre of mass and one of the coordinate directions is placed along the internuclear axis, here  $\bar{z}$  (right figure). Additionally the  $\bar{y}$ -axis is set in the  $xy$ -plane of the laboratory frame.

the distance between the two cores  $R$ . The electronic Schrödinger equation 2.23 is solved for a fixed internuclear distance. This fact is key for understanding the graphical textbook representations of molecular potentials.

The first step to obtain the complete molecular energies and wave functions is to solve the electronic wave function. Equation 2.23 is still written in the laboratory frame. Instead of that, it is advantageous to work in the body-fixed frame where the origin is placed at the centre of mass of the molecule, as shown in fig. 2.6, and one of the coordinate directions is placed along the internuclear axis. The coordinates are then given as shown in fig. 2.8. Note, however, that the treatment of the rotational and vibrational motion of the molecule will have to be done in the laboratory frame. This will make a coordinate transformation necessary once the electronic wave functions have been found. The coordinate transformation can be found e.g. in Appendix 9 of [78].

To start the process of solving the electronic wave function means first to find the observables which can be measured all at the same time to give the full picture of the system. This is equivalent to finding a complete set of commuting operators. When examining the atomic Hamiltonian (see eq. 2.1), one finds that all three components of the electronic orbital angular momentum operator  $L$  as well as  $L^2$  commute with the Hamilton operator (if spin-dependent interactions are not included). This is due to the spherical symmetry of the atomic potential. For molecules this symmetry is partially removed as they are only cylindrically symmetric along the internuclear axis (for heteronuclear molecules on which this chapter focusses; for homonuclear molecules, an additional point symmetry is present in the middle of the internuclear axis, leading to further restrictions on the wave function which will only be briefly discussed in this chapter but can be looked up in more detail e.g. in [78]).

As a consequence of the reduced symmetry,  $L^2$  does no longer commute with the electronic Hamiltonian  $H_e$ . The electronic eigenfunctions  $\Phi_s$  of the electronic state  $s$  will therefore be constructed as eigenfunctions of  $H_e$  and the electronic orbital momentum operator component in the  $\bar{z}$  direction, where  $\bar{x}$ ,  $\bar{y}$ ,  $\bar{z}$  mark the coordinates in the body-fixed frame as

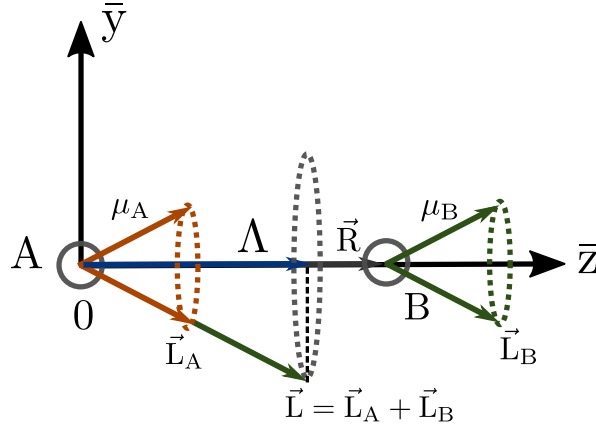


**Figure 2.9: Angular momentum projections in the body fixed frame.**  $\Lambda$  is the absolute value of the projection of the angular momentum of the molecule  $\vec{L}$  onto the internuclear axis. The magnetic moments  $\mu_A$  and  $\mu_B$ , induced by the angular momenta of the atoms  $\vec{L}_A$  and  $\vec{L}_B$ , precess about the internuclear axis  $\vec{R}$ .

depicted in fig. 2.8:

$$\begin{aligned} L_{\bar{z}} \Phi_s &= M_L \hbar \Phi_s, \\ &= \pm \Lambda \hbar \Phi_s, \\ M_L &= 0, \pm 1, \pm 2, \dots, \\ \Lambda &= 0, 1, 2, \dots \end{aligned} \tag{2.24}$$

Here  $\Lambda$  is the absolute value of the projection of  $L_{\bar{z}}$  onto the internuclear axis as can be seen in fig. 2.9. With this it is possible to find a notation similar to the spectroscopic notation in atoms where the angular momentum quantum number  $l = 0, 1, 2, \dots$  is assigned to the letters s, p, d, ...; here  $\Lambda = 0, 1, 2, \dots$  is assigned to  $\Sigma, \Pi, \Delta, \dots$  or in the case of dealing with individual electrons  $\sigma, \pi, \delta, \dots$

Note, however, the two-fold degeneracy in  $\Lambda$ . This degeneracy is linked to a symmetry property of  $H_e$ : All reflections on planes containing the internuclear axis leave  $H_e$  unchanged while two wave functions with different behaviour under these reflections exist, as shall be illustrated now. By choosing the plane of symmetry arbitrarily to be in the  $(\bar{x}, \bar{z})$  plane, a reflection of the electron coordinates on that plane yielding  $\bar{y}_i \rightarrow -\bar{y}_i$  shall be performed by the operator  $A_{\bar{y}}$ . Its eigenvalues are given as:

$$A_{\bar{y}} \phi = \pm 1 \phi \quad , \tag{2.25}$$

with  $\phi$  being an eigenfunction of  $A_{\bar{y}}$ .  $A_{\bar{y}}$  commutes with  $H_e$

$$[A_{\bar{y}}, H_e] = 0 \tag{2.26}$$

but does not commute with  $L_{\bar{z}}$ :

$$A_{\bar{y}} L_{\bar{z}} = -L_{\bar{z}} A_{\bar{y}} \quad . \tag{2.27}$$

From eq. 2.27, it follows that a reflection of the wave function corresponding to  $\Lambda$  for all but  $\Lambda = 0$  converts this wave function into the wave function belonging to  $-\Lambda$ :

$$\begin{aligned} L_{\bar{z}} A_{\bar{y}} \phi &= -A_{\bar{y}} L_{\bar{z}} \phi = -A_{\bar{y}} \Lambda \hbar \phi \\ &= -\Lambda \hbar A_{\bar{y}} \phi \quad . \end{aligned} \tag{2.28}$$

With  $A_{\bar{y}}\phi := \phi^-$ , it follows

$$L_{\bar{z}}\phi^- = -\Lambda\hbar\phi^- , \quad (2.29)$$

with  $\phi$  and  $\phi^-$  being the state wave functions. All electronic terms with  $\Lambda \neq 0$  are two-fold degenerate. This degeneracy is ultimately lifted when the interactions of the rotational motion of the molecule with the motion of the electrons are taken into account, leading to the so-called  $\Lambda$  – *doubling* of the states.

The case for  $\Lambda = 0$  requires a closer examination. Since  $M_L = 0$ , there exists only one eigenfunction which is therefore non-degenerate and can be constructed as a simultaneous eigenfunction of  $H_e$ ,  $L_{\bar{z}}$ ,  $A_{\bar{y}}$ . An eigenfunction for  $H_e$  and  $L_{\bar{z}}$ , say  $\phi_{\Lambda=0}$ , will have the two eigenvalues of  $\pm 1$  for  $A_{\bar{y}}$  which leads to two possible wave functions  $\Sigma^+$  and  $\Sigma^-$  for a state with  $\Lambda = 0$ .

The symmetry properties in a molecule lead to another restriction on the electronic potential curves of two states  $E_{q=1}(R)$  and  $E_{q=2}(R)$  which goes by the name *Neumann-Wigner non-crossing rule* (see e.g. chapter 10.3 of [78]). This rule states that two potential energy curves are forbidden to cross each other in the case that they belong to states with the same symmetry, meaning (for heteronuclear molecules) they have the same value of  $\Lambda$ , the same multiplicities and the same behaviour under reflection on the intermolecular plane.

As stated already, the spin-dependent interactions in the molecule will not be taken into account at this point, which in turn leads to a degeneracy of the states in the total spin

$$S_{total} = \sum_{i=1}^{N_e} S_i , \quad (2.30)$$

where  $S_i$  is the spin of a single electron and  $N_e$  the total number of electrons in the molecule. As in atoms (see eq. 2.7), the state of a molecule is characterised by the value of  $S_{total}$ . The term for a molecular state reads therefore

$$2S_{total}+1\Lambda , \quad (2.31)$$

with the multiplicity  $2S_{total} + 1$ .

After this brief symmetry discussion, the way to find the electronic wave functions  $\Phi_s$  and the electronic potential energy curves  $E_s(R)$  shall be sketched. Different methods are available, but since there are no analytical solutions to the Schrödinger equation 2.23, they all rely on approximation-based approaches. The computational approach finally used to obtain the results presented in chap. 7 still needs more theoretical background than provided up till this point of the chapter and will therefore be discussed in sec. 4.2.

Several approximation based methods need a first-guess trial wave function to start their numerical approach. A possibility to generate such trial wave functions and to gain also some insight into the shape of the potential energy curves is the linear combination of atomic orbitals (LCAO). As an example, the simplest molecule possible, the hydrogen ion  $H_2^+$  containing two nuclei A and B and one electron, is considered. Since there is only one electron present, the atomic ground state for the case of the two nuclei being very far away from each other is the 1s state with the wave function  $\Phi = \psi_{1s}(r_A)$ . In this notation, the assumption was already made that the electron is completely located at core A. This wave function alone does not fulfil any symmetry restrictions nor does it account for the possibility that the electron is located at core B. Therefore, the molecular wave function is constructed by the linear combination of the two atomic orbitals  $\psi_{1s}(r_A)$  and  $\psi_{1s}(r_B)$ :

$$\Phi_{g/u} = \frac{1}{\sqrt{2}}[\psi_{1s}(r_A) \pm \psi_{1s}(r_B)] , \quad (2.32)$$

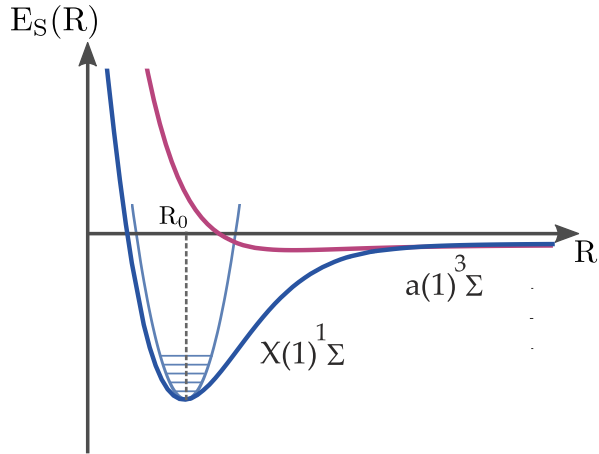


**Figure 2.10: Schematic of molecular potential energy curves.** Two different electronic molecular potentials are shown, a singlet potential (blue curve) and a triplet one (purple curve). The respective spectroscopic term symbols are also given.  $R$  is the internuclear distance and  $R_0$  marks the equilibrium distance at which the electronic potential of the singlet state is approximated by a parabolic curve which. The vibrational levels of the molecule are indicated by the straight lines inside the parabolic curve.

where the index "g/u" of the molecular wave functions refers to the additional point symmetry for reflection at the centre of the internuclear axis, present in two-atomic homonuclear molecules. The term symbol, associated with the wave function in eq. 2.32, would normally be  $\Sigma_{g/u}$ . In this case, because eq. 2.32 describes only one electron, the term symbol reads  $\sigma_{g/u}$  instead. This wave function is a very rough approximation to the molecular wave function, however, it becomes accurate in the asymptotic region for large intermolecular distances  $R$ . This also explains why the asymptote of a molecular electronic potential is labelled with the atomic terms, as can be seen in fig. 1.2 for the upper states. Furthermore, these LCAO wave functions can be used as trial functions for e.g. the variational method to obtain the electronic potential curves via:

$$E_{g/u}(R) = \frac{\int \Phi_{g/u}^* H_e \Phi_{g/u} d\vec{r}}{\int |\Phi_{g/u}|^2 d\vec{r}} \quad (2.33)$$

which can be shown (see chapter 10.3 of [78]) to be the same as

$$E_{g/u}(R) = \frac{H_{AA} \pm H_{AB}}{1 \pm I(R)} , \quad (2.34)$$

where

$$H_{AA} = \int \psi_{1s}(r_A) H_e \psi_{1s}(r_A) d\vec{r}_A \quad (2.35)$$

and

$$H_{AB} = \int \psi_{1s}(r_A) H_e \psi_{1s}(r_B) d\vec{r}_B \quad (2.36)$$

and  $I(R)$  is the *overlap integral*:

$$I(R) = \int \psi_{1s}(r_A) \psi_{1s}(r_B) d\vec{r} . \quad (2.37)$$

The solutions for the energies  $E_{g/u}$  are shown in fig. 2.11 for the hydrogen ion. As can

be seen, the potential energy curves have different characteristics. The one belonging to  $E_g$  has a minimum at distance  $R_0$  and is therefore called binding, whereas  $E_u$  lacks such a minimum and therefore belongs to an anti-binding state. A key role in whether or not the molecular orbital belonging to the  $E_{g/u}$  is binding or anti-binding is played by the two terms  $H_{AB}$  and  $I(R)$  in eq. 2.34. They are the evaluation of the matrix elements of  $H_e$  between the atomic orbitals that are mainly located at core A and B and the overlap integral of this wave functions, respectively. As can be seen in fig. 2.12, this leads either to a binding orbital with a probability for an electron charge distribution between the two cores and an anti-binding orbital where the probability density drops to zero between the cores. The main drawback of the LCAO method is that the wave function  $\Phi_{g/u}(\vec{R}, \vec{r})$  should approach the wave function for an atom formed out of the two cores, merged together when  $R \rightarrow 0$ , which is not the case.

For molecules with more than one electron, the total spin becomes relevant since the Pauli exclusion principle for the complete wave function has to be obeyed, meaning that the product of electronic wave function and spin wave function has to be antisymmetric. This leads to a singlet state for  $S = 0$  and a triplet state for  $S = 1$  (in the case of a system with two valence electrons), equivalent to atoms with more than one electron. For more details on this, see e.g. chapter 10.3 of [78].

To summarize this section, the typical energy curves for molecules as shown in fig. 2.10 represent the energies  $E_q(R)$  of the electronic state  $q$  which are derived from solving the electronic part of the molecular Schrödinger equation (see eq. 2.23). This solution is always obtained for a fixed internuclear distance  $R$  (and has to be calculated for many different values of  $R$  to obtain the complete energy curve). Therefore, the electronic energies  $E_e$  are a function of this internuclear distance. Neither the rotational nor the vibrational motion of the molecule has been taken into account yet and also no spin-dependent interactions were evaluated. This is because rotation and vibration provide smaller shifts to the energies of the molecular states than the electronic part of the Hamiltonian. They are discussed in the following paragraphs. The spin dependence can have significant influence on the energy curves due to the necessity to have totally symmetrized wave functions in the end, and will be addressed in sec. 4.1.2.

Some light could already be shed on the importance of symmetry properties and on how asymptotically the molecular wave functions and energies go over into the sum of the two atoms the molecule is composed of. It also needs to be mentioned that the methods with which the potential energy curves are obtained as well as the calculation of the wave

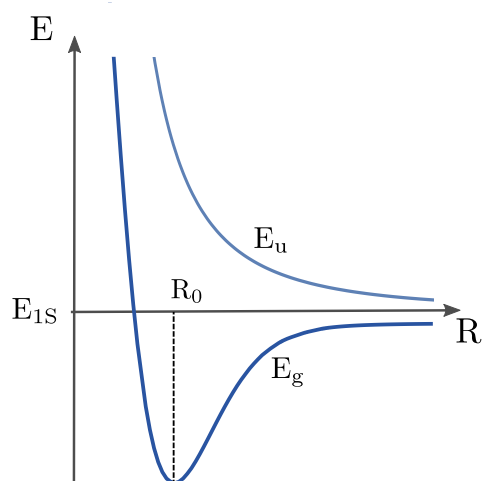


**Figure 2.11:** Schematic of molecular energy curves for the hydrogen ion. The energy curves of a binding ( $E_g$ ) and an anti-binding ( $E_u$ ) state are depicted.

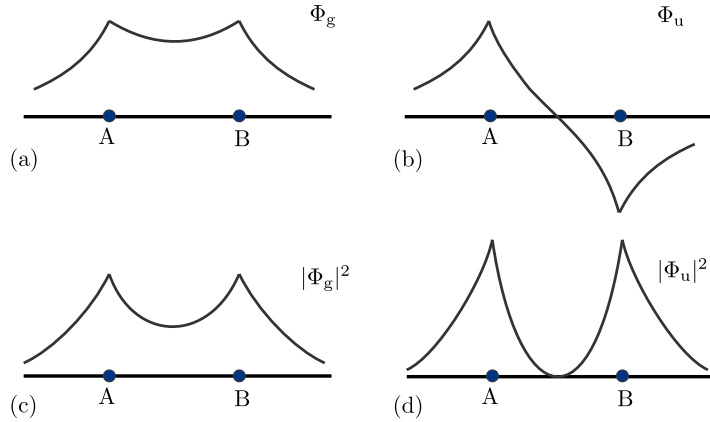


**Figure 2.12: Schematic of binding and anti-binding molecular orbitals.** Shown are the wave functions  $\Phi_{g/u}$  (a, b) and the respective electron probability densities (c, d) for a molecule composed of the atoms A and B. Adapted from [78].

functions are subject to approximations and numerically derived solutions. This already hints at the potential inaccuracy of the outcome of these calculations. In fact, the best a priori methods available today still need to be refined using spectroscopic data and this clearly shows the need for experimental validation of the calculations as well as datasets to which the potential energy curves can be fitted.

## 2.2.2 Vibrational and rotational part of the potentials

For a more complete understanding of graphs like fig. 2.7, the rotational and vibrational structure of a molecule has to be discussed. For this purpose, it is necessary to go back to the complete Hamiltonian for the molecule, eq. 2.18. To derive the complete molecular wave functions, one has to consider the kinetic energies of the nuclei  $T_N$  and the parts of the potential energy associated with the nuclei. Since for any given  $R$  the electronic wave functions  $\Phi_q$ , which have been derived in the section above, form a basis with  $\langle \Phi_q | \Phi_p \rangle = \delta_{qp}$ , the molecular wave functions can be written in this basis:

$$\psi(\vec{R}; \vec{r}_i) = \sum_q F_q(\vec{R}) \Phi_q(\vec{R}; \vec{r}_i) \quad , \quad (2.38)$$

where  $\vec{R}$  is the internuclear distance vector,  $\vec{r}_i$  are the electron position vectors for the  $i$  electrons and  $q$  marks the electronic state. With the electronic part of the molecular wave function already derived in the previous section, to obtain the complete molecular wave function, the coefficients  $F_q(\vec{R})$  need to be found. These coefficients are wave functions which represent the motion of the nuclei against each other when the molecule is in the electronic state  $q$ . To derive these coefficients, eq. 2.18 can be rewritten as

$$(T_N + H_e - E_{total}) \psi(\vec{R}; \vec{r}_i) = 0 \quad . \quad (2.39)$$

Projecting this equation onto the electronic states  $|\Phi_s\rangle$  with  $s = 0, 1, 2, \dots$  and inserting eq. 2.38 leads to:

$$\begin{aligned} \langle \Phi_s | (T_N + H_e - E_{total}) \sum_q F_q(\vec{R}) | \Phi_q(\vec{R}; \vec{r}_i) \rangle &= 0 \\ \Leftrightarrow \sum_q \langle \Phi_s | (T_N + H_e - E_{total}) | \Phi_q \rangle F_q(\vec{R}) &= 0, \quad s = 0, 1, 2, \dots \end{aligned} \quad (2.40)$$

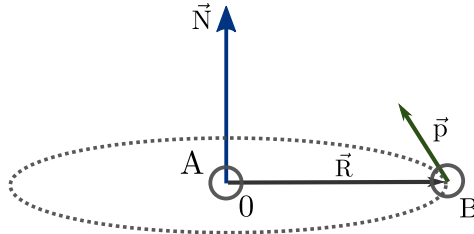


**Figure 2.13: Orbital angular momentum  $\vec{N}$  of the relative motion of two nuclei.** The relative rotation of nucleus  $B$  with momentum  $\vec{p}$  about the position of nucleus  $A$  is related to  $\vec{N}$  via the internuclear distance vector  $\vec{R}$ .

where the bra-ket term denotes an integration over all  $N$  electron coordinates:

$$\langle \Phi_s | (T_N + H_e - E_{total}) | \Phi_q \rangle \equiv \int d\vec{r}_1 d\vec{r}_2 \dots d\vec{r}_N \Phi_s^*(\vec{R}; \vec{r}_1, \vec{r}_2, \dots, \vec{r}_N) (T_N + H_e - E_{total}) \Phi_q(\vec{R}; \vec{r}_1, \vec{r}_2, \dots, \vec{r}_N) . \quad (2.41)$$

It is helpful to rewrite the nuclear kinetic energy operator  $T_N$  in spherical polar coordinates  $\vec{R} = (R, \Theta, \Phi)$ . This leads to:

$$T_N = -\frac{\hbar^2}{2\mu} \left[ \frac{1}{R^2} \frac{\partial}{\partial R} \left( R^2 \frac{\partial}{\partial R} \right) - \frac{N^2}{\hbar^2 R^2} \right] , \quad (2.42)$$

where  $N$  is the orbital angular momentum operator for the relative motion of the two nuclei and is calculated as follows. In fig. 2.13, the related total angular momentum  $\vec{N}$  is illustrated in the body-fixed frame. Together with the orbital angular momentum of the electrons  $\vec{L}$ , it gives the total orbital angular momentum of the molecule  $\vec{K}$ :

$$\vec{K} = \vec{N} + \vec{L} , \quad (2.43)$$

as is also illustrated in fig. 2.14. From fig. 2.14, it also can be seen that  $\vec{N}$  is perpendicular to  $\vec{R}$  and that by this the z-components of  $\vec{K}$  and  $\vec{L}$  are equal in the body-fixed frame (where the z-axis is set along the internuclear axis):

$$\vec{K}_{\bar{z}} = \vec{K} \cdot \hat{\vec{R}} = \vec{L}_{\bar{z}} \quad (2.44)$$

where  $\bar{z}$  marks the z-coordinate in the body-fixed frame and  $\hat{\vec{R}}$  the direction of the internuclear axis. With  $N$  the Schrödinger equation 2.40 can be written as:

$$\sum_q \langle \Phi_s | -\frac{\hbar^2}{2\mu} \frac{1}{R^2} \frac{\partial}{\partial R} \left( R^2 \frac{\partial}{\partial R} \right) + \frac{N^2}{2\mu R^2} | \Phi_q \rangle F_q(\vec{R}) + [E_s(R) - E] \langle \Phi_s | \Phi_q \rangle F_q(\vec{R}) = 0 , \quad (2.45)$$

which is a set of coupled equations since  $\langle \Phi_s | \Phi_q \rangle F_q(\vec{R}) = F_s(\vec{R})$  with  $s = 0, 1, 2, \dots$ . It has to be emphasized that up till this point this set of coupled equations is exact. However, it is at the same time difficult to solve due to the coupling. Therefore, a way to uncouple the equations needs to be found, which will be provided by the so-called *Born-Oppenheimer* or *adiabatic approximation*. The *Born-Oppenheimer approximation* makes use of the fact that the motion of the nuclei is much slower than the motion of the electrons, due to the much higher mass of the nuclei. On the one hand, this means that the electronic wave functions  $\Phi_q$  can

follow adiabatically every motion of the nuclei (that is in the frame of this approximation). On the other hand, it can also be stated that the electric wave functions only vary very slowly with respect to the nuclear coordinates  $R, \Theta, \Phi$ . Hence,  $\frac{\partial \Phi_s}{\partial R} \ll 1$ , so that this term can be neglected. Additionally, only the diagonal term  $\langle \Phi_s | N^2 | \Phi_s \rangle$  needs to be taken into account in equation 2.45. This leads to a decoupling of the N Schrödinger equations:

$$\left[ -\frac{\hbar^2}{2\mu} \frac{1}{R^2} \frac{\partial}{\partial R} \left( R^2 \frac{\partial}{\partial R} \right) + \langle \Phi_s | \frac{N^2}{2\mu R^2} | \Phi_s \rangle + E_s(R) \right] F_s(\vec{R}) = E \cdot F_s(\vec{R}) , \quad (2.46)$$

with  $s = 0, 1, 2, \dots$ . In this equation, the electronic potential  $E_s(R)$  of the electronic state  $s$  plays the same role as the Coulomb potential in the Schrödinger equation of an atom (see eq. 2.1). Each of the  $s$  equations now describes the rotational and vibrational motion of the molecule when it is in the specific electronic state  $s$  (whose energy curve is  $R$ -dependent and of the form shown in fig. 2.10). Due to the decoupling of the equations, it is also possible to write the total molecular wave functions as a product of nuclear and electronic wave function:

$$\psi_s = F_s(\vec{R}) \cdot \Phi_s(\vec{R}; \vec{r}_1, \vec{r}_2, \dots, \vec{r}_N) , \quad (2.47)$$

with  $s = 0, 1, 2, \dots$  and for a molecule with  $N$  electrons. It shall be noted here that this treatment becomes invalid as soon as the motion of the nuclei can no longer be treated as slow, which can be the case in atom-atom collisions. Since the electronic wave functions of the states  $s$  are assumed to be known at this point, the next step is to evaluate the nuclear wave functions  $F_s(\vec{R})$ . For this purpose, it is helpful to return to the total orbital angular momentum  $\vec{K}$ . The total molecular wave functions  $\psi_s$  are eigenfunctions of  $\vec{K}^2$  and of  $K_z$  (note that these are in the laboratory frame now). Therefore, it follows:

$$\vec{K}^2 \psi_s = K(K+1)\hbar^2 \psi_s \quad (2.48)$$

and

$$K_z \psi_s = M_K \hbar \psi_s , \quad (2.49)$$

with  $-K \leq M_K \leq K$ . Due to eq. 2.44, it also follows that

$$L_{\bar{z}} \psi_s = K_{\bar{z}} \psi_s = \pm \hbar \Lambda \psi_s \quad (2.50)$$

and with  $|K| \geq K_{\bar{z}}$  that

$$K \geq \Lambda \Rightarrow K = \Lambda, \Lambda + 1, \Lambda + 2, \dots \quad (2.51)$$

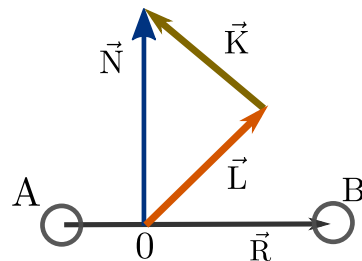


**Figure 2.14: Total orbital angular momentum  $\vec{K}$  of a diatomic molecule.** The schematic shows the relation of  $\vec{K}$  to the orbital angular momentum of the relative motion of the nuclei  $\vec{K}$  with the orbital angular momentum of the electrons  $\vec{L}$ .

This means that the total orbital angular quantum number depends on the eigenvalue  $\Lambda$  of the wave function of the electronic state. With eq. 2.43, 2.24 and 2.49, one can now rewrite eq. 2.46:

$$\left[ -\frac{\hbar^2}{2\mu} \frac{1}{R^2} \frac{\partial}{\partial R} \left( R^2 \frac{\partial}{\partial R} \right) + \frac{\hbar^2 K(K+1)}{2\mu R^2} + E'_s(R) \right] F_s(\vec{R}) = E \cdot F_s(\vec{R}) \quad , \quad (2.52)$$

where now

$$E'_s(R) = E_s(R) - \frac{\hbar^2 \Lambda^2}{2\mu R^2} + \frac{1}{2\mu R^2} \langle \Phi_s | L_x^2 + L_y^2 | \Phi_s \rangle \quad . \quad (2.53)$$

The  $L_x^2 + L_y^2$  term originates from  $N^2 = (K - L)^2$  and  $L = L_x^2 + L_y^2 + L_z^2$ . In the following, all terms in  $E'_s$  will be neglected except the  $E_s$  term because  $1/\mu \ll E_s$ . Consequently, the rotational and vibrational motions of the nuclei are decoupled in eq. 2.52, allowing the use of a separation ansatz for  $F_s(\vec{R})$ :

$$F_s(\vec{R}) = \frac{1}{R} \cdot \tilde{F}_{v,K}^s(R) \cdot \tilde{H}_{K,M_K}^\Lambda(\Theta, \Phi) \quad , \quad (2.54)$$

where  $v$  is the vibrational quantum number,  $\tilde{F}_{v,K}^s(R)$  the wave function of the radial i.e. vibrational motion and  $\tilde{H}_{K,M_K}^\Lambda(\Theta, \Phi)$  the angular wave function which is an eigenfunction of  $K^2$  and  $K_z$  for a given  $\Lambda$ . To solve eq. 2.52 with this separation ansatz, one uses the approximation that for a stable molecule the nuclear motion does not vibrate very much, so that  $R$  is restrained to  $R_0 \pm \Delta R$ , where  $R_0$  marks the minimum of  $E_s(R)$ . To derive the energy spectrum of the rotational motion, the molecular vibration is completely abandoned by setting  $R = R_0$  in eq. 2.52. This directly leads to the rotational energy for the separation ansatz as:

$$E_r(R_0) = \frac{\hbar^2}{2\mu R_0^2} K(K+1) = BK(K+1) \quad , \quad (2.55)$$

where

$$B = \frac{\hbar^2}{2\mu R_0^2} = \frac{\hbar^2}{2I_0} \quad , \quad (2.56)$$

with  $I_0$  being the moment of inertia of the molecule at the equilibrium distance and  $B$  the *rotational constant* (of the electronic state  $s$ ). This approximation is also referred to as the *rigid rotor approach*. With eq. 2.55, a formula for the rotational energy spectrum of a molecular electronic state  $s$  has been derived. The last step is the treatment of the vibrational motion.

Since in a rigid rotor no vibrational motion occurs, it is not suited to find the energy spectrum of the vibrational motion. To derive the vibrational spectrum, one has to allow for  $R = R_0 \pm \Delta R$ . Thereby, a parabolic approximation to the electronic potential  $E_s(R)$  can be applied, using a Taylor expansion to parabolic order around  $R_0$ . This leads to:

$$E_s(R) \simeq E_s(R_0) + \frac{1}{2} k_s (R - R_0)^2 \quad , \quad (2.57)$$

with

$$k_s = \frac{d^2 E_s(R)}{dR^2} \Big|_{R=R_0} \quad . \quad (2.58)$$

Inserting this into eq. 2.52 (with  $E'_s(R) = E_s(R)$ ) gives:

$$\left[ -\frac{\hbar^2}{2\mu} \frac{d^2}{dR^2} + \frac{1}{2} k_s (R - R_0)^2 + E_s(R_0) + \frac{\hbar^2}{2\mu R_0^2} K(K+1) - E \right] F_s(\vec{R}) = 0 \quad . \quad (2.59)$$

With the knowledge that  $E = E_s(R_0) + E_v + E_r$  (for values near  $R_0$ ) and the fact that the first two terms in eq. 2.59 are the operator for the kinetic energy of the molecular vibration and  $E_r = \frac{\hbar^2}{2\mu R_0^2} K(K+1)$ , it is apparent that by separating the terms for  $E_r$  and  $E_s$  from eq. 2.59 with help of the separation ansatz eq. 2.54, the eigenfunctions and eigenvalues for the vibrational motion can be obtained by solving:

$$\left[ -\frac{\hbar^2}{2\mu} \frac{d^2}{dR^2} + \frac{1}{2} k_s (R - R_0)^2 - E_v \right] \tilde{F}_{v,K}^s(R) = 0 \quad , \quad (2.60)$$

which is an equation for a linear harmonic motion with a force constant  $k_s$ . This leads to a vibrational energy in the parabolic approximation of

$$E_v = \hbar\omega_0 \left( v + \frac{1}{2} \right) \quad , \quad (2.61)$$

with  $\omega_0 = (k_s/\mu)^{1/2}$ .

Combining the gathered knowledge about the potential energy curves and eigenstates of a molecule, the picture in fig. 2.7 is now easier to understand. The largest energy in molecules is the electronic energy whose value is dependent on the distance  $R$  between the two nuclei. This distance is changed by vibrations, which behave around the equilibrium position  $R_0$  similar as in a harmonic oscillator. Therefore, their energies are equally spaced. Since the electronic potential is not harmonic for large and very small  $R$ , the spacing of the vibrational energies becomes the smaller the higher the vibrational energy is. The vibrational energies give also an idea of how much the distance between the nuclei varies inside a molecule when it is in a certain electronic-vibrational state. In the classical picture, the energy of the vibrations makes it only possible for the nuclei to separate from each other by certain distance and to approach only up to a certain point. The positions of these points are given by the intersection of the vibrational levels with the electronic potential curve in fig. 2.7. If the vibrational energy becomes larger than  $E_{el}(R = \infty)$ , the Coulomb force of the electrons is no longer able to keep the two nuclei together. Therefore, only a finite number of vibrational motions exists until the vibrations become too strong and thereby their energies too large so that the molecule, being in the specific electronic state  $s$ , dissociates. For the nuclei to even reach very large separations, the molecule cannot be in a low vibrational state. This explains why loosely bound Feshbach molecules are formed in a high vibrational state. For every vibrational motion, the molecule can perform a variety of rotational motions, which add further structure to each vibrational energy level.

At the end of this chapter, it shall be mentioned again that many approximations have been involved to derive the simple textbook picture of fig. 2.7. For more detailed studies, it has for example to be taken into account that every rotation stretches the molecule a little due to the centrifugal forces and therefore a rotation-vibration coupling occurs, making the separation ansatz used for the rotation-vibration wave function imprecise. Moreover, no spin-dependent coupling has been included so far. This is because the energy scale on which the effects occur is below the rotational energy scale. Nevertheless, these spin-dependent effects are the ones which lead to coupling between different electronic states of the molecule and are therefore mandatory for the occurrence of Feshbach resonances.

### 2.2.3 Hund's cases

To understand the notation applied in chap. 4, it is necessary to consider the different coupling schemes of the spins. The spins of all electrons form the total electron spin of the molecule:

$$\vec{S} = \sum_{i=1}^N \vec{S}_i \quad , \quad (2.62)$$

where  $\vec{S}_i$  is the single electron spin and  $N$  is the number of electrons in the molecule. The same applies for the total angular momenta of the electrons:

$$\vec{L} = \sum_{i=1}^N \vec{L}_i , \quad (2.63)$$

where  $\vec{L}_i$  is the single electron angular momentum. Like in atoms, the motion of the electrons induces a magnetic field which leads to the coupling of the total spin to the total angular momentum:

$$A \cdot \vec{L} \cdot \vec{S} , \quad (2.64)$$

where  $A$  is the coupling constant. In distinction to atoms, molecules rotate, leading to the rotational energy structure already discussed. Additionally, it induces another magnetic field which interacts with the electrons in the molecule, resulting in the spin-rotation coupling:

$$\bar{\Gamma} \cdot \vec{N} \cdot \vec{S} , \quad (2.65)$$

where  $\bar{\Gamma}$  is a constant and  $\vec{N}$  is the orbital angular momentum operator for the relative motion of the two nuclei introduced in eq. 2.43.

Ignoring the nuclear spins (which interact with  $\vec{N}$ ,  $\vec{L}$  and  $\vec{S}$ , but this interaction is small and most prominent contributions stem from symmetry effects in the case of homonuclear molecules), the total angular momentum operator for a diatomic molecule reads:

$$\mathbf{J} = \mathbf{L} + \mathbf{N} + \mathbf{S} = \mathbf{K} + \mathbf{S} , \quad (2.66)$$

where  $\mathbf{K}$  is the total angular momentum operator for a spinless molecule (see equation 2.43).

If there are no external fields present, the molecular wave function has to be an eigenfunction of  $\mathbf{J}^2$  and  $J_z$  (where  $z$  is in the laboratory frame). The exact order of the coupling of the different momenta in a molecule will depend on the relative strength of electrostatic, spin-orbit and spin-rotation energy:

- (i) The electrostatic coupling between the nuclei and the electrons forces the electronic wave function to rotate together with the molecule. A measure of the strength of this effect is the separation between two adjacent electronic levels  $|\Delta E|$  with different  $\Lambda$ -values.
- (ii) The magnitude of the spin-orbit coupling depends on its coupling constant  $A$ . The value of  $A$  depends on the multiplet (i.e. the unperturbed level  $(\gamma, L, M)$ ) in which the spin-orbit coupling is investigated as a perturbation.
- (iii) The strength of the spin-rotation coupling depends on the magnitude of the rotational constant  $B = \hbar^2 / (2\mu R^2)$ , see equation 2.56.

Using these three measures, Hund identified five limiting cases, which go by the names Hund's case (a) to (e). A detailed description of these can be found e.g. in [78]. For the representation of the molecules in the context of this work, two cases are of main importance. These are case (a) and (e), which therefore shall be briefly discussed in the following.

### 1. Hund's case (a): $|\Delta E| \gg |A| \gg B$

Hund's case (a) leads to the common spectroscopic notation used in molecules. The electrostatic coupling is the strongest; therefore, the electrons will rotate together with the nuclei. The coupling between their spin and the angular momentum is taken into

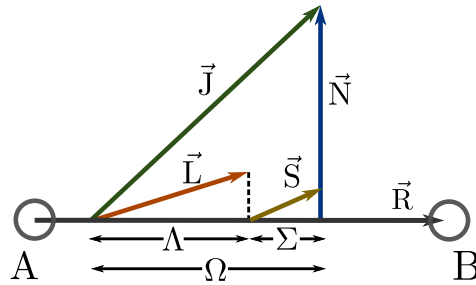


Figure 2.15: Hund's case (a).

account next. The weakest perturbation is the coupling of the total electron spin to the magnetic field, induced by the rotation of the nuclei. This means that because of the axial symmetry of the electrostatic interaction,  $\vec{L}$  presses about the internuclear axis and  $\vec{L}_z = \pm \Lambda \hbar$  is a good quantum number. Since the spin-orbit coupling is large compared to the spin-rotation coupling, the electron spin  $\vec{S}$  is orientated along the intermolecular axis, too.  $S^2$  and  $S_z$  are good operators and commute with the molecular Hamiltonian. This means that a simultaneous eigenfunction can be found for  $S^2$ ,  $S_z$ ,  $L_z$ ,  $J^2$  and  $J_z$ , with  $|S, \Sigma\rangle$  being the eigenstates of  $S^2$ ,  $S_z$  and  $\Omega = \pm \Lambda + \Sigma$  being the eigenvalue of  $J_z$ . The eigenbasis can therefore be chosen as  $|S, \Sigma, \pm \Lambda, J, \Omega, M_J\rangle$ . With  $\vec{N}$  being perpendicular to the intermolecular axis and  $\vec{J} = \vec{\Omega} + \vec{N} = \Omega \cdot \vec{R}$ , this yields the picture of the coupling case (a), as is shown in fig. 2.15. Because  $\Sigma$ ,  $\pm \Lambda$  and  $\Omega$  are good quantum numbers, the spectroscopic notation is:

$$^{2\Sigma+1}\Lambda_\Omega . \quad (2.67)$$

Treating the spin-orbit and spin-rotation coupling as small perturbations in the given eigenbasis gives rise to the energy spacings, as can be seen in detail in [78].

## 2. Hund's case (e): $B \gg |\Delta E| \gg |A|$

This Hund's case describes the case of a molecule with a very large internuclear distance. Thereby, the strongest coupling is the one to the rotation of the two nuclei. The other couplings are basically absent. This means that the description of the atom-pair state can be performed in the atomic basis  $|(i, s, f, m)_A; (i, s, f, m)_B; F, m_f\rangle$  where  $s_A$  is the electron spin,  $i_A$  the nuclear spin,  $f_A$  the total angular momentum and  $m_A$  its projection onto the space-fixed axis of the atom, in this case atom A.  $F$  and  $m_f$  are the total angular momentum and its projection of the state onto the space fixed axis of atom A [4]. For loosely bound Feshbach molecules, this representation can be chosen.

It shall also be mentioned that there are some quantum numbers, which are always preserved as they come from strong symmetries and constants of motion. These are the total energy (stemming from time reversal symmetry), total linear momentum (originating from translation symmetry), the parity (stemming from reflection symmetry) and the total angular momentum (originating from rotational symmetry).

# Chapter 3

## Scattering theory

In a gas of particles, scattering is a major interaction process. It significantly influences the behaviour of the ensemble, creating its thermal contact and its (internal) pressure. On a quantum-mechanical basis even more effects appear, one example are Feshbach resonances. In the following, the theory of scattering processes will be introduced on a level enabling the reader to understand the experiments performed and presented in this thesis. Since scattering theory is a very complex subject, the introduction given here will just scratch the surface of this field of physics.

### 3.1 Classical scattering theory

Basic classical scattering theory deals with the interaction of hard spherical particles which may interact by contact force or even experience an additional central force between them. Already the basic principles give insight into the more complex quantum-mechanical scattering theory employed in the calculation of Feshbach resonances.

As a starting point, the simplest experimental situation is envisioned. A collimated beam of particles with a defined kinetic energy is shot at a target. The target contains scatterers which are spaced so far apart from each other that they can be treated as isolated for the process of scattering (excluding effects like diffraction which appears e.g. when a beam of electrons hits a crystal). Every collision leads to a change in the internal state of the system. This can be e.g. the directions of the particles, their internal energies, or a change in the particle composition in the case of a chemical reaction. The change in the initial (*i*) to final (*f*) state of the system is measured by a detector. This can be a mass or charge-selective detector or a detector placed at a certain angle with respect to the incoming beam, so that only the particles scattered into that direction will be detected. The fundamental quantity in classical

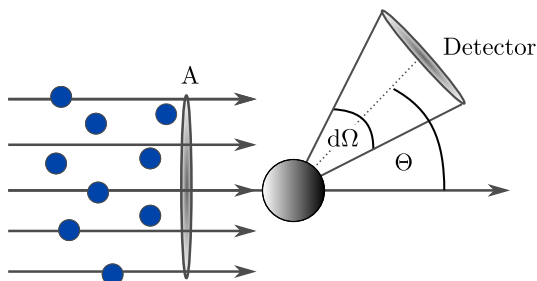


**Figure 3.1: Differential cross section.** A beam of particles (blue dots), passing an area  $A$ , interacts with a scatterer (grey circle). A fraction is scattered into the solid angle  $d\Omega$  and detected. The detector is placed at the angle  $\theta$ . The second angle ( $\phi$ ) is set to zero for lucidity.

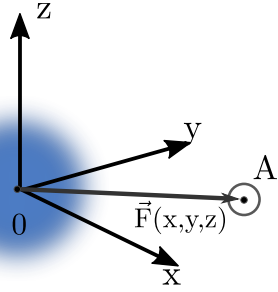


**Figure 3.2: Central force.** The force vector  $\vec{F}$  joins the force centre (positioned at the origin) and the centre of  $A$ .

scattering which describes all these possible processes is the *differential cross section*:

$$\frac{d\sigma_{if}}{d\Omega} = I_{if}(\theta, \phi) \quad , \quad (3.1)$$

where  $I_{if}$  is defined as the number of scattered particles per time and angle divided by the incident current per time;  $d\Omega = \sin(\theta)d\theta d\phi$  is the solid angle. This is illustrated (for  $\phi = 0$ ) in fig. 3.1: The detector, placed at an angle  $\theta$  will detect the particles which are scattered into the solid angle  $d\Omega$ . All relevant quantities in classical scattering can be related to the differential cross section. For example, the total cross section  $\sigma_{if}$  is simply the integral over the complete solid angle of the differential cross section.

One difficulty arises as soon as the experiment setup is no longer a simple beam experiment. Since many experiments are performed in a bulk system (e.g. a gas inside a container), the measurable quantity becomes a rate constant, called the *scattering rate*. In fact, this is the quantity which will play a key role when investigating Feshbach resonances, albeit in its quantum-mechanical description. For classical scattering, the total cross section can be related to the scattering rate  $k(T)$  at temperature  $T$  by:

$$k(T) = \langle k_{if}(T) \rangle = \left\langle \int_0^\infty v \sigma_{if} \left( \frac{1}{2} mv^2 \right) P(v) v^2 dv \right\rangle \quad , \quad (3.2)$$

where  $P(v)$  is the relative velocity distribution,  $v$  is the velocity and the angle brackets indicate an average over all initial internal states of the system.

The simplest possible collision is the elastic scattering of two particles by a central force. For this collision, conservation of particle number and kinetic energy in the centre of mass frame apply. For a central force the magnitude of the force on an object only depends on the distance between the object and the origin of the force directed along a straight line between object and force centre (see fig. 3.2). A conservative central force implies two conservation laws for the scattering process. First, the total angular momentum is conserved in direction and magnitude, second, the total mechanical energy is conserved, too. Conservation of the total angular momentum direction directly leads to the fact that scattering by a conservative central force must take place in a plane. Thus, the problem is effectively two-dimensional. A schematic of a scattering event introducing all parameters which will be used to describe the scattering is shown in fig. 3.3. The magnitude of the vector  $\vec{r}$  is the distance between the two particles,  $\phi$  is the angle between  $\vec{r}$  and the incident axis (here  $z$ ) and  $b$  is the so-called impact parameter which gives the distance of the incoming particle to the  $z$ -axis for  $r \rightarrow -\infty$ . The important parameters with respect to the scattering event are the distance of the classical turning point  $a$  (which effectively marks the shortest distance the two scattering particles will have during the scattering process) and the deflection angle  $\Theta$ . For  $|\vec{r}| \rightarrow \infty$  it follows that  $\phi \rightarrow \Theta$ . The formula for the change of the incident angle  $\phi$  with changing  $r$  in the centre

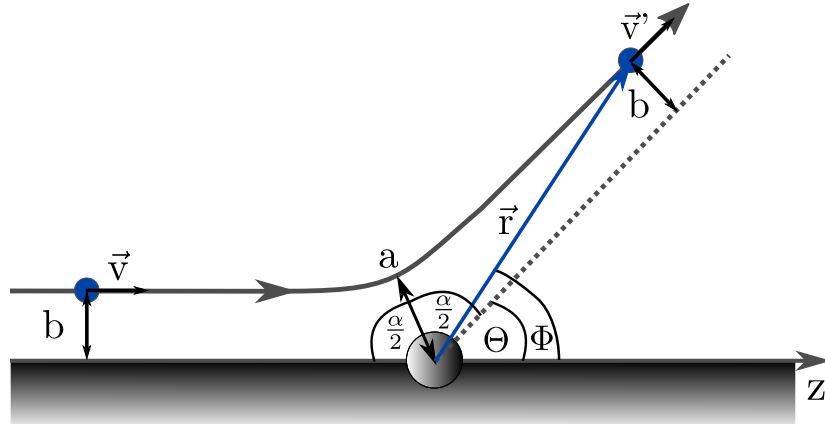


**Figure 3.3: Trajectory of scattering.** A particle (blue circle) approaches a scatterer (grey circle) with velocity  $\vec{v}$  and an impact parameter  $b$ . The classical turning point is reached at the shortest distance  $a$  between particle and scatterer.  $\Theta$  is the angle of deflection. For  $|\vec{r}| \rightarrow \infty$  it follows that  $\phi \rightarrow \Theta$ .

of mass system can be derived from the equations of motion for the classical trajectory which are (see e.g. [79]):

$$L = mvb = mr^2\dot{\phi} , \quad (3.3)$$

$$E = \frac{1}{2}mv^2 = \frac{1}{2}m\dot{r}^2 + \frac{1}{2}mr^2\dot{\phi}^2 + V(r) . \quad (3.4)$$

In eq. 3.4,  $v$  is the initial velocity of the particle far away from the scattering potential. Due to energy conservation, the kinetic energy of the incoming particle has to be equal to the energies in the vicinity of the scattering potential. Because  $L$  is conserved, a representation in polar coordinates is advantageous. With this, it follows:

$$\frac{\dot{\phi}}{\dot{r}} = \frac{d\phi}{dr} = \pm \frac{b}{r^2[1 - b^2/r^2 - V(r)/E]^{1/2}} , \quad (3.5)$$

where the plus sign has to be chosen for outward and the minus sign for inward motion. Due to the mentioned necessity for momentum and energy conservation, the conditions for scattering are completely defined by the incident velocity  $\vec{v}$  and the impact parameter  $b$  as shown in fig. 3.3.

The deflection angle  $\Theta$  is directly related to  $\phi$  via  $\alpha = |\phi(r = \infty) - \phi(r = -\infty)|$  and  $\pi = \Theta + \alpha$ . Therefore, its dependence on the energy and angular momentum as well as on the incident velocity and the impact parameter  $b$  can directly be derived by integrating eq. 3.5 from minus infinity to infinity. For most cases, the effects of a collision are observed by a detector only after the event. Therefore, it is only necessary to integrate from the classical turning point  $a$  outward with  $\alpha/2 = |\phi(r = \infty) - \phi(r = a)|$ , leading to:

$$\Theta(E, L) = \pi - 2b \int_a^\infty \frac{dr}{r^2[1 - b^2/r^2 - V(r)/E]^{1/2}} . \quad (3.6)$$

The deflection function depends on the scattering potential  $V(r)$  which can be repulsive, attractive or composed of an attractive and a repulsive part (such as a molecular potential). In fig. 3.4, the behaviour of  $\Theta(E, L)$  is qualitatively shown for these three cases as a function of the impact parameter  $b$  and for different kinetic energies. For a purely repulsive potential, the deflection angle goes to  $\pi$ , meaning total reflection, when the scattering parameter goes to zero. This is equivalent to a direct collision between two billiard-ball like hard spherical

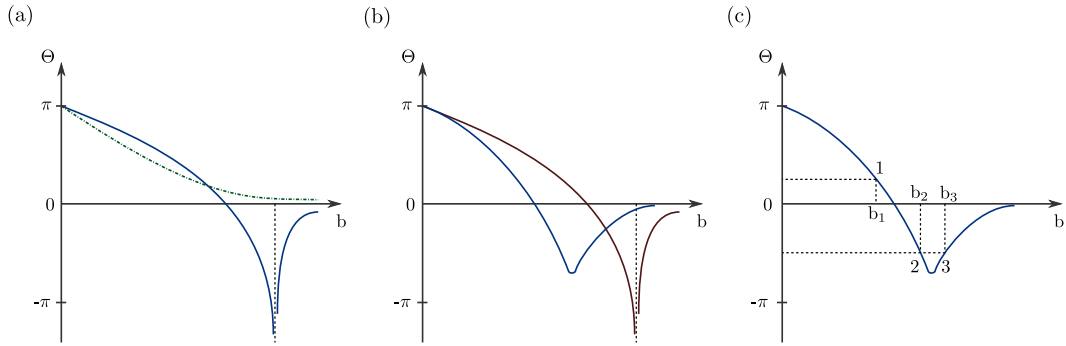


**Figure 3.4: Schematic of classic deflection angle function** The behaviour of the deflection angle  $\theta$  with respect to the scattering parameter  $b$  is shown in (a) for a repulsive (green dashed-dotted curve) and an attractive (blue curve) potential and in (b) for an effectively attractive potential for two different values of the scattering energy  $E$  (blue and red curve, respectively). In (c) the case is shown where two different values of  $b$  lead to the same value of  $\theta$  in case of an effectively attractive potential. For exact calculations and graphs, see [79].

particles. Conveniently, the scattering angle decreases monotonically for ever larger  $b$  as the influence of the repulsive potential decreases further and further.

For an attractive potential, there is no scattering for very small and very large  $b$ . The maximal deflection angle is also called the *rainbow angle*, scattering at the corresponding impact parameter is called *rainbow scattering*. The value of the rainbow angle can reach  $-\infty$  which corresponds to a capture of the colliding particles. This singularity is called an *orbiting singularity*. Fig. 3.5 shows a sketch showing all these possible trajectories.

An attractive potential with a repulsive core finally combines the effects of the two aforementioned cases. For  $b \rightarrow 0$  it shows total backscattering and for  $b \rightarrow \infty$  no scattering occurs. In the intermediate section rainbow scattering is present and, depending on the incident kinetic energy also orbiting singularities can exist.

When examining the dependence of the distance of the classical turning point  $a$  on the impact parameter  $b$ , another feature of scattering theory can be illustrated which will reappear as an argument to simplify calculations for quantum-mechanical scattering of ultracold atoms in sec. 3.2.1 and sec. 4.2. For the distance of the classical turning point  $a$  at which  $\dot{r} = 0$  (since it is the minimal distance between the two colliding particles), it follows

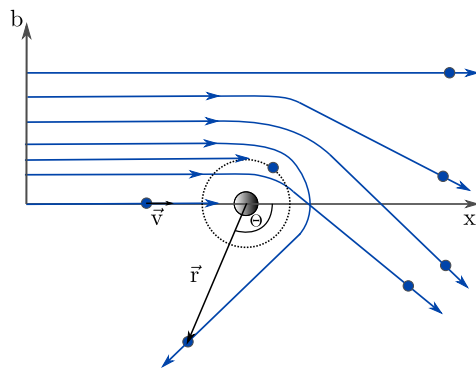


**Figure 3.5: Schematic of scattering on an attractive potential.** Trajectories for particles with velocity  $|\vec{v}|$  are shown for different impact parameter values. Orbiting singularities can appear as indicated by the black dotted circle.

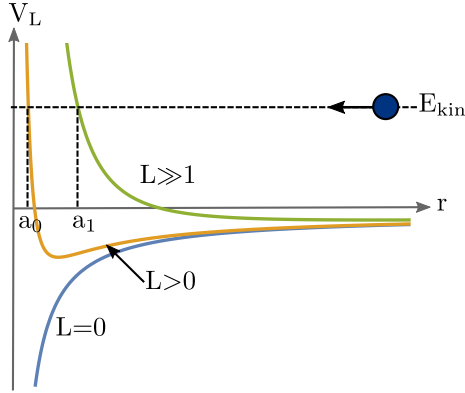


**Figure 3.6:** Dependence of distance of the classical turning point  $a$  on  $L$ . For a scattering process with kinetic energy  $E_{\text{kin}}$  the distance  $a$  increases with increasing  $L$ .

from eq. 3.4 and 3.3 that

$$E = \frac{1}{2}mr^2 + V(r) + \frac{L^2}{2mr^2} = \frac{1}{2}mr^2 + V_L(r) . \quad (3.7)$$

The  $L$ -dependent term acts as an effective centrifugal barrier. This means that the higher the value of  $L$  is, the larger is also the distance of the classical turning point, moving it ever farther away from the central part of the potential  $V(r)$ . This is illustrated in fig. 3.6. Because  $L = m|\vec{v} \times \vec{r}| = mvb$ , a large impact parameter  $b$  also means a large angular momentum  $L$  and vice versa. Because the two colliding particles with large  $L$  do not come close to each other, it is often said that they "only feel the long range part of the potential". Equivalently, the collision only "samples the long-range part of the interaction potential", often making it possible for such cases to ignore the short-range part of the potential when investigating the collision process. This is illustrated in fig. 3.7. On the other hand, the particles experience the full range of the interaction potential in the case of low angular momentum, i.e. small impact parameter or low velocities.

Up to this point, the discussion dealt with the simplest case possible: treating every collision as a separate trajectory. In a real experiment, however, a treatment of every particle collision as a separate trajectory is not possible. This leads to the more appropriate (differential) collision cross section, which has already been mentioned, see eq. 3.1. It is defined as intensity of scattering per unit solid angle and time and is the most closely related

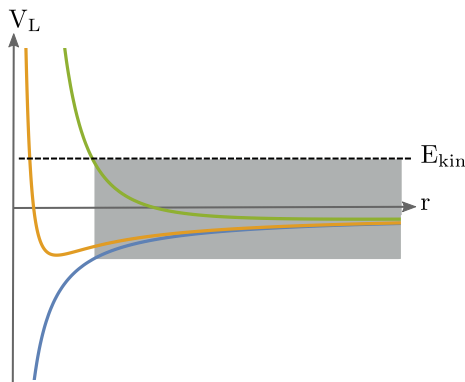


**Figure 3.7:** Probing only the long range-part of the potential. The potential energy curves are given for different values of  $L$ , where  $L$  increases from the blue to the green curve. Particles with a high velocity and/or with a high impact parameter ( $L \propto b$ ) (green curve) only experience the long-range part of the potential, indicated in the figure by a grey shaded area.

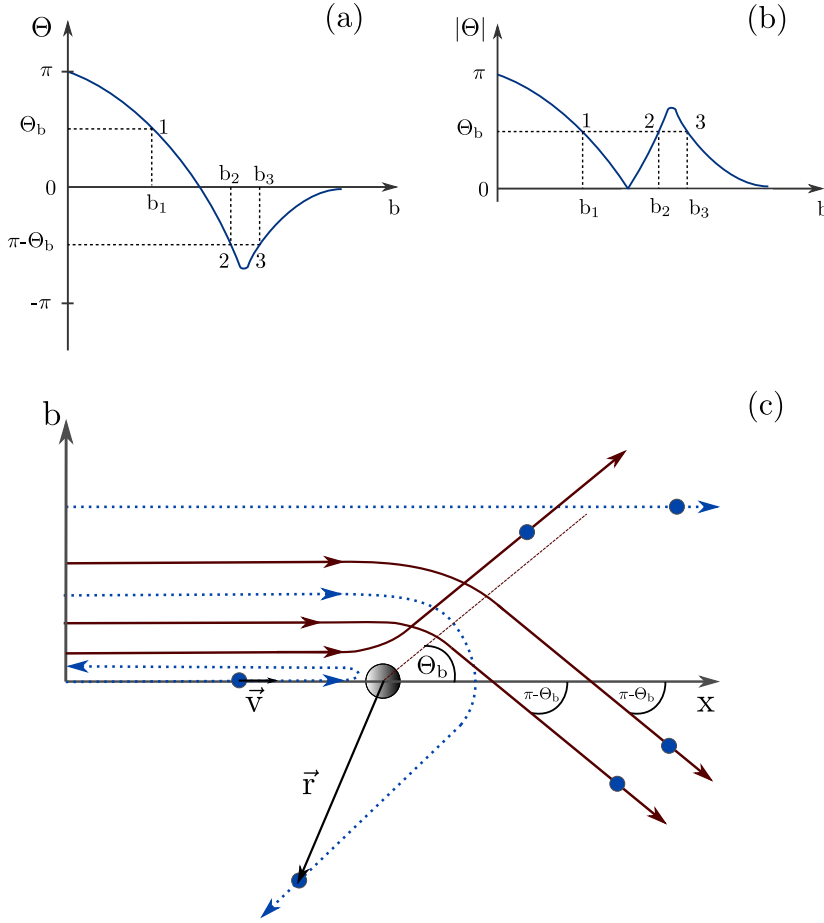


**Figure 3.8: Degeneracy of  $|\Theta|$  in  $b$ .** More than just one value for the impact parameter can lead to the same scattering angle in case of scattering on an effectively attractive potential (a). For  $|\Theta|$  the degeneracy increases further (b). In (c) three different trajectories are shown which all lead to the same value of  $|\Theta|$  (red lines).

representation to the trajectory picture for elastic scattering. However, in an experiment it is not possible to distinguish scattering into positive or negative angles. Thus, the angle  $\theta$  in eq. 3.1 is connected to the deflection angle  $\Theta$  from eq. 3.6 by:

$$\theta = |\Theta|, \quad 0 < \theta < \pi . \quad (3.8)$$

Thus, more than one value for the impact parameter can exist that lead to the same scattering angle. This is illustrated in fig. 3.8. In terms of the impact parameter, the differential cross section can be written as

$$\frac{d\sigma}{d\Omega} = I(\theta, E) = \sum \left| \frac{b}{\sin(\theta)[d\theta/db]} \right| , \quad (3.9)$$

where the sum accounts for the possibility that more than one value of  $b$  lead to the same angle  $\theta$ .

With this formula for the classical differential cross section, the scattering cross sections for different potentials can be calculated, leading e.g. to uniform scattering for a classical hard spherical potential. In the case of Rutherford scattering from a Coulomb potential, the classical calculation interestingly yields the same result as the quantum-mechanical treatment. For more information on the various treatments of classical scattering problems see e.g. [79].

Investigating collisions of quantum-mechanical particles, as in the case of low-temperature atom-atom collisions, the classical scattering theory experiences fundamental problems. One example is the idea of particle trajectories which are used to describe the classical scattering process. No particle trajectory will ever be precisely defined in quantum mechanics due to Heisenberg's uncertainty principle. Say, for example, the uncertainty in the impact parameter is  $\Delta b \approx \hbar/\Delta p_{\perp}$ , stemming from the uncertainty in the transverse momentum of the particle  $p_{\perp}$ . This leads via  $\Delta p_{\perp}/(mv) = \Delta\theta$  to an uncertainty in the final scattering angle. Because the scattering angle is a key variable in the description of scattering processes, it needs to be precisely defined. In that case, a complete uncertainty in the impact parameter has to be accepted. This is the basis for the partial wave formulation in the quantum-mechanical scattering theory, see sec. 3.2.1.

Moreover, possible interferences between different trajectories have to be taken into account which leads to possible oscillations in the differential cross section.

Finally, the orbiting singularity shall be mentioned. It is no longer present in quantum-mechanical scattering but is replaced by another form of particle trapping called *shape resonances*, which will be discussed in sec. 3.2.4.

In summary, this brief overview of the classical scattering theory illustrates that observables which will later play a key role in quantum-mechanical scattering, like the differential cross section, are already used in classical terms. Additionally, some arguments, like the argument of the impact of a high angular momentum on the part of the scattering potential "seen" by the colliding particles will reappear in the next sections. Nevertheless, the laws of quantum mechanics also impose clear restrictions on the usability of classically derived formulas in terms of quantum-mechanical scattering.

## 3.2 Quantum-mechanical treatment of scattering

The molecular potentials discussed in chap. 2 describe the electronic potential energy curves of a two-atomic molecule. They display the various possible states a molecule can be in as well as their energy dependence. Each electronic state has a finer structure of vibrational and rotational states and on top of that there is the fine and hyperfine structure of the molecule.

The potential energies are given as a function of the internuclear distance of the two nuclei. While a stable molecule will exist at the minimum of the potential curves at the mean internuclear distance  $R_0$ , the nuclei could well be also separated farther than this distance or come closer to each other. In fact, this is what happens when the molecule vibrates.

In addition, the  $R$ -dependence of the potential curves allows for a slightly different angle

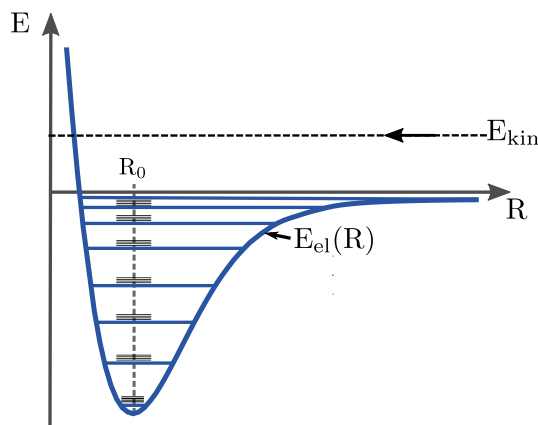


**Figure 3.9: Scattering on a molecular potential.** A scattering process with energy  $E_{kin}$  which lies in the continuum of the molecular potential curve (blue curve) is shown.

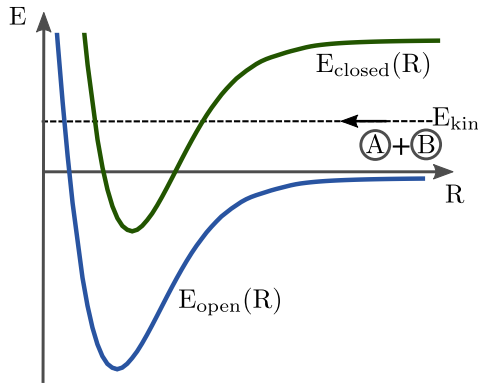


**Figure 3.10: Open and closed channel in scattering process of atoms A and B.** Schematically shown are the PECs of an open (blue curve) and a closed channel (green curve). The energy of the two scattering atoms lies in the continuum of the open channel but is below the threshold of the closed one.

of view: The molecule does no longer exists at the asymptote of the potentials for  $R \rightarrow \infty$  because the state of the system is fully described by two separate atoms. This means that the different potential curves can also be envisioned to describe a scattering process of two atoms. In that case, the atoms can have a certain kinetic energy which will be in the continuum for the ground state of the molecule, as shown in fig. 3.9. This means that the two atoms can come close to each other until they approach the short-range part of the potential where they reach the turning point and depart again. Since their energy is higher than all bound states of the ground-state potential, they will not form a molecule but just scatter with each other. In fact, this process is the quantum-mechanical view of the classical elastic scattering process described above. In fig. 3.10, additionally to the ground state also the first excited state of the molecule is depicted. It can be seen that the impact energy of the two atoms is not high enough to enter this higher-lying state even though a molecule in that state would be stable. This picture leads to the definition of *open* and *closed channels* in a quantum-mechanical scattering process. The first important specification is regarding the notation *channel*. A channel incorporates the full set of information which is needed to clearly identify the state in which the system is at a given moment. Therefore, the channel information consists of the kinetic energy of the state (in the case of collisions in a gas of atoms, this is associated with the temperature of the ensemble) and a full set of quantum numbers to describe the state of the particles. In the case of scattering of two atoms, normally the quantum numbers given in Hund's case *e* are used. An example for a notation for a channel is:

$$|A(n, l, m_l, \dots), B(n, l, m_l), P, E_{\text{collision}}\rangle_{\text{open/closed}} , \quad (3.10)$$

where  $A(n, l, m_l, \dots)$  and  $B(n, l, m_l, \dots)$  describe the state of atom A and atom B in terms of atomic quantum numbers,  $P$  gives the parity of the scattering state and  $E_{\text{collision}}$  the kinetic energy of the collision. The term "open" refers to a scattering (albeit molecular) potential whose threshold lies below the kinetic energy of the scattering state. In the example from fig. 3.10, the lower curve represents an open channel for the atom pair with the given kinetic energy. On the other hand, "closed" means that although there might be a bound state in a higher-lying potential available, the energy of the system is below the threshold of that potential curve and therefore the bound state is not accessible for the two scattering atoms (excluding for the moment coupling).

To derive the total cross section of an elastic collision, it has to be calculated as the sum

over the cross sections of all open channels:

$$\sigma_{total} = \sum_i \sigma_{open}^i , \quad (3.11)$$

where  $i$  runs over all open channels.

In the following, the most prominent scattering process shall be discussed which is also of great importance for Feshbach resonances. This is the scattering by a central, non-relativistic potential. First, a representation of the system is derived. It describes the scattering process as a wave function of an incoming and an outgoing wave with an amplitude which contains the complete scattering information. This scattering amplitude is then related to the physical parameters of interest such as the scattering cross section. Next, the partial wave method is introduced which has substantial benefits for the calculation of scattering processes at low temperatures. In this partial wave method, all information is contained in the scattering phase shift which will be directly related to the scattering amplitude. Finally, considering collisions at ultracold temperatures and using the derived partial wave method and scattering phase shift, important textbook equations for the scattering length are obtained.

The starting point is the time-dependent Schrödinger equation since scattering is a time-dependent process:

$$i\hbar \frac{\partial}{\partial t} \Psi(\vec{r}, t) = \left[ -\frac{\hbar^2}{2\mu} \nabla^2 + V(\vec{r}) \right] \Psi(\vec{r}, t) . \quad (3.12)$$

The equation is already written in the centre of mass system, with  $\mu = \frac{m_a m_b}{(m_a + m_b)}$  being the reduced mass of the two particles  $a$  and  $b$  and  $\vec{r}$  being the distance vector between the two particles. Since the interest for an experiment investigating the scattering inside a sample system often lies in the steady state of the system (though also time-resolved studies of scattering processes are performed, see e.g. [88, 89]), the focus is on the derivation of the steady-state solutions with:

$$\Psi(\vec{r}, t) = \Psi(\vec{r}) \cdot e^{-iEt/\hbar} , \quad (3.13)$$

where  $\Psi(\vec{r})$  is the solution of the time-independent Schrödinger equation and  $E$  is the energy of the particle with

$$E = \frac{p^2}{2\mu} = \frac{\hbar^2 k^2}{2\mu} . \quad (3.14)$$

Since the scattering by a central potential is investigated here, the total energy and the momentum have to be conserved for the initial  $i$  to final  $f$  state, therefore:

$$p = |\vec{p}_i| = |\vec{p}_f|, \quad k = |\vec{k}_i| = |\vec{k}_f| . \quad (3.15)$$

With this and by rewriting the potential in the form  $U(\vec{r}) = \frac{2\mu}{\hbar^2} V(\vec{r})$ , the time-independent Schrödinger equation reads:

$$[\nabla^2 + k^2 - U(\vec{r})] \Psi(\vec{r}) = 0 . \quad (3.16)$$

Next, the behaviour at large distances  $r$  is investigated: The potential can be neglected (as long as it converges to zero faster than  $1/r$  for  $r \rightarrow \infty$ ) and the scattering wave function  $\Psi(\vec{r})$  is a solution of :

$$[\nabla^2 + k^2] \Psi(\vec{r}) = 0 . \quad (3.17)$$

In the region of  $r \rightarrow \infty$ , the scattering wave function describing the steady state of the system must contain both, the incoming (*inc*) as well as the scattered (*sc*) wave function, thereby:

$$\Psi(\vec{r}) \xrightarrow[r \rightarrow \infty]{} \Psi_{inc}(\vec{r}) + \Psi_{sc}(\vec{r}) . \quad (3.18)$$

Since the starting point for the discussion of classical scattering is the beam experiment with an incident homogeneous beam of particles, one can choose the incoming wave function to be a plane wave with amplitude  $A^1$ :

$$\Psi_{inc}(\vec{r}) = A \exp(i \cdot \vec{k}_i \cdot \vec{r}) . \quad (3.19)$$

The scattered wave on the other hand must be an outgoing wave. Since scattering can, in principle, happen in any direction, the outgoing wave function is a spherical wave with an additional amplitude whose dependence on the scattering parameters incorporates all information about the scattering process:

$$\Psi_{sc}^{(+)}(\vec{r}) = A f(k, \theta, \phi) \frac{e^{(ik \cdot \vec{r})}}{r} . \quad (3.20)$$

The (+) superscript indicates that a time-dependent outgoing wave describes a spherical wave with positive phase velocity  $dr/dt = \omega/k$  when using eq. 3.13 and 3.20.  $f(k, \theta, \phi)$  is the aforementioned *scattering amplitude*.

The goal will be to find the wave function  $\Psi_{\vec{k}_i}^{(+)}(\vec{r})$  which is called the *stationary state wave function for scattering* and which has to satisfy the asymptotic behaviour:

$$\Psi_{\vec{k}_i}^{(+)}(\vec{r}) \xrightarrow[r \rightarrow \infty]{} A \left[ e^{(ik_i \cdot \vec{r})} + f(k, \theta, \phi) \frac{e^{(ik \cdot \vec{r})}}{r} \right] . \quad (3.21)$$

Ultimately, this will lead to the scattering amplitude, which can be shown (see [78]<sup>2</sup>) to be directly related to the differential scattering cross section by:

$$\frac{d\sigma}{d\Omega} = |f(k, \theta, \phi)|^2 \quad (3.22)$$

and therefore to the total scattering cross section by

$$\sigma_{tot} = \int_0^{2\pi} d\phi \int_0^\pi d\theta \sin(\theta) |f(k, \theta, \phi)|^2 . \quad (3.23)$$

### 3.2.1 The method of partial waves

The task is to find a wave function which fulfils equation 3.21 and thereby the scattering amplitude. As described earlier, central potentials play an important role in scattering. For a central potential with  $V(\vec{r}) = V(r)$ , whose value depends only on the magnitude of the spacial coordinate, the Hamiltonian  $H_{central} = -\frac{\hbar^2}{2m} \nabla^2 + V(r)$  commutes with the operators  $L^2$  and  $L_z$  of the total orbital angular momentum of the electrons. Thus, the scattering wave function,

<sup>1</sup>The argument in the quantum-mechanical beam experiment for using an infinitively extended wave for a spatially restricted object as a beam is that the beam diameter is much larger than the interaction region of two colliding atoms. This argument also holds true in a similar manner for the case of samples of dilute atomic gases.

<sup>2</sup>In the cited publication, the relation is derived by looking at the probability current density in the context of flux of outgoing particles which are scattered into the spherical surface element  $r^2 d\Omega$ .

which is a solution to  $H_{central}$ , will be expandable into a series of Legendre polynomials, just as it is the case for the hydrogen atom. Therefore, one can write:

$$\Psi_{\vec{k}_i}^{(+)}(\vec{r}) = \Psi_{\vec{k}_i}^{(+)}(k, r, \theta) = \sum_{l=0}^{\infty} R_l(k, r) P_l(\cos(\theta)) , \quad (3.24)$$

where due to the symmetry of the problem the dependence on the azimuthal angle  $\phi$  is lost,  $l$  is the orbital angular momentum quantum number,  $R_l(k, r)$  are the radial wave functions and  $P_l(\cos(\theta))$  are the Legendre polynomials which are already known from the solution of the angular part of the atomic Schrödinger equation for hydrogen (see e.g. [84]). The sum representation of the scattering wave function is called the *method of partial waves*, since every addend of it represents a wave function with ever growing orbital angular momentum  $l$ . To envision the scattering process as the scattering of many separate waves can be beneficial, especially when treating scattering at very low temperatures, hence with very low kinetic energies. This will be discussed in more detail at the end of this section.

Since the Legendre polynomials are known functions, the remaining task is to find the solutions for the radial wave functions  $R_l(k, r)$ . Like for any central force (see e.g. chapter 2.6 in [78]), the equation which has to be satisfied by the radial functions read

$$\left[ \frac{d^2}{dr^2} + \frac{2}{r} \frac{d}{dr} - \frac{l(l+1)}{r^2} - U(r) + k^2 \right] R_l(k, r) = 0 , \quad (3.25)$$

with  $U(r) = 2\mu V(r)/\hbar^2$ . This equation is identical to the radial equation for atoms, eq. 2.3, when using  $u_l(k, r) = rR_l(k, r)$  which simplifies eq. 3.25 to:

$$\left[ \frac{d^2}{dr^2} + \frac{l(l+1)}{r^2} - U(r) + k^2 \right] u_l(k, r) = 0 . \quad (3.26)$$

Without loss of generality, the  $u_l(k, r)$  can be assumed to be real, since real and imaginary solutions would satisfy the radial equation separately. To find the radial wave functions, first a region with  $r > a$  is considered where  $a$  is the value of  $r$  beyond which the potential  $U(r)$  has no significant influence any more.<sup>3</sup> Next,

$$\left[ \frac{d^2}{d\rho^2} + \frac{2}{\rho} \frac{d}{d\rho} - \left( 1 - \frac{l(l+1)}{\rho^2} \right) \right] R_l(\rho) = 0 \quad (3.27)$$

has to be solved, where  $\rho = kr$ . This is basically the spherical Bessel differential equation, which has as general solution a linear combination of spherical Bessel  $j_l(\rho)$  and spherical Neumann  $n_l(\rho)$  functions.

By constructing on the one hand a solution for  $R_l(k, r)$  in the region where  $r > a$  by a linear combination of  $j_l(kr)$  and  $n_l(kr)$  and on the other hand by looking at the behaviour of the Bessel and Neumann functions for  $\rho \rightarrow \infty$  (for  $\rho > l(l+1)/2$ ), one finds (for details on this, see e.g. chapter 12.3 in [78]):

$$R_l(k, r) = \frac{u_l(k, r)}{r} \xrightarrow[r \rightarrow \infty]{} \frac{A_l(k)}{kr} \sin [kr + \eta_l(k)] , \quad (3.28)$$

where  $A_l(k)$  is a constant and independent of  $r$ .

A remark shall be made regarding the phase shift  $\eta_l(k)$  in equation 3.28. The notation for the scattering phase shift can be a bit confusing because the same symbols are used for

---

<sup>3</sup>For this assumption to be justified, it is necessary to demand that  $U(r) \rightarrow 0$  faster than  $r^{-1}$ . This means that for Coulomb-like potentials a more complex treatment is needed which is beyond the scope of this chapter.

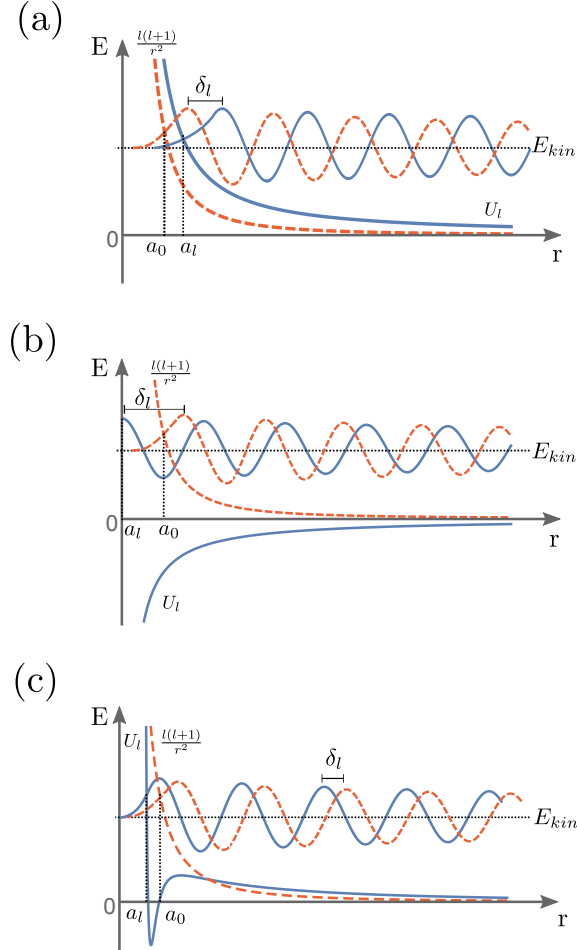


**Figure 3.11: Schematic representation of phase shifts for different potentials.** For three cases the scattering wave function of a pure rotational barrier potential (red dashed curves) is compared to the wave functions of a repulsive potential (a), an attractive potential (b) and an attractive potential with a repulsive central part (c) (for (a)-(c) blue curves). For every case the classical turning points  $a$  are depicted as well as the phase shift  $\delta_l$  between the scattering wave functions. Adapted from [79]. For details see the calculations in this reference.

different phase shifts throughout the literature. In the case of this chapter,  $\eta_l(k)$  refers to the phase shift acquired by the effective potential

$$U_l(r) = U(r) + l(l+1)/r^2 \quad . \quad (3.29)$$

The phase shift introduced by the rotational-barrier part  $l(l+1)/r^2$  can be calculated to be  $l\pi/2$  (see [79]). Because one is mostly interested in the phase shift originating from the actual shape of the scattering potential, i.e.  $U(r)$ , eq. 3.28 can be written as:

$$R_l(k, r) = \frac{u_l(k, r)}{r} \xrightarrow[r \rightarrow \infty]{} \frac{A_l(k)}{kr} \sin \left[ kr - \frac{l\pi}{2} + \delta_l(k) \right] \quad , \quad (3.30)$$

where  $\delta_l(k)$  is the phase shift stemming from the scattering on  $U(r)$ .

Some insights on the scattering phase may be gained at this point by comparing two waves, one being reflected by only the rotational barrier part of the effective potential and the other by the complete potential. In fig. 3.11, the three possible cases for a totally repulsive, totally attractive and attractive potential with a repulsive core are shown qualitatively. The distance of the classical turning point  $a$  is different for the purely rotational barrier potential

$l(l+1)/r^2$  and the effective potential  $U_l(r)$  due to a different steepness of the potential for short ranges. Due to this difference, a phase shift  $\delta_l$  is present between a wave which is reflected by the purely rotational barrier and another one which is reflected by the effective potential. Moreover, the frequency of the oscillation of a wave is changed depending on the shape of the effective potential. For a totally repulsive potential this leads to an always negative phase shift, while for a totally attractive potential the phase shift is always positive. For the more interesting case of the combined potential, the sign of the phase shift depends on  $l$  since the attractive part increases the oscillations and the repulsive part decreases them.

In eq. 3.21, the influence of the scattering process is totally absorbed by the scattering amplitude, whereas in the method of partial waves, the scattering information is contained in the scattering phase shift. Since both are valid representations of the same physical process, the scattering amplitude and the scattering phase shift have to be directly related. This can be demonstrated, by writing  $\Psi_{\vec{k}_i}^{(+)}(\vec{r})$  in two slightly different ways

$$\begin{aligned} \Psi_{\vec{k}_i}^{(+)}(\vec{r}) &\xrightarrow[r \rightarrow \infty]{} \\ A \left[ \sum_{l=0}^{\infty} \frac{(2l+1)i^l}{kr} \sin(kr - l\pi/2) \cdot P_l(\cos(\theta)) + f(k, \theta, \phi) \frac{e^{ikr}}{r} \right] , \end{aligned} \quad (3.31)$$

where the incoming wave now is written using eq. 3.24 with  $R_l(k, r) \xrightarrow[r \rightarrow \infty]{} \sin(kr - l\pi/2)$  for  $U_l(r) = 0$  at  $r \gg a$ , and

$$\Psi_{\vec{k}_i}^{(+)}(\vec{r}) \xrightarrow[r \rightarrow \infty]{} \sum_{l=0}^{\infty} \frac{A_l(k)}{kr} \sin(kr - l\pi/2 + \delta_l(k)) \cdot P_l(\cos(\theta)) , \quad (3.32)$$

following eq. 3.24 and 3.30. By equating the coefficients, one finds:

$$f(k, \theta) = \frac{1}{2ik} \sum_{l=0}^{\infty} (2l+1) [\exp(2i\delta_l(k)) - 1] \cdot P_l(\cos(\theta)) , \quad (3.33)$$

where the scattering amplitude only depends on the scattering phase shift.

A slightly different way of describing the scattering phase is to write eq. 3.30 as:

$$R_l(k, r) \simeq \frac{1}{2i} [-\exp(-i(kr - \pi l/2 + \delta_l)) + \exp(i(kr - \pi l/2 + \delta_l))] , \quad (3.34)$$

where the first exponential-function term is an incoming and the second term an outgoing wave, as expected for a scattering process. By assuming  $\delta_l$  to be real in the case of elastic scattering<sup>4</sup>, it can be seen that the effect of scattering is to introduce a phase shift between the incoming and the outgoing wave, leading to an interference pattern of the two waves. This interference pattern contains the full picture of the scattering process in the steady-state case. The same is true if the scattering process is encoded in the scattering amplitude as can be seen by the direct link between scattering phase and scattering amplitude in eq. 3.33.

Considering the aforementioned relations, it becomes clear that the goal is the calculation of the scattering phase shift. For this calculation, the method of partial waves can be used. In particular the usefulness of this method for collisions at low temperatures shall be discussed in the following. As can be seen from fig. 3.12, the rotational barrier rises ever faster for increasing  $l$ . Thus, for a particle with kinetic energy  $E_{kin}$ , which scatters in an effective potential like the one given by eq. 3.29, the classical turning point moves further outward the larger  $l$  becomes, as pictured in fig. 3.12. This means that if  $l$  increases, the particle

---

<sup>4</sup>For inelastically scattering particles get "lost" in the outgoing beam when they are scattered into other channels and the scattering phase becomes imaginary.

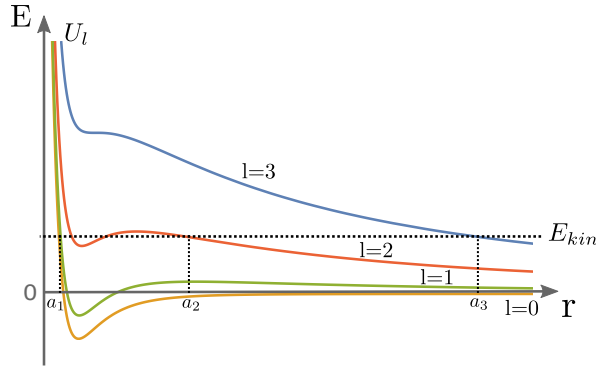


**Figure 3.12: Schematic potentials with rotational barriers for ever increasing  $l$ .** For a scattering process with kinetic energy  $E_{kin}$  the classical turning point  $a$  originates at ever larger values of  $r$  the larger the rotational barrier part becomes in  $U_l(r) = U(r) + l(l+1)/r^2$ .

will need a higher kinetic energy to overcome the rotational barrier and to probe the inner part of the interaction potential. Thus, for low temperatures and high  $l$  the scattering takes place already at large internuclear distance. Therefore, in principle only the shape of the potential at these large distances needs to be known to describe the scattering process. If the kinetic energy is low enough that a partial wave (see eq. 3.24) with e.g.  $l = 2$  (a so-called *d-wave*) would back-scatter already at distances where the potential is effectively the one of two atoms barely interacting with each other, it is reasonable to assume that no significant change in the state of the system could result from that partial wave interaction. Using this argument, the sum of partial waves in eq. 3.24 can often be terminated for  $l > 1$  (*s*- and *p*-wave scattering) or even directly for  $l > 0$  (pure *s*-wave scattering) e.g. when describing scattering processes in ultracold atomic ensembles.

To get a rough estimation on the optimal point to truncate the sum, the so-called *range of the potential*  $a$  can be taken into account. As pictured in fig. 3.13,  $a$  marks the internuclear distance  $r = a$  beyond which the effect of the potential on the two-atom interaction becomes negligible. Additionally, the figure shows the radial part of the scattering wave function. For short distances and small  $l$ , it goes to zero with  $r^l$  for  $r \rightarrow 0$ . The first maximum of the radial function (which is proportional to the Bessel function  $j_l(k, r)$ ) occurs at approximately  $r_0 \simeq l/k$ . If  $a \ll l/k$ , the corresponding wave function with orbital angular quantum number  $l$  and kinetic energy  $E_{kin} \propto k$  does not "see anything" of the potential. Therefore, the cut-off

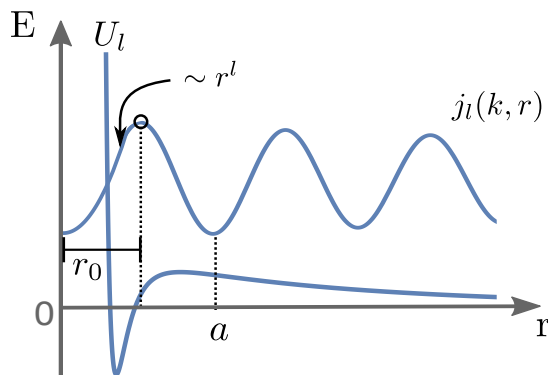


**Figure 3.13: The influence of the potential on the scattering wave function.** Schematic representation of an effective potential  $U_l$  and the radial part of the scattering wave function  $j_l(k, r)$ . Beyond the range of a potential  $a$  its effect on the two-atom interaction becomes negligible.

for the partial wave expansion can be written as:

$$l_{\max} \approx ka , \quad (3.35)$$

with  $a$  being the aforementioned range of the potential. At this point, it is also possible to draw a connection to classical scattering: A particle with an impact parameter  $b > a$  is not scattered while a particle with an impact parameter inside the range of influence of the potential  $b < a$  will be scattered, as shown in fig. 3.14. With  $b = L/p$ , where  $L$  is the angular momentum of the particle and  $p$  its momentum, it follows that particles with  $L > pa$  are not scattered. With the semi-classical argument that  $L \approx \hbar l$  and  $p = \hbar k$ , it again follows that particles are not scattered if  $l > ka$ .

### 3.2.2 Calculation of the scattering phase

The calculation of the scattering phase can be a complex process as will be illuminated in more detail in chap. 4. Nevertheless, the s-wave scattering behaviour shall be derived in this section because it already sheds light onto many features of Feshbach resonances. For  $r > a$ , eq. 3.28 can be written in a normalised form (for details on this see chapter 12.3 in [78]):

$$R_l(k, r) \xrightarrow[r \rightarrow \infty]{} \frac{1}{kr} [\sin(kr - \pi l/2) + \tan(\delta_l(k)) \cos(kr - \pi l/2)] . \quad (3.36)$$

Let this be the radial wave function belonging to a potential  $U(r)$ , then the radial wave function  $\bar{R}_l(k, r)$ , belonging to the different potential  $\bar{U}(r)$ , differs only in the phase shift  $\bar{\delta}_l(k)$  from  $R_l(k, r)$ . By inspecting the derivative of the Wronskian with respect to  $r$

$$\frac{d}{dr} W(u_l, \bar{u}_l) = \frac{d}{dr} \left[ u_l \left( \frac{d}{dr} \bar{u}_l \right) - \left( \frac{d}{dr} u_l \right) \bar{u}_l \right] , \quad (3.37)$$

with  $R_l(k, r) = r^{-1} u_l(k, r)$ , it can be found for the relation of the two phase shifts (see again chapter 12.3 in [78] for more details on that):

$$\tan(\delta_l(k)) - \tan(\bar{\delta}_l(k)) = -k \int_0^\infty r \bar{R}_l(k, r) [U(r) - \bar{U}(r)] r R_l(k, r) dr , \quad (3.38)$$

from which the integral representation of the phase shift can be deduced:

$$\tan(\delta_l(k)) = -k \int_0^\infty r j_l(k, r) U(r) r R_l(k, r) dr , \quad (3.39)$$

where the absolute definition of the phase shift is used, meaning that  $\delta_l = 0$  for  $U_l = 0$  and setting  $\bar{U}_l = 0$ . For  $\bar{U}_l = 0$  the radial wave function  $\bar{R}_l$  reduces to the radial wave function of

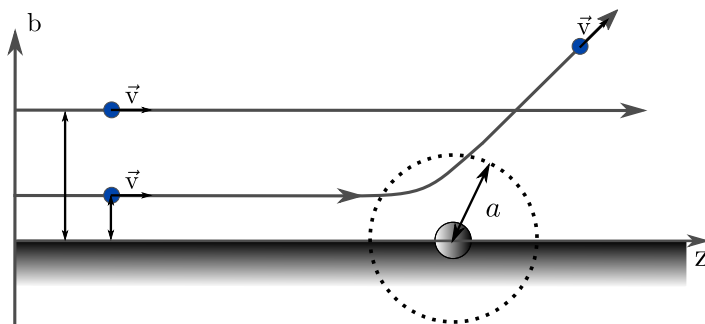


**Figure 3.14: Classical argument on quantum-mechanical scattering.** A particle with an impact parameter  $b$  larger than the range of the potential  $a$  is not scattered, whereas for  $b < a$  the trajectory of the particle is affected by the potential.

a free particle, in this case the Bessel function  $j_l(k, r)$ . To compute the phase shift, the radial wave function must be derived in the internal region  $r < a$ , since the integral runs over all  $r$ . Additionally, requiring that both  $R_l$  and their derivative  $dR_l/dr$  shall be continuous at  $r = a$  is equivalent to demand

$$\gamma_l(k) = \frac{dR_l/dr}{R_l} \Big|_{r=a} = \frac{k \left[ \left[ \frac{dj_l(\rho)}{d\rho} \right]_{\rho=ka} - \tan(\delta_l(k)) \left[ \frac{dn_l(\rho)}{d\rho} \right]_{\rho=ka} \right]}{j_l(ka) - \tan(\delta_l(k)) n_l(ka)} \quad (3.40)$$

to be continuous. Solving eq. 3.40 for  $\tan(\delta_l(k))$  yields:

$$\tan(\delta_l(k)) = \frac{k \left[ \frac{dj_l(\rho)}{d\rho} \right]_{\rho=ka} - \gamma_l(k) j_l(ka)}{k \left[ \frac{dn_l(\rho)}{d\rho} \right]_{\rho=ka} - \gamma_l(k) n_l(ka)} , \quad (3.41)$$

with the spherical Bessel functions  $j_l(\rho)$  and the spherical Neumann functions  $n_l(\rho)$ . By using the properties of these functions for small values of  $\rho$ , which means for low energies because  $\rho = ka \propto E_{kin}$ , it can be shown that  $\tan(\delta_l(k))$  behaves as  $k^{2l+1}$  for  $k \rightarrow 0$  (as long as  $a \cdot \lim_{k \rightarrow 0} \gamma_l(k) \neq -(l+1)$ ). In the case of low kinetic energies, all partial cross sections  $\sigma_l$  for  $l \geq 1$  vanish as  $k^{4l}$  (since they are linked to the scattering phase shift via eq. 3.33 and eq. 3.22) and only the s-wave contribution remains non-zero. This means, the scattering becomes isotropic for very low energies and  $\sigma_{tot} = \sigma_{l=0}$ . In this limit, it is advantageous to define the so-called *scattering length*  $a$  as:

$$a = -\lim_{k \rightarrow 0} \frac{\tan(\delta_0(k))}{k} , \quad (3.42)$$

in which case for the scattering amplitude it follows:

$$f \xrightarrow[r \rightarrow \infty]{} -a \quad (3.43)$$

and for the differential cross section:

$$\frac{d\sigma}{d\Omega} \xrightarrow[r \rightarrow \infty]{} a^2 . \quad (3.44)$$

Finally, for high energies (and fixed  $l$ ) the importance of the potential will become negligible. Thus, the scattered radial wave function will approach the free spherical wave function  $j_l(kr)$ , similar to the arguments which lead to eq. 3.39. Equation 3.39 can then be written in the so-called *first Born approximation*:

$$\tan(\delta_l(k)) \simeq [\tan(\delta_l(k))]^{B1} = -k \int_0^\infty [j_l(k, r)]^2 U(r) r^2 dr . \quad (3.45)$$

It is worth noting that this formula can also be used in the case of large  $l$  with  $l \gg ka$  (where  $a$  here is the range of the potential) because in that case the centrifugal barrier becomes significant. Therefore, it is a good approximation to treat the scattered wave function again as  $j_l(kr)$ , as discussed already in context of fig. 3.7.

### 3.2.3 Scattering on a square potential

In this subsection, the quantum-mechanical scattering on a square potential is illustrated, following the description in [80]. This example of a simple scattering potential can be discussed quantitatively and the scattering processes occurring are qualitatively comparable

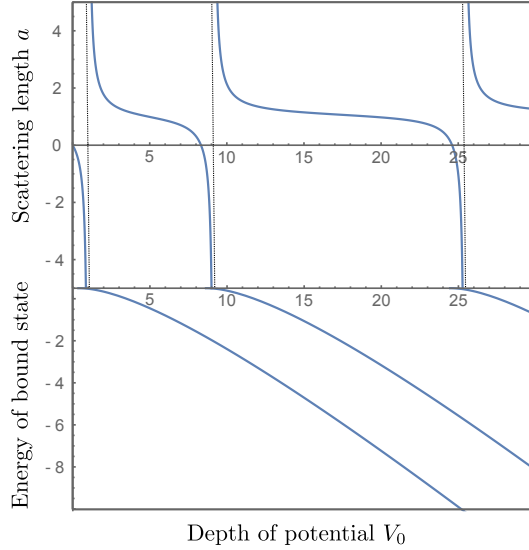


**Figure 3.15: Scattering length and energies for scattering on a box potential.** The scattering length  $a$  diverges (upper graph) for potential depth  $V_0$  at which a new bound state forms at the dissociation limit (lower graph). Schematic representation of  $a$  and bound state energies, for details on the calculation see [80].

to more complex potentials like e.g. the molecular scattering potentials in the case of Feshbach resonances. The square potential is given by:

$$V(r) = \begin{cases} -V_0 & : r < R_0 \quad (V_0 > 0) \\ 0 & : r \geq R_0 \end{cases} \quad (3.46)$$

and the solution of the radial scattering eq. 3.26 for scattering at very low energies  $E$  (i.e. for  $l = 0$ ) is:

$$u_{k,0}(r) \propto \begin{cases} \sin(k'r) & : r < R_0, \quad k' = \sqrt{2\mu(E + V_0)/\hbar^2} \\ C \sin(kr + \delta_0(k)) & : r \geq R_0, \quad k = \sqrt{2\mu E/\hbar^2} \end{cases} \quad (3.47)$$

with  $\mu$  being the reduced mass.  $C$  and  $\delta_0(k)$  are again derived from the demanded continuity of the solutions for  $r = R_0$ . For the scattering phase, it follows that:

$$\delta_0(k) = -kR_0 + \arctan\left(\frac{k}{k'} \tan(k'R_0)\right) \quad (3.48)$$

and with eq. 3.42 the scattering length is given by:

$$a = R_0 - \frac{1}{\sqrt{2\mu V_0/\hbar^2}} \tan\left(\sqrt{2\mu V_0/\hbar^2} \cdot R_0\right) \quad . \quad (3.49)$$

Because the scattering length is directly proportional to the tangent-function in this example, the characteristic form of a Feshbach resonance is directly recognizable (compare with fig. 8.3).<sup>5</sup> Figure 3.15 shows the scattering length as a function of the potential depth  $V_0$ . The poles of the scattering length appear for  $V_0 = V_1(2n - 1)^2$  with  $V_1 = \pi^2 \hbar^2 / (8\mu R_0^2)$ ,  $n > 0$  and  $n$  being an integer. For these potential depths, a new bound state forms at the dissociation limit, as shown in the bottom panel of fig. 3.15. As an analogy, this means that every time when the scattering happens for an energy which matches a bound state

<sup>5</sup>Nevertheless, it needs to be mentioned that the scattering length of a real Feshbach resonance will not necessarily go to infinity.

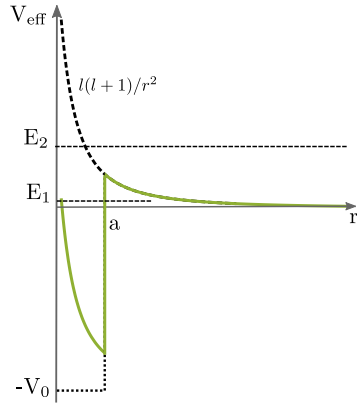


**Figure 3.16: Schematic of a shape resonance.** For an effective potential (green curve) with a potential barrier, a bound state can exist with  $E_1 > 0$ . If the energy of the scattering process  $E_2$  becomes equal to  $E_1$  the scattering wave function can tunnel through the potential barrier and can have a significant amplitude in the region with  $r < a$ .

of the scattering potential, the scattering length diverges. Although only one potential is present in this simple example, in contrast to the situation of a Feshbach resonance where two potentials are involved, the behaviour of the scattering length is very similar.

### 3.2.4 Shape resonances

As discussed in sec. 3.1, for the classical scattering by a central potential with an attractive part, orbiting resonances appear for which the scattering particle starts orbiting around the scatterer. In the quantum-mechanical case a similar situation exists, for which the two particles can get stuck together. It stems from the characteristic shape of a partially repulsive potential with a rotational barrier, as shown in fig. 3.16. If a bound state exists inside the potential which has an energy higher than the zero energy due to the shape of the potential, the scattering process can lead to a temporal population of this state. This happens when the energy of the incoming channel is resonant to the bound-state one. In that case, the scattering wave function can tunnel through the potential barrier and can have a significant amplitude inside the potential. In contrast to e.g. Feshbach resonances, only one potential energy curve (i.e. scattering state) is necessary for this process and the resonance stems from the shape of the potential, hence its name.

### 3.2.5 Scattering of identical particles

Up to this point, the particles under consideration were distinguishable particles. For the scattering processes with atoms, these particles have to be treated as indistinguishable. Figure 3.17 illustrates that for the scattering by a central potential (shown in the centre of mass system), there exist two scattering processes which lead to the same outcome. In a classical description, one would simply have to add the two differential cross sections to obtain the correct result:

$$\frac{d\sigma_{cl}}{d\Omega} = |f(\theta)|^2 + |f(\pi - \theta)|^2 . \quad (3.50)$$

Since the scattering particles are atoms, they can either be fermions or bosons which implies restrictions on the symmetry of their scattering wave functions (which have to be symmetric for bosons, and antisymmetric for fermions). For bosons, this leads to a

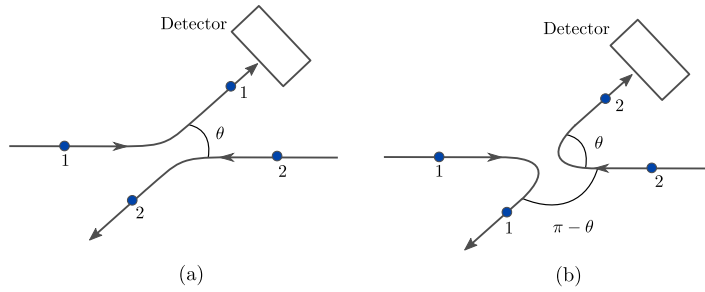


**Figure 3.17: Scattering of identical particles.** Two different scattering processes are depicted (a, b) which lead to the same detected event in the case of scattering of indistinguishable particles.

symmetrized scattering wave function of the type:

$$\Psi_+(\vec{r}) = \Psi_{k_i}^{(+)}(\vec{r}) + \Psi_{k_i}^{(+)}(-\vec{r}) \quad (3.51)$$

which leads to a scattering amplitude

$$f_+(\theta) = f(\theta) + f(\pi - \theta) \quad , \quad (3.52)$$

as can be seen from rewriting eq. 3.51 with the help of eq. 3.21. Hence, the correct quantum-mechanical differential cross section is

$$\frac{d\sigma}{d\Omega} = |f(\theta) + f(\pi - \theta)|^2 \quad . \quad (3.53)$$

In the low energy limit (s-wave scattering,  $l = 0$ ), this leads to a differential cross section four times larger than for distinguishable particles and two times larger than with the 'classical' treatment of eq. 3.50. For fermions, on the other hand, there exists no s-wave scattering (because the scattering wave function has to be antisymmetric if two identical fermions scatter) and therefore the scattering cross section goes to zero for very low temperatures.

To summarize this section about scattering theory, it can be stated that the scattering process is in the end visualized by the total wave function of the system, which is a superposition of all incoming partial waves (which are waves of free particles) and the outgoing scattered waves. Therefore, the whole scattering process is incorporated in the scattering amplitude. It quantifies how much of the incoming wave is scattered into a certain outgoing wave. The scattering amplitude is also related to the phase shift that the scattered particle wave function acquires. Because of this phase shift, interferences between incoming and outgoing waves occur. This leads to a total wave function of the system whose interference pattern resembles the steady state of the scattering process.



# Chapter 4

## Feshbach resonances

With the information given in the previous chapters, a good basis exists for the understanding of the phenomenon of Feshbach resonances. In the following, a phenomenological description of Feshbach resonances will introduce the topic, following the information given in [80]. In the second part of this chapter, a brief overview over the mathematical models and procedures to calculate and analyse Feshbach resonances is presented.

### 4.1 Phenomenological description of Feshbach resonances

In the discussion about atom-atom collisions in the previous chapter, the basic concepts have been introduced with which Feshbach resonances will be described. The example of scattering by a box potential already revealed some features of resonant scattering and the derived scattering length shows similarities to the behaviour close to a Feshbach resonance.

What remains unexplored so far is the influence of the internal structure of atoms and the coupling between these internal structures during a scattering process. It is discussed in sec. 3.2 that a scattering potential can be allocated to a set of good quantum numbers. Together with the energy of the scattering, they describe the so-called *scattering channel*. A channel is referred to as open if the scattering energy lies inside the continuum of that scattering channel's potential energy curve, and closed if it lies below the continuum. The cases of an open and a closed channel are illustrated in more detail in fig. 4.1.

As long as there exists no coupling of any type between these two potentials, the closed channel cannot be entered by the incoming wave function. This can only change for coupling mechanisms which inherit the chance that during the collision the wave function of the open channel can also be written in the basis of the closed channel. If, however, such a coupling mechanism exists (the different coupling mechanisms will be discussed in sec. 4.1.2), chances are that one of the bound states of the closed channels, labelled  $|\chi\rangle$  in fig. 4.1, will be temporarily populated during the collision. The probability for such a temporal population becomes higher the closer the energy of  $|\chi\rangle$  is to the energy of the scattering atoms. Due to the coupling to the continuum of the open channel, the atoms will not form stable molecular states in the closed channel, but will eventually dissociate again. In the example of sec. 3.2.3, a scattering resonance occurs in the case of the box potential when a new bound state forms on the border to the equilibrium. Likewise, a resonance in the case of the scattering of two atoms occurs when the bound state energy  $E_\chi$  becomes equal to the energy of the scattering particles.

In the case of Feshbach resonances, the open and closed channels have different spin configurations and therefore different magnetic moments. Hence, the energies of these channels are shifted differently in an external magnetic field. This makes it possible to shift the energies of the bound states of the closed channel with respect the open channel energy. Thus, the resonances depend on the external magnetic field strength. This is precisely how

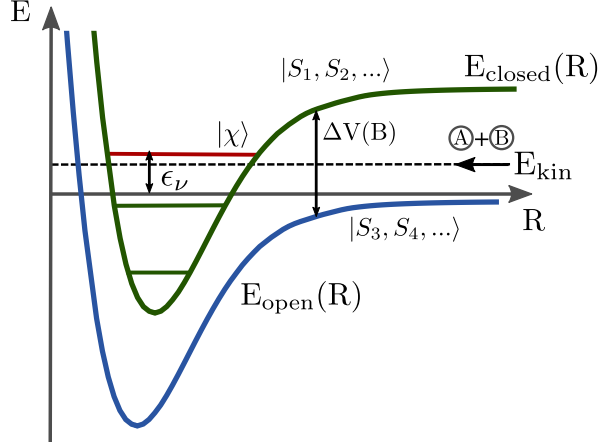


**Figure 4.1: Schematic of Feshbach resonance.**  $E_{\text{open}}(R)$  is the open channel's potential energy curve (blue graph) and  $E_{\text{closed}}(R)$  the one of the closed channel (green graph). Both channels are described by sets of quantum numbers ( $S_1, S_2, \dots$  and  $S_3, S_4, \dots$ , respectively). The dissociation limit of the open channel is set to  $E = 0$ . A bound state of the closed channel  $|\chi\rangle$  (red line) can become resonant with the energy of the scattering process  $E_{\text{kin}}$  if its energy  $\epsilon_\nu$  is changed with respect to  $E_{\text{kin}}$ , e.g. by an external magnetic field

Feshbach resonances were first discussed in the context of ultracold gases [90, 91] and how they are used in many state-of-the-art experiments.

Figure 4.2 shows a qualitative picture of a Feshbach-resonance structure. The background scattering length  $a_b$  rises to infinity as the energy of a bound state in the closed channel approaches the energy of the open channel (which in the case of scattering at low energy is approximately the energy of the scattering particles). The central panel of the figure shows the behaviour of the open and closed channel energies as a function of the external magnetic field. Note that the binding energy of the bound state at any given magnetic field strength is given by the energy difference between the dissociation limit of the open channel and the closed channel energy.

#### 4.1.1 Derivation of the scattering length in the low-energy limit

Following the very detailed discussions in [80], the derivation of the important formula for the scattering length in the limit of low scattering energy shall be presented:

$$a = a_b \left( 1 - \frac{\Delta B_{el}}{B - B_{res}} \right) \quad \text{for } k \rightarrow 0 , \quad (4.1)$$

where  $a_b$  is the background scattering length,  $B_{res}$  is the resonance position and  $\Delta B_{el}$  marks the area where the sign of the scattering length is opposite to the sign of the background scattering length. The already discussed formalism of quantum-mechanical scattering will prove helpful in the following discussion. Although also inelastic collisions can be enhanced in the vicinity of a Feshbach resonance (as will be discussed in chap. 7), the foremost signature of a Feshbach resonance is the strong variation of the elastic scattering length. The procedure to derive the scattering length is very similar to that in sec. 3.2. The scattering length is given by formula 3.42, which becomes even simpler in the case of low-energy s-wave scattering by examining the scattering in a 'hard sphere' potential:

$$a = -\frac{\delta_0}{k} \quad (4.2)$$

for  $k \rightarrow 0$ . In the equation,  $\delta_0$  is the scattering phase shift of the s-wave partial wave.

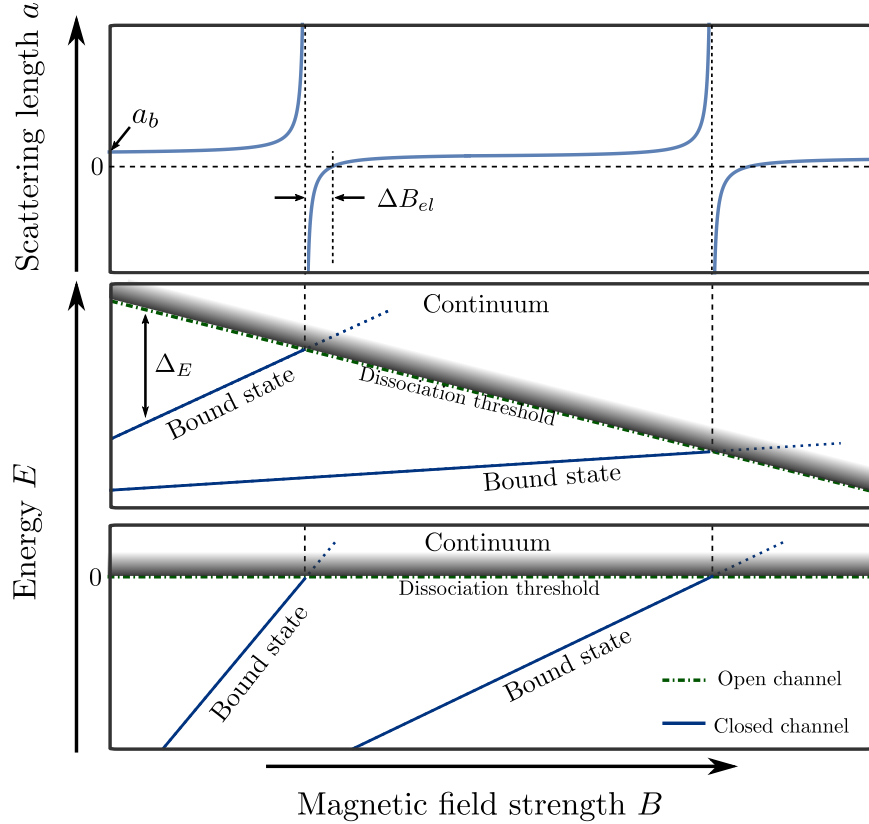


**Figure 4.2: Schematic of a Feshbach resonance structure.** The scattering length  $a$  is depicted as a function of the magnetic field strength  $B$  (upper graph). Resonances occur in this example if a closed channel bound state (blue lines) enters the continuum of the open channel (green dashed-dotted line and grey shaded area), shown in the central graph. The lower graph shows a different representation of the open and closed channel energies in which the open channel energy is set to zero for all values of  $B$ . Adapted from [80].

Therefore, to obtain  $a$ , first an expression for the scattering wave function has to be found, then with this wave function the expression of the scattering phase shift has to be derived, to ultimately deduce the formula for the scattering length given in eq. 4.1.

Let  $|\Psi\rangle$  be the wave function describing the scattering process. It will be similar to the one given in eq. 3.18 and shall be an eigenfunction of the Schrödinger equation

$$(E - \hat{H})|\Psi\rangle = 0 \quad , \quad (4.3)$$

where  $E = \hbar^2 k^2 / 2\mu$ .  $\hat{H}$  is the Hamilton operator describing the situation shown in fig. 4.1 of two scattering channels (the open one  $O$  and the closed one  $C$ ) plus a coupling between the two channels (which is at this point of no specific type). By writing  $|\Psi\rangle$  with the help of two projectors  $\hat{O}$  and  $\hat{C} = 1 - \hat{O}$  in the form  $|\Psi\rangle = \hat{O}|\Psi\rangle + \hat{C}|\Psi\rangle = |\Psi\rangle_O + |\Psi\rangle_C$  (which is essentially equal to eq. 3.18), the Schrödinger equation can be rewritten as a set of coupled equations:

$$(E - \hat{H}_{OO})|\Psi\rangle_O = \hat{H}_{OC}|\Psi\rangle_C \quad , \quad (4.4)$$

$$(E - \hat{H}_{CC})|\Psi\rangle_C = \hat{H}_{CO}|\Psi\rangle_O \quad , \quad (4.5)$$

where the projectors project onto the state of the respective channel and  $\hat{H}_{OC} = \hat{O}\hat{H}\hat{C}$  and so forth. Using Green's formalism (for details see [80]), the equations can be decoupled and

ultimately an expression for the wave function in the open channel can be obtained:

$$(E - \hat{H}_{OO} - \hat{H}_{OC}\hat{G}_{CC}^{(+)}\hat{H}_{CO})|\Psi\rangle_O = 0 \quad , \quad (4.6)$$

where  $\hat{G}_{CC}^{(+)} = \lim_{\eta \rightarrow 0^+} (E - \hat{H}_{CC} + i\eta)^{-1}$  is the so-called *Green's operator* and the third term in eq. 4.6 can actually be seen as a transition of the wave function from the open to the closed channel, followed by a propagation in that closed channel and a re-emission into the open channel. Solving eq. 4.6, one ultimately arrives at an expression for the open-channel wave function of the form:

$$|\Psi\rangle_O = |\Psi\rangle_O^{nr} + \hat{G}_{nr}^{(+)}\hat{H}_{OC}|\chi_\nu\rangle \frac{\langle\chi_\nu|\hat{H}_{CO}|\Psi\rangle_O^{nr}}{E - \tilde{\epsilon}_\nu + i\Gamma_\nu/2} \quad . \quad (4.7)$$

In this expression,  $|\Psi\rangle_O^{nr}$  describes the non-resonant scattering part, incorporating all bound states of the closed channel which do not become resonant with the open-channel energy. This wave function is assumed to be known in the context of this section. Moreover,  $\hat{G}_{nr}^{(+)} = \lim_{\eta \rightarrow 0^+} (E - \hat{H}_{nr} + i\eta)^{-1}$  and:

$$\begin{aligned} \Gamma_\nu/2 &= -\Im \langle\chi_\nu|\hat{H}_{CO}\hat{G}_{nr}^{(+)}\hat{H}_{OC}|\chi_\nu\rangle \\ \Delta\epsilon_\nu &= \Re \langle\chi_\nu|\hat{H}_{CO}\hat{G}_{nr}^{(+)}\hat{H}_{OC}|\chi_\nu\rangle \\ \tilde{\epsilon}_\nu &= \epsilon_\nu + \Delta\epsilon_\nu \quad , \end{aligned} \quad (4.8)$$

where  $\epsilon_\nu$  is the energy of the bound state  $|\chi_\nu\rangle$ ,  $\Delta\epsilon_\nu$  the energy difference between the bound state energy and the dissociation limit of the open channel and  $\Gamma_\nu/2$  the width of the resonance.

The wave function  $|\Psi\rangle_O$  deviates from the complete description of the scattering wave function (which is  $|\Psi\rangle = |\Psi\rangle_O + |\Psi\rangle_C$ ), but in the asymptotic range the contribution of the closed channel is negligible. Therefore, the correct behaviour of the scattering length can still be derived from  $|\Psi\rangle_O$ .

For this derivation, the expression of the scattering wave function as shown in eq. 3.21 is used, with an incoming wave (in the simple case of very low energy, it might be set as a spherical wave) and a phase-shifted outgoing spherical wave:

$$\Psi_{\vec{k}_i}^+(\vec{r}) \xrightarrow[r \rightarrow \infty]{} A \left[ \frac{e^{-ikr}}{r} + e^{2i\delta} \frac{e^{ikr}}{r} \right] \quad . \quad (4.9)$$

Then, the scattering length  $a$  can be derived from the phase shift  $\delta$ . To derive an expression for the scattering phase, eq. 4.7 is compared to eq. 4.9. Thereby, the effective scattering phase is found to be:

$$e^{2i\delta} = e^{2i\delta_{nr}} \left( 1 - \frac{i\Gamma_\nu/2}{E - \tilde{\epsilon}_\nu + i\Gamma_\nu/2} \right) \quad , \quad (4.10)$$

where the width of the resonance (see eq. 4.8) can be written as:

$$\Gamma_\nu/2 = \gamma_\nu k \quad , \quad (4.11)$$

with  $\gamma_\nu = |\xi|^2 \frac{\mu}{4\pi\hbar^2}$  being the reduced width of the resonance where  $\xi$  is the coupling matrix element between the open and the closed channel (see [80] for further details). From eq. 4.11, it also can be directly seen that the width of the resonance is energy-dependent (because of its dependence on  $k$ ).

Using eq. 4.2, the scattering length can be written in the approximation of low-energy s-wave scattering:

$$\begin{aligned} a &= a_{nr} + \frac{1}{2k} \arctan \left( \frac{\Gamma_v(E - \tilde{\epsilon}_v)}{(E - \tilde{\epsilon}_v)^2 + \Gamma_v^2/4} \right) \\ &= a_{nr} - \frac{\gamma_v}{\tilde{\epsilon}_v - E} \quad \text{for } k \rightarrow 0 \\ &= a_{nr} \left( 1 - \frac{\Delta E_{el}}{\tilde{\epsilon}_v - E} \right) \quad \text{with } \Delta E_{el} = \frac{\gamma_v}{a_{nr}} . \end{aligned} \quad (4.12)$$

Yet, no explicit dependence on the magnetic field is visible in eq. 4.12. As discussed already, magnetically induced Feshbach resonances are the most common appearance of this phenomenon. The magnetic field has an influence on the energy distance between the open and closed channel and thereby also on the "detuning"  $\Delta_E = \tilde{\epsilon}_v - E$  of eq. 4.12. The "detuning" can be related to the magnetic field by a Tailor-expansion as:

$$\Delta_E(B) = \Delta_E(B_{res}) + \frac{\partial \Delta_E}{\partial B} \Big|_{B_{res}} \cdot (B - B_{res}) + \dots \quad (4.13)$$

where  $\Delta_E(B_{res}) = 0$ . With this, eq. 4.12 can finally be written as

$$a = a_{nr} \left( 1 - \frac{\Delta B_{el}}{B - B_{res}} \right) \quad \text{with } \Delta B_{el} = \frac{\gamma_v}{a_{nr} [\partial \Delta_E / \partial B]_{B_{res}}} , \quad (4.14)$$

where it also becomes clear that the non-resonant scattering length  $a_{nr}$  is equivalent to the so-called *background scattering length*  $a_b$ .

In fig. 4.2, the behaviour of the scattering length as a function of the external magnetic field is plotted, showing a similar behaviour as already in the case of a box potential. In the central panel, the energy dependence of the asymptotic energy of the open channel and the bound-state energies of the closed channel are plotted as a function of the magnetic field. A Feshbach resonance appears in this simple picture when a closed-channel energy level reaches the continuum of the open channel. The depiction of the bound-state energies is often plotted slightly differently as shown in the lowest panel of fig. 4.2. The energy of the open channel is set to zero for all magnetic field values.

The real position of the Feshbach resonance deviates (sometimes heavily) from the positions of the crossing of the unperturbed channel energies. The reason for this shift can be found in the coupling between the two channels. This means that for an exact calculation of the resonance positions, precise knowledge of the potential energy curves of the contributing channels as well as of the coupling mechanisms and coupling strengths is required.

### 4.1.2 Coupling mechanisms

In sec. 2.2, the representation of molecular potentials is discussed. An overview over the methods for the calculations of these potentials is given in sec. 4.2. What shall be addressed in this subsection are the different coupling mechanisms as an extend to the descriptions in sec. 2.2 where no spin effects are considered. The molecular potential is a function of the inter-atomic distance  $R$ , see eq. 2.17. This potential only contains the Coulomb interactions between the different particles. If also spin-dependent interactions are taken into account, the total interaction potential reads:

$$V = V^C + \sum_{j=1}^2 \left( V_j^{Hf} + V_j^{Zeeman} \right) + V^{SS} + V^{SO} , \quad (4.15)$$

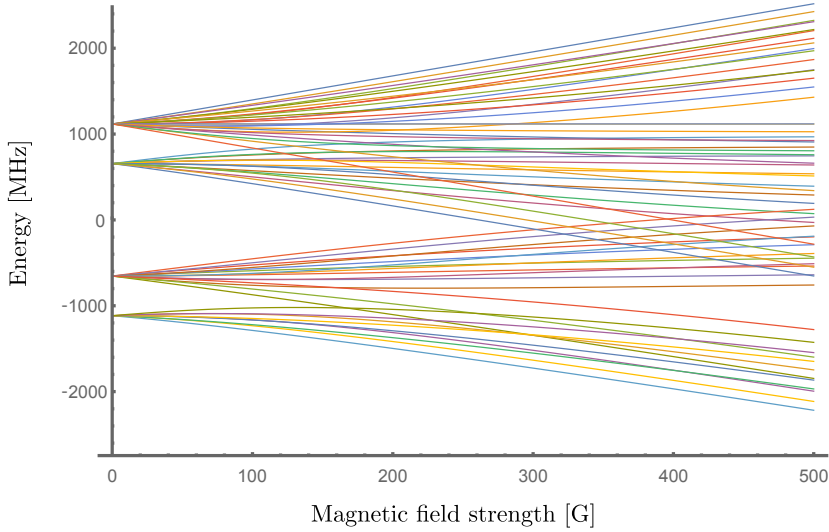


**Figure 4.3: Hyperfine structure of NaK at the asymptote.** The states are, beginning with the energetically highest:  $\text{Na}_{F=2} + \text{K}_{F=2}$ ,  $\text{Na}_{F=2} + \text{K}_{F=1}$ ,  $\text{Na}_{F=1} + \text{K}_{F=2}$ ,  $\text{Na}_{F=1} + \text{K}_{F=1}$ . The  $m_f$  states are left unlabelled.

here  $V^C$  is equal to eq. 2.17 and  $V_j^{\text{Zeeman}}$  describes the interaction with an external magnetic field.  $V_j^{Hf}$  is the hyperfine interaction,  $V^{SS}$  is the spin-spin and  $V^{SO}$  the spin-orbit coupling term and  $j$  numerates the atoms of the molecule.

The coulomb interaction term  $V^C$  is in its mathematical representation dependent on the distance between the two atoms. For very short distances ( $R \rightarrow 0$ ), it is dominated by the pure Coulomb repulsion of the nuclei. For intermediate distances, it is dominated by exchange interaction, where for alkali atoms the relative spin of the two valence electrons leads to a splitting into a singlet  $S = 0$  and a triplet  $S = 1$  potential. The exchange interaction has a significant influence on the potential energy curves as can be seen in fig. 2.10, where the triplet potential is much less deep in comparison to the singlet. For very long distances the attractive Van-Der-Waals interaction plays a dominant role. It is taken into account using a multipole expansion in the form (to third order):

$$V^{vdW} = -\frac{C_6}{R^6} - \frac{C_8}{R^8} - \frac{C_{10}}{R^{10}} , \quad (4.16)$$

where the respective  $C_6$ ,  $C_8$  and  $C_{10}$  coefficients are determined numerically and can be found e.g. in [92].

The hyperfine-interaction term contains only the atomic hyperfine-interaction terms which have already been addressed in sec. 2.1. An interatomic hyperfine interaction can be neglected, meaning  $V_j^{Hf}$  becomes independent of  $R$ . In the absence of an external magnetic field, the quantum numbers of the atomic hyperfine structure  $f_j, m_f^j$  can be used to describe the scattering potentials. This description is called Hund's case (e), see sec. 2.2.3. For small internuclear distances, this is no longer the case (see Hund's case (a)), but the total spin  $F = f_1 + f_2$  and its projection  $m_F$  remain good quantum numbers. In the case of an external magnetic field, as discussed in the following, only  $m_F$  remains a good quantum number at all internuclear distances. For spherical symmetric potentials, also the angular momentum quantum number  $l$  and its projection  $m_l$  are preserved.

Together with  $V_j^{\text{Zeeman}}$ , the hyperfine interaction term leads to the removal of the degeneracy of the hyperfine states as already seen in the context of the atomic Zeeman and Paschen-Back effect in sec. 2.1.1. At the asymptote, the overall hyperfine structure of a certain molecular potential can be obtained by adding the hyperfine structure of the two involved

atoms. The Hamiltonian of the molecular potential at the asymptote is simply (for sodium and potassium as the two atoms which form the molecule):

$$H_{molecule} \xrightarrow{R \rightarrow \infty} H_{Na} + H_K , \quad (4.17)$$

with

$$H_{Na/K} = T + V(r) + H_{fine} + H_{Hf} + H_{Zee} \quad (4.18)$$

being the atomic Hamiltonian of sodium and potassium, respectively, where  $H_{fine/Hf/Zee}$  is the Hamiltonian of the atomic fine structure/hyperfine structure/Zeeman effect, respectively.

The summation of eq. 4.17 has been performed in fig. 4.3 for  $^{23}\text{Na}$  and  $^{39}\text{K}$  for the ground-state hyperfine structure. The zero of the energy scale is set to the centroid of both hyperfine structures and the energies are summed up. Additionally, the behaviour of the hyperfine states in an external magnetic field up to 500 G, calculated with eq. 2.11, is shown. Crossings of two channels in this graph can be a signature of a Feshbach resonance, although this is a simplified picture. As previously mentioned, the real resonance position is shifted compared to a level crossing in fig. 4.3 because of the coupling between the channels. Furthermore, not all channels can couple since selection rules have to be obeyed, as will become more clear in the following.

The dipole-dipole interaction  $V^{SS}$  describes the interaction of the spins of the valence electrons of the two atoms. It depends on the relative orientation of the total spin  $S = s_{Na} + s_K$  of the electrons and the internuclear axis. The interaction lifts the degeneracy of the triplet  $S = 1$  states and leaves the singlet state  $S = 0$  unchanged. The dipole-dipole interaction term commutes with  $\vec{S}^2$  and therefore does not mix the singlet and triplet potentials. This means there are no transitions between singlet and triplet potential initiated by the dipole-dipole coupling. However,  $V^{SS}$  does not possess spherical symmetry and therefore  $l$  is no longer a preserved quantity. Thus, the dipole-dipole interaction can mix different angular momentum states. As can be shown (see [80, 90, 93]), the allowed transitions have to fulfil  $|\Delta l| = [0, 2]$  and  $l = 0 \rightarrow l = 0$  is not allowed. Hence, only a mixing of a s-wave with a d-wave is possible due to dipole-dipole interaction but no pure s- or d-wave mixing.

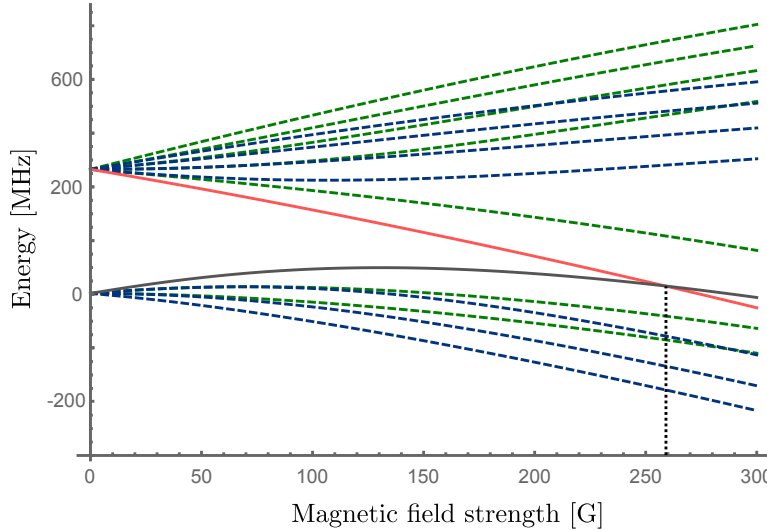
The last interaction which is discussed in this section is the spin-orbit coupling term  $V^{SO}$ . It has the same tensor structure as the spin-spin coupling but with a different dependence on  $r$  and a different sign. The spin-orbit coupling becomes stronger the more the electron orbitals overlap, i.e. the shorter the internuclear distances is. Additionally, it allows for mixing between singlet and triplet states and is therefore of specific importance for a two-photon transfer in molecules. This is especially important in the case of a Feshbach molecule which shall be transferred to the absolute ground state, because often the Feshbach molecular state and ground state have a different multiplicity.

Figure 4.4 shows a zoom into fig. 4.3, where channel crossings are depicted in more detail. Although many channels will cross when the magnetic field is varied, it depends on the coupling mechanism outlined above and the corresponding selection rules if a Feshbach resonance appears or not.

To summarize, the coupling between the open channel and the closed channel is given by  $V_C$ ,  $V^{SS}$  or  $V^{SO}$ :

Due to the spherical symmetry of the Coulomb potential term, the angular momentum is preserved, leading to  $\Delta l = 0$  and  $\Delta m_l = 0$ . Together with the fact that  $m_F$  is always preserved, yielding  $\Delta m_F = 0$ , this determines the set of restrictions for the coupling of the open and closed channel for the case of coupling through the Coulomb interaction.

Coupling through  $V^{SS}$  or  $V^{SO}$  is weaker than the Coulomb coupling part and due to the loss of spherical symmetry, only the total angular momentum  $F_{total} = f_1 + f_2 + l$ , or rather its projection onto the internuclear axis  $m_{Ftotal}$ , is preserved, resulting in the selection rules  $\Delta m_l = 2$  and  $\Delta m_{Ftotal} = \Delta m_F + \Delta m_l = 0$ .



**Figure 4.4:** Level crossing in the hyperfine structure at the asymptote of NaK . The states crossing at 259 G belong to  $|1, 0\rangle_{\text{Na}} + |2, -2\rangle_{\text{K}}$  (red) and  $|1, -1\rangle_{\text{Na}} + |1, -1\rangle_{\text{K}}$  (black). Other  $m_f$  states are left unlabelled. The states at zero magnetic field belong to  $\text{Na}_{F=1} + \text{K}_{F=1}$  (set to energy zero) and  $\text{Na}_{F=1} + \text{K}_{F=2}$ .

With this set of selection rules and the picture of a channel being described by a set of quantum numbers in Hund's case (e) (i.e. for the asymptotic behaviour of the potential), the simple picture of Feshbach resonances which appear when two channels with the appropriate set of quantum numbers cross due to their different behaviour under an external magnetic field, as shown in fig. 4.2, can give a basic understanding of this scattering phenomenon. As already mentioned, the exact position of the resonances deviates from this simple picture and the determination of their precise positions is a complex task of numerical calculations and fitting to experimentally obtained data. A sketch of this process is given in the last section of this chapter.

### 4.1.3 Inelastic scattering

An experimentally detectable signature for a Feshbach resonance is a reduced lifetime of the sample in the vicinity of that resonance. These losses stem from inelastic collisions when in the vicinity of a resonance loosely bound Feshbach molecules are formed and collide with other atoms of the ensemble. For the loss process, three atoms need to be involved since due to energy- and momentum-conservation laws a third particle is required to dissipate the released binding energy of the molecule. This freed energy is high enough for the third atom to leave the trap. The measured loss feature is thereby based on a three-body inelastic collision.

Another inelastic scattering can appear in the case that the scattering channel is not the absolute ground state of the system. In this case, spin-changing collisions can lead to a two-body inelastic loss. Figure 4.5 illustrates the fact that this inelastic loss process can be enhanced in the vicinity of a Feshbach resonance. The increased time the two atoms spend in the bound state, and thereby at short internuclear distances, increases the possibility of a scattering into the open inelastic loss channel.

In sec. 7.5.1, experimental data is shown which illustrates that such inelastic loss features can sometimes be very prominent and at first glance misinterpreted to be a Feshbach resonance feature.

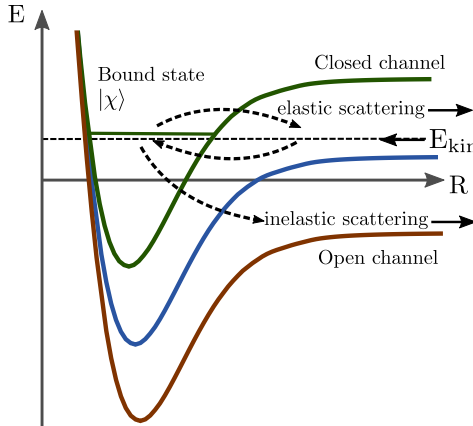


**Figure 4.5: Inelastic two-body scattering.** A Feshbach resonance appears from the coupling of the incoming channel (blue curve) to a bound state in a closed channel (green curve). Inelastic scattering (orange curve) is based on the same process. Due to the resonantly enhanced population of the bound state, a Feshbach resonance also increases the coupling probability to the inelastic channel. Adapted from [80].

## 4.2 Modelling of molecular potentials and Feshbach resonances

In this section, a brief overview over the steps necessary to theoretically predict and model Feshbach resonances shall be given. More details can be found e.g. in [81] and [36, 94]. With this description, it also will become clear why an experimental measurement of the resonances is mandatory to precisely understand the physics underlying atom-atom collisions.

While in sec. 4.1 the scattering of two atoms is discussed in the somewhat simplified frame of only two involved channels (one initial and one final channel or rather an open and a closed channel), for a full treatment of scattering often several channels have to be taken into account at the same time. Inserting the partial wave representation of the system's wave function (see eq. 3.24) into the time-independent Schrödinger equation (see eq. 3.26) leads to an infinite set of coupled differential equations of the form:

$$\sum_f \left[ \delta_{fi} \left( -\frac{1}{2\mu} \frac{\partial^2}{\partial R^2} + \frac{l_f(l_f+1)}{2\mu R^2} - E \right) + V_{fi}(\vec{R}) \right] F_{fi} = 0 \quad , \quad (4.19)$$

where  $F_{fi}$  are the radial functions (similar to  $R_l(k, r)$  in eq. 3.24),  $V_{fi}(\vec{R})$  are the scattering potentials (usually in the Born-Oppenheimer approximation) which contain all interaction terms,  $R$  is the interatomic distance,  $l_f$  the angular momentum quantum number of channel  $f$  and  $\delta_{fi}$  is the Dirac delta. These equations describe the scattering of atoms in the centre of mass system. They incorporate all  $i$  initial channels and take all  $f$  possible final channels of the scattering process into account.

The main objective is to solve these equations, but normally the scattering potentials as well as the wave functions are unknown. This leads to the task to model the potentials as well as to find appropriate wave functions. The potentials are two-atomic molecular potentials (in the case of the scattering of two atoms) of the form as described in sec. 2.2. But to describe the scattering process, they also have to include possible further interaction terms, which couple initial and final scattering channels, as is discussed in sec. 4.1.2.

For the two-body problem of two atoms  $A$  and  $B$ , with the atomic total electron spins  $\vec{s}_A$  and  $\vec{s}_B$  and the atomic nuclear spins  $\vec{i}_A$  and  $\vec{i}_B$ , the description of the scattering potential can be used as introduced for example in [94]. The potentials then have the following form

(given here for one specific channel combination  $f_i$ ):

$$V_{fi}(R) = H_{\text{hf}}(R) + H_{\text{Zeeman}} + V_{SS}(\vec{R}) + U_X(R)P_X + U_a(R)P_a \quad . \quad (4.20)$$

Here

$$H_{\text{hf}}(R) = \sum_{\alpha=A,B} a_{\alpha}(R) \vec{s}_{\alpha} \cdot \vec{i}_{\alpha} / \hbar^2 \quad (4.21)$$

is the hyperfine-contact interaction term. In the limit of infinite internuclear distance,  $a_{\alpha}(R)$  approaches the atomic hyperfine constant  $a_{\text{hf}}$ . To describe the behaviour for smaller  $R$ , the following ansatz can be chosen:

$$a_{\alpha}(R) = a_{\alpha,\text{hf}} \left( 1 + \frac{c_f}{e^{(R-R_0)/\Delta R} + 1} \right) \quad , \quad (4.22)$$

where  $\Delta R$  is a width, and  $R_0$  is the switching point of the ansatz function.  $c_f$  is a fit parameter.

$$H_{\text{Zeeman}} = \sum_{\alpha=A,B} (g_{s,\alpha} s_{z,\alpha} + g_{i,\alpha} i_{z,\alpha}) \mu_B B / \hbar \quad (4.23)$$

is the magnetic Zeeman interaction. The constants  $g_{s,\alpha}$  and  $g_{i,\alpha}$  are the electron and nuclear gyromagnetic ratio of atom  $A$  and  $B$ , respectively.

$V_{SS}(\vec{R})$  is the *effective spin-spin interaction* containing the spin-spin and spin-orbit coupling and the only term in the Hamiltonian which can mix and couple different partial waves  $l$ . It can be written as:

$$V_{SS}(\vec{R}) = \frac{2}{3} \lambda(R) (3S_Z^2 - S^2), \quad (4.24)$$

with  $S_Z$  being the total electron spin projection operator along the internuclear axis  $Z$  (which must not be confused with the laboratory frame axis  $z$ ) and

$$\lambda(R) = -\frac{3}{4} \alpha^2 \left( \frac{1}{R^3} + a_{SO} e^{-b_{SO} R} \right) \quad (4.25)$$

consists of two terms, the first representing the dipole-dipole (spin-spin) interaction and the second the second-order spin-orbit coupling;  $\alpha$  is the fine structure-constant (if  $\lambda(R)$  and  $R$  are given in atomic units).

In order to solve eq. 4.19, one has to construct the potentials of the involved channels. First, the Born-Oppenheimer approximation (see sec. 2.2.2) leads to the potential energy curves which only depend on the internuclear distance  $R$ .  $U_X$  and  $U_a$  are the so-called *Born-Oppenheimer potentials*. The physics contributing to the potentials for different  $R$  change drastically when comparing large to small internuclear distances. The potentials are therefore constructed in regions and have to be connected smoothly in the end to form a complete potential valid for all  $R$ . Figure 4.6 shows an overview over a complete molecular potential and the different regions used in modelling of the PEC.

Working in the basis  $|SM_S IM_I\rangle$  where  $\vec{S} = \vec{s}_A + \vec{s}_B$  and  $\vec{I} = \vec{i}_A + \vec{i}_B$  are the total electron and nuclear spin of the molecule,  $P_X$  and  $P_a$  in eq. 4.20 are the projectors onto this chosen basis functions.

For the inner region with  $R < R_{inn}$ , a strongly repulsive potential is used to account for the Coulomb interaction between the overlapping electron clouds. Furthermore, the orientation of the spins of the valence electrons leads to the splitting of the potential curves into singlet

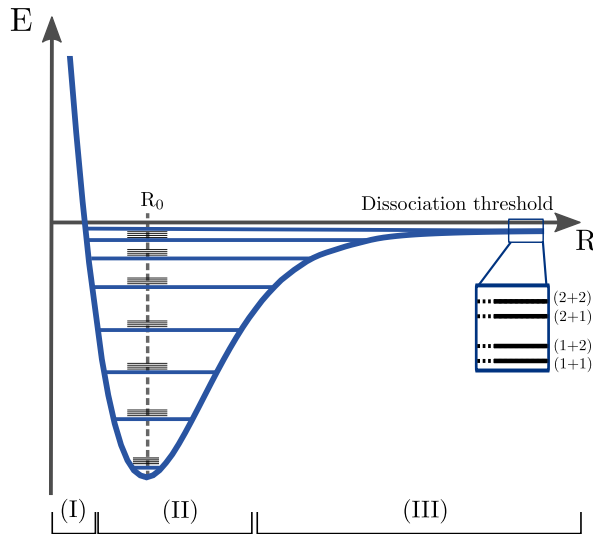


**Figure 4.6: Overview over a complete molecular potential.** The potential can be modelled by separating three regions: an inner one for  $R < R_{inn}$  (I), an intermediate one for  $R_{inn} < R < R_{out}$  (II) and an outer one for  $R > R_{out}$  (III). The inset shows the hyperfine levels at the asymptote which are the sum of the hyperfine state of (in this exemplary case)  $F_{\text{Na}}$  (first number in the bracket) and  $F_K$  (second number in the bracket).

and triplet configurations, as is discussed in sec. 4.1.2. The short-range repulsive wall can be represented in the form:

$$U_{\text{SR}}(R) = u_1 + u_2/R^s \quad , \quad (4.26)$$

where  $u_{1,2}$  are fit parameters to assure a continuous and differentiable connection to the intermediate potential part and  $s$  can be chosen to model the steepness of the potential wall.

The intermediate potential region with  $R_{inn} < R < R_{out}$  is complicated to model. Ab-initio calculations can give a first hint of its shape. Unfortunately, due to the complicated interatomic interactions, ab-initio calculations do not achieve an accuracy with which precise predictions could be made. Where possible, spectroscopic data of the ro-vibrational level structure is used to fit the model potentials to this experimental data. This can significantly increase the accuracy of the potential energy in the intermediate region and is a hint that for a detailed description of molecular potentials experimental data is mandatory. In the intermediate region, the potential can be approximated by a power expansion:

$$U_{\text{IR}}(R) = \sum_{i=0}^n a_i \xi^i(R) \quad , \quad (4.27)$$

with

$$\xi(R) = \frac{R - R_m}{R + bR_m} \quad . \quad (4.28)$$

The fit parameters are  $n$ ,  $a_i$ ,  $b$  and  $R_m$ .

In the outer region with  $R > R_{out}$ , the van-der-Waals interaction dominates. Therefore, the potential can be approximated in this region by the inverse power series of eq. 4.16 and the exchange contribution:

$$U_{\text{LR}}(R) = -C_6/R^6 - C_8/R^8 - C_{10}/R^{10} \mp E_{\text{exch}}(R) \quad , \quad (4.29)$$

where the sign depends on whether a singlet (-) or a triplet (+) state is described and the exchange contribution is given by

$$E_{exch}(R) = A_{ex} R^\gamma e^{(-\beta R)} \quad . \quad (4.30)$$

$A_{ex}$ ,  $\beta$ ,  $\gamma$  and the C-coefficients are fit parameters.

At the asymptote, the energy structure is solely given by the atomic energy levels, as already described in sec. 4.1.2.

Joining these three regions smoothly and fitting them to available spectroscopic data gives the starting potentials. The closer these starting potentials are to the real potential energy curves, the better the results will be for the following calculations.

With the interaction potentials constructed, the coupled channel equations 4.19 are solved in the partial-wave approximation for low interaction energy (taking into account the partial waves of  $l = 0, 1, 2, 3, 4$  at maximum) and with the following boundary conditions:

$$\begin{aligned} F_{fi}(0) &= 0 \\ F_{fi}(R) &\xrightarrow[R \rightarrow \infty]{} \sqrt{\frac{2\mu}{\pi\hbar^2 k_i}} \left[ \frac{e^{-i(k_i R - l_i \pi/2)} \delta_{fi} - e^{i(k_i R - l_i \pi/2)} S_{fi}}{2i} \right] \end{aligned} \quad (4.31)$$

with  $k_i = \sqrt{2\mu E_i / \hbar^2}$ . Since the system contains of many different channels which can be coupled, the scattering amplitude  $f(k, \theta)$  as used in sec. 3.2, where only one initial channel coupled to one final channel, is now replaced by a *scattering matrix*  $S_{fi}$ . As for  $f(k, \theta)$ , all experimentally observable quantities can be derived from that scattering matrix. That means, to correctly determine this scattering matrix is the key to gain access to e.g. the scattering length, which can be expressed by  $S_{fi}$  as follows (for the case of scattering of identical particles from indistinguishable initial to indistinguishable final spin states):

$$\lim_{k_i \rightarrow 0} a_i = -\frac{\ln(\{S\}_{ii})}{2ik_i} \quad , \quad (4.32)$$

where the diagonal scattering matrix elements are related to the scattering phase shift by  $\{S\}_{ii} = e^{2i\delta_i}$  (for more details on the correct inclusion of the spin degrees of freedom into the scattering process see [81]).

Hence, the task is to solve equation 4.19 for the constructed interaction potentials to ultimately derive the scattering matrix and from it e.g. the scattering length  $a$ . Solving the coupled linear differential equations is normally done by applying numerical methods. These methods can be divided into two categories [81], explicit (or "propagator") and implicit ones. In both approaches, the calculations are performed for discretised potential energy curves. Therefore, these methods operate on a *grid* of the spacial variable  $R$ . In explicit methods, the Schrödinger equation needs to be solved at the preceding grid point to be able to determine the value of the scattering wave function at the next point. Methods used here are for example the Numerov method [95] or the Gordon method [96]. The calculations performed for the most up to date molecular potentials and Feshbach resonance positions in NaK, which are presented in the frame of chap. 7 and [1], are calculated using a Numerov algorithm. In implicit methods, large sets of linear equation eigensystems are solved, by this determining the eigenenergies and wave functions of the potential at all grid points at the same time. Examples for implicit methods can be found e.g. in [81].

In the case of cold atomic collisions, often a simpler but yet still sufficient approach to solve eq. 4.19 can be used: So-called *multi-channel calculations* treat the short-range part of the scattering potentials as energy-independent. Thereby, the coupling effects dominant at short distances (like the spin-exchange interaction) need only to be calculated for a very limited set of different  $R$ -values. The final scattering matrix' energy therefore mainly depends on

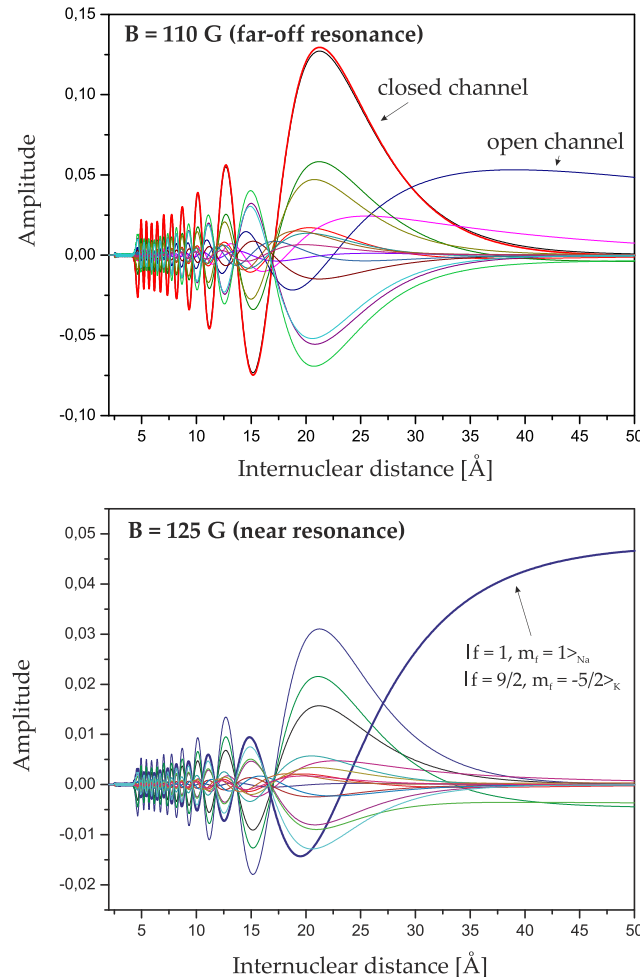


**Figure 4.7: Scattering wave functions.** The graphs show the different components of the total wave function for a Feshbach state in  $^{23}\text{Na}^{40}\text{K}$ , projected onto the basis of Hund's case (e), for two different magnetic field strength. For short internuclear distances (up to  $\sim 5 \text{ \AA}$ ) all wave functions are nearly identical while largely differing at larger distances. Picture taken from [4, 36].

the evolution of the scattering-channel wave functions for large  $R$ . At large  $R$  the channels can be treated as uncoupled, simplifying the problem significantly.

As a consequence of this approach, the scattering wave functions are nearly identical for small internuclear distances while they differ strongly from each other at large distances. This is illustrated e.g. in [81] and also in fig. 4.7. In the figure, the components of a Feshbach state in  $^{23}\text{Na}^{40}\text{K}$  are projected onto the basis of Hund's case (e). For short internuclear distances (up to  $\sim 5 \text{ \AA}$ ), all wave functions are nearly identical while significantly differing at larger distances. For more information on the multi-channel calculation method see [81] and references therein.

The ability to derive quantities from the Schrödinger equation that can be compared with experimental measurements enables the inspection of the quality of the interaction potentials. Thereby, it is possible to model the interaction potentials in an iterative procedure to reproduce experimentally derived data from various measurements. These can be spectroscopic data derived from heat-pipe experiments, measurements of binding energies and scattering rates and experimentally determined positions of resonances. All these experimental observations ultimately have to be described by the interaction potentials (given that

the chosen method to numerically solve the coupled equations is known to be precise and correct). If this can be achieved, confidence is gained that the derived potentials describe the nature of the interaction realistically enough to enable predictions for future experiments. This can e.g. be the precise prediction of transition frequencies and transition dipole matrix elements for a STIRAP process, which reduces the experimental effort substantially.

Feshbach resonance positions depend on the molecular potentials and interaction terms. By measuring the exact Feshbach resonance positions and feeding the results back to the theory, the potential energy curves can be improved. Since Feshbach resonances are usually measured in ultracold ensembles, effects such as Doppler broadening are much less present than in other spectroscopic experiments (such as e.g. measurements in heat pipes). Therefore, the observation of such resonances gives very precise data points to refine the potential energy curves.

# Chapter 5

## Theory of Bose-Einstein condensation

When following the well established path to produce ultra-cold molecules, quantum degeneracy has to be reached in the mixture of  $^{23}\text{Na}+^{39}\text{K}$  before associating them to Feshbach molecules and transferring them to the absolute ground state. Since  $^{23}\text{Na}$  as well as  $^{39}\text{K}$  are bosons, this is tantamount to preparing a BEC for both species. In the experiment setup presented in this thesis, this will be realised inside a harmonic optical trapping potential. The theoretical background of BEC has been reviewed in many textbooks, articles and theses (see e.g. [80, 82, 83]). Therefore, the theoretical methods required for the understanding of the experiments performed in this work will be briefly discussed in this chapter.

### 5.1 Theoretical description of BEC

BEC is a quantum-mechanical phenomenon. In quantum mechanics, particles are no longer accurately described by classical trajectories but are represented by wave packages according to the Heisenberg uncertainty relation. The characteristic length scale of such a wave package is given by the de-Broglie wavelength:

$$\Lambda_{dB} = \frac{\hbar}{\sqrt{2\pi m k_B T}} \quad (5.1)$$

with which the so-called phase space density (PSD) can be expressed as:

$$PSD = n \Lambda_{dB}^3 \quad , \quad (5.2)$$

where  $n$  is the particle density of the sample. The PSD of a sample is an important experimentally accessible parameter. It indicates at each step of an experiment cycle the feasibility for reaching a BEC. Its experimental importance will be illustrated when discussing run-away evaporation in sec. 6.10.

#### 5.1.1 Non-interacting indistinguishable particles

First, no inter-particle interactions will be taken into account. As will be seen in sec. 5.1.2, interactions enhance the complexity of the description of ultra-cold bosonic particles, but also inherit interesting phenomena. BEC occurs when the mean inter-particle distance  $d$  of the indistinguishable bosonic particles becomes comparable to the de-Broglie wavelength  $\Lambda_{dB}$

$$d \lesssim \Lambda_{dB} \quad (5.3)$$

which can be written as

$$n \Lambda_{dB}^3 \gtrsim 1 \quad (5.4)$$

when defining the density of the sample as a normalized number of particles inside a volume spanned by the mean distance between the particles  $n = 1/d^3$ . To describe the behaviour of the indistinguishable bosons, methods from statistical physics can be applied [82]. Thereby, it can be found that the mean occupation number of bosons in a certain quantum-mechanical state  $k$  is (above a critical temperature) correctly described by the Bose-Einstein distribution:

$$\langle n_k \rangle = \frac{1}{e^{\beta(\epsilon_k - \mu)} - 1} , \quad (5.5)$$

where  $\beta = 1/(k_B T)$ ,  $\epsilon_k$  is the energy of state  $k$  and  $\mu$  is the chemical potential. The chemical potential is a measure for the change of the energy of a system if a particle is added to or removed from it. If the chemical potential is negative, it is energetically beneficial to add particles to the system, if it is positive it is unfavourable to add further particles. In case of a BEC, the chemical potential is negative since it is energetically favourable if all bosons occupy the same absolute ground state. In addition, a chemical potential larger than the energy of the state would lead to a negative occupation number (which is physically incorrect). Therefore,  $\mu$  has always to be smaller than the energy of the state. Applying this to the ground state of the system  $\epsilon_0$  imposes a limit on the number of particles in excited states. This can be demonstrated by writing the absolute number of particles in the sample as:

$$N_{total} = \sum_k \langle n_k \rangle = N_0 + \sum_{k \neq 0} \frac{1}{e^{\beta(\epsilon_k - \mu)} - 1} . \quad (5.6)$$

The sum can be solved approximately for high temperatures ( $T \gg \epsilon_k/k_B$ ) by using the Riemann Zeta function  $\zeta_3(\tilde{z})$ . It then follows that

$$N_{total} = N_0 + \left( \frac{k_B T}{\hbar \omega} \right)^3 \cdot \zeta_3(\tilde{z}) , \quad (5.7)$$

where  $\tilde{z} = \exp(\beta(\mu - \epsilon_0))$  and  $\omega = (\omega_x \omega_y \omega_z)^{1/3}$  is the geometric mean of the oscillator frequencies of a harmonic trapping potential for which eq. 5.6 has been solved here. The harmonic trapping potential has been chosen as it resembles the optical trapping potential used in the experiments performed in the course of this thesis (see sec. 6.11).

Because  $\mu > \epsilon_0$ , it follows that  $0 < \tilde{z} < 1$  and with this the Riemann Zeta function is limited to  $\zeta_3(\tilde{z}) \approx 1.2$  for  $\tilde{z} \rightarrow 1$  (which means  $\mu \rightarrow \epsilon_0$ ). Hence, the second term in eq. 5.7 is limited and by setting  $N_0 = 0$  and solving the equation for  $T$ , the formula for the critical temperature can be derived:

$$T_C = \frac{\hbar \omega}{k_B} \left( \frac{N_{total}}{\zeta_3(1)} \right)^{1/3} . \quad (5.8)$$

When the temperature of a bosonic sample becomes lower than this critical temperature, a phase transition occurs. Because  $T < T_C$  means that the number of particles in the excited states  $N_{exc}$  in eq. 5.8 has to become  $N_{exc} < N_{total}$ , the remaining particles have to accumulate in the ground state, leading to an increasing  $N_0$ . This process is called Bose-Einstein condensation. All bosons in the absolute ground state share the exact same quantum numbers which leads to a macroscopic object being described by a single quantum-mechanical wave function. Note that this process will only occur for bosons, as the Pauli-exclusion principle forbids two fermionic particles to share the exact same set of quantum numbers. The percentage of particles in the ground state can now be expressed with eq. 5.7 and eq. 5.8 as:

$$\frac{N_0}{N_{total}} = 1 - \left( \frac{T}{T_C} \right)^3 . \quad (5.9)$$

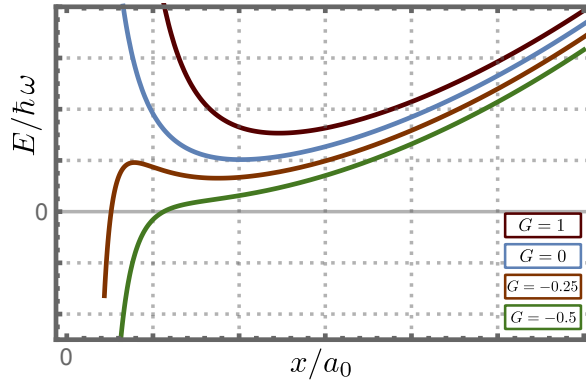


**Figure 5.1: Graphical representation of solutions to the GPE.** The GPE has been solved for different interaction strength giving the energy of the system as a function of the spacial extend in  $a_0$  of the BEC. An offset has been added to the graphs to separate the different solutions for better visibility.

Note that this formula is valid only for the specific case of a harmonically trapped sample, for particles in free space for example, the solution will look slightly different, see e.g. [36]. The critical value for BEC can also be expressed in terms of the PSD. In that case condensation starts when

$$PSD_C \simeq 2.612 , \quad (5.10)$$

though finite size effects and interactions in a real atomic gas influence the exact value of eq. 5.10.

### 5.1.2 Interacting bosons

A full theoretical discussion about calculating interactions in ultracold bosonic gases and BECs is beyond the scope of this section. It is covered by several articles and textbooks (see e.g. [97–100]). Only a flavour of the underlying theory will be given here with the focus on showing the relations important for the investigations done in this thesis.

The complex problem of interacting bosonic particles in a cold dense ensemble can be vastly simplified when using the following approximations. The assumption that only s-wave scattering occurs in the ensemble (which is reasonable taking into account the ultra low temperatures at which BEC takes place) leads to a simplified interaction potential. A mean-field description in the limit of large particle numbers enables the separation of condensed and thermal fraction in the wave function of the system. This leads to a nonlinear Schrödinger equation describing the interacting bosons at low temperatures. It is called the Gross-Pitaevskii equation (GPE) (here already stated in the stationary form) and reads:

$$\mu\psi_0(\mathbf{r}) = \left[ -\frac{\hbar^2}{2m} \nabla^2 + V_{ex}(\mathbf{r}) + g |\psi_0(\mathbf{r})|^2 \right] \psi_0(\mathbf{r}) \quad (5.11)$$

with  $\psi_0(\mathbf{r})$  being the condensate wave function,  $V_{ex}(\mathbf{r})$  an external potential (e.g. a magnetic or optical trapping potential) and  $\mu$  the chemical potential. The interaction potential is given by a pseudo-potential of the form  $g |\psi_0(\mathbf{r})|^2$  where  $|\psi_0(\mathbf{r})|^2 = n_0(\mathbf{r})$  is the density distribution of the condensate. The interaction strength  $g$  is given in the form

$$g = \frac{4\pi\hbar^2}{m} a \quad (5.12)$$

where  $a$  is the scattering length taken in the low temperature s-wave scattering regime. With this formulation of the interactions, it is apparent that they depend directly on the

inter-particle scattering length  $a$  which is discussed extensively in sec. 4.1.1. Additionally, the applicability of Feshbach resonances in BEC is indicated due to the possibility to change the interaction term drastically in the vicinity of a Feshbach resonance by applying an external magnetic field. To get an understanding on how different interactions change the behaviour of the Bose gas, the GPE can be solved for a Gaussian condensate wave function. In fig. 5.1, the energy of the system is plotted for four different values of the interaction strength  $G \propto a$  versus the spacial dimension of the BEC. Three different cases can be distinguished:

- A negative interaction strength, meaning an attractive interaction, leads to an ever increasing density in the condensate: The atoms come closer due to the attraction, thereby further increasing the attractive interaction. Due to this ever reinforcing process, the sample becomes unstable and ultimately collapses (which has been named a *Bosenova* and was first measured in [101]). Only samples with very few atoms remain stable in a BEC with attractive interactions (represented in fig. 5.1 by the graph with  $G = -0.25$ ).
- In the case of no interactions, i.e.  $a = 0$ , the sample acts like an ideal gas and the GPE becomes a linear Schrödinger equation, leading to the behaviour discussed in sec. 5.1.1. Since the particles do not interact with each other, they also do not thermalize.
- For a positive scattering length, the interaction potential energy increases with increasing density. This leads to a repulsive interaction and an enlarged density distribution for BECs of increasing particle number, visible in fig. 5.1 where for  $G = 1$  the minimum of the energy is situated at larger distances  $x$  compared to the case with  $G = 0$ , meaning the stable state of the system leads to a larger extended BEC. Furthermore, in a trapping environment the interaction energy is minimized if the wave function is spread as uniformly as possible, leading to the situation that the shape of the BEC takes the form of the trapping potential. This will be discussed in more detail in the following.

When comparing the interaction energy with the kinetic energy for samples in experimental conditions, one finds that the interaction energy is on the order of  $10^3$  to  $10^4$  times larger than the kinetic energy of the particles [80]. Therefore, the operator for the kinetic energy in the GPE 5.11 can be neglected (Thomas-Fermi approximation), leading to an analytically solvable equation where the density distribution is then given by:

$$|\psi_{TF}(\vec{r})|^2 = \begin{cases} (\mu - V_{ex}(\vec{r})) / g & , \quad \mu \geq V_{ex}(\vec{r}) \\ 0 & , \quad \text{else} \end{cases} \quad (5.13)$$

With this the density distribution of a trapped Bose-Einstein condensate can be seen to follow the shape of the trapping potential. The chemical potential can be expressed in the Thomas-Fermi approximation as follows:

$$\mu = \frac{N}{2\bar{a}} \hbar (15a)^{2/5} \left( \omega_x \omega_y \omega_z \right)^{1/3} \quad (5.14)$$

where  $\bar{a} = \sqrt{\hbar/m\omega}$  is the oscillator length of the trap potential.

### Two-component Bose gases

Since this thesis investigates a Bose gas mixture of two different elements, it is necessary to investigate how the interspecies interactions will modify the behaviour of the sample, especially when it comes to the task of forming two stable BECs in a mixture. For this

purpose, the GPE can be modified with an interspecies interaction term, leading to a set of coupled GPEs (for details see [36, 102]):

$$\begin{aligned}\mu_1 \psi_1(\mathbf{r}) &= \left[ -\frac{\hbar^2}{2m_1} \nabla^2 + V_{ex}(\mathbf{r}) + g_{11} |\psi_1(\mathbf{r})|^2 + g_{12} |\psi_2(\mathbf{r})|^2 \right] \psi_1(\mathbf{r}) , \\ \mu_2 \psi_2(\mathbf{r}) &= \left[ -\frac{\hbar^2}{2m_2} \nabla^2 + V_{ex}(\mathbf{r}) + g_{22} |\psi_2(\mathbf{r})|^2 + g_{12} |\psi_1(\mathbf{r})|^2 \right] \psi_2(\mathbf{r}) .\end{aligned}\quad (5.15)$$

Since negative intraspecies interactions would lead directly to an unstable sample, they are assumed to be both positive. Depending on the interspecies scattering length, the two components will either mix or separate; additionally, the possibility of a collapse exists. As can be shown [36], an investigation of the coupled GPEs yields (in the mean-field approximation) the following three possibilities:

$$\begin{aligned}\text{miscible: } |g_{12}| &< \sqrt{g_{11}g_{22}} \\ \text{immiscible: } |g_{12}| &> \sqrt{g_{11}g_{22}} \quad \text{when } g_{12} > 0 \\ \text{collapse: } |g_{12}| &> \sqrt{g_{11}g_{22}} \quad \text{when } g_{12} < 0 .\end{aligned}\quad (5.16)$$

For the experiments performed during this thesis, especially the miscible region is of importance as only there rethermalization between the two atomic samples will occur. The relations given above can be incorporated in one parameter [103–105]:

$$\delta g(B) = \frac{g_{12}^2(B)}{g_{11}(B) \cdot g_{22}(B)} - 1 \quad (5.17)$$

with which a condensed mixture is miscible if  $\delta g(B) < 0$  and  $\delta g(B) > 0$  leads to either immiscibility or mean-field collapse, depending on the sign of  $g_{12}(B)$  (see cases 5.16). More details on this will be given in connection with the experimental realisation of a double BEC in a mixture of  $^{23}\text{Na}$ + $^{39}\text{K}$ , see sec. 8.2. It shall be also mentioned here as a side note that at the points where repulsive intraspecies interactions exactly cancel the attractive interspecies interactions, the mean field effects are very small and by this beyond-mean-field effects can become significant. As shown in [102], this can lead to the formation of so-called *quantum droplets*. These droplets are self-stabilising and do not expand even if there is no external confinement.

## 5.2 Experimental signatures of BEC

There are different experimentally observable signatures which prove that a BEC has formed. In some experiments, the coherence of the BEC wave function leads to the observation of interference patterns when BECs interacted with themselves (see e.g. [106, 107]). In this thesis, two other signatures are used to identify the BEC. The first one is the bimodal distribution which is detectable when only a part of the sample is in the BEC phase, the second one is the turning of the aspect ratio for a BEC released from an anisotropic trapping potential.

### 5.2.1 Bimodal distribution

As discussed in sec. 5.1.2, the density distribution of a BEC takes the shape of the trapping potential. For a harmonic trapping potential, this shape differs from the Gaussian distribution of a trapped thermal cloud. As has been shown (first on the basis of semi-classical models in [108] and [109] and later based on superfluid hydrodynamic equations [110]), a freely expanding BEC conserves its functional form during TOF. Thus, the first clear experimental observation of a forming BEC is the so-called bimodal distribution. In such a distribution

the thermal cloud is Gaussian shaped and the much denser BEC is emerged inside it. This BEC is described by an inverted parabola (for a harmonic trapping potential).

When a picture is taken of a BEC in TOF using absorption imaging (see sec. 6.9.1 for details on absorption imaging), the density of the sample is integrated along the imaging axis (here  $y$ ), leading to a recording of the column density  $\tilde{n}_y$ . The column density is fitted along the trapping axis with a parabola for the BEC part (in case of a previously harmonically trapped sample) and a Gaussian for the thermal cloud<sup>1</sup>:

$$\tilde{n}_y(x) = \tilde{n}_{BEC} + \tilde{n}_{Thermal} \quad (5.18)$$

for a fit along the  $x$ -axis. Here

$$\tilde{n}_{Thermal} = \frac{\tilde{n}_{thermal,0}}{\sqrt{2\pi}\sigma_x} \cdot \exp\left[-\frac{(x - Pos_x)^2}{2\sigma_x^2}\right] + \text{Offset}_x \quad (5.19)$$

and

$$\tilde{n}_{BEC} = \tilde{n}_{BEC,0} \left[1 - \frac{(x - Pos_x)^2}{W_x^2}\right]^{3/2} \cdot \Theta\left[1 - \frac{(x - Pos_x)^2}{W_x^2}\right] + \text{Offset}_x \quad (5.20)$$

with the Heavy-side Theta-function  $\Theta[\dots]$  and  $W_x$  given by eq. 5.21.  $\text{Offset}_x$  is an additional fit parameter for the case that the images feature a global offset. From a fit to the image, all information can be gathered, be it the condensate fraction or the temperature. Since a BEC does not follow a Boltzmann distribution, it is not possible to assign a temperature to it by analysing the expansion of the condensate in TOF. Therefore, the thermal part of the distribution is used to derive the temperature of the system, making the assumption that the condensate is in thermal equilibrium with the thermal cloud. By fitting only the wings of the distribution with a Gaussian profile, the temperature of the system can be obtained from a series of TOF images. A temperature analysis of a BEC can be found in sec. 8.1.

## 5.2.2 Turning of aspect ratio

The reason for the turning of the aspect ratio of an expanding condensate can be illustrated with a classical argument following [108]. Inside the trap, an equilibrium is reached where all forces acting on a particle of the condensate compensate each other, i.e.  $\vec{F}(\vec{r}) = -\vec{\nabla}(V_{ex}(\vec{r}) + g|\psi_{TF}(\vec{r})|^2) = 0$ . When the external potential is switched off ( $V_{ex}(\vec{r}) = 0$ ), the force present during free expansion is given by the force derived from the density distribution of the trapped condensate:  $\vec{F}(\vec{r}) = -\vec{\nabla}(g|\psi_{TF}(\vec{r})|^2)$ . For an anisotropic density distribution, as it is usually present in optical traps with different trap frequencies along each main axis, the expansion will also be anisotropic. The maximal circumference of the trapped condensate wave function in the Thomas-Fermi approximation is given by

$$W_j = \frac{1}{\omega_j} \sqrt{\frac{8\mu}{m}} \quad , \quad (5.21)$$

where  $j = x, y, z$  represents the respective main axis of the condensate and  $\omega_j$  is the trap frequency of the trapping potential along this axis.  $\mu$  is to be taken from eq. 5.14. The time

---

<sup>1</sup>The most accurate treatment would be a two dimensional surface fit of the image. In the experiment this can sometimes be complicated, especially when the imaging axis is not perpendicular to one of the trapping axis. This is the case in the experiment setup used in this thesis, see sections 6.9.2 and 8.1.

dependence of the free expansion can be described by adding a scaling factor along each main axis  $b_j(t)$  which fulfil a set of coupled equations of the form

$$\frac{d^2 b_j(t)}{dt^2} = \frac{\omega_j^2}{b_j(t)b_x(t)b_y(t)b_z(t)} \quad \text{with} \quad \frac{db_j(0)}{dt} = 0 \quad \text{and} \quad b_j(0) = 1 \quad . \quad (5.22)$$

For a cigar-shaped trap where  $\omega_x = \omega_y$ , the maximal circumferences in these directions are equal:  $W_x = W_y = W_\perp$ . For a trap frequency ratio of  $\kappa = \omega_\perp/\omega_z \ll 1$ , there exists an approximate solution for eq. 5.22 [111] of the form:

$$\begin{aligned} b_\perp(\tau) &= \sqrt{1 + \tau^2} \\ b_z(\tau) &= 1 + \kappa^2 \left( \tau \arctan(\tau) - \ln \left( \sqrt{1 + \tau^2} \right) \right) \end{aligned} \quad (5.23)$$

where  $\tau = \omega_\perp t$ . By plotting the time evolution of the aspect ratio  $W_\perp(t)/W_z(t) = \Gamma b_\perp(t)/b_z(t)$ , with  $\Gamma = W_\perp/W_z$  being the aspect ratio at  $t = 0$ , the characteristic turning of it can be seen for a BEC released from a cigar shaped trap as shown for experimental data in sec. 8.1.



## **Part II**

# **Experiment**



# Chapter 6

## Experiment setup

In this chapter, all components of the experiment apparatus are described and characterisations of every important part in the experiment sequence are presented. The chapter is structured as follows: First, an overview is given how the different parts of the experiment are arranged in the laboratory, next the vacuum components are discussed. This is followed by a description of the experiment control system and the presentation of the different laser systems which are used to manipulate the atoms in the experiment. Subsequently, the procedure of cooling and trapping the atomic species is outlined by describing the different experiment steps, starting with the atom sources, followed by the 3D MOT, the optical molasses stage, the magnetic trapping and imaging of the atoms, the evaporative cooling of  $^{23}\text{Na}$  and  $^{39}\text{K}$  and their transfer into the cODT. The final section discusses the radio frequency transfers (RF transfers) of the atomic species.

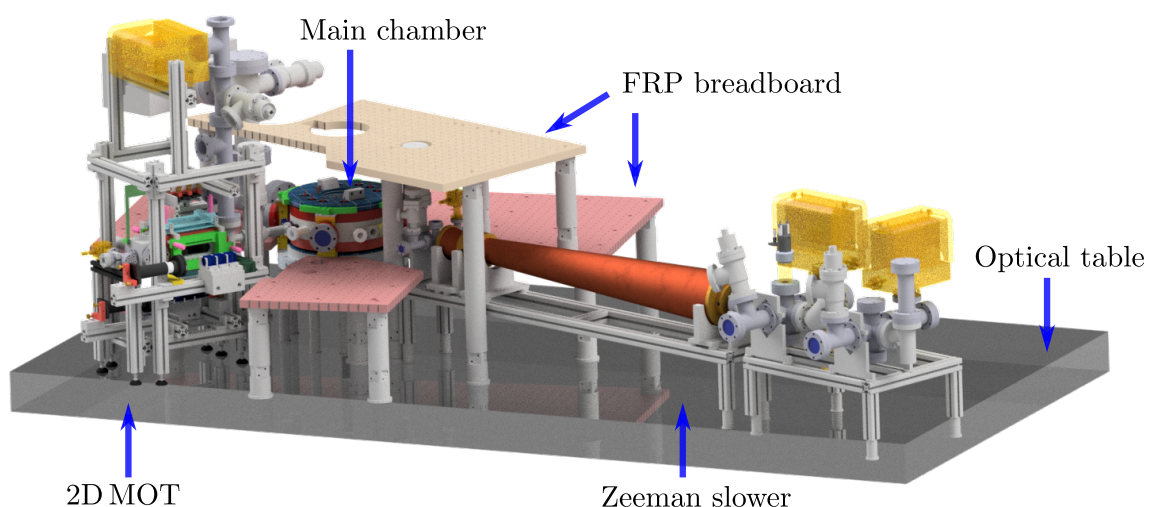


**Figure 6.1: Schematic of the experiment apparatus.** Optical components can be placed on three levels, the optical table and the custom made fibre-reinforced plastic (FRP) breadboards. The apparatus consists of the main chamber and the two atom sources: 2D MOT and Zeeman slower.

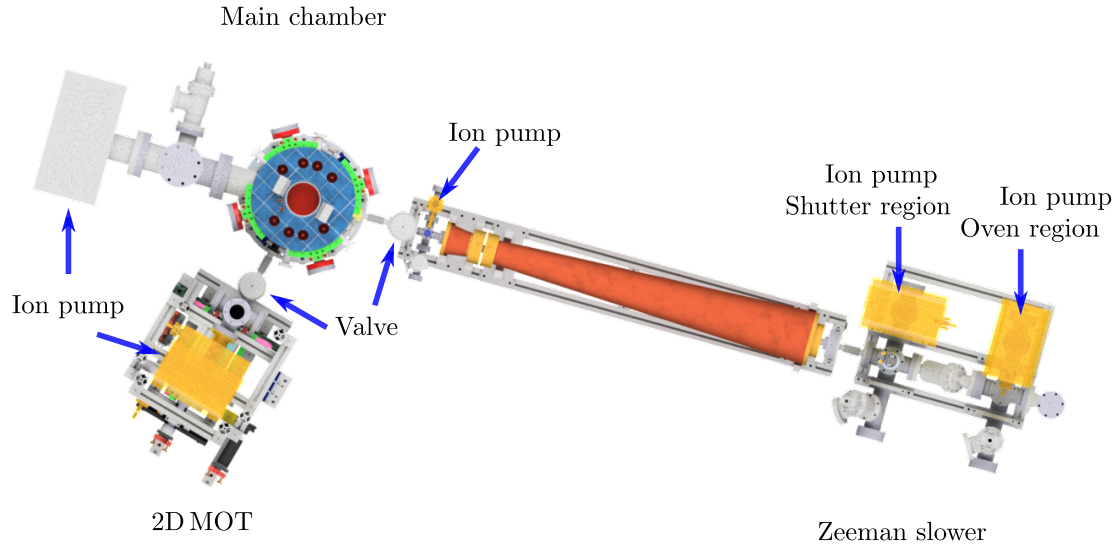


**Figure 6.2: Schematic of the vacuum apparatus.**

## 6.1 Experiment setup in the laboratory

The various components which form the experiment setup are distributed over four optical tables in the laboratory. On the first table, lasers are set up for the production of ground-state molecules, see sec. 9.2. The optics of the three laser systems used to trap  $^{23}\text{Na}$  and  $^{39}\text{K}$  (see sec. 6.4) are situated on the second and third table. On the fourth table, the main experiment is set up as well as the laser for the optical blue plug (see sec. 6.4.3). An image of the main experiment table is shown in fig. 6.1, visualizing the status of the system at the time this thesis was written. The optical components are not shown for lucidity.

A vacuum apparatus maintains the required ultra-high vacuum conditions. Its design is presented in sec. 6.2. The magnetic fields to trap and manipulate the atomic samples are generated by sets of coils which are described in sec. 6.5.1. Radio and Microwave frequencies are generated and emitted by different antennas. Their setup is discussed in sec. 6.12.

On the main experiment table, optical elements are placed on three different levels of height. The first level is the optical table, onto which two levels of custom-made breadboards are mounted. These breadboards are manufactured from fiber-reinforced plastic (FRP), primarily to prohibit eddy currents [112]. They are induced in conductive materials e.g. when magnetic fields are switched on or off in the vicinity. Moreover, FRP does not possess any magnetizability, an additional important property which prevents parasitic stray magnetic fields. This could also be achieved by using breadboards made from metal. However, this metal would then have to be non-magnetic (like the following types of stainless steel: 1.4404, also called 316L, 1.4406, also called 316LN or 1.4429, also called 316 LN-ESU) and slotted to disable currents. Since the mechanical stability of FRP is similar to metal while being lighter, cheaper and much easier to manufacture, this material has been chosen for the experiment setup presented here.

## 6.2 Vacuum apparatus

The complete vacuum apparatus is shown in fig. 6.2 in its recent configuration. The setup consists of the main chamber to which the two atom sources, the Zeeman slower for  $^{23}\text{Na}$  (described in sec. 6.6.1) and the two-dimensional magneto-optical trap (2D MOT) for  $^{39}\text{K}$  (described in sec. 6.6.2), are connected via a valve (*All-metal gate valve, Series 481, 48124-*

*CE01-0001, VAT Group AG*). By these valves, the main chamber vacuum can be separated from the vacuum of the atom sources. The separate vacuum sub-parts are described in more detail below. The apparatus has been modified since its first description in [77]. The changes will be addressed in the corresponding sections. The current pressures in the subsequent parts of the apparatus are as follows:  $< 1 \cdot 10^{-11}$  mbar at the ion pump of the main chamber (a current of  $\sim 3.2$  nA is displayed on the ion pump controller),  $3 \cdot 10^{-10}$  mbar at the ion pump of the 2D MOT,  $2 \cdot 10^{-8}$  mbar in the oven section of the Zeeman slower,  $1 \cdot 10^{-10}$  mbar in the shutter region and a displayed current of  $\sim 0.2$  nA (which equals  $< 1 \cdot 10^{-11}$  mbar) for the ion pump on the front section of the Zeeman slower. Before discussing the separate vacuum sections, an insight into the theory of ultra-high vacuum shall be given. The focus is on providing information and formulas necessary to understand the modifications which have been applied to the system during the course of this thesis.

### 6.2.1 General theory of vacuum

This subsection gives a brief overview of the theory of vacuum conditions. A much more detailed perspective can be found e.g. in [113]. Vacuum is specified in different categories which also address the physical behaviour of the particles in the gas. The terminology for the different ranges of vacuum follows that in [113] which is:

Low vacuum: Atmospheric pressure to 1 mbar,

Medium vacuum: 1 to  $10^{-3}$  mbar,

High vacuum (HV):  $10^{-3}$  mbar to  $10^{-8}$  mbar,

Ultra-high vacuum (UHV):  $10^{-8}$  mbar to  $10^{-12}$  mbar,

Extreme high vacuum (XHV): Less than  $10^{-12}$  mbar.

In the experiment apparatus described in this thesis, the pressures are in the range of UHV, on the border to XHV in parts of the main chamber. When discussing the vacuum conditions of the experiment setup, only the terminus UHV will be used for simplicity.

During the transition from atmospheric pressure to UHV, the behaviour of the gas particles changes due to the constantly decreasing overall pressure. In the low to medium vacuum regime, the gas particles first follow the intuitive behaviour of a viscous flow, similar to a liquid. Therefore, the particles flow from regions of higher pressure to those of lower pressure. This behaviour changes eventually and the flow becomes a statistical process of individual particles scattering off walls and seldom with other particles. This is due to the fact that the mean free path of the particles becomes larger, meaning the interactions with other particles become fewer for lower pressures. The mean free path  $\lambda$  of a particle in an ideal gas is given by:

$$\lambda = \frac{1}{\sqrt{2\pi d^2 n}} , \quad (6.1)$$

where  $n$  is the number of particles per unit volume (also called the *number density*) and  $d$  is the diameter of the particle. Table 6.1 (taken from [113]) lists the number density and the mean free path for different pressures.

As can be seen from the table, at the latest at around  $10^{-3}$  mbar the mean free path of a particle becomes larger than the characteristic size of a vacuum container. At that point, the gas stops behaving like a liquid and its behaviour becomes statistical. The flow of the

**Table 6.1: Number density  $n$  and mean free path  $\lambda$ .** The values for  $n$  and  $\lambda$  are listed for N<sub>2</sub> at 295 K for different pressures  $p$ .

$p$ [mbar]	$n$ [m <sup>-3</sup> ]	$\lambda$
$10^3$	$2.5 \cdot 10^{25}$	64 nm
1	$2.5 \cdot 10^{22}$	64 μm
$10^{-3}$	$2.5 \cdot 10^{19}$	64 mm
$10^{-6}$	$2.5 \cdot 10^{16}$	64 m
$10^{-10}$ (UHV)	$2.5 \cdot 10^{12}$	640 km

particles is then called a *molecular flow*. A way to quantify this change in behaviour is the Knudsen number:

$$Kn = \frac{\lambda}{D} , \quad (6.2)$$

where  $D$  is the characteristic length of the enclosure. With  $Kn$  the different regimes can be distinguished as follows:

$Kn < 0.01$ : continuum, or viscous flow,

$Kn > 1$ : statistical, or molecular flow,

$0.01 < Kn < 1$ : transitional region.

For the process of evacuating a vacuum vessel and also for maintaining different vacuum pressures at different points of a vacuum apparatus, the transition between continuum and molecular flow imposes certain constraints. However, it also creates design options as will be described in the following.

When creating a vacuum in the laboratory, gas has to be removed from an enclosure (usually made out of metal or glass or a combination of both). The removal is performed by a pump which sucks (or better guides) the gas out of the enclosure. This process eventually reaches an equilibrium in which the amounts of gas that are removed by the pump and flowing into the enclosure are equal. This is an important point because there is no enclosure which is absolutely leak-tight. Every connection present between two parts of the enclosure (be it just the connection of the enclosure to the pump) has a certain leak rate and so does every material (some materials have a relatively high permeability for some components of the air). These leak rates depend on the particles trying to pass through. Air is a combination of different atoms and molecules and therefore, it has to be described by the separate amounts and partial pressures of those components. Additionally, materials are attached to every inner wall of an enclosure. They can be remnants from the manufacturing process of the enclosure like machine oils, or simply water molecules attached to the surface of the wall. These attached materials are in an equilibrium of adsorption and desorption. Finally, but very importantly, atoms can be trapped within the material of the enclosure. This trapping happens during the manufacturing process of some materials, a prominent example being stainless steel. During its manufacturing process, large amounts of hydrogen molecules become trapped within the metal, leading to a so-called *outgassing rate* of the metal surface. All these different processes have to be accounted for when designing an enclosure which shall be capable of maintaining a low pressure of a certain value.

The leak rate has the unit [mbar · l/s]. It indicates how much the pressure rises (in [mbar]) inside a vessel of a certain volume (in [l]) per time (in [s]). The leak rate of an enclosure  $q_{total}$  is the sum of all  $i$  single leak rates which may originate from the different vacuum connections, the inner walls of the enclosure, etc.:

$$q_{total} = \sum_i q_i . \quad (6.3)$$

Values for leak rates of vacuum components are usually given by the manufacturer. For example, for a CF viewport with a fused silica window the *standard helium leak rate* [114] is  $\sim 1 \cdot 10^{-10}$  mbar · l/s [115]. This means that for helium at atmospheric pressure at the outside of a vessel with volume of 1 l and a pressure difference of 1 bar to the inside of the vessel, the vacuum will get worse by  $1 \cdot 10^{-10}$  mbar per second. Since different gas particles have different permeabilities through materials (e.g. due to their size or polarity), this standard helium leak rate usually has to be multiplied by a factor, for air it is [114]:

$$q_{Air} \approx 0.34 \cdot q_{He} . \quad (6.4)$$

To calculate the leak rate due to permeation through a material (e.g. through a copper gasket), the following formula can be used:

$$q_{gas}^{permeation} = \bar{p} \cdot \frac{A}{L} \Delta p \left[ \frac{\text{Pa} \cdot \text{m}^3}{\text{s}} \right] , \quad (6.5)$$

where  $A$  is the cross-section area (i.e. the surface of the material),  $L$  is the permeation length (i.e. the thickness of the material),  $\Delta p = (p_1 - p_2)$  is the pressure difference and  $\bar{p}$  is the material-dependent permeation coefficient. For copper, it is for example  $10^{-11} \frac{\text{mbar} \cdot \text{l}}{\text{s} \cdot \text{m}^2 \cdot \text{bar}}$  [116]. For a CF40 copper gasket with an area of  $\sim 24.6 \text{ cm}^2$  and a permeation length of  $\sim 2 \text{ mm}$  this leads to a permeation leak rate of  $q_{gas}^{permeation} \approx 10^{-14} \text{ mbar} \cdot \text{l/s}$  for a pressure difference of 1 bar. This low leak rate is the reason why vacuum components are sealed using copper gaskets if the UHV regime shall be reached with a vacuum vessel.

Molecules which are adsorbed at the walls of a vacuum vessel can desorb over time and impair the vacuum due to the additional leak rate. Water molecules are often the main contributor to this process. To remove this water, heating the walls while pumping away the desorbing molecules is an appropriate approach and this procedure is often referred to as *vacuum baking*. The temperature dependence of the mean adsorption time  $\tau_a$  is exponential and thereby quite drastic [113]:

$$\tau_a = 10^{-13} \exp[q/kT] , \quad (6.6)$$

where  $q$  is the binding energy of the molecule to the surface. For water, this is approximately  $80 \text{ kJ mol}^{-1}$  for many surfaces [113]. At room temperature,  $\tau_a \approx 15 \text{ s}$  whereas at around  $300^\circ\text{C}$  this time decreases to  $\tau_a \approx 1 \mu\text{s}$ . This already illustrates the benefits of increasing the temperature until the particles are desorbed from the surface. Normally, a baking process for a duration of about ten hours at  $250^\circ\text{C}$  reduces the surface desorption leak rate by a factor of  $\sim 10^3$  [113].

The last contribution to the total leak rate which shall be mentioned here<sup>1</sup> is the outgassing of materials. This refers to the fact that particles which are trapped within the material of the wall (in contrast to those which stick to the surface of the wall which already have been discussed) diffuse to the wall surface and desorb into the vacuum. These can be the already mentioned hydrogen in stainless steel, but also water which can be trapped in porous

---

<sup>1</sup>The contributions due to so-called *virtual leaks* which are basically construction flaws of the vacuum vessel are left aside. These virtual leaks will be addressed in sec. 6.2.2 in more detail.

materials like e.g. graphite or the oxide layers often found on metal surfaces (prominent examples being copper and aluminium). A treatment of this leak rate is more complex than for the other two processes discussed so far. For an untreated and not vacuum-baked metal surface, the leak rate is constant for the case that the particles reaching the surface due to diffusion are desorbed immediately. Thus, the time constant of this process is solely given by the desorption. The outgassing rate due to hydrogen for untreated stainless steel is  $\sim 10^{-10} \text{ mbar} \cdot \text{l} \cdot \text{s}^{-1} \cdot \text{cm}^{-2}$  [117]. For a large metal vessel, this rate can already be limiting for the procedure of reaching UHV conditions. Therefore, in [118] the time has been investigated that is required to reduce the outgassing rate of hydrogen in a 2 mm slab of stainless steel to  $10^{-16} \text{ mbar} \cdot \text{l} \cdot \text{s}^{-1} \cdot \text{cm}^{-2}$  (which is then limited by the permeation of hydrogen through stainless steel). To achieve this reduction in the thin slab, eleven days are estimated for a heat treatment at  $300^\circ\text{C}$  and only one hour for baking at  $635^\circ\text{C}$  (while the steel slab is kept under vacuum to remove all outgassing hydrogen). This shows that also for the process of diffusion temperature is an important factor for time-efficient preparation of a vacuum vessel.

With all the possible leak rates added up, pumping a vacuum vessel will ultimately lead to an equilibrium pressure:

$$P_{eq} = \frac{q_{total}}{S_{eff}} , \quad (6.7)$$

where  $S_{eff}$  [l/s] is the effective pumping speed [119]. The time evolution of the pumping process shall not be discussed here. Normally, for ultracold atom experiments, the volumes which have to be pumped are small enough that the evacuation of the vessel will not take too long. This is different e.g. for large industrial vessels where cycling time of the vacuum is a cost factor. In that case, the required time to evacuate a vessel of known volume to a target vacuum pressure by pumps with known pumping speed can be estimated.

The pumping speed of a vacuum pump is usually specified by the manufacturer. It gives the value of volume of gas removed from a container per time unit. The important point is that this value is only valid if the gas can reach the pump without any obstruction. In a vacuum apparatus, this is often not the case as the pump is connected to the volume e.g. by a pipe of a certain length. In the vacuum regime of molecular flow, the gas no longer behaves like a fluid. In this case, the pipe will modify the pumping speed. The effective pumping speed is then calculated with:

$$\frac{1}{S_{eff}} = \frac{1}{S} + \frac{1}{L} , \quad (6.8)$$

where  $S$  is the nominal pumping speed of the pump as specified by the manufacturer and  $L$  is the so-called *total conductance* which is the combination of the conductances of the different components in the path of the gas [119]. It is calculated as:

$$\frac{1}{L} = \frac{1}{L_1} + \frac{1}{L_2} + \dots . \quad (6.9)$$

The conductance for an aperture can be calculated with:

$$L_{ap} = \frac{\bar{c}}{4} A , \quad (6.10)$$

where  $A$  is the area of the aperture and  $\bar{c}$  is the mean velocity of the gas at a certain temperature:

$$\bar{c} = \sqrt{\frac{8RT}{\pi M}} , \quad (6.11)$$

where  $R$  is the gas constant,  $T$  the temperature of the gas and  $M$  its the molar mass [120]. For air at a temperature of 25 °C, this leads to  $\bar{c} \approx 462$  m/s.

For a pipe of length  $l$  and diameter  $d$ , the conductance is given by:

$$L_{\text{pipe}} = \frac{\bar{c}\pi d^3}{12l} \quad \left[ \frac{\text{m}^3}{\text{s}} \right] . \quad (6.12)$$

The effects of molecular flow also allow for the process of *differential pumping* where two containers, connected by a pipe and each pumped by an appropriate vacuum pump, can inherit vastly different pressures.

### Differential pumping

When designing a vacuum apparatus for ultracold atom experiments, one has to deal with quite different pressures required at different places of the apparatus. While in the main chamber, where the experiments shall be performed, a pressure in the UHV is needed, the atom sources often heat up a solid sample of the material of choice until it evaporates, thereby providing hot, gaseous atoms which then are guided to the main chamber (see sec. 6.6 for more details on the construction of the atom sources). Where the evaporation takes place, the pressures are orders of magnitude higher than in the main chamber. Still, an unobstructed connection has to exist so that the atoms are able to travel from the source to the main chamber.

Differential pumping enables the combination of unobstructed connections and a large pressure gradient. Figure 6.3 shows an exemplary case. The pressure  $p_2$  in chamber  $B$  shall be much lower than  $p_1$  in  $A$ . In chamber  $A$ , there exists a gas load  $Q_L$  of which a large part is removed by the pumping speed  $S_1$  and a smaller load  $q$  will be present in chamber  $B$ . The pressure in  $B$  depends on  $q$  and  $S_2$ , see eq. 6.7. The load  $q$  depends on the pressure difference and the conductance  $L$  of the pipe which connects the two chambers by [113]

$$q = L(p_1 - p_2) . \quad (6.13)$$

Therefore, one can write with eq. 6.7:

$$S_2 = \frac{L(p_1 - p_2)}{p_2} . \quad (6.14)$$

The pressure  $p_2$  is often restrained by the demands of the experiment which shall be performed in chamber  $B$  whereas the load  $Q_L$  might be fixed by the atom source. Thus, by choosing appropriate vacuum pumps and by designing the connection between the two chambers to possess a certain conductance (which can be calculated with eq. 6.9 and 6.12 in the molecular flow regime), the required pressure gradient can be designed. Intersecting

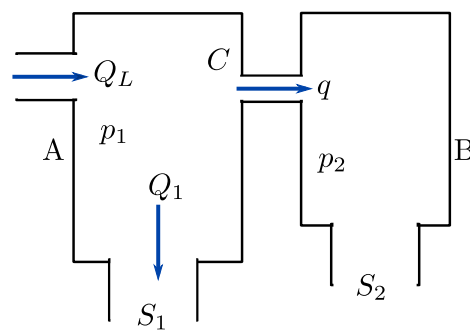


**Figure 6.3: Illustration of differential pumping.** Adapted from [113].

several differential pumping stages can enable large pressure gradients even for moderate individual pumping speeds and relatively large conductances.

### Measuring UHV conditions

Measuring a pressure in the UHV regime is not straight forward. Several issues have to be taken into account.

When using an ion gauge to measure the pressure, the gauge will ionize gas particles which scatter into it. By measuring the ionization current, a transformation into a pressure reading can be performed. This transformation is different for different particles due to their different ionization energy. Therefore, an inaccuracy can emerge at very low pressures when the composition of the gas inside the vacuum vessel becomes e.g. mostly dominated by hydrogen. Since ion pumps also measure the ionization current while pumping, they can be used as a vacuum gauge as well. This means on the other hand that an ionization gauge itself acts as a pump (usually with a pumping speed of a few litres per second).

Another point to keep in mind is that due to the statistical flow in the UHV regime, the pressure measured at one point of a vacuum vessel is not necessarily the same as at another point. One obvious example for this is a differentially pumped apparatus. Another situation can arise when the gauge measuring the pressure is closer to a vacuum pump than to the point of interest. In that case, the pump might reduce the amount of particles reaching the gauge which thereby will depict too low a pressure.

In the field of ultracold atom physics, the UHV is required to reduce collisions between the background gas particles and the atoms in the ensemble under investigation. The major gauge for the quality of the vacuum *at the point of the atomic sample* is given by the lifetime of the atoms inside a trapping potential. In fact, there are recent attempts to develop a new pressure standard in the UHV by using cold trapped atoms [121]. The lifetime of the atoms in the vacuum has been found to be connected to their loss-rate coefficient [122, 123]:

$$\tau = \frac{1}{P\gamma} \quad , \quad (6.15)$$

where  $\tau$  is the lifetime in seconds,  $P$  the pressure and  $\gamma$  the loss rate coefficient. For Na and K the coefficients are quite similar:  $\gamma_{\text{Na}} \approx \gamma_{\text{K}} \approx 4 \cdot 10^7 \text{ mbar}^{-1} \cdot \text{s}^{-1}$  [36]. For experiments with ultracold atoms and molecules, usually background-gas-limited lifetimes in the order of 30 s and longer are required.

#### 6.2.2 Main chamber

The main chamber of the setup is described in detail in [77]. In the main chamber, all experiments are performed. The vacuum in the main chamber is produced and sustained by an ion getter pump (75S-DI-4V-SC-N-N, *Gamma Vacuum*) and a titan sublimation pump (*ST22, former VG Scientia, now Vacgen*). As described in [77], the experiment suffered from the conditions of the vacuum inside the main chamber which resulted in insufficient lifetimes for the atoms in the magnetic trap of only 4 s (the details of the magnetic trap will be discussed in sec. 6.8.2).

The vacuum conditions in the main chamber showed a somehow peculiar behaviour. To prepare the UHV, all metal components were cleaned in an ultrasonic bath, first in distilled water with an solvent added (*Tickopur TR3, Dr. H. Stamm GmbH*) at  $\sim 60^\circ\text{C}$  followed by pure distilled water. Then, all surfaces were wiped clean with acetone. After sealing the chamber, a vacuum bake-out has been performed at a temperature of  $\sim 150^\circ\text{C}$  which is limited by the soldering connections of the metal-to-glass connections of the vacuum windows and the indium tin oxide (ITO) electrodes on the top and bottom viewport (see sec. 6.2.2 for details). This temperature was kept for up to seven days. The chamber was pumped in the first days

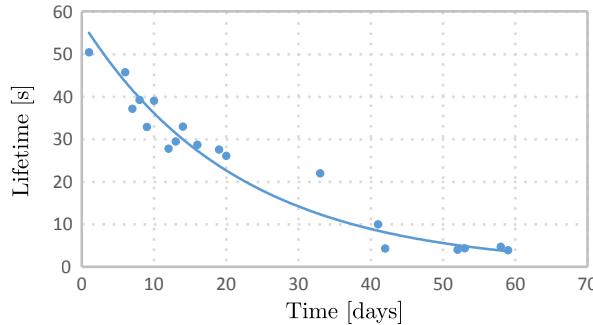


**Figure 6.4: Development of main-chamber vacuum before modification of the chamber.** The lifetime of magnetically trapped atoms is given, measured on consecutive days after the bakeout. A fit to the data yields a 1/e decay time of 57 days.

by a turbo molecular pump and in the last two to three days of the bake-out by the ion getter pump, with the ion pump being also at  $\sim 150\text{ }^{\circ}\text{C}$ . After the bake-out and the cool down, the system had decent vacuum conditions. The pressure reading was  $< 10^{-11}\text{ mbar}$  (effectively "under range" for the ion pump controller used (*Digital SPCE, Gamma Vacuum*), the current depicted was 3.2 nA) and the lifetime of  $^{23}\text{Na}$  atoms in the magnetic trap was on the order of 50 s.

As can be seen from fig. 6.4, this situation was not stable. The pressure increased over the course of several days and the lifetime reduced correspondingly up to a point where it settled at only 4 s. The long time period (60 days) in which this effect occurred was puzzling. Several investigations have been carried out, ruling out various possible contributors to the insufficient vacuum conditions. In the following, the informations gathered are summarized and the modifications of the vacuum chamber are presented.

### Investigated subjects

**Possible small leaks in the chamber:** Leak testing in the regime of ultra-high vacuum demands special care. A very large leak on the 1 mbar range can often be identified by simply listening to the air being sucked into the apparatus. In the intermediate regime from  $\sim 10^{-5}\text{ mbar}$  to  $\sim 10^{-8}\text{ mbar}$ , a possibility is to use acetone or isopropanol and apply it to the connections under investigation. If there is a leak, the acetone will be sucked into the vacuum chamber and eventually reach the vacuum gauge of the apparatus. Since the ionization potential for acetone deviates from that of nitrogen, to which cold cathode gauges are normally calibrated [124], the reading of the vacuum gauge will change rapidly. This indicates the existence of a leak at the tested connection. If the path from the connection to the gauge is relatively long, the response on the gauge to the burst of acetone on the connection can be time-delayed which can hinder the diagnosis. The same becomes true the smaller the leak is. Another method is to use commercially available leak testers. These devices are normally connected to the vacuum chamber and possess a turbo as well as a fore-pump. They also incorporate a mass spectrometer which normally only detects helium. Helium is sprayed from the outside onto the connections and will enter the chamber through possible leaks. These devices normally work very well. For the main chamber vacuum, however, it has been found that more diagnosis options for different gases are needed. That is why a residual gas analyser (*RGA 100, Stanford Research Systems*) has been used for the leak testing in the UHV regime. It has been found that the best way to leak test a connection and to find also leaks on the  $10^{-9}\text{ mbar}$  scale is to use a plastic back or rubber glove and to tape it over the flange with the connection under investigation. The glove is filled with helium at slight overpressure ( $\sim 1.5\text{ bar}$ ) and the helium fraction inside the vacuum chamber is monitored over time.

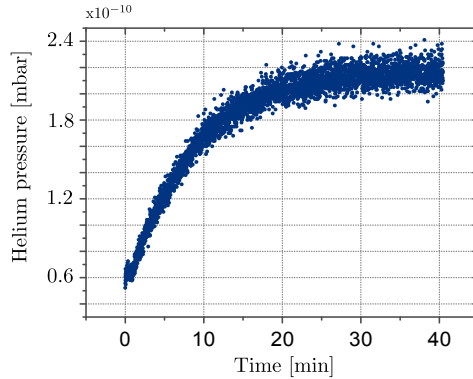


**Figure 6.5: Helium leak rate of modified main chamber after complete assembly.** The partial pressure of helium is measured by a residual gas analyser while the chamber is packaged in a plastic bag filled with helium gas at overpressure.

After all vacuum components had been connected, the overall leak rate of the chamber was measured. This was done by packaging the whole chamber into a plastic back and filling this plastic back with an overpressure of helium. Then the concentration of helium in the chamber was monitored until it reached a stable state. Figure 6.5 shows a measurement performed in that way on the modified main chamber. For an equilibrium helium pressure of  $p_{eq} \approx 2.2 \cdot 10^{-10}$  mbar which is reached after  $\sim 25$  min, the related leak rate can be calculated.

First, it has to be noted that the leak rate for helium is 2.7 times higher than for air [125]. Moreover, for the leak test leading to the measurement of fig. 6.5, the helium was above atmospheric pressure. This influences the leak rate as:

$$\frac{q_{atm}}{(p_{atm}^2 - p_{vac}^2)} = \frac{q_{overP}}{(p_{overP}^2 - p_{vac}^2)} , \quad (6.16)$$

where  $q_{atm}$  is the leak rate at atmospheric pressure,  $p_{atm} \approx 1000$  mbar,  $p_{vac} \ll 1$  mbar and  $p_{overP}$  and  $q_{overP}$  are the higher pressure of the leak test gas and the resulting leak rate, respectively. For a helium pressure of 2 bar, this leads to a four-fold higher leak rate.

For an ion pump with a pumping speed of 75 l/s, the effective pumping speed given by eq. 6.8 and eq. 6.12 when pumping through a  $\sim 100$  mm long pipe with a diameter of 36 mm (as it is the case in the modified main chamber, see also the next section) is  $S_{eff} \approx 32.21$  l/s. In total, the leak rate of the main chamber can be calculated by using eq. 6.7:

$$q_{mainCh} = p_{eq} \cdot S_{eff} / 2.7 / 4 \approx 6.5 \cdot 10^{-10} \text{ mbar/s} . \quad (6.17)$$

The leak rate is therefore well acceptable and should not limit the vacuum conditions in a way interfering with the purpose of the main chamber.

**Virtual leaks in the chamber:** Besides leaks from untight connections or damaged view ports, there is the possibility of so-called *virtual leaks* inside a vacuum apparatus [126]. These leaks can occur if a small gas volume is trapped e.g. inside a screw hole and is pumped inefficiently, by this constantly adding a leak rate to the total vacuum leak rate of the apparatus. This is the reason why every screw hole inside the vacuum apparatus should be deaerated e.g. by using special screws which feature a central bore through the whole screw. To find virtual leaks, a mass spectrometer can be used. The vacuum apparatus is first filled with a noble gas at atmospheric pressure, e.g. argon. Afterwards, the vessel is evacuated and the argon concentration is monitored. If there is a virtual leak, one will recognize this as a stable and enhanced argon concentration inside the apparatus (see e.g. [126]). During the search for the reasons for the peculiar vacuum problems of the main chamber, also a virtual leak measurement has been performed as described above. No virtual leak has been found.

**The ITO vacuum suitability:** As described in sec. 6.2.2, the vertical windows of the main chamber feature an electrode structure which is realised by a pattern of thin ITO. To the best of the author's knowledge, there exist no detailed studies on the suitability of ITO for ultra-high vacuum. One possibility would be that gas particles are trapped in the porous structure of the ITO layer. This would add a leak rate and could thereby negatively effect the absolute vacuum pressure. To rule this out, one set of the main windows has been covered with an additional anti-reflection coating. Although this coating does not improve any optical properties, it should seal the surface of the windows. Even with these new windows installed, the peculiar behaviour of the vacuum still remained.

### Main chamber modifications and vacuum testing

One important information gathered during all the performed tests is that most of the processes which can impair the vacuum of an apparatus are more or less instantly present. A virtual leak for example could maybe open up due to some mechanical relaxation after a bake-out (although already this case seems highly unlikely), but would from there on be present with its full leak rate. Thus, contributions from small or virtual leaks, a higher outgassing rate of ITO because of trapped atoms, etc. should all appear - even if delayed - as an instant effect, showing up as a jump in the vacuum pressure and/or bump in the lifetime of the trapped atoms.

The effect witnessed in the main chamber was instead very slow on the time scale of days to weeks. Only one physical process seems to share these time scales and this is diffusion. The diffusion coefficient of hydrogen inside steel is on the order of  $10^{-13} \text{ m}^2/\text{s}$  at room temperature [127]. That means that a hydrogen atom travels a few millimetres through steel during 60 days.

When the main chamber had first been designed, all known leak rates, coming from the different sealings and windows, had been added up by using eq. 6.3. Taking the leak rates for the windows of  $\sim 1 \cdot 10^{-11} \text{ mbar} \cdot \text{l/s}$  as specified by the manufacturer and an approximation for the leak rate of a copper sealing (see sec. 6.2.1), this leads to a total leak rate of  $\sim 1.5 \cdot 10^{-10} \text{ mbar} \cdot \text{l/s}$  for the 15 viewports of the main chamber. The pumping speed of the installed ion pump is 751/s and the pumping speed of the titan sublimation pump is given by the manufacturer as 31/s/cm<sup>2</sup> (for hydrogen). For a titanium-covered area inside the tower of the main chamber of 540 cm<sup>2</sup>, this gives a pumping speed of  $\sim 1600 \text{ l/s}$ . The pumping was originally performed through a 100 mm long pipe with an opening with a diameter of 20 mm. Using the formula for the conductance, eq. 6.12, this leads with eq. 6.8 to an effective pumping speed at the main chamber of  $\sim 10 \text{ l/s}$ . This pumping speed together with the calculated leak rate yields with eq. 6.7 an equilibrium pressure of  $1.5 \cdot 10^{-11} \text{ mbar}$ . Thereby, the vacuum would be in the acceptable range for the purposes of the main chamber.

The only process not taken into account was a possible out-gassing of hydrogen from the steel parts of the chamber. In publications dealing with vacuum conditions, it is often mentioned that one important component limiting the performance in the UHV regime is hydrogen. What often remains unexplained in detail is where this hydrogen originates from. A presumption at the beginning of this thesis had been that the stated hydrogen is on the steel surface and therefore has to be removed using a standard bake-out procedure. That is in part true. But what is even more important is that hydrogen is stored inside the steel as a by-product of the manufacturing process of stainless steel. The out-gassing rate of an untreated steel wall of a vacuum vessel is calculated to be  $\sim 10^{-10} \text{ mbar} \cdot \text{l} \cdot \text{s}^{-1} \cdot \text{cm}^{-2}$  [117]. If this rate is used and the total out-gassing rate is calculated for the vacuum-side-facing steel surface of the main chamber (which is  $\sim 1450 \text{ cm}^2$ ), this leads to  $\sim 1.5 \cdot 10^{-7} \text{ mbar} \cdot \text{l} \cdot \text{s}^{-1}$ . By comparison with the pumping speed originally present at the main chamber, an equilibrium pressure of  $\sim 1.5 \cdot 10^{-8} \text{ mbar}$  is obtained. This means that the untreated steel surface worsens the vacuum conditions by three orders of magnitude.

The lifetime of a sodium sample trapped inside a magnetic potential was at the steady state of the unmodified main chamber 4 s. When calculating the background pressure from this measurement, eq. 6.15 yields  $P = 0.6 \cdot 10^{-8}$  mbar, which supports the hypothesis of the untreated steel being the major contributor to the bad vacuum conditions. As a side note, it shall be mentioned here that the pressure depicted at the ion pump controller was  $\sim 1 \cdot 10^{-10}$  mbar, i.e. two orders of magnitude lower than the calculated one. This shows that the ion pump is not suitable for an accurate pressure determination at the point of the atomic sample. Since the ion pump is mounted such that the titan sublimation covers the walls of the vacuum apparatus between the main chamber and the point where the ion pump is mounted, the fact that it gives a lower pressure than is calculated from the lifetime measurement in the main chamber becomes comprehensible.

The question still remained why this was not the pressure immediately after the bake-out. As a treatment for steel components for ultra-high vacuum, most companies offer the option of *vacuum glowing*. It had not been clear in the beginning of the setup of the experiment apparatus why this should be a beneficial option and also requests to companies did not shed light onto the topic.

What happens when steel is heated up to high temperatures is that the hydrogen is removed from the steel if this heating is performed under vacuum conditions (hence, "vacuum glowing"). When heated up for one hour to around 1000 °C, the hydrogen outgassing rate of stainless steel drops down to  $\sim 10^{-16}$  mbar · 1 · s<sup>-1</sup> · cm<sup>-2</sup> [118]. In the main chamber, most likely, a thin surface layer of the stainless steel facing towards the inside of the chamber was depleted from hydrogen over the course of a baking cycle at  $\sim 150$  °C, leading at first to a lower hydrogen outgassing rate. But since the majority of the steel had been untreated, the hydrogen diffusion due to the concentration gradient inside the steel led to an ever increasing hydrogen out-gassing rate over the course of days, until the rate of untreated steel was eventually reached again. This is the current explanation for the slow degeneration of the vacuum which had been always present after a baking cycle, since the chamber had not been vacuum-glowed in the first place.

As a consequence, the approach to modify the main chamber has been two-fold. First, the relative pumping speed should be increased and secondly, the hydrogen out-gassing rate of as much steel surface as possible should be reduced. For increasing the pumping speed, the opening in the chamber was increased by a factor of 1.8 in radius by milling. Due to this, a new flange had to be attached to the chamber. This was done by welding a custom-made flange to the chamber. The welding was performed by an external company (*SKODOCK Germany*) which specialises in welding of UHV parts. Figure 6.6 shows a schematic of the modified main-chamber setup.

The modifications unfortunately limit the maximum temperature which can be applied to the main chamber to around 350 °C because of the new welded connection. This made a vacuum glowing at 1000 °C impossible. The time needed for vacuum glowing scales exponentially with the temperature applied (see [118]). A maximum temperature of 350 °C would therefore have meant a vacuum glowing procedure of  $\sim 40$  days duration (for a simple linear model using the value for the time to degas a 2 mm steel slab at 350 °C from [118] and a chamber wall thickness of 27 mm). This time span is quite impractical.

Fortunately, another procedure exists to reduce the out-gassing rate of stainless steel for which similar results as for vacuum glowing have been reported [128]. It is called *air bake-out*. The idea behind it is that due to heating of the steel in air (for an even faster effect, the bake-out can also be done in an oxygen atmosphere), an oxide layer will form on the surface of the steel. This layer has a much smaller diffusion constant for hydrogen than untreated steel. A reduction of the out-gassing rate by three orders of magnitude is reported in [128]. The steel parts of the main chamber were therefore first baked out at  $\sim 350$  °C for one week while being pumped by a turbo pump. After this, the chamber was vented with normal

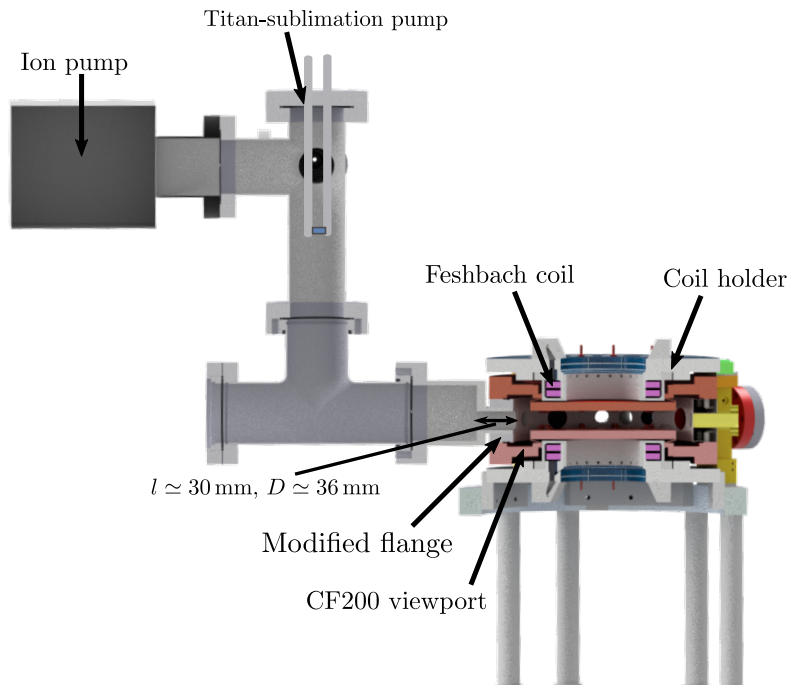


**Figure 6.6: Schematic of main-chamber vacuum setup.** A vertical cut through the assembly is shown. The main chamber is manufactured from stainless steel. CF16 and CF40 viewports are attached to the horizontal flanges. The viewports at top and bottom are custom designed CF200 flanges. Also visible are the coils which generate the magnetic fields, labelled as Feshbach coils. On the side of the main chamber, the modified flange is welded to the chamber which enables for a larger pumping speed. The connection has a length of  $l \approx 30$  mm and an opening with a diameter of  $D \approx 36$  mm. An ion pump and a titan-sublimation pump are attached at the side of the main chamber.

atmospheric air and baked for two more days at the same temperature. The air bake-out could only be performed with the body of the main chamber since for the viewports the specified maximum temperature is 150 °C. Additionally, it is unknown how the metal-to-glass sealings would stand the air-bake procedure. Since the CF200 viewports contribute significantly to the steel surface, only 84 % of the inner surface of the main chamber could be treated by the air bake-out. Recalculating the new expected total leak rate of the main chamber for the remaining 230 cm<sup>2</sup> of untreated steel surface yields  $Q \approx 2.3 \cdot 10^{-8}$  mbar · s<sup>-1</sup>.

After the air bake, the viewports have been attached and the atom sources have been reconnected. The main chamber has been evacuated and every connection has been leak tested by the "glove method" (see sec. 6.2.2). Moreover, the total external leak rate has been measured. The measurement is shown in fig. 6.5, yielding a total external leak rate of  $q_{mainCh} \approx 6.5 \cdot 10^{-10}$  mbar/s as expected from adding all theoretical leak rates of the connections and the viewports.

After the leak testing, the titan sublimation pump was activated for two minutes. Due to the larger opening in the modified chamber, the effective pumping speed is now  $S_{eff} \approx 188 \cdot 1 \cdot s^{-1}$  (with a pipe length of now 30 mm). The effective pumping speed increased therefore by a factor of 19. This results in a theoretical equilibrium pressure of  $P \approx 1.2 \cdot 10^{-10}$  mbar.

The final reading of the ion pump controller is 3 nA and a 1/e-lifetime of <sup>23</sup>Na of  $(54.3 \pm 5.1)$  s has been measured (see fig. 6.7). A calculation with eq. 6.15 for that lifetime yields a pressure of  $P \approx 4.6 \cdot 10^{-10}$  mbar which is in the same order of magnitude as the pressure estimated by adding the determined leak rates.

The values indicate a sufficient vacuum condition. This condition is now stable for over

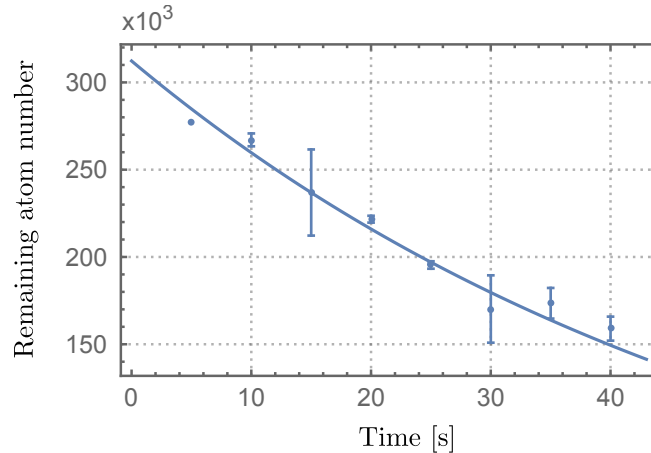


**Figure 6.7: Measurement of the atom loss induced by background-gas collisions.** The measurement is performed with trapped sodium atoms. The lifetime is derived from an exponential-decay fit to be  $(54.3 \pm 5.1)$  s.

three years which is why there is a high chance that the vacuum issues are solved. The pressure reading on the ion pump is in the "under range" region and it is used as an indicator when to activate the titan sublimation pump again. This is normally done when the current shown on the ion pump controller rises above 4 nA. It shall be mentioned here, too that the main windows currently assembled with the main chamber do not possess an additional AR coating to seal the ITO. Thus, the ITO structures are regarded to be suitable for UHV conditions.

### Vacuum windows

Vacuum windows, or viewports, are present in the new version of the chamber in the size of CF40 and CF16. They have been purchased from *MPF Products Inc.* and are coated with a broad-band anti-reflection coating (550 to 1100 nm). On the vertical axis of the main chamber, CF200 custom-made windows are mounted which have been designed by M. W. Gempel and are described in detail in [77] and [3]. They feature ITO-coated electrodes which due to their transparency for the wavelengths used in this experiment (by a margin of > 92 %) enable full optical access while also enabling for electric field values of up to  $10 \text{ kV cm}^{-1}$ . These electric fields will be used in future experiments to induce the electric dipoles of the molecules as explained in sec. 9.3.1. The windows are recessed into the main chamber with a spacing of 22 mm between them. Together with the large optical access provided by them this enables for high-resolution imaging of the atoms and molecules [77].

### 6.2.3 2D MOT and Zeeman slower

In the following, the vacuum components of the two atom sources are described. The description does not cover the laser systems used for the atom sources, which instead can be found in sec. 6.4.

#### Zeeman slower

In the experiment apparatus, the Zeeman slower provides a flux of sodium atoms. The theory behind the functioning of a Zeeman slower is discussed in sec. 6.6.1. The design of the Zeeman slower setup is described in detail in [129] and [77]. In the recent experiment setup, changes have been implemented to the original design. A sketch of the actual setup

can be found in fig. 6.8. It contains of three segments: The oven section where the reflux oven is attached to, the shutter region with the atom beam shutter and the Zeeman-coil section.

The oven is designed as a reflux oven [130, 131]. This means that it has a two-chamber design in which the first is the oven itself, which is heated to  $\sim 310^\circ\text{C}$  in the experiment setup described in this work. The gaseous Na atoms leave the oven through a 3 mm hole in a divergent beam. The oven part is followed by a second chamber which has a conical aperture of 2 mm in diameter located 25 mm away from the aperture of the oven and aligned to it on a common central axis. Thereby, the second aperture acts as a collimator by cutting the cone of atoms leaving the oven, letting only those atoms pass which have a sufficient orientation towards the main chamber. The other atoms hit the walls of the reflux chamber. The reflux chamber is heated up to  $\sim 245^\circ\text{C}$  and is connected via a reflux pipe with the bottom of the oven. Thereby, in theory, the Na collected in the reflux region should flow back to the oven.

As a modification to the original oven design, an additional pipe segment on top of the oven has been added. It has been found that over the course of several oven refills the broken glass pieces of the ampules which contain the sodium (see sec. 6.2.3 for details on the process of oven refilling) can clog the reflux pipe of the oven. This led to an insufficient performance of the oven. Together with the additional pipe segment, a double flange was added between the segment and the oven which has holes in it, too small for the ampules to fall through but large enough that the liquid sodium can run down into the bottom of the oven once it is heated up.

As a visual measure of the flux of the oven, three pictures of the fluorescent cone of atoms taken in the shutter region are shown in fig. 6.9. All pictures were recorded with the same camera settings and show the atom flux for a freshly refilled oven, the flux when the MOT loading is half the maximum efficiency and the fluorescence visible if the oven is completely empty. In the latter case, the few remaining atoms originate from sodium which accumulated over time in the oven section of the Zeeman slower. Using this visual guide, the performance of the sodium atom source can be evaluated with respect to the status of

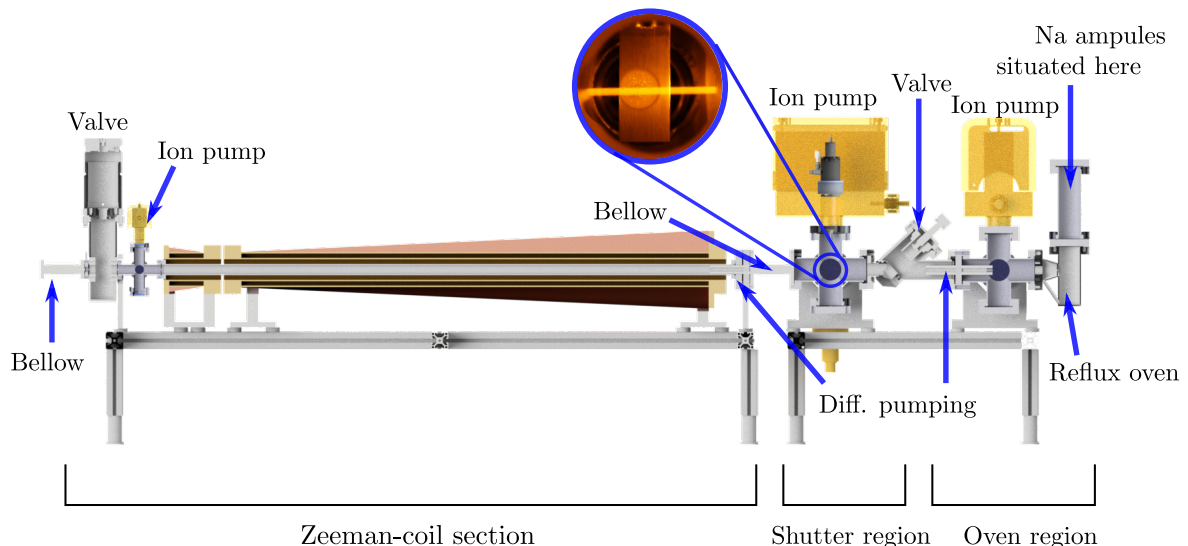


**Figure 6.8: Schematic of Zeeman slower.** The setup is divided into three sections, the oven region, the shutter region and the Zeeman-coil section. Valves allow the separation of the vacuum in the different parts. Flexible bellows counteract mechanical stress in the apparatus. The inset shows a picture taken of the fluorescent atom beam inside the shutter region, see also fig. 6.9.

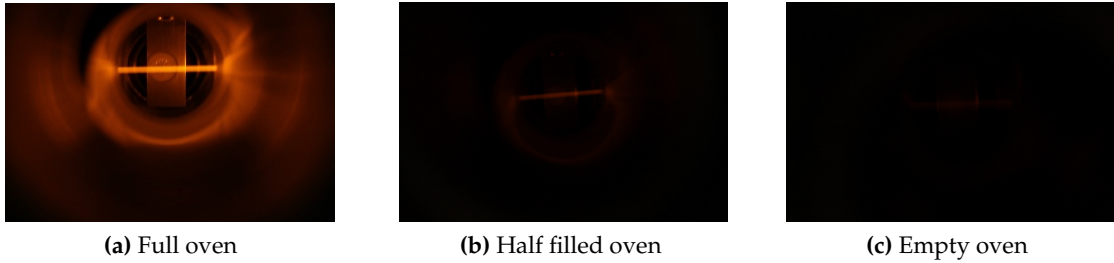


**Figure 6.9: Pictures taken of the fluorescence of the sodium atom beam in the shutter region of the Zeeman slower.** (a) Fluorescence with a freshly refilled oven, (b) significantly reduced flux with half filled oven, (c) fluorescence with an empty oven. All pictures were recorded with the same camera settings.

the oven infill.

The oven is attached to the first pumping section where an ion getter pump (*RVIP-55-ST-M, Varian, rebuilt*) keeps the vacuum at  $\sim 5 \cdot 10^{-8}$  mbar during operation. The oven is connected and sealed with nickel gaskets (*Gasket Nickel Annealed, Kurt J. Lesker Company*) since the reactive vapour of sodium can destroy copper sealings over time. All screws used to connect the oven vacuum parts have been greased with heat resistant grease (*Molykote*, a paste consisting copper particles, rated to 650 °C), because otherwise cold shut can happen in which case it is no longer possible to unscrew the connections.

The oven section is connected via a differential pumping tube and a straight valve (316001-*InlineValve MIV-150-V All Metal, MDC Vacuum Products LCC*) to a second pumping region. The valve enables to preserve the vacuum conditions in the major part of the apparatus when the sodium oven has to be refilled. The differential pumping stage consists of a 105 mm long metal tube into which tubes made from graphite are put, which have a central hole with 2 mm diameter. The graphite is intended to add an additional pumping effect [132]. The graphite is fixed inside the metal tubes by nuts. This has been done because during a vacuum failure in the oven region, the graphite tubes were shot towards the main chamber since they had not yet been fixed inside the metal tubes. The second region is pumped by an ion getter pump (45-CV-2V-SC-N-N, *Gamma Vacuum*) maintaining  $\sim 1.2 \cdot 10^{-10}$  mbar which is monitored by a vacuum gauge. In this section, a mechanical shutter can be toggled into the sodium atom beam via a pneumatic rotator (*Rotary Source Shutter MD20RAIX000Z, UHV Design*). It is TTL controlled by the experiment control unit via a custom designed electronic board. This electronics also close the shutter in case of a black out, thereby reducing the amount of atoms passing towards the main chamber. Shutting the atom flux has been found to be crucial for later steps in the experiment, as the lifetime in the magnetic trap (see sec. 6.8.2) is significantly worse when the atom flux is not shut off.

After passing the shutter region, the atoms enter a second metal pipe for differential pumping, identical to the first one. The two differential pumping stages enable for a pressure gradient of six orders of magnitude between oven region and main chamber. The shutter section is attached via a flexible bellow to a 100 cm long CF16-pipe made from stainless steel. The bellow reduces mechanical stress on the CF sealings by allowing small displacements of the shutter section with respect to the tube. The tube is situated inside the coil support structure of the Zeeman slower coils. A constantan wire is wound around the metal tube and is temperature-isolated with mineral wool and aluminium foil against the coil housing. Four negative temperature coefficient thermistors (NTC thermistors) are placed along the tube to monitor its temperature. This construction is used when the tube has to be baked in case of a vacuum failure or rebuild. A temperature of 120 °C can be reached at the tube and should not be exceeded because of the solder used during the assembly of the coil holder.

A final CF16 cross forms a last pumping section before the Zeeman slower is connected via a straight valve (*All-metal gate valve, Series 481, 48124-CE01-0001, VAT Group AG*) and another flexible bellow with the main chamber. The last pumping section is evacuated by a small ion getter pump (*3S-CV-1V-5K-N-N, Gamma Vacuum*). Its controller displays a pressure of  $< 1.0 \cdot 10^{-11}$  mbar. An angled valve is placed at the cross for the possibility to connect a turbo pump to the front section of the Zeeman slower. This was especially helpful during the first back-out of the complete Zeeman slower, when the valve to the main chamber was closed and the slower pipe had to be evacuated.

The two bellows in the slower vacuum apparatus design require a geometrical alignment to direct the beam of sodium atoms emerging from the oven to the centre of the main chamber where the atoms will be trapped by magnetic and optical potentials. A first mechanical alignment has been performed upon assembly of the whole vacuum apparatus. Rulers and air levels have been used to align the slower tube centred to the main chamber. The oven section has also been coarsely adjusted in height first. By aligning a laser beam centrally along the tube, the back section of the slower has carefully been adjusted with the goal that the laser beam reaches the oven section. Mechanical fine tuning has been performed by monitoring the flux of the Zeeman slower in terms of MOT-loading speed while slightly adjusting the back of the slower in height and angle.

### Two-dimensional magneto-optical trap

The design of the 2D MOT is described in [77]. Therefore, it is only briefly recapitulated in the following. A sketch of the 2D MOT is shown in fig. 6.10. The advantage of a 2D MOT

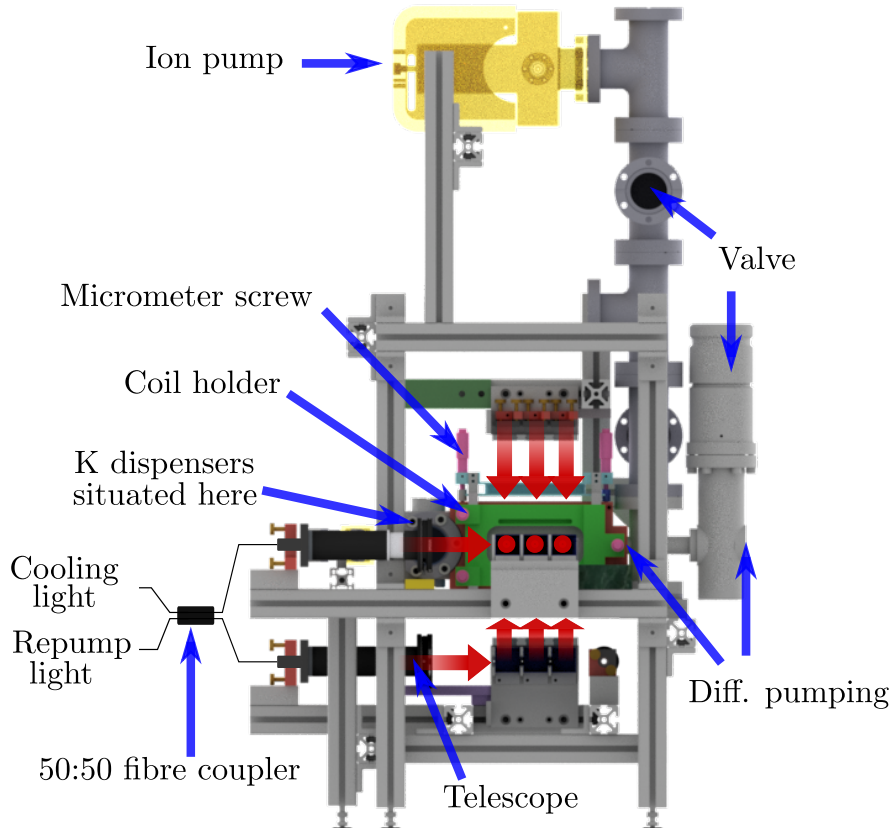


**Figure 6.10: Schematic of 2D MOT.** The vacuum components as well as the laser light paths (see also sec. 6.6.2) are indicated.

design in comparison to a Zeeman slower is mainly the smaller build volume and the absence of an oven at high temperatures. The vacuum system consists of a custom-made chamber made from 316LN stainless steel and standard stainless-steel vacuum parts. The windows on the 2D MOT chamber are sealed with indium due to their elongated shape for which no copper sealings are available. Indium has the downside of restricting the possible bake-out temperature to 120 °C [133] due to its low melting point of 156.6 °C. Two pipes are mounted for differential pumping, one between the 2D MOT chamber and the intermediate pumping section and the other between that section and the main chamber. The intermediate section is pumped by an ion getter pump (45S, *Gamma Vacuum*). The vacuum is in the order of  $2.5 \cdot 10^{-10}$  mbar during operation. A valve (*All-metal gate valve, Series 481, 48124-CE01-0001, VAT Group AG*) makes a separation of 2D MOT and main-chamber vacuum possible which aids when exchanging the atom sources. The atoms are produced by dispensers (*Alvasource-2-K40(5.5%)-5-S, Alvatec, now Alfa Vakuo e.U.*) which contain the potassium in chloride form. Since the system is designed for the possibility to work with both the fermionic as well as the bosonic potassium isotopes, the same enriched dispensers as in [77] are used for the experiments with the bosonic  $^{39}\text{K}$  performed within the course of this thesis.

It has been found that the dispensers have an approximate life time of 1100 working hours. To avoid opening the vacuum system every time a dispenser is depleted, three dispensers are mounted inside the 2D MOT and can be activated consecutively. At the end of this work, all three dispensers had been depleted and they have been exchanged by not enriched dispensers (*K/NF/2.2/12 FT10+10, Saes Getters S.p.A.*).

The 2D MOT is connected to the main chamber by a flexible bellow. This reduces possible mechanical tension in the vacuum apparatus which could otherwise lead to problems when trying to seal the different parts against each other via copper sealings.

### Important details on ultra-high vacuum

During the preparation of stable and decent vacuum conditions, information has been gathered. In the following a list is presented in the spirit of sharing the made experiences.

**Ion pumps:** Ion pumps are a suitable tool to reach the ultra-low vacuum regime. They are often complemented by a titan sublimation pump. The pressure reading displayed by an ion pump controller is calculated from the ionization current which is present in the ion pump. The higher the pressure, the more particles are inside the volume of the ion pump which can be ionized, thus, a higher ionization current is present. Thereby, a quite accurate measurement of the vacuum in the vicinity of the ion pump is possible. This information gets lost when the ion pump experiences leak currents. These can for example occur if small needles of material grow on the electrodes of the ion pump, leading to an increase of the ionization current. Normally, this problem can be solved by *high potting* the ion pump. For this procedure, a voltage on the order of twice the operation voltage is applied to the ion pump, potentially burning away the needles.

At the ion pump of the main chamber, such a leak current was experienced but its origin was unclear. Possible contributors were identified with the available knowledge. The titan sublimation pump could dispose titan inside the ion pump, leading to the formation of metal needles. There exists also the possibility of noble gas pollution (see e.g. [134]) which can lead to an unstable behaviour of the current flowing inside the ion pump as noble gas atoms are cyclically emitted and recaptured by the electrodes of the pump. In the early stages of the experiment, the vacuum apparatus was flooded with argon several times during venting of the apparatus. Although not all of the investigated behaviours of the system were exactly pointing towards a noble gas poisoning of the ion pump, at that time it was decided to exchange the ion pump with another model which can also pump noble gases (the aforementioned 75S-DI-4V-SC-N-N, *Gamma Vacuum*). Directly after the exchange, the new ion pump behaved normally. But after it was used in new baking cycles during

which it was heated up together with the apparatus while still pumping, it showed the exact same behaviour of an increasing leak current. What was learnt by explicitly asking the manufacturer of the ion pump if it is allowed to run the pump while it is heated up (as it is stated in the manual, see [135] pages 8 and 9), the manufacturer reassured that this operation mode is not damaging the pump. But it was also mentioned in addition that it is a totally normal behaviour of the ion pump to develop leak currents during this operation mode. In fact, during the manufacturing process, the pumps are operated that way for testing and are high potted before they are delivered to customers. With this knowledge, the controller of the main ion pump has been upgraded to the model *Digitel SPCe, Gamma Vacuum* which features a built-in high-potting option. Since using this feature after every bake-out, the ion pump functions normally.

**A general remark on bake-outs:** It has been found that during the subsequent procedure of heating up and cooling down the vacuum apparatus, some connections became loose, most likely because of different expansions of the metal chamber, the copper gaskets and the screws used to tighten the connections. Due to this issue, vacuum leaks can occur on an otherwise already leak-tight chamber. It proved beneficial to check each screw after a bake-out using a torque wrench set to the recommended torque for the specific connection.

**Hidden leaks:** One leak on the main chamber was especially hard to identify. As it turned out in the end, the sealing of the high-voltage feed through of a new vacuum gauge was faulty. Since this sealing was covered by the plug to connect the gauge with the controller, a helium leak test on the plug showed only a very minor helium signal on the leak tester used at that time. Only after removal of the plug which made the feed through directly accessible by the helium probe enabled a distinct leak detection. This leak was hard to find for two reasons. First, the plug acted as an additional sealing on the feed through for the helium measurement, but since the volume between plug and feed through was still on ambient pressure, the air leak was much larger. Second, the gauge was straight from the factory and therefore it was not to be suspected to be faulty.

**Zeeman slower refilling:** When refilling the oven, the straight valve between the oven section and the shutter section (*CF40 All metal inline valve MIV-150-V, MDC Vacuum Products LLC*) is closed. A turbo pump is attached to the angled CF40 valve (*Series 541 Easy close all-metal angle valve, VAT Group AG*) which is then opened. The ion pump of the oven section is switched off and the whole section is vented with nitrogen through the turbo pump. A slight overpressure is maintained (~ 1.2 bar) and the oven is opened. In the experiment it has been found that the oven has to be refilled every three to six months with 10 g of sodium. The sodium is delivered in glass ampules with 5 g of sodium per ampule. The ampules are filled by the manufacturer under protective gas atmosphere and have to be broken open when putting them into the oven. When the oven has been closed, the oven section is usually pumped down by a turbo pump before switching back to the ion getter pump of the oven section. It has been found that although the oven section was already well below  $10^{-7}$  mbar before switching to the ion pump, when heating up the oven section to roughly 100 °C, the ion pump switched off after some time. First it was assumed that with new ampules, already too much sodium is in the gas phase at 100 °C. On a closer look this can be ruled out since the oven section can be operated without problems at over 300 °C while only being pumped by the ion pump. Within the solid sodium inside the ampule often a small gas bubble is visible which is gas trapped during the process of filling the ampules. The final conclusion is that when the ampules are broken open this gas volume is not released since it is sealed inside the solid sodium. But when the oven is heated to around 100 °C, the sodium becomes liquid and at some point releases the gas bubble in a burst of high-pressure gas which causes the ion pump to switch off for protection. With this knowledge, the turbo pump is kept running until the oven is at 150 °C for a day. Then, one can switch to the ion pump configuration without any further problem.

**Clogging of the Zeeman slower oven:** It has been found that not only the part of the reflux oven where the sodium is evaporated has to be heated, but also the nozzle at the reflux section. The temperature is at 245 °C during operation of the Zeeman slower, in order to prevent sodium vapour to condense at the nozzle and clog it. Usually, this works well, but during one operation cycle a leak was present at the oven in the 10<sup>-7</sup> mbar regime which was not immediately spotted. The oven section was operated for one day with the leak present. At the following day the nozzle of the oven clogged and it was not possible to remove the clogging by heating. The reason was that the air leak provided enough water to enable the reaction of sodium to sodium hydroxide, which then condensed on the surface of the oven section as well as on the nozzle. Since the melting point of sodium hydroxide is at 318 °C and this high temperature can hardly be reached at the reflux section, this led to the clogging of the oven.

### 6.3 Experiment control

The experiment is controlled by a personal computer (PC) which runs the experiment control software. This software is programmed in *LabVIEW* and is based on the one described in [136]. The commands are sent to and then executed by the *ADwin Pro II* system (*Jaeger Messtechnik GmbH*), a modular control unit which is equipped with digital (TTL, ~ 3.5 V) and analogue (-10 to +10 V) output channels.

In the *LabVIEW* program, a matrix-like grid relates each digital and each analogue channel as well as devices connected to the PC via COM ports to a row and each entry in this rows represents a time step of the experiment sequence. Each column therefore contains one time slot of the experiment sequence which can have a duration between 10 µs and maximal 50 s (these restrictions originate for the lower limit from the timing of the *ADwin* system, see below, and for the upper limit from the experiment software). For each time slot, every digital channel can either be on or off and for each analogue channel a value can be set. Additionally, the analogue channels can be linearly ramped over the time slot from the value set in that time slot to the value of the following slot. Figure 6.11 shows a screen shot of an exemplary experiment sequence.

A dedicated routine allows for the definition of a transfer function, making it possible to map the voltage output of the analogue channels of the *ADwin* system onto a parameter of choice (which could be e.g. a frequency in MHz for a voltage-controlled oscillator (VCO)). These transfer functions have to be calibrated by hand once. In addition, VISA commands can be set in the software and are sent to the devices connected to the COM ports of the PC during the time slot in which they are implemented.

The *LabVIEW* software allows for single experiment runs, continuous cycles of the same experiment sequence or for a scan of up to two analogue channels or time-slot lengths within boundaries and with step sizes defined by the user. For every experiment run, the *LabVIEW* software generates a matrix containing all information set for that sequence. This matrix is translated into the programming language of the *ADwin* and then sent via Ethernet to the *ADwin* control unit. The *ADwin* control unit then processes the sequence by controlling the digital and analogue channel boards attached to it while constantly giving feedback of the current time step it is executing to the PC which runs the *LabVIEW* software. Every time slot in the *LabVIEW* program is broken down into intervals of 10 µs length which is the timing of the clock attached to the *ADwin* control unit. The clock frequency is a 100 kHz-reference TTL signal which is generated by a function generator (33521A, *Agilent*) and fed to the *ADwin*.

The feedback of the current time step to the PC enables the PC to send the VISA commands at the appropriate time to the devices connected to it. These devices are frequency generators in the case of the experiment setup described in this work. The digital channels trigger shutters, acousto-optic modulators (AOMs), the different cameras and switches for

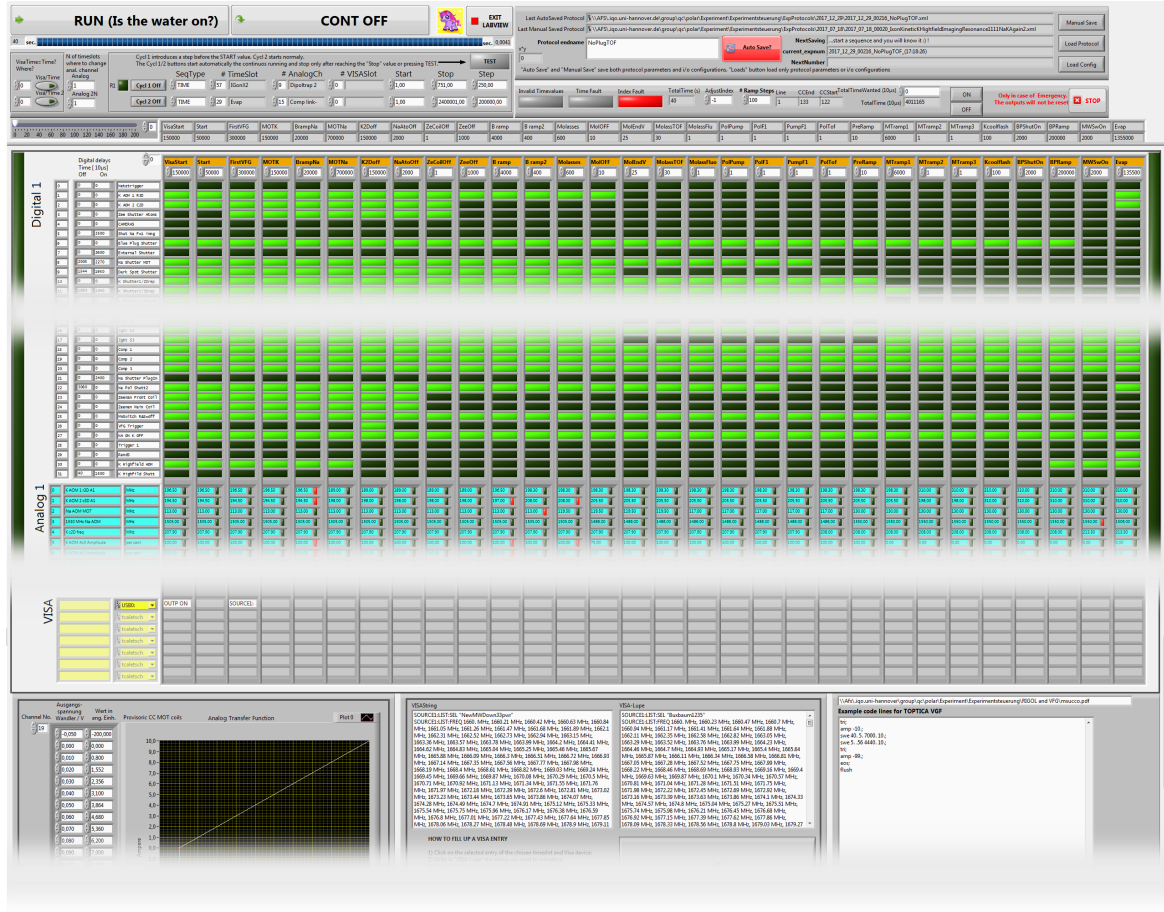


**Figure 6.11: Picture of the experiment control interface.** The experiment control program is written in *LabVIEW* and has a matrix-like structure. Each column marks a time slot of variable length. Each row is assigned either to a digital channel which can be on (light green) or off (dark green) during each time slot, an analogue channel which can be set to a specific value, or an external device which is controlled using VISA commands. The bottom panel enables the definition of calibrations for the analogue channels (left) and VISA commands (right). In the upper segment of the panel, the controls for starting, stopping, cycling and saving the sequence are situated.

the current flowing through the magnetic-field-generating coils. The analogue channels control AOM frequencies and amplitudes and the value of the current flowing through the magnetic-field coils.

The timing of every device has to be thought of carefully. Delays can be imposed on the actual reaction of the process triggered. For example, the reaction time of a mechanical shutter is given by the time the electric signal needs to reach the device plus the time the mechanics need to open or close the shutter. The shutters used in the experiment are characterised in detail in [137]. The experiment software therefore allows for taking these delay times into account, but they have to be determined for every time-critical device in the experiment.

For every experiment run which shall be recorded, the experiment software generates a file on the intranet which is saved in a folder of the corresponding date of the day. This file is also used by the picture handling software to assign recorded pictures to that specific experiment run.

For a first evaluation of the data gathered during e.g. a scan of a certain parameter, a data handling software programmed by D. Edler (described in [138]) is used. Since the complete

information of each experiment run is saved together with the recorded pictures and backed up by the university, also every other possible software could be used for data evaluation later on.

## 6.4 Laser systems

The current state of the experiment features four different laser light sources. For each atomic species, a laser system provides all required frequencies to trap and image the atoms. Additionally, a laser source for the blue-plug light (see sec. 6.10.3) and one for the crossed optical dipole trap (see sec. 6.11) exists. In this section, these laser systems are described.

### 6.4.1 Sodium laser system

For several decades, laser light at the sodium transition wavelength of 589 nm has only been available from dye laser sources. While these lasers offer a wide tuning range and are still operated in several laboratories, including other NaK experiments (see e.g. [58]), nowadays solid-state laser sources are available which require much less maintenance and offer therefore a higher comfort in daily operation. In this experiment, a visible Raman fibre amplifier (VRFA) (VRFA-P-1800-589-SF, MPB communications) is seeded by a custom-built laser source, tunable in the wavelength range of 1177.5 – 1179.5 nm (featuring a *Toptica* DFB

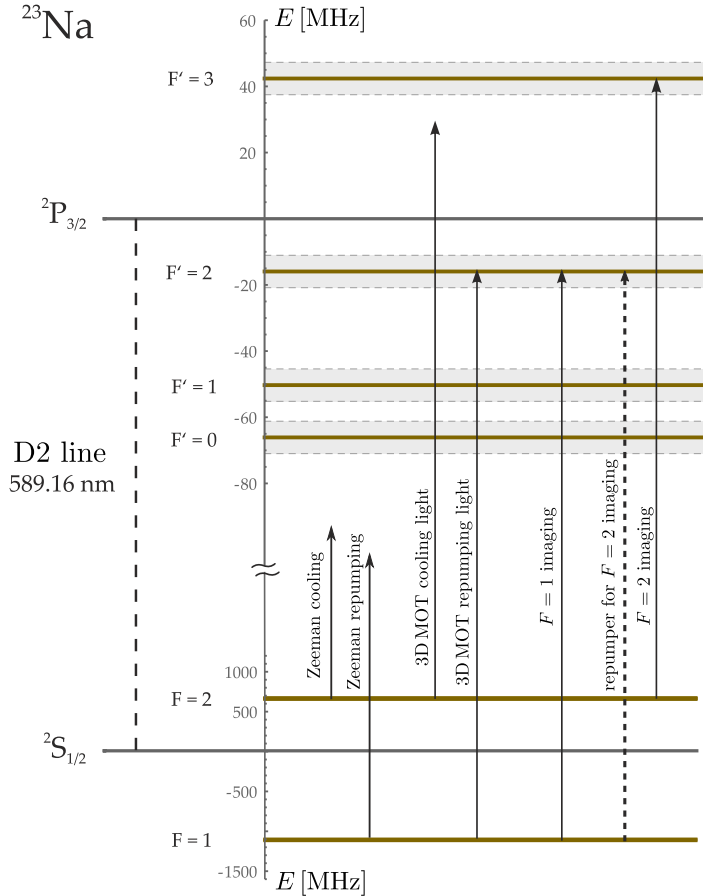


**Figure 6.12: Compendium of  $^{23}\text{Na}$  information.** The hyperfine energy splitting for the  $^2\text{S}_{1/2}$  ground state and the  $^2\text{P}_{3/2}$  excited state of the sodium D2 line are given in MHz. All relevant laser transitions are schematically shown. For details on the different laser transitions see the respective sections in this thesis. Schematic adapted from [36, 85].

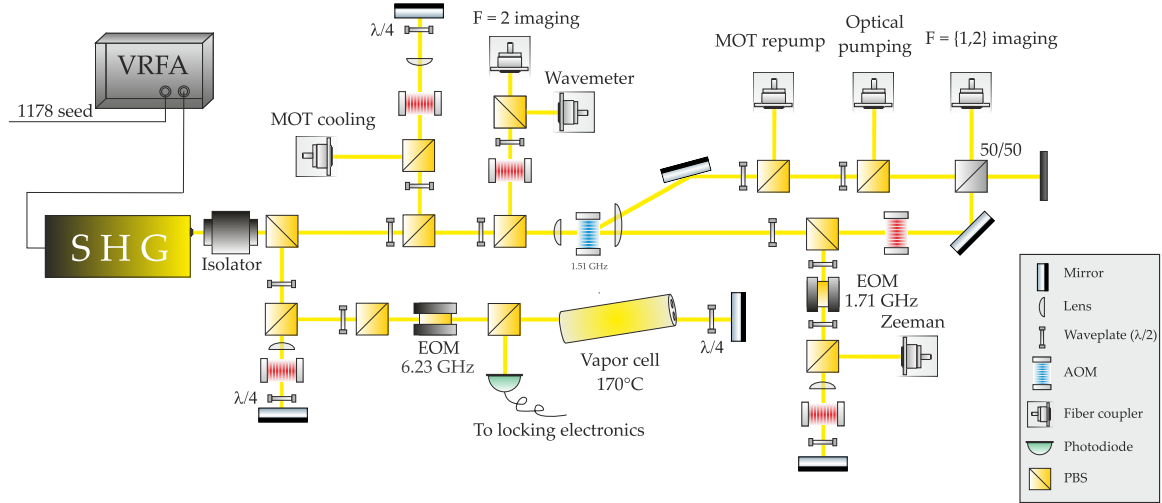


**Figure 6.13: Laser system for the sodium transitions.** Figure taken from [36].

laser diode, type *LD-1178-0030-DFB-1*). The VRFA produces 1.8 W of laser light at about 589.158 nm.

During operation of the fibre amplifier, a stepwise reduction in output power has been recognised twice over the years the system is in use. To regain the output power, the current of the laser diode stacks which pump the fibre had to be increased as well as the seed power. The degeneracy is most likely due to a reduced performance of the pump diode stacks. As stated by the manufacturer, complete rows of diodes in the stack can fail over time, leading to a stepwise reduction in pump power.

The Na laser system is described in detail in [36]. Here, the main features shall be mentioned. The laser is locked via frequency modulation spectroscopy [139] to the Doppler-free crossover signal of the  $^{23}\text{Na}$  D2 line by feeding the generated error signal to the current control of the DFB diode of the seed laser. The locking point for the fundamental frequency  $\omega_0$  is set to 207.5 MHz blue-detuned from the  $|f = 2, m_f = 2\rangle \rightarrow |f' = 3, m_{f'} = 3\rangle$  transition of the D2 line. Its precise locking point is determined by absorption imaging of a cold atomic sample. From that fundamental frequency, all other required laser frequencies are generated by appropriately chosen EOMs and AOMs (in single or double passage), as can be seen in fig. 6.13. All laser frequencies and powers are summarised in tab. 6.2. The powers are

**Table 6.2: Frequencies and powers of the Na laser system.** The frequencies are given with respect to the respective atomic transition. The powers have been measured at the experiment table.

Purpose	$ f\rangle \rightarrow  f'\rangle$	$\Delta$ [MHz]	Power at experiment [mW]
Zeeman slowing	$ 2\rangle \rightarrow  3\rangle$	-400	73
Zeeman repumper	$ 1\rangle \rightarrow  2\rangle$	-400	7
Cooler 3D MOT	$ 2\rangle \rightarrow  3\rangle$	-18.5	87
Repumper 3D MOT	$ 1\rangle \rightarrow  2\rangle$	0	11
Imaging F=2	$ 2\rangle \rightarrow  3\rangle$	0	0.2
Imaging F=1	$ 1\rangle \rightarrow  2\rangle$	0	0.2

measured behind the fibre out-couplers at the main experiment table.

Where necessary, cat-eye double-passages [140] through the AOMs ensure the possibility to tune the frequency by several ten MHz. This is especially important for the beam of the MOT cooling light, which for the molasses phase has to be red-detuned by 6.5 MHz from the frequency it has during the MOT loading, see sec. 6.8.1. Where demanded by the experiment sequence, the AOMs can be shifted in frequency and power by analogue channels of the experiment control and can be switched off completely using TTL signals. To avoid temperature-dependent effects of the AOM performance, the AOMs are only used for fast on- and off-switching of certain laser beams. Each laser beam port also features a mechanical shutter which is used to block the laser beam permanently, allowing it to switch the AOMs back on after the shutter is closed.

The different laser beams are coupled into single-mode polarisation maintaining fibres (*PM FC/APC to FC/PC Patch Cable: PANDA Style, Thorlabs*) which guide the light onto the main experiment table.

#### 6.4.2 Potassium laser system

The laser system and its components are described in detail in [77]. The setup of the laser system was constantly upgraded and modified where necessary e.g. to enable a better

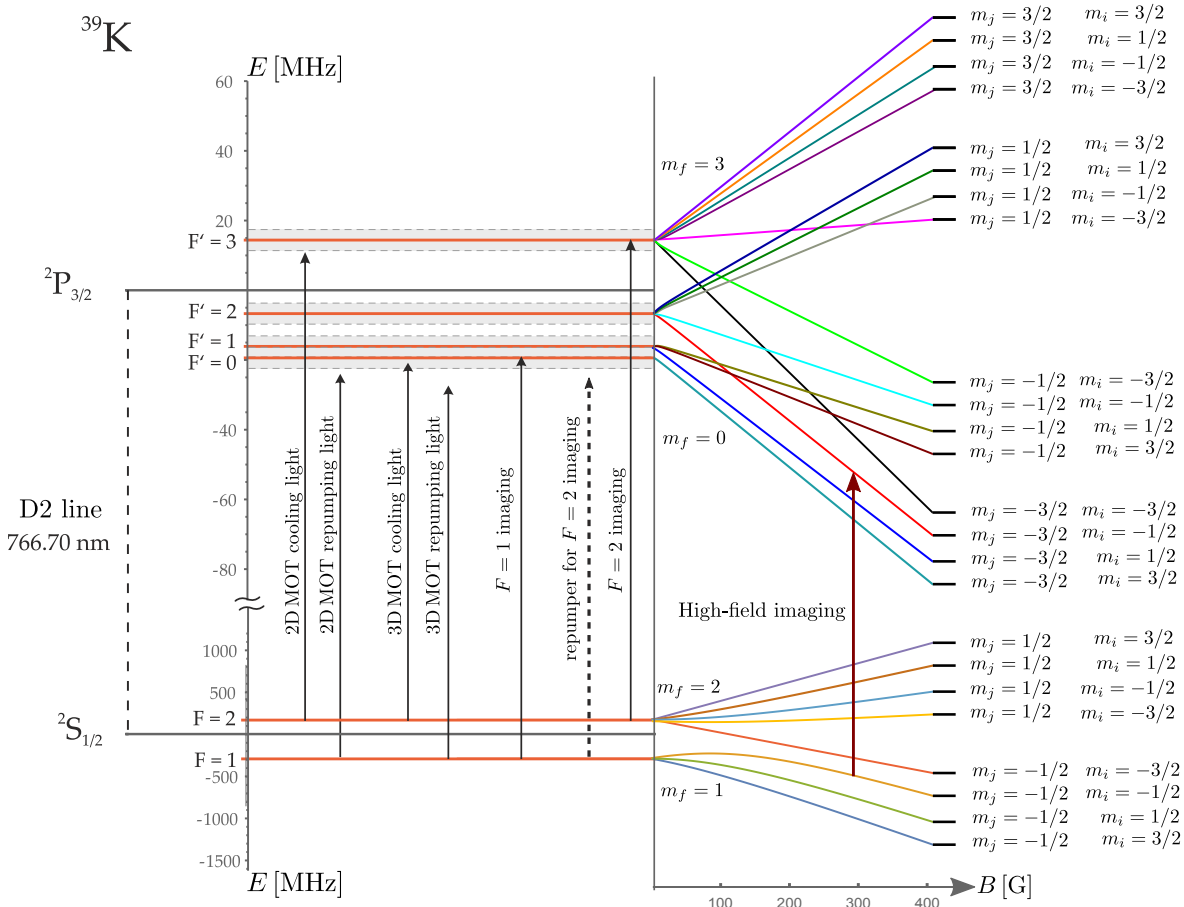


**Figure 6.14: Compendium of  $^{39}\text{K}$  information.** The hyperfine energy splitting for the  $^2\text{S}_{1/2}$  ground state and the  $^2\text{P}_{3/2}$  excited state of the potassium D2 line are given in MHz. All relevant laser transitions are schematically shown, as well as the Zeeman hyperfine level structure for  $^{39}\text{K}$  under the influence of an external magnetic field. For details on the different laser transitions see the respective sections in this thesis. Picture adapted from [36, 86, 141].

stability of the laser locks by spatially separating the diode lasers and their locks from the laser light distribution part. Therefore, the setup shown in fig. 6.15 differs from the one shown in [77] in terms of the spacial arrangement of its components. A detailed description of all modifications can be found in [142].

A diode master laser is locked via Doppler-free absorption spectroscopy to the crossover of the D2 line of  $^{39}\text{K}$ . The frequencies of two diode lasers (one called the cooler the other the repumper laser) are offset-locked to the master laser. This is achieved by generating a beat signal of the master laser with the cooler and repumper laser, respectively. The beat signal is compared to a stable frequency reference to generate the locking signal. The stable reference is produced by a frequency generator (*SML1, Rohde & Schwarz*) which can be controlled by the experiment PC via VISA commands. The error signal is fed to proportional-integral-derivative controllers (PID controllers) which stabilise the lasers.

The powers of the cooler and repumper diode lasers are amplified using tapered amplifiers (TA) and all required frequencies are generated using appropriate AOMs in single or double passages. In tab. 6.3, all power values are listed at different positions in the laser system and on the experiment table. The positions are marked in fig. 6.15 by blue dots. Single-mode polarization maintaining optical fibres (*PM FC/APC to FC/PC Patch Cable: PANDA Style, Thorlabs*) are used to guide the light from the laser system to the experiment. As for the Na laser system, the AOMs are used for fast switching of the laser light. Mechanical shutters ensure that no spurious light can enter the fibres while the respective port is not used in the sequence.

The spacial separation of laser sources and amplification stage (see fig. 6.15) has been conducted because the numerous mechanical shutters used to block the light of the various laser ports can disturb the laser lock. This leads to either an unlocked laser after a shutter is flipped or to a short shifting of the laser frequencies out of the lock point during the mechanical kick of the shutter. Thereby, undesired effects in the experiment can occur, induced by wrong laser frequencies transmitted through the fibres. With the spacial separation of

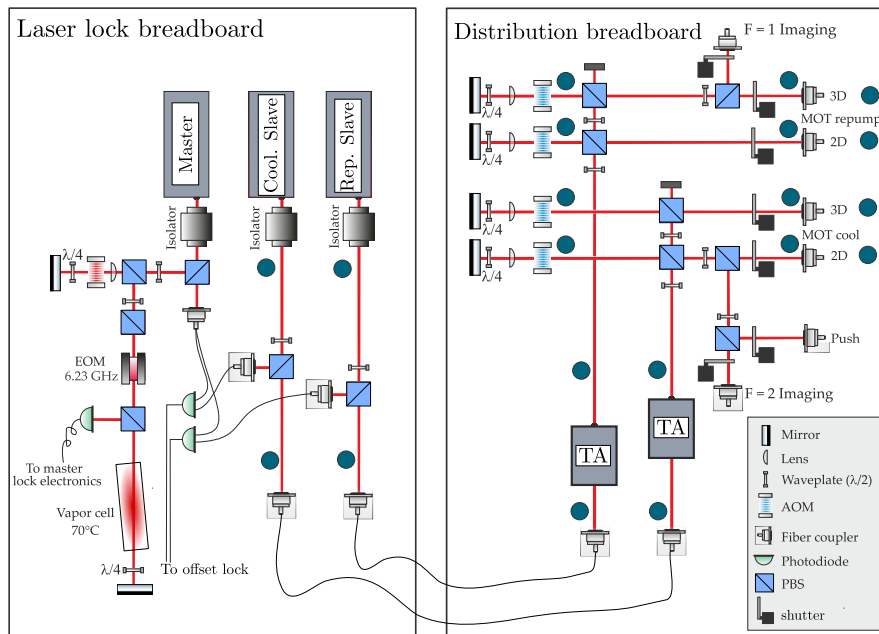


**Figure 6.15: Laser system for the potassium transitions.** The laser system is built on two breadboards to separate the mechanical shutters in front of the fibres from the laser lock setup. Blue dots mark the points where reference measurements for the laser powers are taken, see tab. 6.3. Picture adapted from [36, 77].

**Table 6.3: Laser powers at different positions of the K laser system.**

Position	$P_{\text{cooler}}$ [mW]	$P_{\text{repump}}$ [mW]
Diode laser output	43	60
Used for lock	2.5	2.8
In front of coupler to amplification stage	40	44
Behind out-coupler at amplification stage	16	22
After TA (operated at 1 A)	277	174
In front of 3D AOM (TA at 2 A)	640	520
In front of fibre coupler 3D MOT	262	190
After fibre out-coupler 3D MOT, horizontal axis	40	36
In front of 2D AOM (TA at 2 A)	300	195
In front of fibre coupler 2D MOT	110	80
After fibre out-coupler horiz. 2D MOT (1/2 total power)	18	15

the lock components and the shutters, these possible disturbances of the experiment are eliminated now.

The experiments performed in [77] focussed on  $^{40}\text{K}$ . In this thesis,  $^{39}\text{K}$  is the isotope under investigation. When comparing the level structure of the fermionic  $^{40}\text{K}$  with the bosonic  $^{39}\text{K}$ , see fig. 6.14 and [86], it becomes clear that  $^{40}\text{K}$  will act differently than  $^{39}\text{K}$ . This is due to its larger excited state hyperfine splitting, the integer nuclear spin and an inverted hyperfine structure of the ground state.<sup>2</sup> As has been pointed out in [141] and the references therein, the much smaller hyperfine structure in the excited state compared to  $^{23}\text{Na}$ ,  $^{85}\text{Rb}$  and  $^{87}\text{Rb}$  leads to a much stronger decay into  $|F = 1\rangle$  of the ground state when cooling on the  $|F = 2\rangle \rightarrow |F' = 3\rangle$  transition. Therefore, a rather different scheme for the laser setup for the magneto optical traps (MOTs) has been shown to work more efficiently (see [141]). This scheme has been implemented in the 2D MOT used in this work.

The frequencies of the different laser transitions used in the experiment are listed in tab. 6.4 where they are given with respect to the respective atomic transition. The detunings used for the MOTs in this work have been found to be quite close to those used in [141].

### 6.4.3 Blue-plug and cODT laser systems

Two high-power laser systems provide the light for the blue plug (see section 6.10.3) and the cODT (see sec. 6.11) and will be described in detail in the following.

<sup>2</sup>The other stable bosonic isotope  $^{41}\text{K}$  acts quite similar to  $^{39}\text{K}$  but is not subject of this work and will therefore not be discussed.

**Table 6.4: Laser frequencies and powers of K laser system.** The frequencies are given with respect to the respective atomic transition. The powers are measured at the experiment table.

Purpose	$ f\rangle \rightarrow  f'\rangle$	$\Delta$ [MHz]	Power at experiment [mW]
Cooler 2D MOT	$ 2\rangle \rightarrow  3\rangle$	-8.7	36
Repumper 2D MOT	$ 1\rangle \rightarrow  2\rangle$	-20.4	30
Cooler 3D MOT	$ 2\rangle \rightarrow  3\rangle$	-35.5	80
Repumper 3D MOT	$ 1\rangle \rightarrow  2\rangle$	-22.2	72
Imaging F=2	$ 2\rangle \rightarrow  3\rangle$	0	0.2
Imaging F=1	$ 1\rangle \rightarrow  2\rangle$	0	0.2

### Blue-plug laser system

As explained in sec. 6.10.3, a laser whose frequency is blue-detuned with respect to both the sodium and the potassium transitions is required in the experiment to prevent atom loss from the magnetic trap. This laser light is provided by a 5 W solid-state laser with a wavelength of 532 nm (*VERDI-V5, Coherent*). The light is coupled to a large-mode-area photonic-crystal fibre (*NKT Photonics*) and guided by this to the top breadboard of the experiment setup. These fibres offer a good performance over a wide wavelength range, but they are delicate to handle during high-power in-coupling.

First it shall be noticed that the fibres are angled cut fibres ( $8^\circ$  facet angle) with out-couplers specifically made for them (*Schäfter & Kirchhoff*) but that they lack any alignment mark or pin to properly align the angle of the fibre to the angle of the out-coupler. An incorrect alignment leads to bad in-coupling performance or a distorted not collimated out-coupled beam. Since this is the case for both ends of the fibre, properly setting up a fibre link with them is cumbersome. The method found to work best is to first couple light from the sodium laser system to the in-coupler of the NKT fibre. With this light the out-coupler beam profile is optimised by adjusting the out-coupler and the fibre in terms of angle-cut matching. Then the process is repeated for the other end of the fibre. Especially a good matching of the angle cut has been found to be crucial within a few degrees for a stable in-coupling performance.

When high laser powers (meaning the 5 W of the VERDI) have to be coupled into the NKT fibre, the coupling procedure is first performed with low laser light power of a few ten mW. The input power is then increased in steps of 1 W. For every step, the incoupler is left to thermalize for around ten minutes. If the in-coupling efficiency drops over time, careful realignment is performed. A coupling efficiency of at least 65 % has been found to be necessary for stable operation conditions. Coupling at high power is a delicate process. All the power which is not in-coupled properly gets lost inside the fibre within the first few millimetres, being transferred into heat. This heats the copper cladding which surrounds the last centimetres of the NKT fibre core. Thereby, the fibre can be squeezed which can significantly reduce the in-coupling efficiency. In turn, the heat of the copper increases further. Ultimately, this process can lead to the destruction of the fibre as it happened once within the course of the experiments. Since the highest coupling efficiency which has been achieved is  $\sim 70\%$ , the maximum amount of input power is limited by the fact that the in-couplers are only air cooled. A trial with an 8 W VERDI led to a temperature of  $52^\circ\text{C}$  at the in-coupler and was abandoned due to the risk of damaging the fibre.

Since mechanical drifts in the in-coupling optic mounts can lead to a decreasing in-coupling efficiency over time, the in-coupled power is monitored by a pick-up diode on a daily basis, so that no self-energizing process can occur which would lead to a fibre breakdown. Furthermore, it is important to keep the in-coupler at a constant temperature over the course of an experiment day. This is why the laser light is blocked on the main experiment table by a mechanical shutter which is placed behind the out-coupler. Thereby, always the full laser power is in-coupled to the fibre, keeping it at a constant temperature.

### Laser system for the cODT

The optical trapping potentials of the cODT are generated from a solid-state laser system (*Mephisto MOPA, Innolight,  $\lambda = 1064\text{ nm}$ , 42 W maximal output power*) which is coupled into high-power optical fibres (*PMJ-A3AHPC-1064-6/125-3AS-7.5-1, OzOptics*) and by them guided to the two dipole trap axes. An AOM is placed in front of each fibre and is used for fast switching of the traps. Additionally the AOMs impose different frequencies (by 80 MHz) onto the beams to time-average out possible interference effects of them. To maintain a stable fibre coupling, the AOMs should be active for the most part of an experiment sequence. After the fast switch-off with the AOMs is completed, a mechanical shutter blocks the fibre, thereby enabling that the AOMs can be switched back on. For the mechanical shutters, a design with a simple metal flag which blocks the high-power beam suffered from the heat load. Therefore, a shutter has been built which uses a mirror to direct the laser light onto a beam dump. Figure 6.16 shows a picture of one of the custom-built shutters.

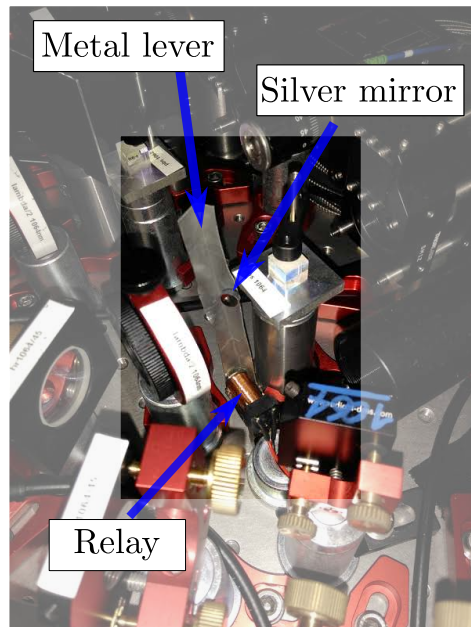


**Figure 6.16: Custom-built mirror shutter.** A relay is used to move a metal lever onto which a silver mirror is attached.

It has been found that the beam profile of the laser source changes with increasing output power, making it impossible to fibre-couple first at low laser powers and then to increase the output power. To prevent destruction of the fibre in the process of coupling, a half-wave plate and a polarizing beam splitter (PBS) have been placed in front of the fibre. Thereby, most of the light can be reflected out during the alignment procedure and reflected back in after the alignment has been finished.

A power stabilisation for each of the two cODT beams is implemented in the experiment [143] which regulates the laser power inside the fibres by controlling the diffraction efficiency

of the AOMs in front of them.

## 6.5 Magnetic field coils and current switching

Two sets of coils provide the required magnetic fields for the experiments preformed in the main chamber. One set of two coils, situated close to the centre of the chamber and are called *Feshbach coils* throughout this thesis, runs currents of up to 270 A at some points of the experiment sequence and is switched using insulated-gate bipolar transistors (IGBTs). The other set of six coils is used to generate compensation fields. The setups are described and characterised in the following.

### 6.5.1 Feshbach coils and compensation cage

The Feshbach coils are situated on top of and below the main chamber. Their design is described in detail in [77] and consists of a pair of coils with 24 windings each. Each coil is enclosed inside a housing made from FRP. The housing enables for water cooling of the coils. The quadrupole field generated by the Feshbach coils has a field gradient of  $dB/dz = 0.8 \text{ (G/cm)}/\text{A}$  along the strong confining magnetic field axis. The coils can be operated safely with currents up to  $\sim 320 \text{ A}$  for up to 30 s. Two power supplies (*SM 30-200, Delta Elektronika*) in a master-slave configuration generate these currents.

The overall magnetic field can be modified by a set of six additional coils mounted in a cage configuration around the main chamber, as described in [77]. The six coils form three pairs of Helmholtz coils, thereby allowing to shift the magnetic trap centre or to apply guiding fields of up to 4.5 G. The coil performance is 0.38 G/A. It has been found that applying currents higher than 12 A in a continuously cycling experiment causes a too high

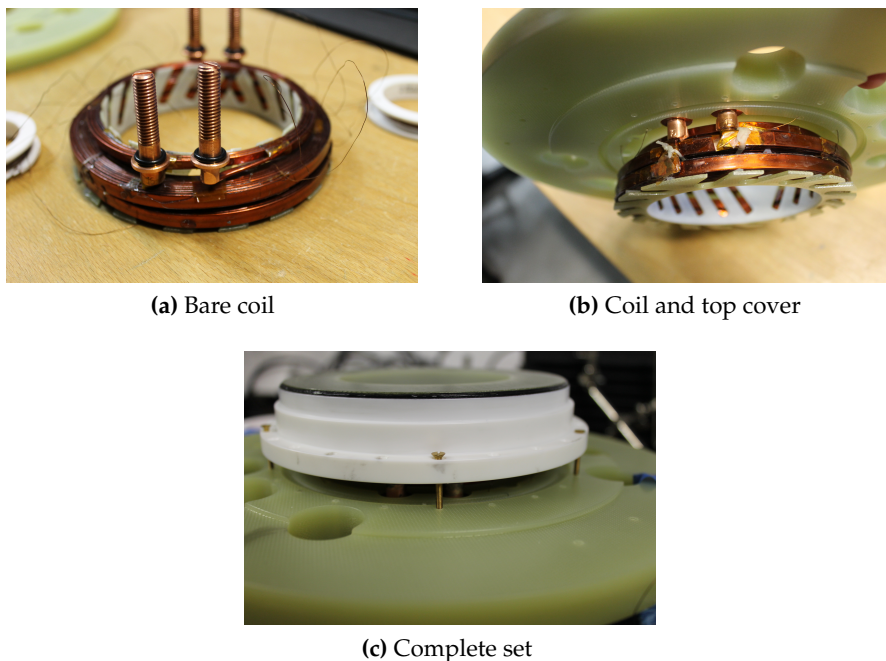


**Figure 6.17: Assembly of upgraded Feshbach coils.** In (a) the bare coil is shown as it was delivered by the manufacturer. The two sets of coils are visible as well as the wires of the NTCs which are placed in between the coil windings. (b) shows the coil inserted into the FRP top cover to which also the cooling water pipes are connected. In (c) the assembly is almost complete, the bottom made from plastic has still to be tightened against the top cover.

**Table 6.5: Temperature development during Feshbach coil operation.** The temperatures are measured in between two coil windings ( $T_{\max, \text{coil}}$ ) and of the cooling water inside the coil housing ( $T_{\max, \text{water}}$ ) for variable times of operation. For all cases, only the maximal temperature measured by the multiple temperature sensors placed in the coils or the cooling water is given to maintain clarity.

Coil current [A]	$t$ [s]	$T_{\max, \text{coil}}$ [ $^{\circ}\text{C}$ ]	$T_{\max, \text{water}}$ [ $^{\circ}\text{C}$ ]
100	0	21	22
	30	27	22
	60	27	22
200	0	21	22
	30	46	22
	60	42	22
250	0	21	22
	5	43	22
	15	58	23
	30	61	23
	60	61	23
300	0	21	22
	5	55	23
	15	68	23
	25	80	23
350	0	21	22
	5	66	23
	15	98	24
	25	104	24

heat load. Each coil is connected to a power supply (*PS 3032-20 B, Elektro Automatik*) which is remote-controlled by the experiment control unit.

Recently, the Feshbach coils had to be exchanged and have at the same time been upgraded in their design by M. W. Gempel. The coils themselves have been manufactured by *Elektrowerk Hannover Behncke Maschinenbau GmbH*, the housing by *Erhard Hippe KG* and assembly has been performed during the course of this work. Figure 6.17 shows different stages of the assembly process.

The exchange became necessary because an electric shortcut appeared in the upper coil, resulting in an unstable magnetic field. This was visible by shot-to-shot jumps in the vertical position of the magnetic trap centre often by several micrometres. The shortcut appeared most likely because the water used to cool the coils has been, albeit provided by an own cooling cycle containing deionized water, carrying small particles into the coil housing. These

particles then blocked certain regions from the cooling water. This led to overheating of these parts of the coil and melting of the insulation material of the copper wire. Therefore, during the exchange of the coils a new water filter system has been installed (*DP3 PFAPCBPCA, pureway CrysAl Group*), allowing for filtration of particles down to  $0.3 \mu\text{m}$  diameter. To still achieve the required water flow rate, the pressure of the input water had to be increased to 4.5 bar. A water flow sensor monitors the flow rate and interlocks the power supplies if the water flow drops below a critical value.

In addition, the new coils feature upgrades originating from experiences made with the first set of coils. In the new coil housing, an additional coil with four windings is installed on top of the main coil with 24 windings. This will allow in the future for implementation of fast switchable magnetic fields. For this, the main coils will provide a certain magnetic field strength on top of which the smaller coils can be switched to allow fast magnetic field jumps. In the new design, the lower part of the coil housing is made from plastic as it has been found that FRP can become permeable for water along its layers over time.

Moreover, the temperature of the first set of coils could only be monitored indirectly by NTC temperature sensors placed inside the coil housing measuring the temperature of the cooling water. In the new set of coils, several temperature sensors are placed in between the windings of the coil, allowing to monitor the temperature inside the coils. In tab. 6.5, a set of data is presented showing the temperature development inside the water-cooled coils when they are operated with different currents. Only the maximal temperatures inside the coil and the water, measured by the different sensors in between the coil windings and the cooling water, are listed for clarity. Operating the coils at currents higher than 300 A is only recommended for durations shorter than 30 s. It becomes also clear that measuring the temperature of the cooling water does not yield a reliable indication of the temperatures inside the coils. A further value of interest is the time required for the cool down of the coils after the currents have been switched off. This has been measured for a coil operating for 60 s at a current of 250 A. The maximal temperature reached was 61 °C and the time to cool down again to 21 °C was 17.5 s.

### 6.5.2 IGBTs and current control system

The Feshbach coils described in the previous paragraph are used to create magnetic fields in Helmholtz, Anti-Helmholtz and Stern-Gerlach configuration. Each of these different configurations requires the electric current to flow in a different way through the coils. While for the generation of a homogeneous Helmholtz field the current in both coils need to flow in the same direction, Anti-Helmholtz fields require the currents to flow in opposite directions and a magnetic gradient field as necessary for Stern-Gerlach type experiments needs the current to flow only through one coil.

All these different configurations can be realised in the experiment by four IGBTs operated in an *H-bridge configuration* as shown in fig. 6.18. The IGBTs are of the n-channel, normally open type. The IGBTs are controlled by driver boards specifically designed to work with standard TTL signals as an input and to generate the necessary high currents to drive the gate of an IGBT (*BG2A - Universal Gate Drive Prototype Board equipped with VLA500-01 hybrid gate drivers, POWEREX*). A custom-designed logic board uses three TTL signals from the experiment control unit to switch between the four different coil operation modes (Helmholtz, Anti-Helmholtz, Stern-Gerlach, off). In fig. 6.18, the configurations are shown with respect to the operation mode of each IGBT. The IGBTs are mounted on a water-cooled plate and are protected against excess voltage by varistors which are connected in parallel with the IGBTs. A varistor is an electronic component which has an electrical resistance that is high up to a component-specific threshold voltage above which the resistance drops abruptly. While operating the system, it has been found that the originally mounted IGBTs (*CM300DY-24NF, Mitsubishi*) are not capable of sustaining the currents used at some stages

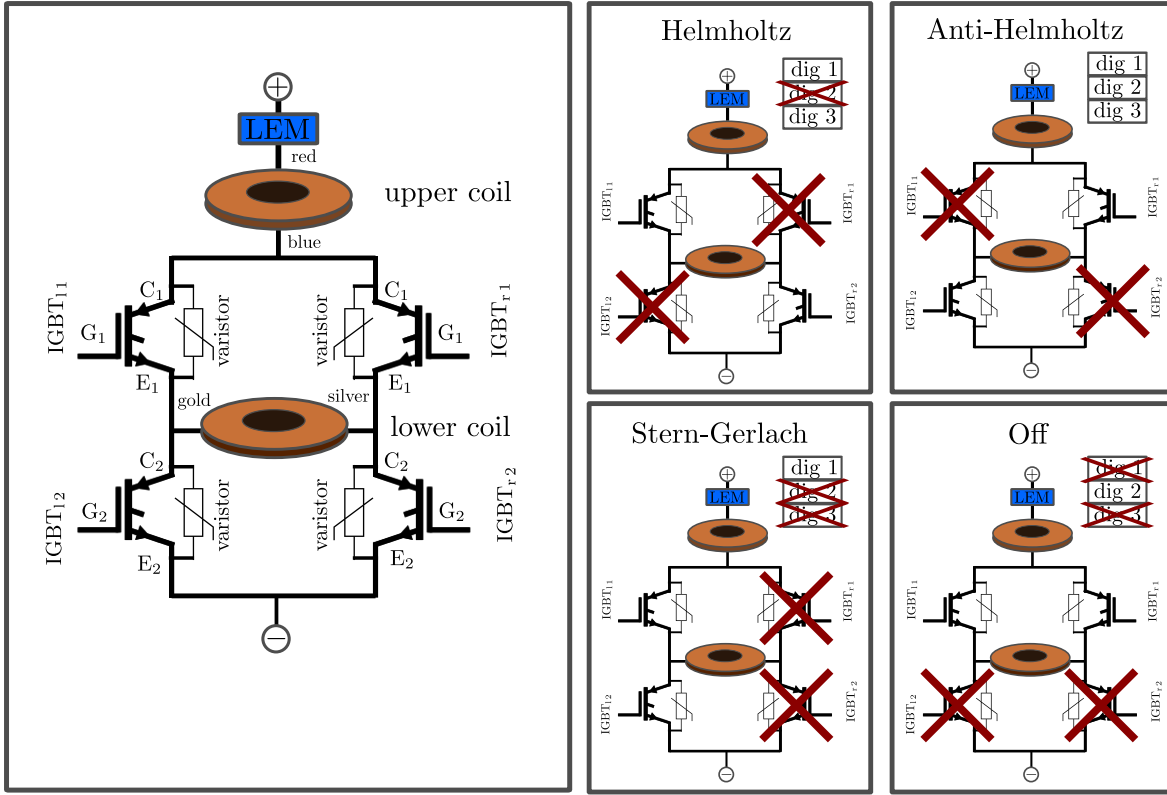


**Figure 6.18: H-bridge configuration for Feshbach coils.** The left picture shows the setup in detail. The H-bridge is formed around the lower coil using four IGBTs. Each IGBT is protected against peak voltages by a varistor. A current transducer (LEM) measures the current directly behind the positive output of the power supply. The colours next to the coils are related to markings on the cables at the actual experiment apparatus. On the right, the four operation modes are shown together with the chosen configuration of the three digital channels used for control. A cross marks a digital channel output which is switched off and a closed IGBT, respectively.

of the experiment sequence. Most likely, the cooling provided by the cooling plate is not sufficient to operate the IGBTs at their upper operation limit over a long time interval. The problem has been solved by implementing IGBTs of the same build volume but with a higher maximal current rating (*CM400DY-24NF, Mitsubishi*).

The IGBTs can be used to cut off the current through the coils in a very short time (on the order of microseconds). Fast switching of high magnetic fields, however, imposes respectable technical challenges since due to Lenz's law a fast change will lead to self-induced currents. The inset of fig. 6.19 shows that when switching a current of 50 A using the IGBTs, oscillations around the zero current are damped within  $\sim 20 \mu\text{s}$ . Negative current values indicate the mentioned self-induced currents in the coil. The measurements were performed by using a current transducer (*IT-400S Ultrastab, LEM*) to measure the current flowing through one of the supply cables of the Feshbach coil pair. Normally, the damp-out time shown in the inset of fig. 6.19 would be acceptable for the experiments performed in this thesis and the fast switch-off time can be beneficial. When investigating the complete picture, however, it can be seen that not all energy stored in the coils could be depleted during switching off. When opening the IGBTs again after 12 ms to ramp the magnetic field to a value of 40 A, heavy oscillations of the current are detected. For this reason, the IGBTs are used in this experiment to switch off only moderate currents of up to around 20 A. All other changes in the coil current are controlled by the power supplies. The LEM is used to feed the information about

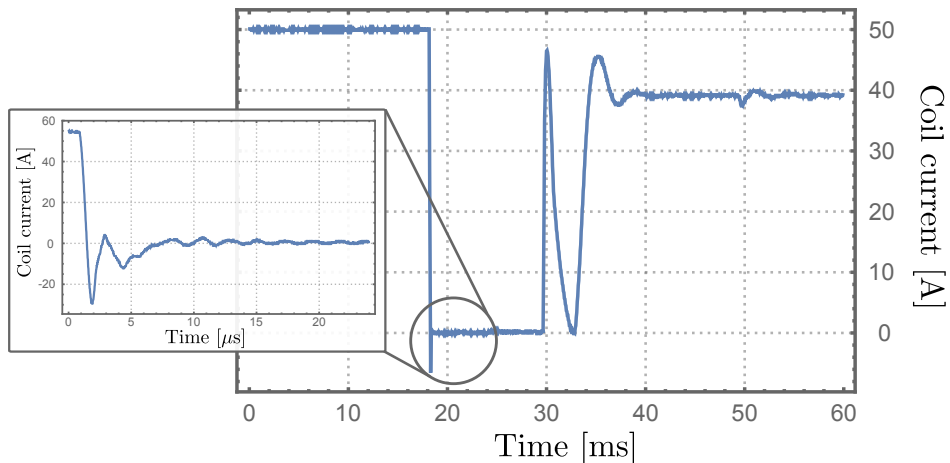


**Figure 6.19: Current flowing through Feshbach coils during fast switching.** The current is switched using the IGBTs. Thereby, a fast reduction of the current to zero is possible with acceptable overshoots (inset). When opening the IGBTs again, to ramp the field to 40 A, heavy oscillations indicate that the PID controller cannot compensate the energy still stored in the coils.

the actual current flowing through the coil circuit to the internal PI controller of the master power supply. A calibrated analogue channel from the experiment control unit is used to set the output current of the master-slave assembly.

It has been found that for switching high currents without shifting the atoms with induced magnetic fields, the electric currents have to be ramped with care. In fig. 6.20, the current flowing through the Feshbach coils is shown for different sections of the experiment sequence. At point (A), the magnetic trap (see sec. 6.8.2) is ramped up in two steps. The first fast ramp-up shows sizeable overshoots of the current value. This is a natural characteristic in any PI-controlled circuit if a fast response time is required. The following ramp to the final trap value of 270 A is slower so that no further overshoots appear (B). A cut in the time axis hides the part of the forced MW evaporation inside the magnetic trap (see sec. 6.10.1). At point (C), the magnetic trap is switched off in two subsequent steps by first ramping the current down to 50 A in 50 ms and further reducing it to zero in another 100 ms. At point (D), the IGBTs are switched to Helmholtz configuration and the current is ramped up in preparation for the following measurements. Two zooms to the regions (C) and (D) are shown, too. It can be seen that no substantial overshoots or oscillations in the current are present.

For experiments performed in experiment chambers made from conducting materials such as steel, switching off magnetic fields will induce so-called *eddy currents* in the metal. For this experiment, it has been found that 3.4 ms are required after switching the coil current off until these currents are completely damped out. This time of zero coil current can be seen in the zoom to region (D) in fig. 6.20.

## 6.6 Atom sources

This section describes the optics and operation of the atom sources for  $^{23}\text{Na}$  and  $^{39}\text{K}$ , the Zeeman slower and the 2D MOT. The vacuum components of the setups are described in sec. 6.2.3.

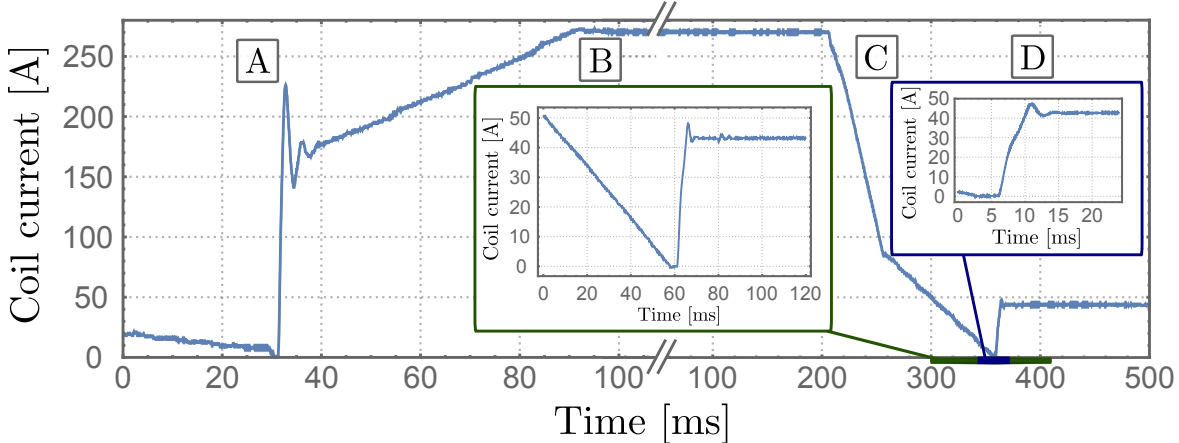


**Figure 6.20: Current flowing through Feshbach coils.** The current flowing inside the coils is shown for a section of a standard experiment sequence. At point (A), the magnetic trap confinement is ramped up, at point (B) the forced evaporation in the magnetic trap starts (note the interruption of the time axis at this point and the change in the time intervals). The magnetic trap is switched off at point (C) without introducing unwanted current oscillations. At point (D) the IGBT configuration is switched from Anti-Helmholtz to Helmholtz and the current is ramped up again in preparation for the following experiment steps. The two inserts show zooms to the regions (C) and (D), the exact position of the inserts are colour coded in the insert frames and on the time axis.

### 6.6.1 Zeeman slower

A Zeeman slower uses the combination of the magnetic field dependent energy splitting of hyperfine levels in an atom together with the Doppler effect to slow down a beam of atoms using counter-propagating circularly polarized laser light.

In this experiment, the hot sodium vapour is emitted and pre-collimated by the reflux oven described in sec. 6.2.3. At an operating temperature of 330 °C, the mean speed of the atoms is 750 m/s. After passing the pneumatic shutter region, the atoms enter inside the coils placed around the 100 cm long vacuum tube. The coils produce a spatially dependent magnetic field of the so-called *spin-flip* type, its exact shape together with all details on the calculations and exact coil design can be found in [129]. By the magnetic field, the hyperfine state energies of sodium are spatially modulated. A single  $\sigma^+$  polarized laser beam containing two laser frequencies both 400 MHz red-detuned to the MOT cooling and repumper transition (see sec. 6.4.1) is focused over the length of the Zeeman slower close to the nozzle in the oven section (the exact position being subject to experimental optimisation while monitoring the performance of the slower).

The counter-propagating atoms scatter photons due to the Doppler shift dependent on their actual velocity. Thereby, part of the atoms are slowed down, shifting the velocity distribution inside the atom beam to lower velocities. Due to the spatially varying magnetic field produced by the coils, the resonance condition for the laser light is kept in such a way over the length of the slower that the Doppler shift for the fastest atoms is always compensated. Thereby the mean longitudinal velocity in the beam is constantly reduced (partial transversal cooling is achieved due to the focusing of the laser beam). Parameters such as the coil currents and the exact shape of the coils determine the maximal capture velocity as well as the reached mean velocity at the end of the slowing process. In the case of the slower presented here, the maximum capture velocity is 900 m/s and the mean velocity at the end of the slowing process is 30 m/s.

The exact values for the coil currents are determined experimentally since they depend

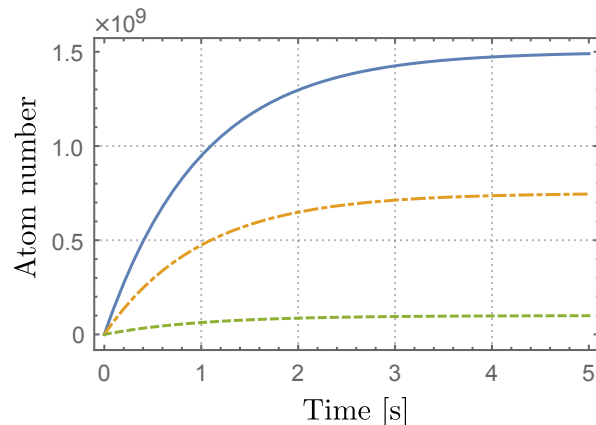


**Figure 6.21:** Simulated MOT loading curve for different Zeeman slower flux values. Three different values of the flux are plotted for the same loss rate present in the MOT:  $1.5 \cdot 10^9$  atoms/s (blue solid line),  $0.75 \cdot 10^9$  atoms/s (orange dashed-dotted line) and  $0.1 \cdot 10^9$  atoms/s (green dashed line).

on the temperature of the oven as well as on the laser detunings. During the experimental optimisation, the MOT loading rate is the figure of merit. The absolute number of atoms which can be trapped in the MOT depends on the flux of the Zeeman slower. Figure 6.21 shows a simulation of loading curves for different flux values of the Zeeman slower. It is obtained by solving

$$\frac{dN(t)}{dt} = +F - \Gamma_{loss}N(t), \quad (6.18)$$

where  $N(t)$  is the time-dependent atom number in the MOT,  $F$  [n/s] the flux of  $n$  atoms per second and  $\Gamma_{loss}$  [1/s] is the loss rate which depends on the losses due to background gas collisions and other loss processes in a MOT. The three curves in fig. 6.21 are plotted for the same loss rate but for different values of the flux. As can be seen, not only the loading speed but also the total atom number reached in the MOT depend on the flux.

To achieve a MOT of  $\sim 3 \cdot 10^9$  atoms (see also sec. 6.7.1), a flux of  $\sim 0.5 \cdot 10^9$  atoms/s is needed in the experiment. For optimal operation conditions a flux of up to  $\sim 1.5 \cdot 10^9$  atoms/s is reached.

### Alignment of the Zeeman slower laser beam

To align the laser beam optimally, first the focus is approximately adjusted to the correct distance by reflecting the beam out of its original beam path by introducing a mirror in front of the vacuum chamber viewport. By shifting the out-coupler lens, the focus can be adjusted to a distance from the out-coupler matching the distance from the out-coupler to the oven section. Next, the beam is aligned onto the atom shutter blade in the shutter region using two mirrors. Thereby, only minor adjustment is required to reach the oven section. In that section the beam can be investigated by monitoring the fluorescence it produces when interacting with the sodium atoms which leave the reflux oven nozzle. The final laser beam alignment is performed by optimising the flux of the Zeeman slower.

### 6.6.2 Two-dimensional magneto-optical trap

The source for the potassium atoms is a 2D MOT [144, 145]. This section discuss the changes which have been applied when switching the system to investigate the bosonic  $^{39}\text{K}$  instead of the fermionic  $^{40}\text{K}$  used during the work presented in [77].

As described in the sec. 6.4.2 about the potassium laser system, the frequencies of the cooler and repumper laser have been adjusted to the bosonic isotope. The optics to deliver the cooling and repumper light are a set of three polarizing beam splitter cubes per axis through which the light is divided into three circular beams of approximately 20 mm in diameter. The setup is identical to the one described in [77]. The laser powers at the experiment table are 36 mW for the 2D cooler and 30 mW for the 2D repumper. These powers are divided equally onto the two axes of the 2D MOT using a fibre splitter as can be seen in fig. 6.10.

The magnetic confinement is produced by two sets of coils in Anti-Helmholtz configuration, one set for the vertical and one for the horizontal axis. Each coil has its own power supply (*EA-PS 3016-40 B, EA Elektro Automatik*). Hence, the magnetic trap zero can be shifted in the horizontal and vertical direction independently by adjusting the currents in each coil. All power supplies can be switched on and off as a unit by the experiment control using a TTL signal. The coil holders form a cage with micrometre screws on each corner of the top and both side coil holders as can be seen in fig. 6.10. The screws have ball pins with which they lay on the 2D MOT chamber. The chamber possess special pockets for the ball pins. With this construction, it is possible to tilt the angle of the magnetic field zero axis with respect to the chamber by pivoting the coil cage with respect to the 2D MOT chamber.

### Alignment of the 2D MOT

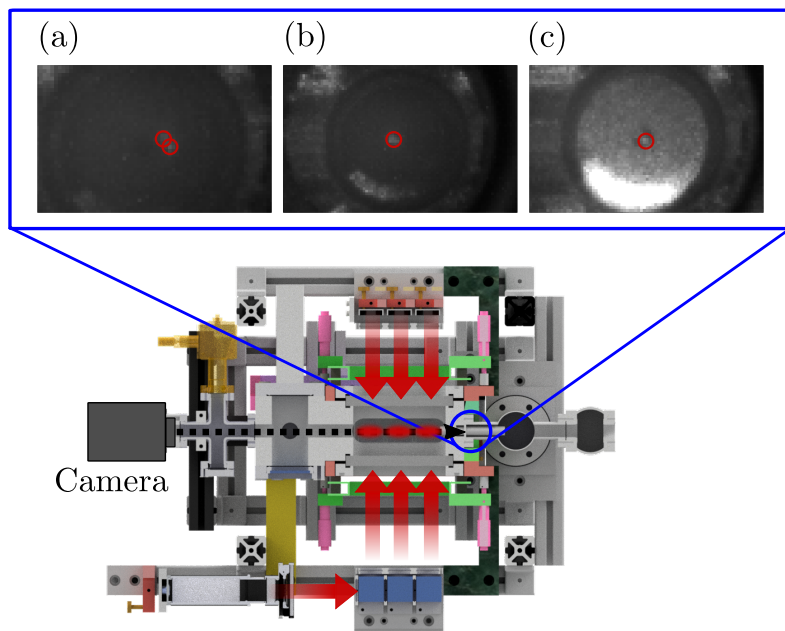


**Figure 6.22: Alignment of 2D MOT.** Three separate 2D MOT areas are formed (red ellipses) by the three parallel MOT light beams (red arrows). By imaging them with a camera along the central axis of the 2D MOT chamber (dashed arrow), it can be investigated whether the MOTs line up. If this is not the case, as in (a), the MOTs can be shifted onto a common axis by adjusting the light power balancing in each beam pair, (b). Additionally, the orientation of the magnetic field coils with respect to the chamber can be tilted to align the magnetic field zero parallel to the central axis of the chamber. The ensemble is as final step moved onto the central axis of the chamber by adjusting the currents of the MOT coils (c).

While other 2D MOT designs use elliptically shaped single beams [146] and therefore form a single elongated trapping volume, the construction used in this work forms three

adjacent 2D MOTs. To achieve the maximal atom flux in the direction of the main chamber, these three MOTs have to line up with the hole in the first (and second) differential pumping stage. The alignment is performed by imaging along the atom flux axis with a CCD camera. The fluorescence of the 2D MOTs is then visible. As can be seen in fig. 6.22 (a), the single 2D MOTs do not line up properly. With the help of the power balancing of the MOT beams and the adjustable cage of the 2D MOT coils, it is possible to line up the different 2D MOTs, see fig. 6.22 (b). By changing the currents in the appropriate coils, all MOTs as a set can then be shifted onto the central axis of the differential pumping, see fig. 6.22 (c).

The flexible bellow between main chamber and 2D MOT reduces mechanical stress in the system, but requires a more detailed alignment of the atom source and the trap centre of the 3D MOT in the main chamber. For that purpose, a strong flash light is placed at the back of the 2D MOT. Its light can then be seen from the main chamber view port opposite to the 2D MOT. By moving the 2D MOT and aligning this light spot to the centre of the main chamber flange, a decent first mechanical alignment is achieved. The final position is obtained by carefully moving the 2D MOT while monitoring the loading rate of a potassium 3D MOT.

## 6.7 3D magneto-optical trap

The pre-cooled sodium and potassium atoms are trapped and further cooled inside a two-colour 3D MOT. A 3D MOT uses a set of counter-propagating circularly polarized light beams in each spacial direction and a magnetic quadrupole field to spatially confine and cool the atoms [144]. For  $^{23}\text{Na}$  and  $^{39}\text{K}$ , the optical transitions on the D2 line are used, where the  $|f = 2\rangle \rightarrow |f' = 3\rangle$  hyperfine transition is the main cycling albeit cooling transition. Couplings to the  $|f = 1\rangle$  state lead to losses in this cycle, thereby making a repumping frequency on the  $|f = 1\rangle \rightarrow |f' = 2\rangle$  transition necessary.

In this experiment, the magnetic Anti-Helmholtz field is produced by the main coils described in sec. 6.5.1. The optical setup is sketched in fig. 6.23. The laser light for both species is guided from the laser table to the experiment table via single-mode polarization-maintaining optical fibres. In the case of the light for the potassium MOT, the cooler and repumper light is superimposed using fibre combiners before two collimated beams of 2.2 mm diameter are out-coupled (*Fixed Focus Collimation Package, Thorlabs Inc.*). The first generates the vertical MOT beam the second is further divided into the two horizontal beams using a  $\lambda/2$  wave plate and a PBS. In the case of sodium, the cooler light is divided into three beams forming the three MOT axis and the repumper is overlaid onto the horizontal axis using PBS cubes. For each of the three axes, the beams for sodium and potassium are overlaid using dichroic beam combiners and then enlarged in diameter to 22 mm by telescopes. After the telescopes, the horizontal beams are split into the two counter-propagating MOT beams for each horizontal axes and directed to the main chamber by 2 inch dichroic mirrors. The vertical beam is not divided since a retro-reflection configuration is applied on the vertical axis. Before entering through CF40 viewports into the main chamber, dichroic  $\lambda/4$  waveplates (provided by *Döhrer Elektrooptik GmbH*) impose the required circular polarization. The powers in each beam can be adjusted separately with the  $\lambda/2$  waveplates which are an important tool in the alignment of the molasses stage (see sec. 6.8.1).

The vertical beam is set up in a retro-reflection configuration because it follows the same beam path as the vertical imaging, see below in fig. 6.27. Therefore, it passes the imaging objective and is reflected out behind it by a movable 45° mirror. Next, it passes through a lens system and a  $\lambda/4$  wave plate before it hits a zero degree retro-reflection mirror. The combination of lens system and  $\lambda/4$  plate ensures that the retro-reflected MOT beam is re-collimated when entering the main chamber again. The stability of the flip mirror has been found to be crucial. A first version (*KSHM 65, Owis*) had to be dismissed as it experienced

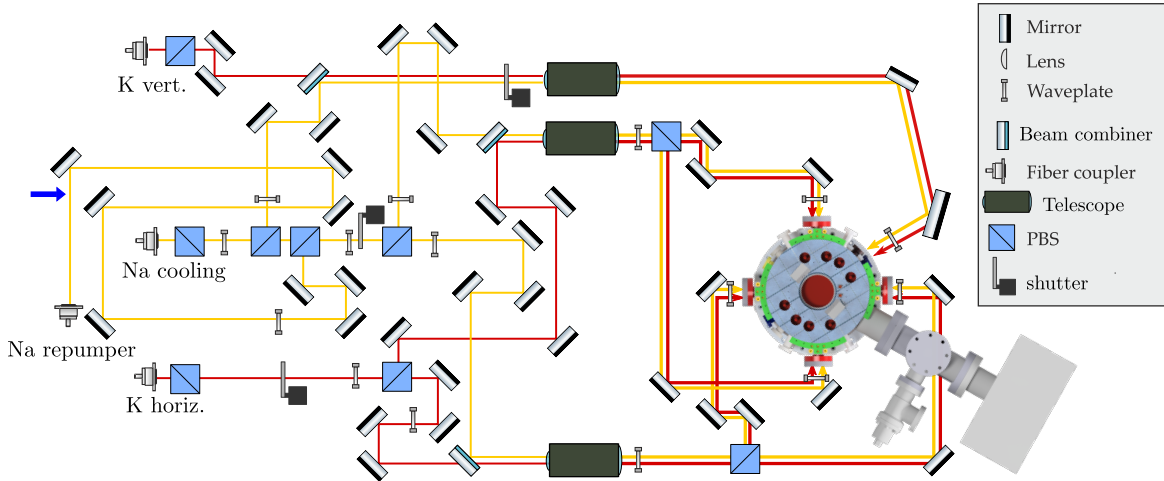


**Figure 6.23: Schematic of 3D MOT optics.** To account for a possible Dark-SPOT 3D MOT for sodium, the optics are set up to enable the 1:1 image of a point aperture (position indicated by blue arrow) inside the main chamber. Therefore, the sodium repumper beam is only present on the horizontal axis. The Dark-SPOT MOT was abandoned eventually (see sec. 6.7.2), the optical setup has been kept. For details see text.

instability in its rest position, thereby leading to a different MOT performance over the course of about ten experiment runs. The mirror mount has been exchanged by a version with a higher stability (*MFF102/M - Motorized Filter Flip Mount, Thorlabs Inc.*).

To prevent atom number fluctuations in the MOT, it is crucial to ensure that fluctuations in the polarization of MOT beams at the out-coupler do not translate into varying laser powers in the different MOT axes. In the experiment, oscillating atom numbers in the MOT were found and the period of the oscillation matched the air conditioning regulation cycle of the laboratory. The optical fibres guiding the laser light from the laser table to the experiment table, although being polarization maintaining, have been experiencing a polarization rotation due to the changing temperatures in the laboratory. The problem has been solved by adding a PBS directly behind the out-coupler. Thereby, the polarization fluctuations are translated into overall power fluctuations in the complete MOT but not into a fluctuation of the power in the different MOT axes against each other.

Since all atom and laser beams as well as the magnetic trap zero are aligned to the centre of the main chamber, the MOT has to be situated as close as possible to this geometrical point. Alignment of the MOT beams is therefore performed by first ensuring that the vertical beam passes through the centre of the main chamber. This is realised by monitoring the stray light of the vertical beam on the top and bottom vacuum window with cameras from two horizontal directions. Thereby, the beam can be moved to the centre of the windows. Next, the diameter of the horizontal beams is reduced to about a millimetre using irises. Then, the beams are aligned using customised caps on the CF40 viewports. Due to the geometry of the chamber, all MOT beams will now overlap in the centre of the chamber.

This geometric pre-alignment is followed by balancing the powers in the different MOT beams. The MOT positions can be shifted by different tuning knobs which are, however, all entangled with each other to a certain extend. For example, the powers in the MOT beams could be set to perfect 50:50 ratios on the counter-propagating beams. If the polarizations of all beams would be perfectly adjusted and if the beams would be perfectly overlaid with each other and the magnetic trap centre, this should lead to an optimal MOT. Unfortunately, there is a high chance that the polarizations will never be perfectly equal, since the light has to pass through six different viewports (one on each axis) which all might change the

polarization in a slightly different way. One can move the magnetic centre with the help of the compensation coils, balancing out uneven light pressures. This, however, leads to a difficulty in the subsequent molasses step when the magnetic field is reduced to zero and different light pressures accelerate the atoms. Furthermore, altering the beam alignment is entangled with the power balancing in the beams, as a misalignment can balance out too high a light pressure in a beam. For these reasons, the geometric alignment is performed as precise as possible and the polarizations in the beams are carefully adjusted. Thus, only the power balancing in the beams is left as a free parameter and is primarily used to optimise the MOT performance.

The potassium laser powers at the experiment table are 80 mW for the 3D cooler and 72 mW for the 3D repumper, of which 40 mW for the 3D cooler and 36 mW for the 3D repumper are distributed to the horizontal axes and the same amount to the vertical axis. For sodium, the powers in the MOT beams are 87 mW for the 3D cooler of which  $\sim 10$  mW are distributed to the vertical axis and the rest is divided among the horizontal axes. The 3D repumper has a total power of 11 mW and is only present on the horizontal axes.

### 6.7.1 Two-species 3D MOT

The use of two different atomic species in the same experiment imposes challenges in terms of optimisation of the trapping parameters. In some cases, trapping of two different elements in a combined MOT is impossible due to light-assisted collisions [147]. In this experiment, no major problems for dual-species MOT operation related to loss mechanisms stemming from light-assisted collisions have been observed. However, the parameters for optimal MOT performance have shown to be different for  $^{23}\text{Na}$  and  $^{39}\text{K}$ , rising the challenge of finding an optimal compromise. As a starting point, the MOT loading has been investigated for the two species separately. It has been found that due to the much higher flux of the Zeeman slower a  $^{23}\text{Na}$  MOT of up to  $3 \cdot 10^9$  atoms can be loaded in  $\sim 10$  s using a field gradient of 20.5 G/cm, see fig. 6.24 (b). On the other hand, the  $^{39}\text{K}$  MOT requires 20 s until fully loaded, then containing up to  $1.5 \cdot 10^8$  atoms for a field gradient of 4.8 G/cm, see fig. 6.24 (c). The difference in the optimal field gradients imposes the first necessity for a compromise.

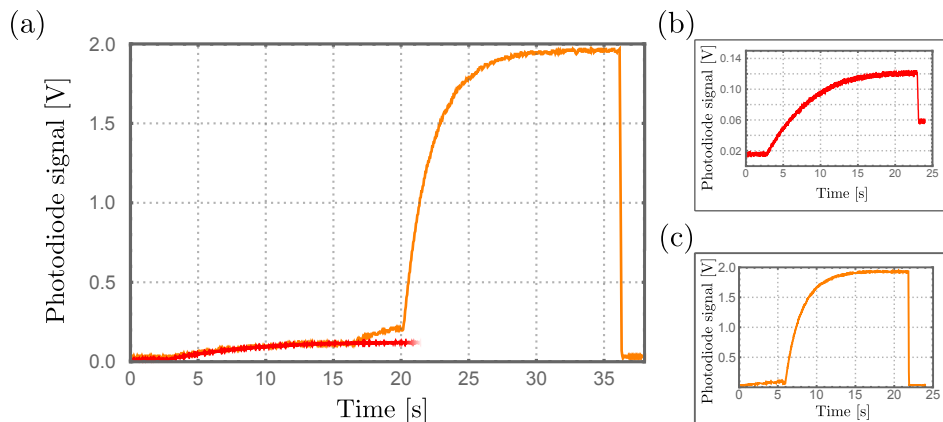


**Figure 6.24: Loading curves for MOTs.** The fluorescence light of the MOT is detected by a photodiode as a measure of the number of trapped atoms. In (a), the dual-species MOT operation is shown. The red graph indicates the fluorescence signal originating from the  $^{39}\text{K}$  MOT, the orange curve the signal from the  $^{23}\text{Na}$  MOT. The single-species operation is shown in (b) for  $^{39}\text{K}$  and in (c) for  $^{23}\text{Na}$ . The  $^{39}\text{K}$  MOT is saturated after  $\sim 18$  s, the  $^{23}\text{Na}$  MOT needs  $\sim 8$  s and is also significantly larger, indicating the much higher atom flux of the  $^{23}\text{Na}$  Zeeman slower in comparison to the  $^{39}\text{K}$  2D MOT. Fully loaded, the single-species sodium MOT contains up to  $3 \cdot 10^9$  atoms, the single-species potassium MOT up to  $1.5 \cdot 10^8$  atoms.

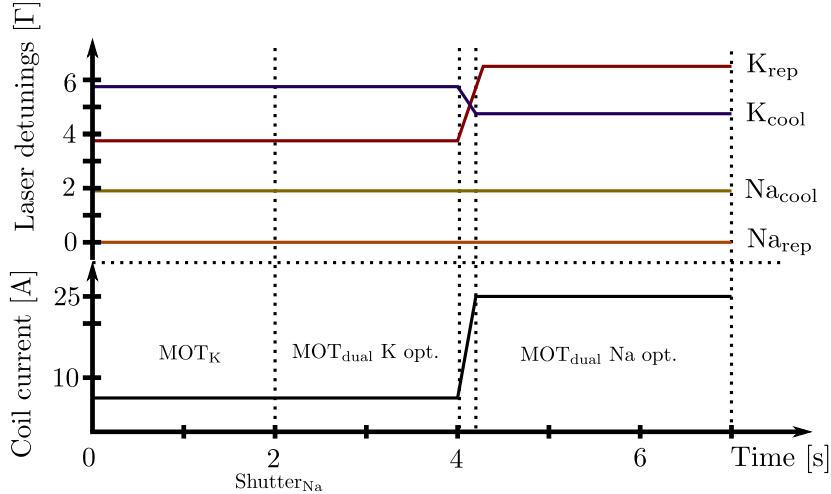


**Figure 6.25: Sequence of dual MOT loading.** The laser detunings from the respective atomic transitions (see sec. 6.4) are given in units of the natural linewidth  $\Gamma$  of the respective species. The pure potassium MOT loading time is adapted to the loading rate of the 2D MOT and can take up to 15 s. It is set to 2 s for this graph. After the pure potassium MOT phase, the atom shutter of the Zeeman slower is opened, thereby starting the dual MOT operation.

As in the following steps of the experiment sequence, cooling of the two species to quantum degeneracy is performed by sympathetically cooling  $^{39}\text{K}$  by  $^{23}\text{Na}$ , a configuration leading to a higher absolute number of  $^{23}\text{Na}$  in the MOT (and subsequently also in the magnetic trap, see sec. 6.8.2) is favourable. For this reason and because of the longer MOT loading times for  $^{39}\text{K}$ , the sequence implemented in the experiment is shown in fig. 6.25. First, a MOT of  $^{39}\text{K}$  is loaded for up to 15 s using the optimal magnetic field gradient for  $^{39}\text{K}$ . The atom shutter of the Zeeman slower is flipped after the potassium MOT is saturated, thereby starting the dual MOT loading. For  $\sim 2$  s, the dual MOT is loaded keeping the optimal configuration for potassium. The magnetic gradient is changed within 200 ms to the optimal  $^{23}\text{Na}$  MOT configuration and the  $^{23}\text{Na}$  MOT is loaded. It has been found that for the  $^{23}\text{Na}$  MOT loading times of  $\sim 8$  s, the  $^{39}\text{K}$  MOT degenerates significantly if the laser frequencies are not adjusted. The  $^{39}\text{K}$  laser frequencies are therefore changed to values which enhance the  $^{39}\text{K}$  MOT lifetime significantly (see fig. 6.25). Figure 6.24 (a) shows the combined MOT loading signal.

It has to be pointed out that the final figure of merit for the optimisation of the experiment sequence, including the experiment steps of MOT loading, optical molasses (see sec. 6.8.1) and magnetic trap loading (see sec. 6.8.2), is the number of atoms of both species at a sample temperature of  $\sim 50 \mu\text{K}$  in the magnetic trap (see sec. 6.10.1). Moreover, for the experiments performed to investigate Feshbach resonances in the  $^{23}\text{Na}+^{39}\text{K}$  mixture, the loading times of the MOTs are one tuning knob to adjust the minority and majority atom species (see chap. 7).

## 6.7.2 Dark-SPOT MOT vs. bright MOT

The somewhat complex beam paths described in the previous section originate from the idea of implementing a Dark-SPOT MOT [148]. For this configuration, a point aperture is placed in the beam path of the repumper and imaged onto the MOT region via an appropriate lens system. Due to the point aperture, a central spherical region inside the MOT is generated where no repumper is present. This leads to an accumulation of atoms in the  $f=1$  state in the centre of the MOT which is a dark state for the cooling laser light. With this technique, the light pressure limit of bright MOTs [149, 150] can be bypassed, leading to larger MOTs.

A Dark-SPOT MOT was implemented for  $^{23}\text{Na}$  at an early stage of the experiment by

inserting a point aperture into the horizontal MOT repumper beam and producing an 1:1 image of it at the place of the atomic sample, similar to the setup in [151]. The Dark-SPOT MOT was operated for a few month, leading to around  $1 \cdot 10^9$  trapped  $^{23}\text{Na}$  atoms. The precise placement of the point aperture and its imaging optics in combination with the telescopes used for beam enlargement proved to be critical. The Dark-SPOT was eventually abandoned due to its much larger alignment expenditure compared to a bright MOT which in this experiment can contain up to  $3 \cdot 10^9$  sodium atoms as seen in the previous section.

## 6.8 Optical pumping, molasses and magnetic trap

To overcome the limits related to Doppler temperature and light pressure in a MOT, the next step to reach quantum degeneracy is to transfer the atoms into a magnetic trap where they can be further cooled using evaporative cooling techniques (see sec. 6.10). While the trapping force of a MOT is independent on the Zeeman hyperfine states which the atoms are in, in a magnetic trap only the low-field seeking states will be captured. For the ground states of  $^{23}\text{Na}$  and  $^{39}\text{K}$ , these are  $|f = 1, m_f = -1\rangle$  and  $|f = 2, m_f = -2, -1\rangle$ . To prevent losses from spin-changing collisions inside the magnetic trap, it is favourable to trap both species in the same state. To transfer the atoms to the desired state, so-called *optical pumping* is performed, which will be described in the following. While trying to optically pump the potassium atoms to the  $f = 1$  state, the need for an additional experiment step became clear, as will be detailed in the following section. An optical molasses step has therefore been implemented in the experiment sequence and is explained in detail below. Finally, the magnetic trapping is described.

### 6.8.1 Optical pumping and optical molasses

Before setting up the appropriate experiment sequence, it has to be decided whether to trap the atoms in the  $|f = 1, m_f = -1\rangle$  or the  $|f = 2, m_f = -2\rangle$  Zeeman hyperfine state. Although choosing the  $f = 2$  state leads to a higher trap confinement, early attempts to evaporatively cool  $^{23}\text{Na}$  in the  $f = 2$  state inside a magnetic trap were discontinued as the  $f = 1$  state evaporation showed to be more robust [152]. With this knowledge in mind, also for the experiment sequence presented in this thesis the  $f = 1$  state is chosen for both atomic species.

Optimally, all atoms would be transferred into the chosen Zeeman hyperfine state. In principle, this can be achieved by spin polarization [10] for which a  $\sigma^-$ -polarized laser beam resonant on the  $m_f \rightarrow m_f - 1$  transition is applied together with a magnetic field to generate the appropriate quantization axis. Atoms scattering photons from that laser will accumulate in the  $f = 1$  Zeeman hyperfine state with the largest negative  $m_f$  component. While in theory an efficient method, it has been shown that such a polarizer only performs mediocre for  $^{23}\text{Na}$ , yielding conversion efficiencies of only 0.35 [153]. Only when applying high magnetic fields of 80 to 100 G, this value could be increased to 0.75 [154, 155]. In the experiment setup presented here bias fields of maximally 4.5 G can be generated by the compensation field coils (see sec. 6.5.1) and the maximal enhancement of atoms in the  $m_f = -1$  state has been a factor of 1.6 for  $^{23}\text{Na}$  compared to a sequence without a polarizing laser beam. Because of the high technical demands of a polarizer including very precise optical shutter timings and struggles with the magnetizability of the steel main chamber interfering with the required bias field axis, the polarizer was excluded and has not been used for the measurements presented in this thesis.

The alternative to a polarizer is to simply optically pump the atoms to the  $f = 1$  hyperfine state shortly before trapping them in the magnetic quadrupole field. This is achieved by ramping the magnetic field to zero and switching off the MOT repumper beams 250  $\mu\text{s}$

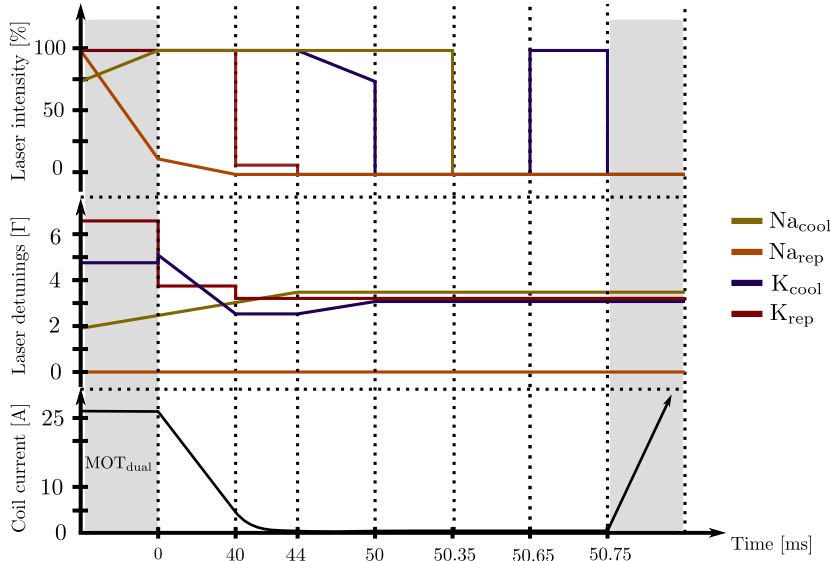


**Figure 6.26: Sequence for optical molasses.** After the dual-species MOT is loaded (first grey shaded area), the sequence for the optical molasses is performed by sweeping the magnetic field strength as well as the intensities and detunings of the sodium and potassium cooling and repumping lasers. The second grey shaded area indicates the start of the magnetic trap loading (see sec. 6.8.2). Note the changes in the time axis scaling.

before also switching off the cooling MOT beams, thereby transferring all atoms to the  $f = 1$  state (this is the scheme for  $^{23}\text{Na}$  but varies slightly for  $^{39}\text{K}$  as will be explained in the next paragraphs). As soon as the magnetic trapping potential introduces a new quantization axis, the atoms will be projected onto the Zeeman hyperfine states. Assuming an equal population of all three states of the  $f = 1$  hyperfine level, this should lead to a trapping of up to one third of the atoms initially loaded to the MOT.

For  $^{23}\text{Na}$ , the scheme is as explained above, leading to a transfer efficiency of 26 to 31 % of the atoms to the magnetic quadrupole trap (after optimizing the magnetic trapping as is explained in sec. 6.8.2). To confirm that the atoms are in the  $f = 1$  state state-selective absorption imaging of the atoms inside the trap is performed.<sup>3</sup>

For  $^{39}\text{K}$ , however, it was not possible to transfer the atoms in the same manner to the  $f = 1$  state, most likely because residual magnetic fields disturbed the optical pumping. A comparison of the sequence for the magnetically trapping of  $f = 1$   $^{39}\text{K}$  atoms with the sequences presented in the literature indicated that the optical pumping should be performed at the end of an optical molasses stage when all magnetic fields are clearly damped out [156]. Following the sequence presented in [156], *polarization gradient cooling*, also known as optical molasses [157, 158], has been implemented in the experiment sequence. Thereby, after releasing the atoms from the 3D MOT, both species are cooled by the optical molasses step before they are pumped to the  $f = 1$  hyperfine state.

The first step for setting up the optical molasses has been to align and balance the MOT laser beams in a way that they allow for optical molasses. For this, no mismatch in the light pressures in any of the six spacial directions has to be present as otherwise the atoms will be accelerated away from the centre of the chamber. Moreover, to prepare optimal conditions for loading of the atoms into the magnetic trap, the molasses position should overlap with the centre of the magnetic trap. To assure this, the position of the magnetic trap centre has been determined by imaging a strongly compressed MOT where the dominating force dictating

<sup>3</sup> At first, the atoms were imaged inside the magnetic trap by fluorescence imaging which is not state selective and thereby led to confusions about the trapped hyperfine state. This in turn hindered the MW evaporation.

the MOT position is given by the magnetic field. The molasses has then been geometrically moved to this position. Optimally, the MOT is already positioned at the chamber centre due to the alignment procedure described in sec. 6.7. Since in an optical molasses the position of the atoms in space is only supported by the light pressures, the balancing of those is critical. To achieve an optimal performance, the magnetic field of the MOT is ramped down within a few seconds to an ever lower value while the position of the atomic sample is balanced by carefully adjusting the powers in every of the three MOT beam pairs. This is done by turning a  $\lambda/2$  wave plate for each beam pair which is mounted in a precision rotation mount (*CRM1P/M Precision Cage Rotation Mount, Thorlabs Inc.*).

In fig. 6.26, the dual-species molasses sequence is shown. The sequence implemented in this experiment differs from the textbook style e.g. in that the magnetic fields are not switched off instantaneously but ramped down. The sequence has been found empirically by adjusting the different parameters of the molasses step while monitoring the PSD of the magnetically trapped atomic samples. Sub-Doppler temperatures measured by time of flight (TOF) expansions have been found to be  $53 \mu\text{K}$  for  $^{23}\text{Na}$  and  $106 \mu\text{K}$  for  $^{39}\text{K}$ . The temperatures are similar or slightly higher than reported in other publications, being e.g.  $56 \mu\text{K}$  for  $^{23}\text{Na}$  in [159] and  $25 \mu\text{K}$  for  $^{39}\text{K}$  in [160].

Moreover, since the atomic samples can be balanced in space during the molasses for several milliseconds at zero magnetic field, all residual magnetic fields are damped out. Thereby, the  $^{39}\text{K}$  atoms can be transferred to the  $f = 1$  hyperfine state by a  $100 \mu\text{s}$  long pulse of cooling light directly before the magnetic trap gradient is ramped up. This yields exclusively  $f = 1$   $^{39}\text{K}$  atoms in the magnetic trap.

### 6.8.2 Magnetic trap

The magnetic quadrupole field is produced by the Feshbach coils described in sec. 6.5.1. The atoms are trapped after the molasses step by ramping the current flowing through the coils to  $160 \text{ A}$  (inducing a gradient of  $128 \text{ G/cm}$ ) as fast as possible. This is achieved by jumping to the set current without setting any ramp time by the experiment control. Thereby the set current is solely regulated by the internal PI controller of the power supplies. As can be seen from fig. 6.20 at point (A), this method leads to an overshooting of the coil currents. After the first step, the currents are ramped to the final value of  $270 \text{ A}$  (corresponding to  $216 \text{ G/cm}$ ) adiabatically within  $60 \text{ ms}$ . Although the first jump is quite drastic, this method leads to the highest atom numbers in the magnetic trap.<sup>4</sup>

With the sequence outlined here,  $\sim 1 \cdot 10^9$   $^{23}\text{Na}$  and on the order of  $10^6$  to  $10^7$   $^{39}\text{K}$  atoms, both in the  $|f = 1, m_f = -1\rangle$  Zeeman hyperfine state, are magnetically trapped at initial temperatures on the order of  $100$  to  $200 \mu\text{K}$ .<sup>5</sup>

## 6.9 Imaging setup

Imaging of atoms and molecules can be divided into two major branches. The first is the destructive imaging, which can either use fluorescence or absorption of light to produce images of the investigated sample. The second is non-destructive imaging. The latter type of imaging will become important for future experiments planned with the apparatus described here (see [77]). All measurements in this work can be done using absorption imaging without loss of any information. The procedure of obtaining information about the

---

<sup>4</sup>After the measurements presented in this thesis had been completed, the setup has been upgraded with a new set of Feshbach coils (see sec. 6.5.1) and the complete sequence has been revised, leading to a lower first trapping gradient of currently  $80 \text{ G/cm}$ .

<sup>5</sup>The determination of the initial temperatures of the atomic samples inside the trap is difficult because of the limitations on imaging large thermal clouds of hot atoms in this experiment setup.

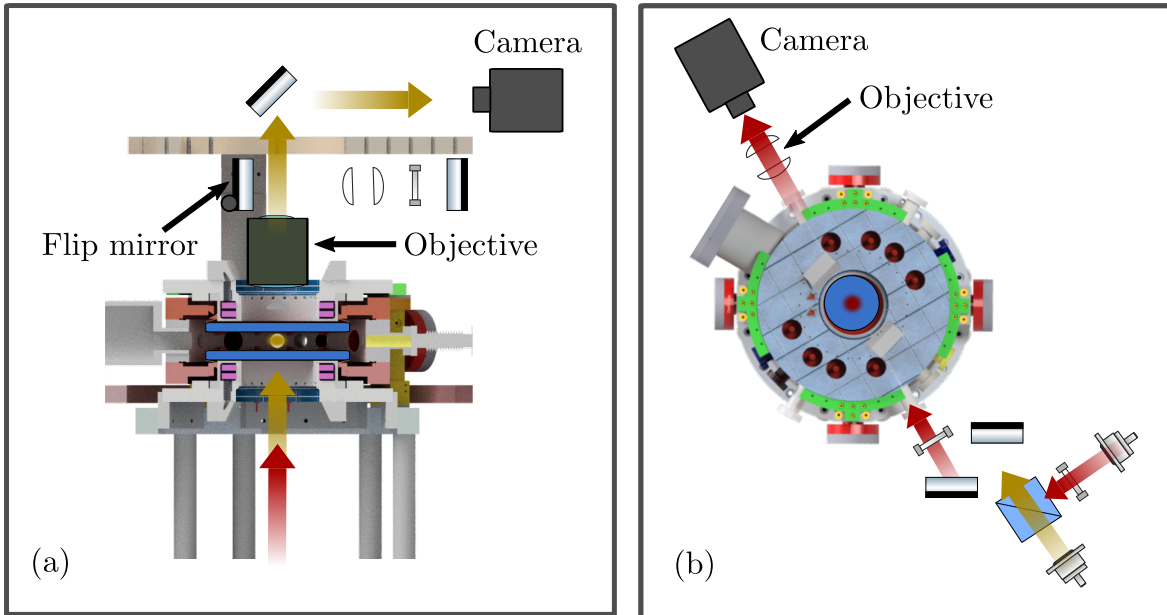


**Figure 6.27: Schematics of the imaging setups.** Absorption imaging at the main chamber can be performed along two spacial axis, the vertical (a) and on one horizontal axis (b). On both axis, sodium as well as potassium samples can be imaged. On the vertical axis, a flip mirror which is used for the retro-reflection of the vertical 3D MOT beam can be toggled out of the imaging beam path.

performed experiments is identical for all measurements presented in this thesis: An atomic sample (of either a single or both species at the same time) is prepared, following a set of experiment sequence steps and then imaged. Since the sample will be destroyed during imaging, a new sample is prepared in the next experiment run. During these cycles, the parameter of interest (e.g. a magnetic field value) is changed for each run of the experiment. The influence of this change on the atomic sample is imprinted in the recorded pictures.

The used destructive imaging techniques will be discussed in detail in this section. In the experiment, pictures can be taken along a horizontal as well as along the vertical axis of the main chamber. The imaging paths are shown in fig. 6.27. The pictures taken on the different axis are evaluated using a picture-handling software programmed in *LabVIEW* by A. Zenesini.

### 6.9.1 Theory of imaging atoms

In the following, a brief overview over the theory behind fluorescence and absorption imaging is presented.

#### Fluorescence imaging

Fluorescence imaging detects the photons absorbed and then re-emitted by the atoms. Only those photons will be registered which are emitted in the direction of the detection setup, given by the solid angle  $\Omega$  of the surface of the imaging lens. The amount of scattered photons depends on the total photon scattering rate  $\gamma_{scat}$  of the cycling transition(s) which are used to excite the atoms. (Due to the not completely closed transitions in  $^{23}\text{Na}$  and  $^{39}\text{K}$  these transitions always are covered by a combination of two laser frequencies, named cooling and repumping transition in context of the MOT, see sec. 6.7.) The signal response of a detector on a photon, for a photodiode given by the output voltage  $U[\text{V}]$ , is depending on the photon energy  $\hbar\omega$ , on the sensitivity of the detector for that specific wavelength  $S(\omega)$  and

on its gain  $G$  set. To account for possible stray light, a background value  $U_{bg}[V]$ , recorded without the atomic sample, has to be subtracted. In total, the atom number detected by fluorescence is given by:

$$N = (U - U_{bg}) \frac{4\pi}{\Omega} \frac{1}{\gamma_{scat.} \hbar\omega S(\omega) G} . \quad (6.19)$$

Fluorescence imaging is a very accurate method to determine exact atom numbers up to single atom precision [161]. It also proved superior for single-site resolved atom imaging in optical lattices [18, 162]. However, a high level of control over and detailed knowledge of the imaging parameters is required. This rendered such precise Fluorescence imaging impractical for the current status of the experiment setup [36].

### Absorption imaging

Absorption imaging uses the shadow cast when light is shone through an atomic sample as the signal to gather information about the atoms. The process behind this, is the same as in fluorescence imaging. However, absorption imaging does not use the photons scattered towards the detector but instead the shadow produced by the photons scattered away from it. This normally leads to a higher contrast which is why absorption imaging is widely used in cold atom experiments. Absorption images can be taken of trapped samples or in TOF.

While passing through the atomic sample, the intensity of the light  $I_0(x, z)$  is modified according to Lambert-Beer's law as

$$I(x, z) = I_0(x, z) e^{-OCD(x, z)} \quad (6.20)$$

with the *optical column density* given by

$$OCD(x, z) = \frac{\sigma_0}{2} \tilde{n}(x, z) . \quad (6.21)$$

Here,  $\sigma_0 = \hbar\omega\Gamma/(2I_{sat})$  is the resonant cross section, with  $\Gamma$  being the natural line width of the transition. Tabulated values for  $\sigma_0$  can be found in [86] for  $^{39}\text{K}$  and in [85] for  $^{23}\text{Na}$ . For obtaining the correct atom number, it is important that the sample is dilute enough to not absorb all of the imaging light photons. Such a situation can occur for very dense samples of cold atoms, especially for BECs. In that case, either a longer TOF has to be performed (so that the sample becomes more dilute), a higher imaging light power has to be shone in (which can lead to unwanted heating of the imaged sample), or the imaging wavelength has to be tuned off resonance on purpose (which then demands an adjustment of the scattering rate). If the imaging light is detuned by  $\delta$ , the scattering cross section can be calculated from

$$\sigma(\delta) = \frac{3\lambda^2}{2\pi} \frac{f}{1 + fI/I_{sat} + 4\delta^2/\Gamma^2} , \quad (6.22)$$

where  $\lambda$  is the actual imaging light wavelength,  $I_{sat}$  the saturation intensity and  $f$  a constant which depends on the Clebsh-Gordon coefficients of the optical transition (for details, see [80, 163]). For very dense clouds, the formula might have to be further modified, see [164].

The so-called *column density*  $\tilde{n}$ , used in eq. 6.21, is given by the integration of the density distribution of the sample  $n(x, y, z)$  along the imaging axis (here  $y$ ):

$$\tilde{n}(x, z) = \int dy n(x, y, z) . \quad (6.23)$$

In the experiment, the absorption feature is detected using a charge-coupled device (CCD) camera. The pictures are a measurement of the density distribution of the sample,

integrated along the imaging beam propagation axis and thereby proportional to the column density. The imaging path can inflict distortions, such as diffraction patterns, on the imaging light. A higher contrast of the image can be achieved when dividing the picture taken from the atomic sample by a picture containing only the imaging light (here called background image,  $I_{bg}$ ). To enhance the quality of the measurement further, a so-called dark image can be subtracted from both pictures. The dark image is recorded with the CCD completely covered (normally by the camera shutter). It therefore accounts for possible bright pixels on the CCD or any other residual noise. From the three recorded pictures, the optical column density can be derived by:

$$OCD(x, z) = \ln\left(\frac{I_{bg}(x, z) - I_{dark}(x, z)}{I_{atoms}(x, z) - I_{dark}(x, z)}\right) . \quad (6.24)$$

To calculate the number of atoms, one has to sum the OCDs detected on every single pixel of the CCD ( $(x_i, y_j)$ ), divide by the scattering cross section and multiply the result by the area in space  $\Delta_x \Delta_z$  which was imaged onto the single pixel:

$$N = \frac{\Delta_x \Delta_z}{\sigma_0} \sum_i \sum_j OCD(x_i, y_j) . \quad (6.25)$$

The area which is actually imaged onto a single CCD pixel depends on the magnification of the imaging system. Although this magnification is in principle given by the used set of lenses (or the objective), imperfections in the alignment can alter it. A precise way to determine the actual magnification is to observe atomic samples which fall under the influence of gravity for a variable time. By fitting:

$$z_{atoms}(t) = z_{atoms}(0) + A \cdot \frac{1}{2} g t^2 \quad (6.26)$$

to the data, the magnification can be deduced from the fit parameter  $A$  by comparing the pixel size derived from the fit with the actual size of the camera pixels.

### 6.9.2 Imaging on horizontal axes

In the experiment setup presented in this thesis, the detection of fluorescence is used to monitor the atom number in the MOT. Its fluorescence is imaged onto a photodiode (*PDA36A-EC*, *Thorlabs*). The voltage output is monitored with an oscilloscope.

The setup for imaging on the horizontal axis is shown in fig 6.27 (b). For fluorescence imaging, the MOT laser beams can be used. For the absorption imaging, the collimated light for potassium and sodium is combined, using a PBS. The light is then circularly polarized, using a quarter wave plate (which is optimized for the sodium imaging) and aligned onto the atoms with two mirrors. The diameters of the imaging beams are approximately 14 mm and the imaging light power is  $\approx 0.2$  mW for sodium as well as for potassium (see tab. 6.2 and tab. 6.4).

The imaging transitions for sodium and potassium are illustrated in fig. 6.12 and fig. 6.14 respectively. Imaging at zero magnetic field strength is performed on the  $f = 2 \rightarrow f' = 3$  transition. Since the atoms are magnetically trapped in the  $f = 1, m_f = -1$  state, this means that to be imaged, they first have to be optically pumped into the  $f = 2$  state. For this purpose, a pump pulse of  $\approx 300 \mu s$  with  $\approx 0.2$  mW is applied on the  $f = 1 \rightarrow f' = 2$  transition, before the imaging light is shone in for  $\approx 100 \mu s$  (compare with the "F = 2 imaging" schemes in fig. 6.12 and fig. 6.14). It has been found that too long pump pulses can heat the sample. For TOF imaging, this can lead to a wrong deduced sample temperature. For sodium and potassium, pure "F = 1 imaging" (meaning imaging directly on the  $f = 1 \rightarrow f' = 2$  transition) has also been implemented in the experiment. Since it is leading to pictures with

a slightly worse quality, usually the " $F = 2$  imaging" is used. This is except for state selective measurements like the magnetic field calibration measurement described in sec. 7.4.1.

The light for both, fluorescence as well as absorption imaging, is captured by a pair of 2 inch anti-reflection coated achromatic lenses with 200 mm and 400 mm focal length. They direct the light onto a CCD camera (*Andor iXon<sup>EM+</sup> 885, Andor Technology Ltd*). The CCD has a pixel size of  $8 \times 8 \mu\text{m}^2$ . In fig. 6.28, a TOF measurement, performed with a BEC of  $^{23}\text{Na}$ , is shown. With the obtained data, the horizontal imaging magnification is calibrated, following the method outlined in sec. 6.9.1. The magnification is found to be  $M_{\text{horz.}} = 0.57$ , yielding a value for  $\Delta_x = \Delta_y$  of  $14.02 \mu\text{m}/\text{pixel}$ .

The pictures are transferred from the camera to the PC which performs the image handling and executes the *LabVIEW* program for the picture analysis. For absorption imaging, always a background picture is recorded and the software also allows for the subtraction of a dark background image. The readout and processing time per picture is about 40 ms. Thus, two subsequent pictures in a dual-species experiment have to be spaced in time by at least 40 ms. Normally, this does not impose problems for the measurements performed in this work.

It has been found that with the chosen illumination times not always all atoms are removed if in-trap images are taken. This leads to a wrong atom number count since the remaining trapped atoms are present in the background picture and are thereby subtracted from the first image. To circumvent this issue, an additional flash of resonant light is applied for 40 ms in between imaging the atoms and taking the background picture. With this method, remaining atoms are reliably removed from the trap. This issue is absent in TOF images since during the 40 ms in between the two pictures, the atoms already have left the imaging region.

In the experiments on double BECs, described in sec. 8.2, a duration of 40 ms between two images is impractical. Both species have to be imaged in TOF and leave the imaging region already after  $\sim 25$  ms. For that reason, a fast-kinetic mode has been implemented by A. Zenesini which allows to take two pictures with a duration of only 3 ms in between. In this mode, only a section of 350 pixel of the CCD is used to record the image. The rest of the chip is used as buffer. By shifting the first image to this buffer in  $\sim 3$  ms before taking the second picture, the 40 ms read-out time is eliminated. However, by using the fast-kinetic mode, at least half of the CCD has to be blocked from the imaging light to serve as the image buffer. Hence, the usable size of the CCD is reduced. Since the BECs are reasonably small in size for the set magnification, the reduced active pixel area does not obstruct the measurements. The two atom clouds are imaged with  $\sim 3$  ms in between the two images and the two pictures which have been stored on the CCD are then read out together. After the

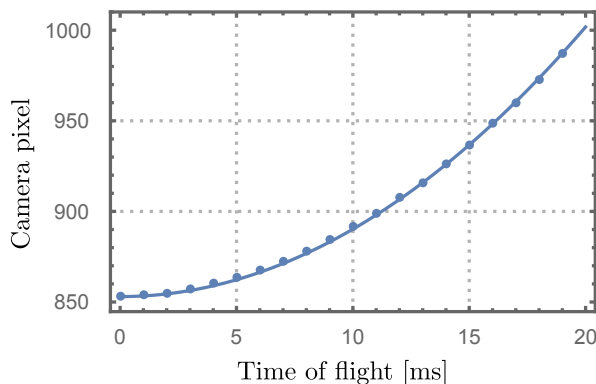


**Figure 6.28: Determination of the magnification of the imaging setup.** The vertical position of a sodium BEC is recorded as a function of the time of free fall. By fitting eq. 6.26 to the data, the magnification can be calculated.

usual 40 ms read-out time, the two background images are recorded, one for each species.

### Determining the temperature of an ensemble

The knowledge of the temperature of an ensemble is critical. It is required for the evaluation of BECs (see sec. 5.1) and is needed to evaluate scattering processes of atoms and molecules because it inherits information on the correct termination term in a partial wave expansion (see sec. 3.2.1). A common method to obtain the temperature of an ensemble is to release the sample from its trapping potential and image the cloud expansion in TOF. By assuming a harmonic trap confinement, the temperature can be deduced from the expansion in any of the three spacial directions using the formula:

$$\sigma_i(t) = \sqrt{\sigma_i(0)^2 + \frac{k_B T}{m} t^2} , \quad (6.27)$$

where  $\sigma_i(t)$  is the time-dependent width of the Gaussian density distribution in direction  $i = x, y, z$ ,  $\sigma_i(0)$  is the initial width in the trap,  $k_B$  is the Boltzmann constant,  $m$  the mass of the particles of the ensemble and  $T$  is the temperature.

### *In-situ* and TOF imaging

*In-situ* imaging, meaning imaging of the atoms inside a trapping potential is possible in the experiment for both species in the magnetic as well as in the optical dipole trap. However, some restrictions have been found for this method. Sodium pictures can be recorded for magnetically trapped atoms at all magnetic field strength used during the experiments and also for evaporated as well as not evaporated samples. However, an absorption image of potassium only yields a consistent sample size if the ensemble has been evaporatively cooled (see sec. 6.10.4).

To deduce the temperature of sodium in trap, a factor to convert the size of the trapped sample to temperature has been derived. It has been found to be  $0.145 \mu\text{K}/\mu\text{m}$ , using the formulas given in [165] (for details on the derivation, see [36]). The in-trap atom number calculated by the imaging software needs to be corrected by a factor of 3–3.7 with respect to TOF images. The factor has been determined experimentally by comparing the atom numbers in trap and in TOF for various sample temperatures. With the well known formula (see eq. 5.2), the phase space density can be calculated from the images recorded *in-situ*.

The deduction of atom numbers from TOF images does not require additional scaling factors. Since the pictures are taken without any trapping potentials, those potentials cannot interfere with the imaging process e.g. by shifting the transition frequencies. However, as described in sec. 6.5.2, the magnetic fields cannot be switched off arbitrarily fast and it has been found that the required slow ramp down of the fields acts as an adiabatic cooling. Thus, the temperatures deduced from a subsequent TOF yield lower temperatures than in-trap measurements.

Especially for optimisation of the microwave evaporation (see sec. 6.10.1), a time efficient method is to deduce the PSD of both species in the same experiment run. Sodium atom numbers and temperatures are calculated from pictures taken inside the magnetic trap at the end of the forced evaporation. The information about the potassium sample is then derived from TOF images taken after switching off the magnetic fields.

Images recorded in the cODT are usually inferior to TOF images. This is partially due to the much smaller size of the trapped atom cloud, which is therefore imaged onto fewer camera pixels. This makes precise atom number and size determination more error-prone. The inferiority of the images recorded in the cODT can also be partially attributed to the AC Stark shift [166] in combination with the Gaussian intensity profile of the optical trapping potential.

### High-field imaging

For the investigation of physical effects at high magnetic fields, it can be beneficial to record the images at magnetic fields close to or even exactly on that high field value. In the case of the Feshbach resonance scans performed during this work, high-field imaging becomes important if several resonances have to be crossed from zero magnetic field to the resonance of interest (see sec. 7.4.4). Hence, high-field imaging for  $^{39}\text{K}$  has been implemented in the setup.

The term high-field refers to a magnetic field strength for which potassium is in the Paschen-Back regime of the hyperfine structure. For potassium, this magnetic field starts at  $\sim 200\text{ G}$  [136]. As explained in sec. 2.1.1, in the Paschen-Back regime the total spin of the electron  $m_j$  and the spin of the core  $m_i$  couple directly to the external magnetic field and  $f$  and  $m_f$  are no longer good quantum numbers. Due to the selection rule  $\Delta m_i = 0$ , it is always possible to find a transition with  $\Delta m_j = +1$  or  $\Delta m_j = -1$  on the potassium D2 line, which serves as closed imaging transition. As an example, consider the imaging transitions for the  $|f = 1, m_f = m_f\rangle_K$  states with  $m_f = -1, 0, 1$ . As shown in fig. 6.14, these Zeeman states go over into  $|f = 1, m_f = 1\rangle_K \rightarrow |m_j = -1/2, m_i = 3/2\rangle_{K'} |f = 1, m_f = 0\rangle_K \rightarrow |m_j = -1/2, m_i = 1/2\rangle_K$  and  $|f = 1, m_f = -1\rangle_K \rightarrow |m_j = -1/2, m_i = -1/2\rangle_{K'}$ , since the coupling of  $m_j$  to the magnetic field leads to the larger energy splitting. For the case of imaging on the  $f = 1, m_f = -1 \rightarrow f' = 2, m_f = -2$  transition (arrow named "High-field imaging" in fig. 6.14), which is a transition with  $\Delta m_j = -1$ , one finds that on the D2 line always only one transition can be found and for this transition only one decay channel exists. In the example,  $\Delta m_i = 0$  and  $\Delta m_j = -1$  for  $|f = 1, m_f = -1\rangle_K$  (or in terms of  $m_j$  and  $m_i$ ,  $|m_j = -1/2, m_i = -1/2\rangle_K$ ). Hence, the only possible transition is  $|m_j = -1/2, m_i = -1/2\rangle_{K,1/2S} \rightarrow |m_j = -3/2, m_i = -1/2\rangle_{K,3/2P}$ . For the decay also only  $\Delta m_i = 0$  and  $\Delta m_j = \pm 1$  are allowed, but  $\Delta m_j = -1$  would lead to  $m_j = -5/2$  and no such state exists. The only other possible decay channel is given for  $\Delta m_j = 1$ , but since  $\Delta m_i = 0$ , the atom can only fall back into  $f = 1, m_f = -1$ . Therefore, the discussed case (and all other possible optical transitions) is a closed transition. In the experiment, high-field imaging needs only one imaging frequency, since no repumper has to address possible dark states.

For the implemented potassium high-field imaging, the cooler laser of the 2D MOT, from which also the zero-field absorption imaging is derived, is shifted in frequency to match the imaging transition at the investigated magnetic field strength. Due to the offset-lock technique applied in the potassium laser system (see sec. 6.4.2), the frequency of the cooler can be shifted by up to 600 MHz without complications since only the reverence frequency, which is provided by the frequency generator, is set to the new appropriate value. Because the frequency generator is controlled via VISA commands (see sec. 6.3), this frequency shift is easily implemented into the experiment sequence. Since the VISA command needs some time to be processed, the new frequency for high-field imaging is set several seconds before the first image is taken with it.

The exact atom number determination is difficult for high field imaging. To get a conservative estimate, high field images have been taken for several experiment runs at different magnetic fields and compared with zero-field imaging for the same experiment sequence. With this method, a correction factor of  $\sim 1/2$  has been derived, meaning that the deduced high-field atom number is by a factor of two too small.

#### 6.9.3 Imaging on the vertical axis

Due to the much larger diameter of the horizontal vacuum windows and their closer spacing of only 22 mm (see [77]), a much higher magnification is possible. This is because magnification is ultimately limited by the numerical aperture (NA) of the imaging system, which is

related to the diameter of the lens  $D$  and their distance to the object  $f$  by:

$$NA \propto \frac{D}{2f} . \quad (6.28)$$

The main chamber has been designed to ultimately enable single-site resolution in an optical lattice of  $(1064/2)$  nm lattice spacing, as is described in detail in [77]. For the measurements presented in this work, a simpler objective composed of two lenses, as shown in fig. 6.27(a), is used. The magnification of this system is  $M_{vert.} = 10.33$ . The alignment of the focus has been performed by imaging a BEC of sodium atoms inside the cODT. As also shown in fig. 6.27(a), the atoms are imaged with a CCD Camera (*Andor iXon Ultra 888, ANDOR Oxford Instruments*) mounted above the main chamber. For absorption imaging, the vertical beams of the sodium and potassium MOT are used which are tuned in power and frequency using AOMs. Additionally, the horizontal MOT beams have to be blocked, using mechanical shutters as depicted in fig. 6.23. Moreover, as described in sec. 6.7, the vertical MOT beams are retro-reflected after passing the objective. To gain optical access to the camera, the mirror which guides the MOT light onto the retro-reflection mirror can be toggled out of the way.

Imaging on the vertical axis is used for alignment of the blue plug (BP) and the cODTs (see sec. 6.10.3 and sec. 6.11.2) as well as for imaging the BECs presented in sec. 8.3. Due to its much higher resolution, it will also become useful for future experiments with optical lattices, as sketched in the outlook in sec. 9.3.

## 6.10 Evaporation in the magnetic trap and blue plug

Evaporative cooling of thermal samples in magnetic traps [167–169] is a widely used tool to efficiently increase the PSD of an atomic sample by more than six orders of magnitude. The first BECs were realized using this technique [8–10].

The main idea is to reduce the depth of the trapping potential using either MW or RF radiation in a way so that the hottest atoms will leave the trap. They carry away more than the average kinetic energy and rethermalization of the remaining atoms (in on average 2.7 collisions [170]) leads to a decrease in the overall temperature of the sample [171, 172]. This cooling has to be performed in the form of so-called *run-away evaporation*, where the elastic collision rate  $\Gamma_{el}$  has to stay large enough during the complete evaporation to maintain rethermalization. It also always has to be much larger than the vacuum background scattering length, since scattering with the background gas will remove atoms from the ensemble without temperature selectivity. Since  $\Gamma_{el} \propto N/T$  (for a harmonic trap) [173], where  $N$  is the particle number of the ensemble and  $T$  its mean temperature, one has to "lose less atoms than losing temperature", meaning that the PSD of the sample always rises. Since it also holds that  $\Gamma_{el} \propto \sqrt{T}$ , this generally means that a frequency sweep of a forced evaporation will have to slow down the deeper the potential is cut (see also next section).

Figure 6.29 shows the magnetically trapped  $|f = 1, m_f = -1\rangle$  Zeeman level of  $^{23}\text{Na}$  together with the three states of the  $f = 2$  manifold which can be coupled by electromagnetic radiation inside the spatially dependent magnetic field of a quadrupole trap. The energy difference of the  $^{23}\text{Na}$   $3^2\text{S}_{1/2}$  ground-state hyperfine structure of 1771.626 MHz [85] is subtracted and a MW field of 8 MHz is added corresponding approximately to the end of the MW evaporation ramp (above the trap bottom, see below) performed in the experiment sequence. In a classical picture, the crossing of two of the levels marks the magnetic field strength at which a transition between the two levels is resonant for the applied MW radiation (which is 1771.626 + 8 MHz in the case shown in fig. 6.29). Only atoms whose internal energy is high enough will be able to climb the magnetic trapping potential far enough to reach this resonance condition. As soon as the resonance condition is fulfilled, the atoms are

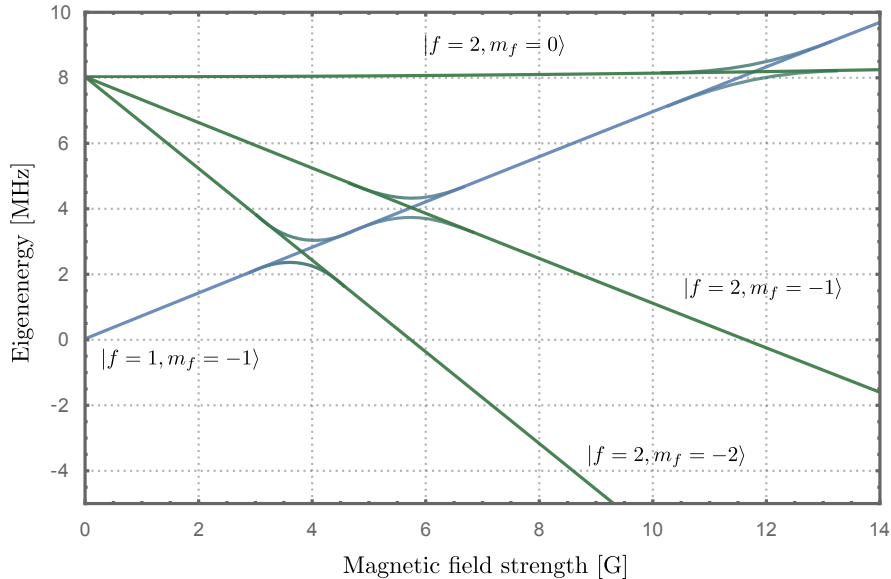


**Figure 6.29: MW transfer scheme.** Shown are eigenenergies of Zeeman states of the ground state hyperfine structure of  $^{23}\text{Na}$  (blue and green lines). The hyperfine splitting has been removed and a MW frequency of 8 MHz above trap bottom has been added. The trap bottom of the magnetic trap represents the zero energy of the  $|f = 1, m_f = -1\rangle$  state. Dressed states are schematically indicated by avoided crossings between the Zeeman states.

transferred to the not trapped Zeeman level of the  $f = 2$  state and thereby get lost from the trap. Hence, for the case shown in fig. 6.29, only the atoms with an internal energy smaller than  $\sim 2.25$  MHz remain trapped.

The process can also be seen in a dressed state picture, where the MW radiation leads to avoided crossings between the different levels. An atom in the lowest state, moving adiabatically about the crossing, will be transferred to a  $f = 2$  state and will get lost from the trap. This is indicated in fig. 6.29 by the bended lines, where the width of the splitting is given in the experiment by the Rabi frequency which is proportional to the MW power. This in turns means that the MW power has to be large enough to avoid that the atoms can diabatically move across the avoided crossings without changing their Zeeman hyperfine state.

By continuously sweeping the MW frequency towards resonance at zero magnetic field strength, the trapping potential is effectively lowered ever further, thereby leading to an ever colder ensemble. The efficiency of the overall evaporation process can be quantified by an efficiency parameter  $D$ :

$$D(t) = -\frac{d \log (PSD(t))}{d \log (N(t))} \quad (6.29)$$

with  $N$  being the remaining atom number of the ensemble [36, 174].

### 6.10.1 RF and MW evaporation

As discussed above, forced evaporation can be performed by applying either RF or MW radiation. In the first case, coupling to the Zeeman levels of a single hyperfine state occurs and in the second case also the hyperfine state of the atom changes when it traverses an avoided crossing.

### RF evaporation

radio frequency evaporation (RF evaporation) of magnetically trapped sodium was successfully performed in the experiment [77]. However, because  $^{23}\text{Na}$  and  $^{39}\text{K}$  have the same g-factors, a RF evaporation is not species-selective and leads to an equal reduction of the trapping potential for both species. Due to the large sodium atom numbers in the MOT and thereby high atom numbers of sodium in the magnetic trap compared to potassium, an evaporation method which only evaporates sodium and cools the potassium by means of elastic collisions is beneficial for the experiment setup presented in this thesis. The process of sympathetic cooling will be discussed in sec. 6.10.4, but it shall be mentioned already here that using MW radiation on the hyperfine transition of  $^{23}\text{Na}$  does not couple to  $^{39}\text{K}$  which enables a selective evaporation of sodium. For this reason, RF evaporation has been abandoned and microwave frequency evaporation (MW evaporation) has been implemented in the setup.

### MW evaporation

The frequency sweeps are designed by using a *Mathematica* script which splits continuous linear ramps into steps of constant frequencies with dwell times of around 18.5 ms. These digitalized ramps can be interpreted and output by the used function generator (*SMB100A*, *Rhode & Schwarz*). The ramp data are transferred to the function generator via VISA commands. Since the transfer of the VISA-string takes around 2 – 3 s, it is executed during the MOT-loading phase of the experiment sequence. The start of the ramp is triggered by a TTL signal which is sent from the experiment control unit to the frequency generator. To efficiently evaporate, it is mandatory to have a sufficient MW power at the place

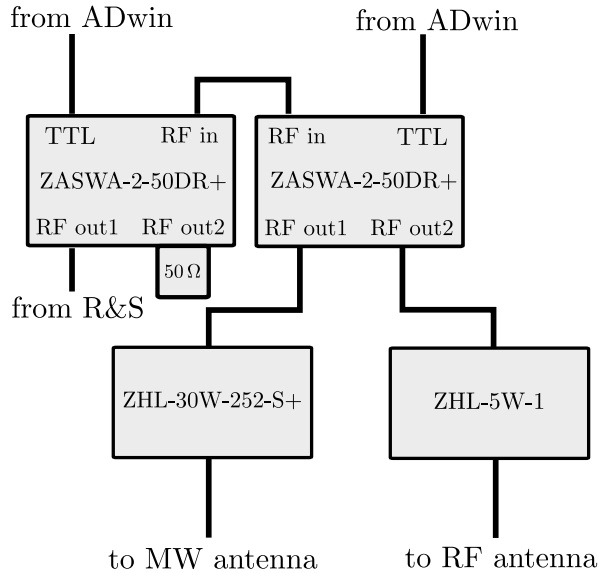


**Figure 6.30: Setup of the MW and RF amplifier.** Two high-isolation switches (ZASWA-2-50DR+, *Mini Circuits*), toggled by TTL signals from the *ADwin* experiment control unit, switch on and off and direct the signals from the *R&S* frequency generator. Two amplifiers, one for the RF antenna (ZHL-5W-1, *Mini Circuits*) and one for the MW antenna (ZHL-30W-252-S+, *Mini Circuits*) are used. The setup possess an attenuation of 13 dB measured between the *R&S* input and the MW antenna output.

of the atomic sample. In fact, evaporation in the experiment was first not performing in the run-away regime because the MW power delivered by an in-vacuum antenna, which is mounted to a CF16 flange (described in [77]), was too low (more details on this subject

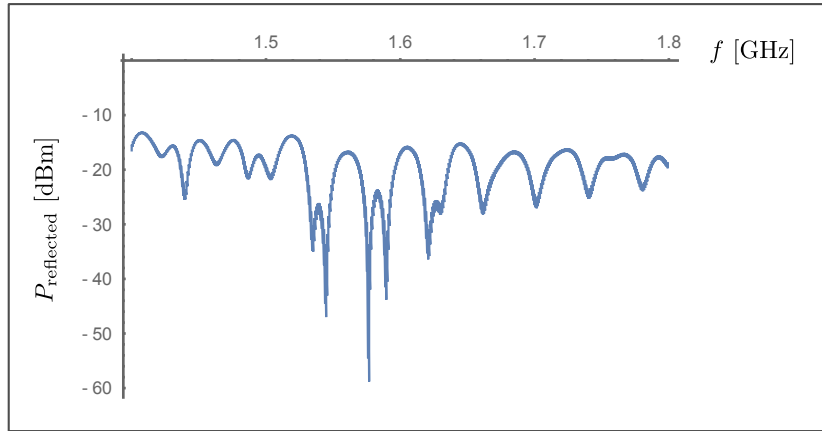


**Figure 6.31: Transfer function of the double-loop antenna used for MW evaporation.** The power which is reflected from the antenna is measured at the dump output of a circulator for the relevant frequency range from 1.4 to 1.8 GHz. Dips in the spectrum indicate resonances of the antenna as only a small fraction of the power is reflected due to impedance mismatch. The absolute power values give no indication of the power actually emitted by the antenna, but the relative depth of the resonance dips indicates an up to 40 dB difference between optimal and worst emittance.

are given in sec. 6.12.2). A single winding of copper wire has been glued into each of the Feshbach coil holders (see sec. 6.5.1) and chain-connected (with empirically ensuring the optimal configuration) to deliver MW radiation along the vertical axis of the experiment. It has been found that still high MW power (max. 44 dBm are sent to the antenna) is needed, making it necessary to amplify the output of the frequency generator. Figure 6.30 shows the amplifier setup which is also used to deliver the RF radiation for the state transfers (see sec. 6.12). A first switch (ZASWA-2-50DR+, *Mini Circuits*) is used to block the signal from the frequency generator during the complete sequence, except for the segments where MW evaporation or RF transfers are performed. This on the one hand ensures that no parasitic frequencies, originating from the frequency generator feedline, can reach the amplifier and on the other hand enable a truncation of the MW evaporation ramp. A second subsequent switch distributes the frequencies to either the MW amplifier (ZHL-30W-252-S+, *Mini Circuits*, water-cooled) or the amplifier for the RF radiation (ZHL-5W-1, *Mini Circuits*). A circulator between the MW amplifier and the antenna ensures that back-reflected MW power (due to imperfect impedance matching, see sec. 6.12.2) cannot damage the amplifier. Using a function generator connected to the input and a spectrum analyser connected to the dump output of the circulator enables the measurement of the transfer function of the antenna. Figure 6.31 shows the transfer function of the double-loop MW antenna. Dips in the plot mark frequencies with high emitted power, whereas peaks indicate a high back reflection from the antenna. The detected spectrum is by far not ideal since it does not show a plateau region where the emitted power would be frequency-independent. However, for the geometric restrictions given by the setup, it is currently the best possible solution. Keep also in mind that the depicted power values in fig. 6.31 only show the power detected by the spectrum analyser and no information of the power which finally reaches the atoms can be extracted from it. Nevertheless, the relative difference between peaks and dips indicate a frequency-dependent performance with a difference in emitted power of up to 40 dB.

### Evaporation ramp optimisation

The MW evaporation in the magnetic trap is performed at a magnetic field gradient of 216 G/cm. First, the evaporation of pure <sup>23</sup>Na is investigated to construct the evaporation

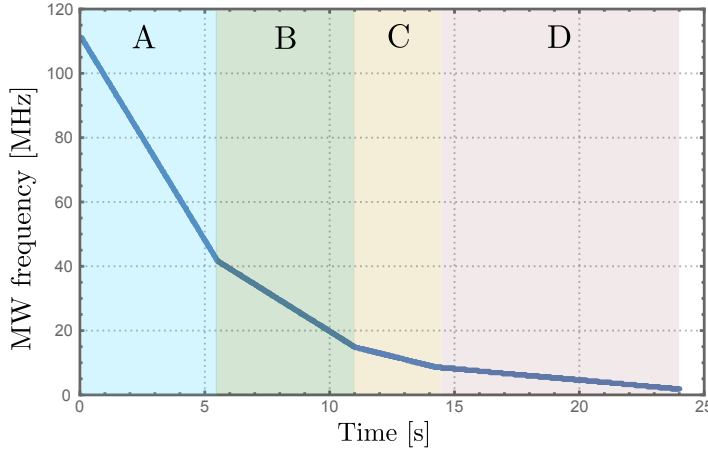


**Figure 6.32: Experimentally optimized MW ramp for the forced evaporation of  $^{23}\text{Na}$  in the magnetic quadrupole trap.** The frequencies are given modulo the hyperfine splitting of 1771.626 MHz. Zero frequency thereby marks the trap bottom. The coloured sections A to D mark the ramp steps which have been optimized separately. The MW power is identical for all ramp steps.

ramp. The ramp is constructed with linear segments which are varied in length and slope as well as in terms of the output MW power during the optimisation process. The PSD is used as figure of merit and is deduced from a single TOF picture. This method enables a fast optimisation process without the necessity to measure the real PSD for every single optimisation attempt (such a process would include a series of TOF images to deduce the temperature). To ensure comparability of the optimisation attempts, the strategy presented in [175] is used. In this method, the ramp segment under investigation is followed by an unoptimized segment which is kept unchanged. By observing the PSD, the ramp segment under investigation is optimized. After the optimisation, the last segment is removed and a final PSD measurement is performed to ensure that the ramp performs in the run-away regime. Figure 6.32 shows the experimentally optimized MW ramp which has been used to obtain the experimental results presented in this thesis. As the experiment setup progresses on the way towards ground-state molecules, the MW evaporation is subject to constant further tailoring to account for added features of the apparatus and for new experimental needs. The ramp therefore has been changed since the time of the measurements which are presented in this thesis have been performed, see [142].<sup>6</sup> The final ramp is constructed out of four segments and has an overall duration of 24 s. Segment A starts 116.626 MHz above the trap bottom (i.e. a total frequency of 1660 MHz) and goes to 41.5 MHz within 5.5 s, segment B goes to 14.5 MHz within 5.5 s, segment C to 8.5 MHz within 3.2 s and segment D goes to 1.826 MHz above trap bottom within 9.8 s.

The MW power is also investigated for the ramp. Figure 6.33 shows the MW power directly in front of the MW amplifier versus the PSD measured for  $^{23}\text{Na}$ . It becomes apparent that the necessary MW power is very high. In fact, what appears to be the onset of a saturation at  $-6\text{ dBm}$  is instead the saturation of the MW amplifier output power which has an amplification of 50 dB but is limited to 44 dBm total output power.

When investigating the atom number of the sodium sample during the evaporation,

<sup>6</sup>Because the experiment setup has been changed shortly after the measurements presented in this thesis were taken, the evaluation of the evaporation performance relies on datasets recorded with the former setup of the experiment. Therefore, for an all-embracing analysis the available data might seem incomplete. From an experimental point of view, the data has been sufficient to optimize the setup to the point at which the measurements of interest could be taken and therefore fulfil their purpose. Newer data, taken in a more complete way, enabled a detailed investigation of the evaporation dynamics and are presented in [36].

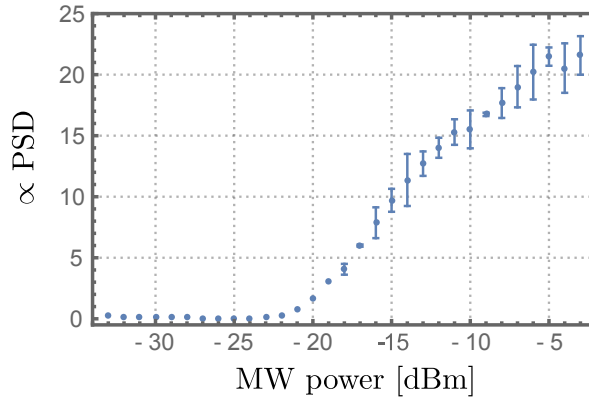


**Figure 6.33: Forced evaporation efficiency as a function of MW power.** For a fixed evaporation time in the magnetic trap, the MW power is scanned and a value proportional to the PSD is detected. The value is derived by measuring the atom number and widths of the atomic sample after a fixed TOF for a single experiment run. The MW power depicted is the power directly in front of the MW amplifier, which has a gain of 50 dB and saturates for an output power of 44 dBm.

massive losses lead to a vanishing atom signal in the magnetic trap for evaporation depths lower than 7.5 MHz above trap bottom. Figure 6.34 shows a measurement with a gradient of 150 G/cm. No atoms are left after 15 s which in this case equals 7.5 MHz above trap bottom (a slightly different evaporation ramp was used in this measurement). The reason for these massive losses are unwanted spin-changing events at the magnetic trap centre, known as *Majorana spin flip losses* which are discussed in the following section.

### 6.10.2 Majorana spin flip losses

As discussed in sec. 6.8.1, only the  $f = 1, m_f = -1$  and  $f = 2, m_f = -2, -1$  Zeeman hyperfine states of  $^{39}\text{K}$  and  $^{23}\text{Na}$  are trapped in a magnetic quadrupole field. Semi-classically speaking, the  $m_f$  component is given by the magnetic moment of the atom being oriented along the magnetic field axis. In the centre of a magnetic quadrupole trap, the magnetic field strength is zero, leading to a loss of the quantization axis. This in turn can lead to a spin flip inside an atom passing through the magnetic field zero. Its magnetic moment realigns with the magnetic field axis after being completely freely rotating at the place of zero magnetic field.

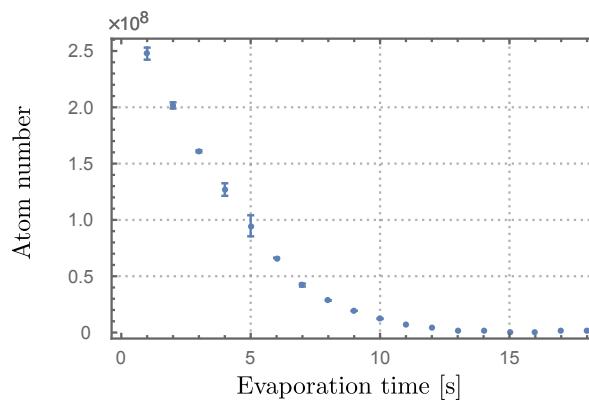


**Figure 6.34: Atom number during MW evaporation in magnetic quadrupole trap.** For different evaporation depths, the sodium atom number in a magnetic quadrupole trap is given. For evaporation durations beyond 15 s, no atoms remain in the trap.

Its realignment eventually happens in a different orientation than it had before reaching the trap centre. If the new spin orientation is associated to a magnetically not trappable state, the atom gets lost from the trap. This process of *Majorana spin flip losses* [176] happens less frequently the hotter the atoms are because the probability distribution of trapped atoms maximises at the semi-classical turning points of the potential. This means the hotter the atoms are, the less time they spend at the trap centre. Hence, they experience less spin-flip losses. For evaporative cooling, this is an unwanted effect because it means that especially the coldest atoms get lost from the trap. As can be shown, the Majorana loss rate is given by [177]

$$\Gamma_M = \chi \frac{\hbar}{m} \left( \frac{\mu_B g_f m_f B'}{k_B T} \right)^2 \quad (6.30)$$

with  $B'$  being the magnetic trap gradient.  $\chi$  is a geometrical factor related to the trap zero. Although it could in principle be calculated, it is usually used as a fit parameter when investigating the Majorana losses in an experiment [177]. A detailed analysis of the Majorana losses in the quadrupole trap of this experiment led to  $\chi = 0.196$  [36] which is found to be in accordance with another  $^{23}\text{Na}$  experiment, where  $\chi = 0.14$  [174].

### 6.10.3 Blue plug

To suppress the losses originating from spin flips due to the zero magnetic field at the trap centre, different options exists. Either one uses additional field coils to introduce a permanent magnetic field at the trap centre, as is done e.g. in *Ioffe-Pritchard*-type magnetic traps [178], generates time-averaging fields, as used in so-called *TOP traps* [179], or one combines the magnetic trapping potential with a repulsive optical potential at the trap centre (for a more detailed theoretical discussion on atom-light interaction see sec. 6.11.1). The latter is the idea behind the so-called *blue plug* (BP), where a far blue-detuned laser is focussed onto the magnetic trap centre [180]. As discussed in sec. 6.4.3, laser light at 532 nm is used for the BP in this experiment setup.

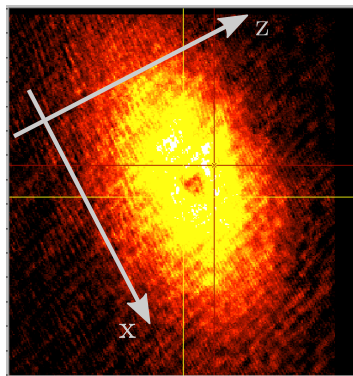


**Figure 6.35:**  $^{23}\text{Na}$  atoms in the magnetic trap with horizontal plug. The picture is directly taken from the experiment imaging program. Due to the imaging setup, the axis are tilted as indicated. The blue plug is visible as a dark spot in the centre of the magnetically trapped atomic cloud.

To plug the magnetic trap zero, the laser light can be directed into the main chamber either on a horizontal or on the vertical axis. Many practical reasons favour a horizontally introduced plug laser in the case of the presented experiment setup. First, the main chamber possesses many viewports on the horizontal plane, making optical access easy. Additionally, on the vertical plane, the plug laser beam has to pass through the imaging objective, imposing difficulties for alignment as well as beam parameter control. The beam alignment on the

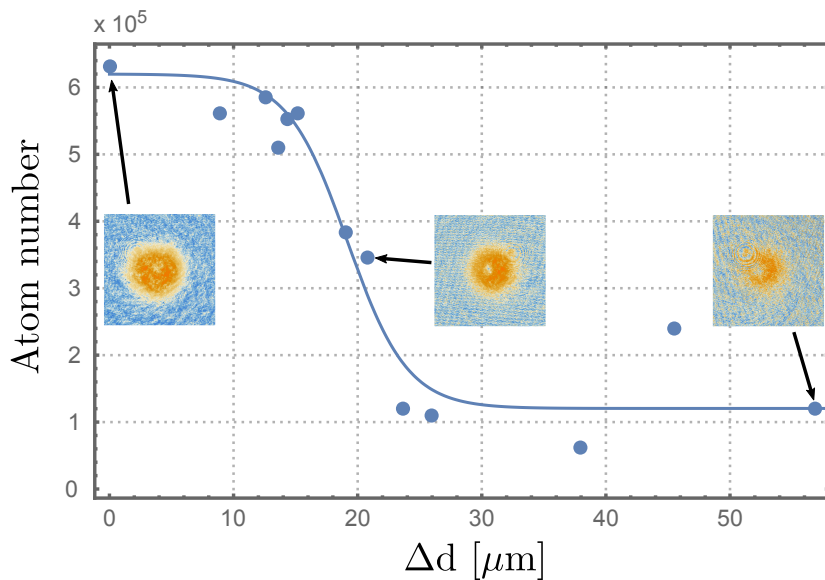


**Figure 6.36:**  $^{23}\text{Na}$  atom number versus displacement  $\Delta d$  of the vertical blue plug with  $\sim 40 \mu\text{m}$  waist at the focus. The pictures of the atomic cloud, imaged with the vertical imaging setup, show the plug position for three displacements as a hole in the sample. Moreover, the reduction in atom number when the plug focus is moved out of its optimal position (set to zero displacement) is visible. The curve is a phenomenological fit function, mainly serving to guide the eye.

horizontal axis can be performed by placing a camera at the opposite viewport of the main chamber. With this camera, the magnetically trapped atoms are observed using fluorescence imaging. The focus of the imaging optics is adjusted onto the atomic sample and their position is detected. Subsequently, a low-power plug beam is introduced. By moving around the plug laser beam and overlaying the images of atoms and plug beam on the camera, a decent pre-alignment can be achieved. Alternatively, by using band-pass filters which reduce the plug beam power enough so that the camera is not damaged, a picture of the punctuated atomic sample can be recorded.<sup>7</sup> The first successful realisation of a plugged magnetic trap in the experiment setup was achieved with a blue plug propagating along a horizontal axis. Figure 6.35 shows a picture of the horizontal blue plug. The punctuated  $^{23}\text{Na}$  sample inside the magnetic trap is clearly visible.

Two crucial parameters for the visibility of the blue plug in a picture of the trapped atomic sample are its barrier height (which depends on the power of the plug laser at the point of the atomic sample) and the sample temperature. If the barrier is too small or the temperature of the ensemble too high, too many atoms will still be at the location of the blue plug focus, therefore no puncture of the atomic cloud will be visible in the picture.

The blue plug has to be aligned with a precision of half a beam waist onto the magnetic trap centre, as can be seen in fig. 6.36. Here, the plug displacement  $\Delta d$  is plotted versus the number of  $^{23}\text{Na}$  atoms inside the magnetic trap, given already for the vertical blue plug realisation (see below). The waist at the focus is  $40 \mu\text{m}$  and for a displacement of  $\sim 20 \mu\text{m}$ , the blue plug already lost half of its efficiency. This required precision demands a stable optical setup. It also demands for a stable magnetic trap position. The latter requirement could

<sup>7</sup>When using band-pass filters to attenuate the plug laser power, it should be made sure that absorbing attenuators are used, or if the band-pass filters are of reflective kind that they are placed under an angle so that the reflected plug laser light cannot propagate into the atomic sample again. In fact, this happened during the first attempts of setting up the blue plug. It led to some confusion because although the plug was properly adjusted onto the atomic cloud, it did not prevent any spin-flip losses, most likely because the back reflected light disturbed the combined potential.

not be fulfilled in the experiment setup, as the trap position tends to oscillate by  $\sim 15\ \mu\text{m}$  in the vertical direction over the course of several experiment runs. This led to an unstable performance of the horizontal blue plug realisation. Since all following experimental steps rely on a stable evaporation performance, the side blue plug had to be abandoned. Instead, a vertical plug has been implemented.

The plug laser beam is overlaid with the vertical imaging beam using two mirrors, both mounted in high-precision mirror mounts (*Ultima U200-A, Newport*), and a third dichroic mirror. With a fourth 2 inch mirror, the imaging light as well as the plug beam are directed through the objective into the main chamber. As already discussed in sec. 6.7, the mirror for the retro-reflected MOT light can be toggled out of the beam path during blue plug operation and imaging. The plug-beam outcoupler contains of a two-lens system, designed to account for the objective in the beam path and to produce a circular focus of  $\sim 40\ \mu\text{m}$  waist. Pre-alignment of the divergence of the outcoupled beam is performed by altering its direction with an additional mirror before it hits the dichroic mirror. Then, the divergence is adjusted to an estimated value with which the focus size should be achieved. The final focus alignment is done after the BP is adjusted onto the atomic sample in the magnetic trap. The size of the puncture of the atoms is minimized and additionally, the plug performance

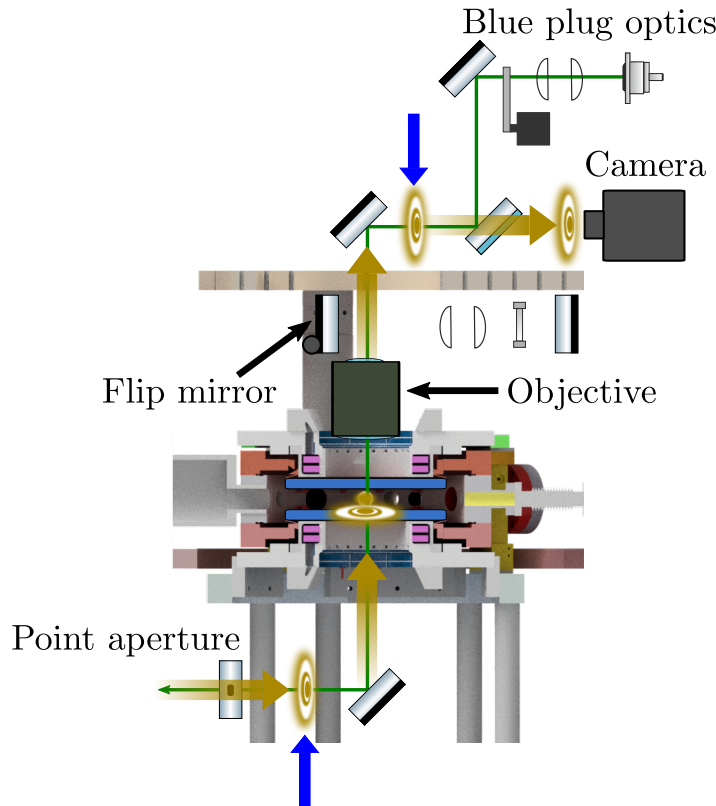


**Figure 6.37: Schematic of the setup for the vertical blue plug beam.** The blue plug beam is overlaid with the vertical imaging, using a beam combiner mirror. The blue plug optics are chosen such that the focus of the blue plug is at the position of the atomic ensemble. A mechanical shutter blocks the light when the blue plug is not used. The flip mirror toggles between retro-reflected 3D MOT beam and blue plug operation and/or vertical imaging. Additionally illustrated in the schematic is the alignment procedure of the blue plug beam. A point aperture is placed inside the vertical imaging beam and the centre of its diffraction pattern is adjusted onto the atomic ensemble and imaged using the camera. The blue plug beam is overlaid with the diffraction pattern at the two points indicated by blue arrows. Thereby, it is ensured that the beam also passes the atomic ensemble.

in terms of reducing Majorana losses as function of the focus parameters is investigated. After the beam passed through the chamber, it is directed onto a beam dump using another dichroic mirror. In fig. 6.37, the setup of the BP optics is shown.

The main challenge when using the vertical blue plug is to hit the atomic sample with the plug beam at all. Only then the puncture of the plug is visible somewhere inside the atomic sample and can be used to adjust the plug position onto the centre of the magnetic trap. The difficulty mainly originates from the circumstance that no camera for pre-alignment can be installed in a similar way as for the horizontal BP for the experiment setup presented here. In [36], one possible method to align the BP beam is described. Here, an alternative and fast way of alignment is presented.

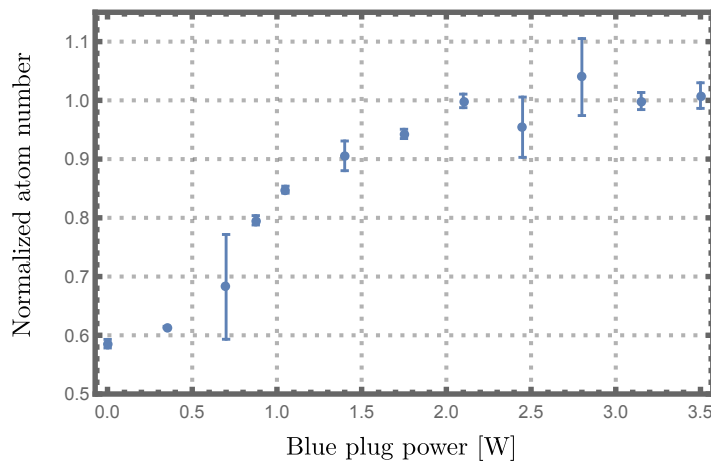


**Figure 6.38: Normalized  $^{23}\text{Na}$  atom number versus power of the blue plug laser.** The atom number is normalized to the mean of the measured numbers for an optimal plug performance.

Figure 6.37 illustrates the alignment method. For the coarse alignment, first the vertical imaging beam is adjusted onto the camera. Because the  $45^\circ$  mirror directly above the telescope is the only mirror with which the imaging beam can be directed onto the camera and the plug beam uses it, too, adjusting the imaging after the plug beam is aligned will destroy that alignment. Next, a picture of the atomic sample in the magnetic trap is recorded using the vertical imaging. The position of the centre of the sample is marked in the imaging software program. Then, a point aperture is placed behind the telescope of the vertical MOT beam, leading to a diffraction pattern on that beam. The image of the central diffraction maximum is adjusted to hit the camera chip by shifting the point aperture position. Another vertical image is recorded on which the diffraction structure of the imaging beam is visible (when the camera program is operated without background image subtraction). The central diffraction feature is moved on top of the marked position for the trap centre by carefully adjusting the point aperture. Next, the blue plug laser is activated with low power. It is overlaid with the central diffraction feature at one point before it enters the objective and at one point after it passed through the chamber. These points are marked by blue arrows in fig. 6.37. Finally, the point aperture is removed and an image of trapped atoms together with the full power plug beam is taken on the vertical axis, normally revealing a puncture in the atomic sample already decently close to the trap centre. With this method, a fast and reliable plug alignment can be performed whenever the plug laser beam path has been changed, e.g. when the top breadboard had to be removed for maintenance purposes.

On a daily basis during the start-up procedure of the experiment, the position of the blue plug is checked and if necessary adjusted. Shortly after the measurements for this thesis were finished, one of the high-precision mirror holders has been exchanged with a remotely controlled one (8821, *New Focus*, identical to the ones used for the cODT setup, see below)

which allows for comfortable adjustment of the BP position.

In fig. 6.38, the dependence of the power of a perfectly aligned BP to the atom number of  $^{23}\text{Na}$  atoms at  $10.5\ \mu\text{K}$  in the magnetic trap is depicted for a field gradient of  $216\ \text{G/cm}$ . The atom number is normalized to the mean atom number for an optimally performing BP. As can be seen, the BP nearly doubles the remaining atoms in the magnetic trap.

#### 6.10.4 Sympathetic cooling of $^{39}\text{K}$

The *sympathetic cooling* technique has originally been proposed in context of plasmas. Its first demonstration has been with cryogenically cooled helium as buffer gas in the context of neutral atoms [181]. The technique proved immensely helpful for cooling fermionic atoms to quantum degeneracy by adding another species to the trap which serves as the coolant [182–184]. Because s-wave scattering is forbidden in spin-polarized Fermi gases by the Pauli principle and p-wave scattering decreasing quadratically with decreasing temperature [185], elastic collisions and thereby a rethermalization is hindered at low temperatures. Introducing a bosonic atom as a bath circumvents this problem.

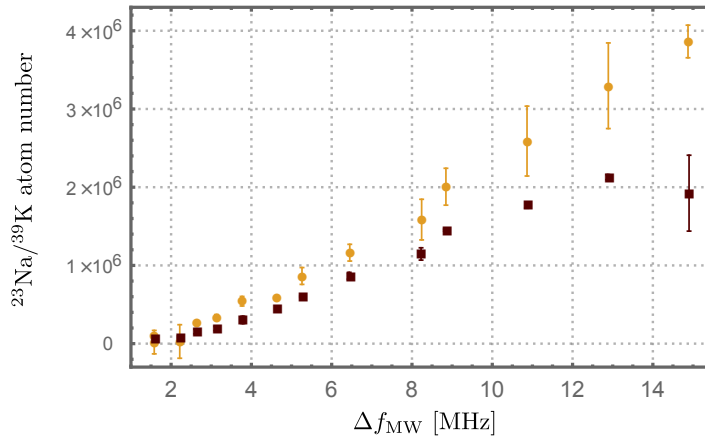


**Figure 6.39: Atom number in dual-species evaporation.** A zoom into the evaporation procedure is shown, starting at  $\Delta f_{\text{MW}} = 14.86\ \text{MHz}$ , given as frequency above trap bottom. The respective atom numbers of  $^{23}\text{Na}$  (yellow circles) and  $^{39}\text{K}$  (red squares) are depicted. The atom numbers have been obtained by the *in-situ* imaging method (see sec. 6.9.2) which only yields qualitative information for  $^{39}\text{K}$  and underestimates the atom numbers for temperatures above  $20\ \mu\text{K}$  (most right point). The  $^{39}\text{K}$  atom numbers are scaled for better visibility.

For the experiment setup presented here, no fermionic species is involved. However, because of the large atom number imbalance between the two species, sympathetic cooling is still beneficial. Since the goal of the setup is to achieve dual degeneracy in the cODT, the evaporation in the magnetic trap is truncated, using the first MW switch (see fig. 6.30) for a duration which is optimized by determining the best loading efficiency into the cODT. Usually, this means that the evaporation in the magnetic trap takes about 16 s and therefore stops at about 7.4 MHz above the trap bottom which corresponds to a temperature of  $\sim 11\ \mu\text{K}$  for both species. As will be discussed in sec. 7.4.3, the atom number ratio of the two species in the trap is used as a tuning knob for the interspecies dynamics which have been investigated within the course of this thesis. Therefore, no information on absolute atom numbers for the combined evaporation are given at this point. A deeper analysis of the evaporation dynamics for sympathetic cooling has revealed that the cooling efficiency for  $^{23}\text{Na}$  is not affected by the  $^{39}\text{K}$  while the potassium is cooled efficiently ( $D_K = 8.6$  compare eq. 6.29) until a temperature of  $10\ \mu\text{K}$  is reached. Below that temperature, three-body loss processes have been identified to lead to a drastic reduction in evaporation efficiency [36]. This is an additional reason for a transfer to the cODT at the stated evaporation point. Figure 6.39 shows the atom number of

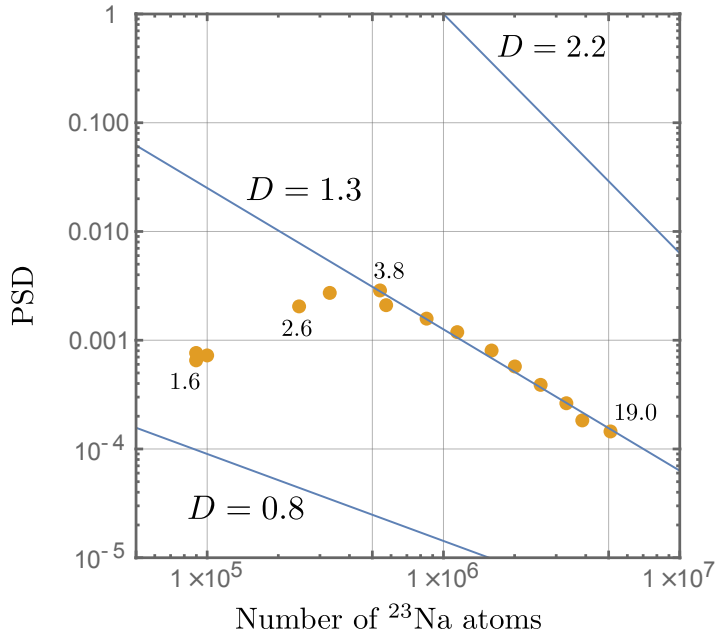


**Figure 6.40: Efficiency of the evaporation ramp in dual-species operation.** The PSD is plotted in a log-log scale versus the atom number of  $^{23}\text{Na}$  for a zoom into the evaporation ramp, starting at  $\Delta f_{\text{MW}} = 19.0$  MHz, given as frequency above trap bottom. The numbers next to the data points mark the respective depth of the evaporation in MHz. The efficiency is  $D = 1.3 \pm 0.05$  up to 3.8 MHz above trap bottom, indicated by the blue line through the yellow dots. The other lines depict an efficiency of  $D = 2.2$ , which is comparable to values found for other  $^{23}\text{Na}$  evaporation [76, 174], and  $D = 0.8$ , which marks the boundary for run-away evaporation in a quadrupole trap [171].

$^{23}\text{Na}$  and  $^{39}\text{K}$  versus the evaporation depth measured with the *in-situ* imaging method (see sec. 6.9.2). Since the *in-situ* imaging cannot give quantitative information for  $^{39}\text{K}$ , the atom number for the plot has been rescaled for better visibility. Furthermore, it can be seen that the atom number for hotter samples is underestimated for  $^{39}\text{K}$ , leading to the lower atom count with larger deviations for the most right data point in the graph. Due to the stated loss mechanisms for frequencies  $< 3.2$  MHz above trap bottom, only a very small amount of atoms is left in the magnetic trap. This means that the last section of the forced evaporation is rather inefficient in the case of dual-species operation.

In fig. 6.40, the performance of the evaporative cooling is shown for a dual evaporation of  $^{23}\text{Na}$  and  $^{39}\text{K}$ . The PSD is calculated for  $^{23}\text{Na}$ . By investigating the efficiency as defined in eq. 6.29 up to a frequency of 3.8 MHz above trap bottom, a fit to the data yields  $D = 1.3 \pm 0.05$ . For this frequency range, which is the relevant range for the dual-species operation, the efficiency is comparable to those determined in experiments of other groups [76, 174] (indicated in the plot as the blue line with  $D = 2.2$ ). The blue line for  $D = 0.8$  marks the boundary for run-away evaporation in a quadrupole trap [171]. The lines with  $D = 2.2$  and  $D = 0.8$  are shifted in the plot for clarity. Since  $D$  is related to the slope of the lines, it can be seen that the efficiency of the MW evaporation presented in this section reduces below the run-away limit for evaporation depths lower than 3.8 MHz above trap bottom.

## 6.11 Crossed optical dipole trap

As seen in sec. 6.10.4, reaching quantum degeneracy in dual-species operation is very challenging in the magnetic trap. Additionally, with regard to the goal of investigating Feshbach resonances, the magnetic field strength needs to be tunable and also magnetically not trapped

Zeeman hyperfine states shall be investigated. Taking all that into account, the atoms have to be transferred to a purely optical trapping potential, which is realized by crossing two high-power laser beams.

### 6.11.1 Theoretical description

The theoretical description of an optical dipole trap is based on the same effect which is also responsible for the effect of the blue plug (see sec. 6.10.3): The *AC Stark shift* describes the energy shift of atomic levels in a light field. Following the *dressed atom approach*, as given in [186] for a two-level atom, the light couples the ground state  $|g\rangle$  and the excited state  $|e\rangle$ . In this case, the atom-light Hamiltonian has two eigenstates,  $|+\rangle$  (low field seeker) and  $|-\rangle$  (high field seeker), whose energies depend on the detuning  $\delta$  of the light with respect to the atomic transition and on the Rabi frequency, which depends on the light power  $\Omega(\vec{r}) \propto I(\vec{r})$ :

$$E_{\pm}(\vec{r}) = \pm \hbar/2 \sqrt{\delta^2 + \Omega(\vec{r})^2} . \quad (6.31)$$

As pointed out in [186], the detuning of the light influences which is the dominant dressed state and thereby whether the atoms will be expelled by higher light intensity (for dominant  $|+\rangle$ ) if  $\delta > 0$  (blue-detuned light) or attracted (for dominant  $|-\rangle$ ) if  $\delta < 0$  (red-detuned light). While the first case is the wanted situation for a blue plug laser, the latter is the one desired for trapping the atoms.

Following [187], the important trap parameters are given as follows. The potential for a single ODT can be written as:

$$V_{ODT}(x, y, z, P) = -\frac{1}{2\epsilon_0 c} \Re(\alpha) I(x, y, z, P) \quad (6.32)$$

with  $\epsilon_0$  being the vacuum permittivity,  $c$  the speed of light,  $I(x, y, z, P)$  the intensity of the light, depending on the geometry of the laser beam and on its power  $P$  and  $\alpha$  being the complex polarizability of the atom. As can be seen from eq. 6.32, the real part of  $\alpha$  gives the trapping potential (for a red-detuned laser). The imaginary part on the other hand is proportional to the rate with which photons of the laser light are scattered by the atoms:

$$\Gamma_{sc}(x, y, z, P) = \frac{P_{abs}}{\hbar\omega} = \frac{1}{\hbar\epsilon_0 c} \Im(\alpha) I(x, y, z, P) . \quad (6.33)$$

By approximating the atom as a classical oscillator with the electron bound elastically to the core with an eigenfrequency of  $\omega_0$ , which is the transition frequency in the two-level model above, [187] derives the formula for the real part of  $\alpha$  as:

$$\Re(\alpha) = \frac{3\pi c^3 \epsilon_0}{\omega_0^3} \left( \frac{\Gamma}{\omega_0 - \omega} + \frac{\Gamma}{\omega_0 + \omega} \right) \quad (6.34)$$

with  $\Gamma$  being the linewidth of the transition  $|g\rangle \rightarrow |e\rangle$ . By inserting eq. 6.34 into eq. 6.32, it can be seen that the potential depends on the light detuning  $\delta = \omega_0 - \omega$  as  $V_{ODT} \propto I/\delta$ . From  $\Im(\alpha)$ , it follows that the scattering rate has the dependency  $\Gamma_{sc} \propto I/\delta^2$ . This is the reason why far detuned laser light (meaning detuned by several hundreds of nanometres from the atomic transition) is favourable for generating optical trapping potentials, since the unwanted light scattering reduces faster with the detuning than the wanted trapping effect.

Moreover, since  $\Re(\alpha)$  depends on the linewidth of the atomic transition, it is different for the two species used in this experiment. The trap depth ratio can be calculated to be  $V(0)_{\text{Na}}/V(0)_{\text{K}} \approx 0.4$  by using the values for  $\Re(\alpha)$  for  $\lambda = 1064 \text{ nm}$  which are given in [188].

For the optical trap realized in this experiment (which happens to be the most common realisation of an ODT), the trapping potential is generated by a Gaussian-shaped laser focus.

The intensity of a Gaussian laser beam of wavelength  $\lambda$  propagating along the  $x$ -axis is given by:

$$I(r, x) = \frac{2P}{\pi w^2(x)} \exp\left(-\frac{2r^2}{w^2(x)}\right) , \quad (6.35)$$

where  $w(x) = w_0 \sqrt{1 + (x/x_R)^2}$ , with  $x_R = \pi w_0^2/\lambda$  being the Rayleigh length and  $w_0$  the waist of the focus. For cold atoms trapped inside such a laser focus, the potential can be approximated by a harmonic shape. With this approximation, simple formulas for the trap frequencies of a single ODT can be given:

$$\omega_x = \sqrt{\frac{2V_0}{mx_R^2}}; \quad \omega_r = \sqrt{\frac{4V_0}{mw_0^2}} . \quad (6.36)$$

Since the Rayleigh range is much larger than the waist of the Gaussian focus, a single ODT offers only relatively weak confinement in longitudinal direction. This leads to a quite elongated trapped atomic sample which can be unfavourable for evaporation attempts (for more details, see sec. 6.11.3). As already mentioned, a cODT is implemented in the experiment setup presented in this thesis which counteracts the weak longitudinal confinement. For a cODT, the trap frequencies in each direction depend on the two single ODT trap frequencies in that direction:

$$\omega_{i,cODT}^2 = \omega_{i,1}^2 + \omega_{i,2}^2, \quad (i = x, y, z) . \quad (6.37)$$

### Gravitational sag

When using optical trapping in experiments performed in a laboratory on earth, an additional potential has to be taken into account which is gravity. Albeit a small effect for high laser powers and thereby deep optical traps, it becomes relevant when the optical trap is relaxed, for example to evaporatively cool (see below). In that case, the so-called *gravitational sag* has to be considered and the overall potential (approximated as harmonic in the vicinity of the trap centre) is modified to

$$V(\vec{r}) = -\frac{1}{2}m\omega_z z^2 + mgz . \quad (6.38)$$

The modified potential leads to a mass-dependent trapping effect, where the displacement in vertical direction for atoms in the ODT is given by:

$$z_{sag} = -\frac{g}{\omega_z^2} , \quad (6.39)$$

where  $\omega_z$  is a function of the mass of the atom, see eq. 6.36. For a trap with a final trap frequency of  $\omega_z = 50\text{ Hz}$ , as it is used in this thesis for the experiments performed with BECs (see chap. 8), the different masses  $m_{\text{Na}}$  and  $m_{\text{K}}$  lead to a displacement between the two species that can be as large as  $32\text{ }\mu\text{m}$ . This can significantly influence their possibility to interact.

Different approaches exist to counteract the gravitational sag. One option is to choose a so-called *magic wavelength* for the cODT laser light which will compensate the sag [146]. Another possibility is to use a magnetic gradient field in combination with different Zeeman hyperfine levels of the two species. Since for the ground-state Zeeman hyperfine levels high- and low-field seeking states exist, as well as such which do not couple to the magnetic field at all, a small gradient field is in principle sufficient to counteract the sag [189]. With the new Feshbach coil design implemented in the experiment setup (see sec. 6.5.1), the additional set of coils inside the Feshbach coil housing could be used for such purposes. That is, if for the

following steps of molecule creation feasible Feshbach resonances in the different Zeeman hyperfine state mixtures exist (see chap. 7).

### 6.11.2 Experimental implementation

Using the laser source described in sec. 6.4.3, a cODT is realized in the experiment. Two fibre outcouplers are mounted on the bottom of the FRP breadboard which is at chamber height (see sec. 6.1). One of the two beams is shaped to form an elliptical focus and propagates along  $x$  (beam waists:  $w_{\text{horiz.}} \approx 143 \mu\text{m}$ ,  $w_{\text{vert.}} \approx 40 \mu\text{m}$ ) while the other one produces a radially symmetric focus and propagates along  $y$  (beam waists:  $w_{\text{horiz.}} \approx 46 \mu\text{m}$ ,  $w_{\text{vert.}} \approx 46 \mu\text{m}$ ). While the latter ensures for a high trapping depth, the former enlarges the trapping volume. The beams are guided via high precision mirror mounts (*Ultima U100, Newport*) and two motorized mirror mounts (*8821, New Focus*) per beam onto a  $45^\circ$  dichroic mirror (transparent for the MOT light) which overlays the dipole trap beams with the MOT beams. After the cODT beams passed the experiment chamber, a small amount of the power is directed onto a photodiode while the majority of the light hits a beam dump. The photodiodes are used to control the laser powers in the beams via a PI controller. A detailed description of this setup can be found in [143]. The powers in the beams are 4.7 W for the radial symmetric beam and 3.8 W for the elliptical one.

#### Alignment procedure

The main idea to precisely align the cODT beams is to place the beam below the centre of the magnetic trap and release the cold trapped atoms. While falling through the optical trapping potential, some atoms will get caught and can be imaged as a striped feature inside the released expanding atom cloud. By moving the ODT beams and observing the position of the striped feature, the optical traps can be precisely aligned onto the position of the magnetic trap. While this principle works excellently once a first signal of the described striped feature has been obtained, to find this signal in the first place is the main task.

The coarse alignment of the cODT beams was first tried by coupling resonant light into the fibres. With this, atoms should have been depleted from the magnetic trap. Since the optics used for the cODT are not high-reflecting for the sodium or potassium wavelength, only a small amount of laser light reached the atoms, rendering this procedure unfavourable.

The best procedure to reliably coarsely align the beams, so that they hit the atomic cloud, has been found to be similar to the alignment procedure used for the horizontal BP (see sec. 6.10.3). An imaging system consisting of two lenses and a camera is placed in the beam path of the ODT beam. The focus of the system is adjusted with respect to the atomic sample, using fluorescence imaging of sodium atoms in the magnetic trap. With this imaging setup, the position of the ODT beam is moved onto, or even purposefully a little below, the recorded position of the magnetically trapped atoms. By switching to the horizontal absorption imaging (see sec. 6.9.2) and ramping up the laser beams to full power (after having protected the ODT camera), the above described stripe can be observed in TOF images.<sup>8</sup> With the striped features visible on the horizontal imaging axis, the vertical trap alignment is performed for both trap beams using the magnetic trap position as the reference. Figure 6.41 (a) shows a picture taken with the horizontal imaging setup, where the spherically

---

<sup>8</sup>For the first alignment using the ODT camera achromatic optics are recommended as well as removing any not needed optical element from the combined beam path. During the first attempts with this alignment procedure, the mirror directing the MOT light into the chamber was left in the beam path for the ODT beam images, as it is transparent for the ODT wavelength (it can also be toggled out of the beam path, because it is mounted on a flip mirror mount). Although the positions of atomic signal and ODT beam were matching on the camera chip, no stripe signal was found in TOF. After investigating the displacement of the ODT beam due to diffraction when passing the MOT mirror, it has been found that this can be on the order of several tens of micrometres, making a decent pre-alignment impossible.

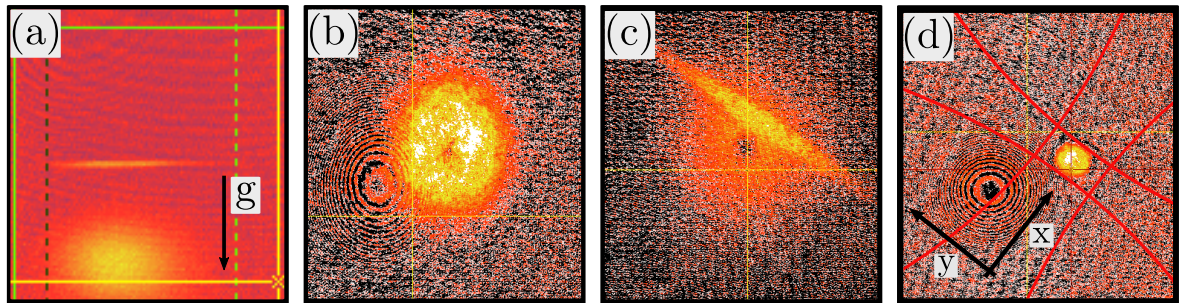


**Figure 6.41: Alignment procedure of the cODT.** (a) shows the radially symmetric ODT as a stripe of trapped atoms as well as a thermal cloud of  $^{23}\text{Na}$  in TOF. (b) and (c) show pictures of  $^{23}\text{Na}$  atoms inside the plugged magnetic trap without and with the cODT active, taken with the vertical imaging. In (d), a  $^{23}\text{Na}$  BEC is imaged inside the cODT. The cODT beams are indicated by red lines. All pictures are taken directly from the experiment imaging software.

shaped ODT is visible as a stripe of  $^{23}\text{Na}$  atoms together with a free falling thermal cloud. The horizontal alignment can only be partially performed using the horizontal imaging because the camera is placed under an angle of  $45^\circ$  to the cODT beams. By switching to the top imaging and inspecting a cold atomic sample in the magnetic trap (see fig. 6.41 (b)) while also applying the cODT, it is possible to adjust the horizontal positions, see fig. 6.41 (c). The highest precision in alignment has been achieved once a BEC of  $^{23}\text{Na}$  could be produced in the cODT (see sec. 6.11.3) because it is situated at the point where the two ODT beams cross, see fig. 6.41 (d).

The coarse longitudinal alignment of the trap foci has been performed in two complementary ways. First, each ODT laser beam has been reflected onto a beam cam (*DAT-BladeCam-HR, Laser 2000 GmbH*) by placing a mirror in front of the viewport through which it enters the main chamber. By mapping out the beam profile and the distance of the focus from the mirror, a rough geometric alignment can be achieved. For this purpose, the distances of the mirror to the focus and the distance of the mirror to the centre of the main chamber are made equal. Second, the imaging setup with which the ODT beams are overlaid with the fluorescence signal from the magnetically trapped atoms can be used. By shifting the ODT focus position and minimizing the size of the imaged beam, the focus can be aligned longitudinally. Both methods are error-prone because for the first one, one relies on the precision of the distance measurements and for the second one on the adjustment of the focal plane of the imaging setup. Therefore, for the precise alignment of the foci along the beam directions, trap frequency measurements are used (see below).

### Trap frequencies

The trap depth of an optical trap is related to the waist of the focus and the power of the light and can be given in terms of trap frequencies as explained in sec. 6.11.1. By measuring the laser power of the ODT beam and determining the trap frequencies, the exact focus parameters can be deduced. Trap frequencies are measured in this thesis by two different methods, the first one being the observation of oscillations of the atoms inside the cODT after exciting them by an external force, the second one being so-called *parametric heating* [190, 191]. For the vertical trap frequency, the first method of detecting the spacial oscillation of the atomic sample is used. To excite the oscillations, the cODT is switched off for 0.5 ms using the AOMs in front of the fibre incoupler (see sec. 6.4.3). This leads to a vertical displacement of the atomic sample. Afterwards, the cODT is switched on again and hold for a variable time during which the dynamics inside the trap can evolve. Then, the trap is switched off and the vertical position of the thermal cloud is detected after a fixed TOF.

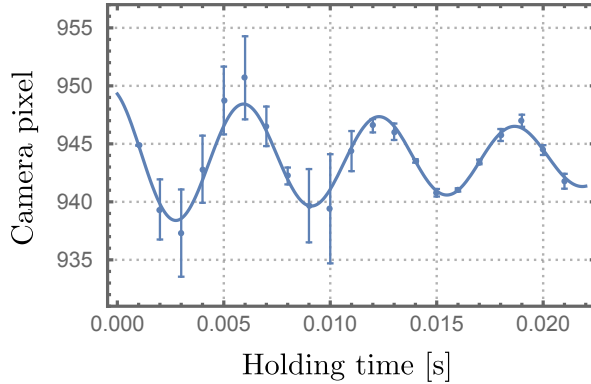


**Figure 6.42: Measurement of the vertical trap frequency of the cODT.** By exciting oscillations of the trapped atomic sample and measuring the spacial position after a variable holding time, the vertical trap frequency is determined by fitting a damped sine to the recorded data. The derived trap frequency is 157.1 Hz for a trapping potential as it is used for the BEC measurements presented in chap. 8 with trap beam powers of  $P_{\vec{e}_y} = 47 \text{ mW}$  and  $P_{\vec{e}_x} = 152 \text{ mW}$ .

Plotting this position versus the evolution time spent in the cODT after the excitation and fitting the oscillation with a damped sine directly gives the trap frequency in the vertical direction. Figure 6.42 shows such a measurement, performed for the trap configuration which is used to produce the double BEC, as discussed in chap. 8.

The method used for the vertical trap frequency experiences complications for the horizontal axis. First, since the horizontal imaging is under an angle of  $45^\circ$  to the dipole trap axis, the frequencies measured will be a combination of the frequencies in  $x$  and  $y$  direction. Secondly, it is technically challenging to excite a horizontal oscillation in the cODT. Kicking the atoms by using the compensation cage coils did not lead to a measurable signal. Therefore, parametric heating is performed to measure the horizontal trap frequencies, which has the advantage that it addresses each trap frequency individually. In the method of parametric heating, the trapping frequency is modulated to introduce heat into the system of trapped atoms. When the modulation frequency comes close to a value of two times the trap

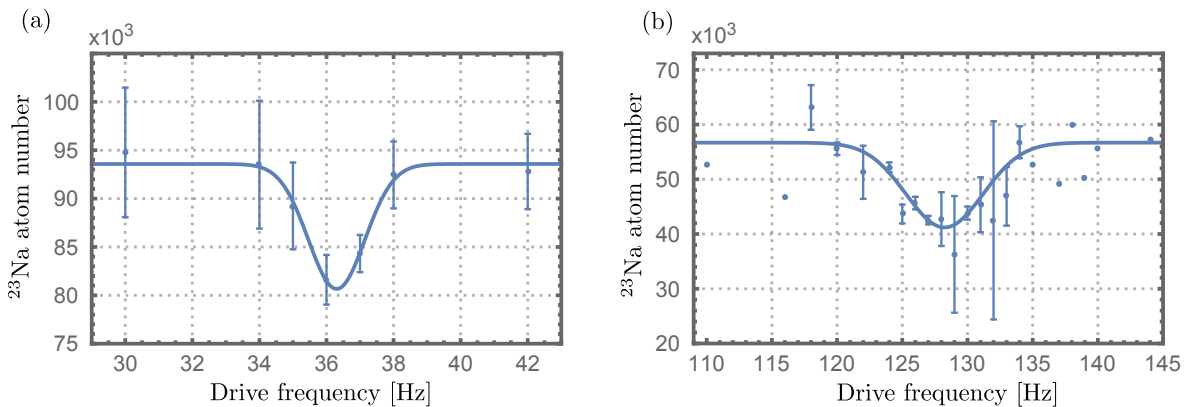


**Figure 6.43: Horizontal trap frequencies of the cODT, measured using parametric heating.** The trap frequencies are shown for the elliptically shaped focus trap (a) and the spherically shaped focus trap (b), measured as an atom loss signal as function of the parametric heating frequency. A Gaussian fit determines the trap frequencies to be 36.3 Hz (a) and 128.2 Hz (b) for a trapping potential as it is used for the BEC measurements, presented in chap. 8 with trap beam powers of  $P_{\vec{e}_y} = 47 \text{ mW}$  and  $P_{\vec{e}_x} = 152 \text{ mW}$ .

frequency, this process becomes resonant and the introduced energy is sufficient that atoms can leave the trap. Thus, plotting the modulation frequency versus the number of atoms which remain in the cODT allows for the determination of the trap frequencies. Figure 6.43 shows such measurements, again taken for the cODT values used for the double BEC production discussed in chap. 8. For the measurement, a frequency generator is connected to the voltage-controlled amplitude modulation input of the driver which controls the AOM in front of the fibre incoupler (see sec. 6.4.3). The modulation frequency is scanned and the related atom signal is detected.

**Table 6.6:** Trap parameters for the optical traps forming the cODT.

ODT	Power[W]	$w_{vert.}[\mu\text{m}]$	$w_{hor.}[\mu\text{m}]$	$(f_x, f_y, f_z)_{N_a} [\text{Hz}]$	$(f_x, f_y, f_z)_K [\text{Hz}]$
$\text{ODT}_{\vec{e}_x}$	3.8	43.5	148	(1, 181, 615)	(1.2, 220, 749.5)
$\text{ODT}_{\vec{e}_y}$	4.7	43.2	43.2	(1280.5, 7, 1280.5)	(1559, 8.6, 1559)
cODT				(1280.5, 181, 1421)	(1559, 220.5, 1728)

For a trap beam power of  $P_{\vec{e}_y} = 47 \text{ mW}$  and  $P_{\vec{e}_x} = 152 \text{ mW}$ , the precise focus parameters can be calculated for the recorded trap frequencies. They are  $43.2 \mu\text{m}$  for the spherical focus trap along  $y$  and  $43.5 \cdot 148 (\mu\text{m})^2$  for the elliptically shaped focus trap along  $x$ . With the derived focus parameters, the maximal trap frequencies can be calculated. The complete characterisation of the dipole trap configuration, as it is used for all measurements presented in this thesis, is given in tab. 6.6.

### Loading efficiency

To transfer the magnetically trapped atoms into the cODT, the laser beam powers are ramped up in 1 s after the MW evaporation in the magnetic trap is finished. Since the blue plug laser disturbs the trapping potential of the cODT, its positions is purposefully misaligned with respect to the magnetic trap centre. As can be seen in fig. 6.36, a displacement of up to  $\sim 10 \mu\text{m}$  is acceptable in terms of Majorana-loss reduction efficiency. Figure 6.41 shows that the cODT is also placed aside the magnetic trap centre. The combined potential of repulsive BP light and attractive magnetic trap plus cODT potential leads to the best transfer efficiency for the experiment setup presented here. In other experiments, so-called *hybrid traps* have been implemented successfully, where the cODT is aligned onto the magnetic trap centre in the horizontal plane but vertically displaced to be situated underneath it [192, 193]. No BP is used in these traps and the cold atoms which are lost due to Majorana spin flips are collected by the cODT. A similar approach was tested in the course of this thesis, but the achieved performance was not on par with the trap configuration described in the beginning. Moreover, although being more simplistic in terms of the amount of needed different laser beams, the atoms collected in the cODT of a hybrid trap have lost their pure spin character. This would imply the necessity of spin purification for the experiments presented here. Hence, the idea of a hybrid trap was not pursued for the experiment apparatus.

The combined trapping potential is kept for 300 ms after which the BP light is switched off rapidly, using the mechanical shutter. Three milliseconds after that, the magnetic trap is ramped down to zero in 200 ms. This relatively long time is chosen to ensure that switching off the IGBTs will not disturb the atomic sample (see sec. 6.5.2 for effects observed on the coil currents for fast switching times). After the magnetic fields are ramped down to zero, the H-bridge can be used to switch the coil configuration to provide e.g. Helmholtz fields. Switching the configuration takes 25 ms (see sec. 6.5.2 on how in the experiment apparatus

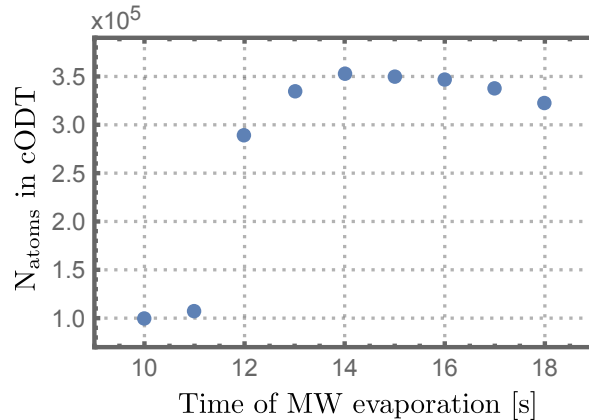


**Figure 6.44: Number of  $^{23}\text{Na}$  atoms in the cODT versus evaporation time in the magnetic trap.** By truncating the MW-evaporation shown in fig. 6.32 after varying times, the atom number loaded into the cODT is optimized. The atom number is obtained after a subsequent optical evaporation in the cODT to ensure comparability between the different loading conditions. TOF measurements of the sample are used to obtain the temperature of the atoms. As an example, for a MW evaporation truncated at 15 s, the obtained temperature is  $\sim 700 \text{ nK}$ .

the different field configurations are switched). Since no magnetic field is present during that 25 ms, the atoms in the cODT would no longer experience a defined quantization axis. This could lead to mixing of the spin states when the magnetic fields are switched back on. To prevent this, a constant guiding field of 2.49 G along the vertical direction is applied already during the magnetic trap and kept on until the cODT is switched off (see below). The guiding field is generated by the vertical coil pair of the compensation coils (see sec. 6.5.1). TOF measurements with a Stern-Gerlach field (which will be presented in greater detail in sec. 6.12.3) show only a single spin component to be present, indicating that the guiding field has a sufficient performance.

An important task is to find the optimal transfer point from the magnetic trap to the cODT in terms of PSD. Transferring an atomic sample with a high temperature will lead to a small number of trapped atoms in the relatively shallow optical potential. On the other hand, the evaporation efficiency in the magnetic trap decreases drastically for a mixed atomic sample of  $^{23}\text{Na}$  and  $^{39}\text{K}$  when going below  $\sim 10 \mu\text{K}$  (or  $\sim 3.8 \text{ MHz}$  above trap bottom), see sec. 6.10.4.

To find the optimal transition point, the atom number of  $^{23}\text{Na}$  which has been transferred into the cODT (measured in TOF) is detected as a function of truncated MW-evaporation ramps, see fig. 6.44. The time given in the plot has to be compared with the time given in fig. 6.32. For the measurements, the powers of the cODT were reduced after the transfer, leading to an additional optical evaporation step which ensures the comparability of the different transfer points. This method is comparable to the one presented in sec. 6.10.1, where the optimisation of the different ramp steps for the MW evaporation is discussed. As can be seen, a MW evaporation time of 14 to 16 s leads to the best transfer efficiencies. It shall be mentioned already at this point that the evaporation time in combination with the atom-number ratio of  $^{23}\text{Na}$  and  $^{39}\text{K}$  initially loaded into the magnetic trap is a tuning knob used in chap. 7 to adjust the minority and majority species for the Feshbach resonance measurements.

### 6.11.3 Evaporation in the cODT

Evaporation in a cODT is rather straight forward (for single-species operation, where no interspecies scattering has to be taken into account). The trap depth can be reduced by simply

reducing the power in the laser beams. This leads to an evaporation process similar to the one explained in the context of forced evaporation in a magnetic quadrupole trap (where the trap depth has to be changed by the use of RF or MW radiation, see sec. 6.10). However, for forced evaporation in the quadrupole magnetic trap, the trap frequencies remain constant for the complete evaporation, thereby always ensuring for a high scattering rate and by this a short re-thermalization time. In an ODT on the other hand, the trap frequencies reduce during the evaporation process. This can lead to an inefficient evaporation up to a point at which no gain in PSD is possible any more. This can prevent reaching the critical PSD for a BEC.

Different possibilities exist to overcome this issue, for example so-called *dimple traps* [194, 195], where even run-away evaporation has been achieved [196], or a combination of optical and magnetic trapping potentials [197].

In the case of the experiment setup presented here, the goal is to achieve a BEC in the  $|f = 1, m_f = -1\rangle$  state of  $^{23}\text{Na}$  by only lowering the cODT potential. By optimizing the loading to the cODT, as seen in fig. 6.44, it is ensured that the cODT evaporation starts with an optimal PSD. The cODT laser powers are then reduced in linear segmented ramps using the power stabilisation which is implemented for each ODT beam (see sec. 6.11.2). By scanning the ramp times and depths of the different segments in a similar manner as described for the forced MW evaporation in sec. 6.10.1, BEC of  $^{23}\text{Na}$  has been achieved with  $\sim 1.5 \cdot 10^5$  atoms (see chap. 8 for details on the exact ramp parameters).

In the case of dual-species operation,  $^{23}\text{Na}$  will sympathetically cool  $^{39}\text{K}$  due to its lower trapping potential ( $V(0)_{\text{Na}}/V(0)_{\text{K}} \approx 0.4$ ). This means that by achieving Bose-Einstein condensation for  $^{23}\text{Na}$ , a BEC of  $^{39}\text{K}$  should occur "on the way", as long as the interspecies scattering length is sufficiently large to ensure thermalization between the two species (for more details see chap. 7).

## 6.12 RF transfer in the cODT

To perform the measurements of Feshbach resonances presented in chap. 7, the experiment setup has to support the transfer of  $^{23}\text{Na}$  and  $^{39}\text{K}$  to all possible hyperfine state combinations of interest. For this purpose, radio and microwave frequency antennas have been designed and characterized.

### 6.12.1 Theory of RF transfers

The theory behind the experimental implementation of the RF transfer is four-fold and is presented in the following. First, the theory of adiabatic rapid passage (ARP) is summarised, second, the importance of polarization of the electromagnetic wave is stressed, third, a short note on wave guide cut-off frequencies is given and fourth, the theory behind dipole antenna design is touched.

#### Adiabatic rapid passage

For atoms in a static magnetic field, the hyperfine states split into their  $m_f$  components and a coupling between those  $m_f$  levels can be introduced by shining in a resonant electromagnetic field with the appropriate polarization. By ramping either the frequency of the electromagnetic field or the strength of the static magnetic field across this resonance in an adiabatic way, atoms in one  $m_f$  state can be transferred to another. This technique is called ARP [198]. The transition probability to transfer atoms from state 1 to state 2,  $P_{12}$ , can be described by

the Landau-Zener formula<sup>9</sup> [199]:

$$P_{12} = 1 - \exp\left(-\frac{\pi\Omega^2(t)}{2|\dot{\Delta}(t)|}\right) \quad , \quad (6.40)$$

where  $\dot{\Delta}(t)$  is the rate of change in the detuning, evaluated for the crossing time  $t$  and  $\Omega(t)$  is the value of the Rabi frequency for the crossing time  $t$ . The Rabi frequency depends on the transition dipole matrix element  $d_{12}$  and on the laser electric field amplitude  $E(t)$  with:

$$\Omega(t) = d_{12}E(t)/\hbar \quad . \quad (6.41)$$

For the ground states of  $^{23}\text{Na}$  and  $^{39}\text{K}$ , the energy difference and thereby the resonance frequency of the different  $m_f$  levels can be calculated using the Breit-Rabi formula (eq. 2.11). From the theory, the coupling strength of the transitions and thereby the level splitting of the avoided crossing of the ARP can be deduced. However, the problem often exists that there is no feasible method to measure how much RF power reaches the atomic sample. This is because impedance mismatches of the feedline as well as geometrical restrictions of the experiment chamber can have significant effects on the power reaching the atoms. These effects are difficult to quantify in practice.

### Polarization of the RF field

The polarization of the RF field is imperative for a working transfer. To be able to drive transitions with  $\Delta m_f = \pm 1$ , the magnetic field vector has to be circularly polarized. For a RF field emitted by an antenna, this means that the field vector has to have components perpendicular to the quantization axis. For example, the magnetic component of the RF field emitted along the central axis of a loop antenna points along that axis. If this central axis is aligned with the quantization axis, no circular components exists along the quantization axis, making transfers with  $\Delta m_f = \pm 1$  impossible.

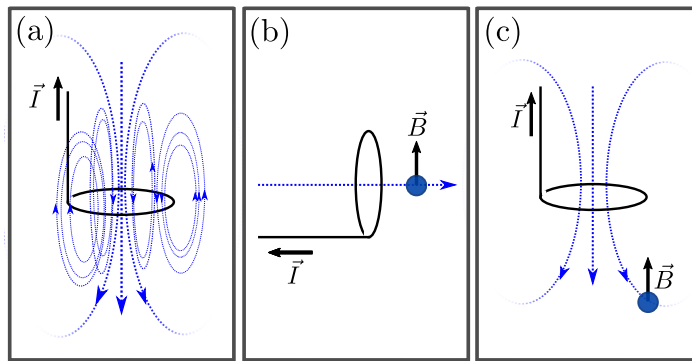


**Figure 6.45: Schematic of the alignment of a RF antenna to the quantization axis.** An electric current  $\vec{I}$  flowing through the RF-antenna induces a magnetic field as indicated by the blue dashed lines (a). If the centre axis of the antenna is perpendicular to the quantization axis (which is given by the magnetic field vector  $\vec{B}$ ), optimal conditions for RF transfers are present (b). If a placement as in (b) is impossible, the antenna has to be placed off-centre to allow for perpendicular components of the emitted magnetic field to be present at the place of the sample (blue circle) (c).

Optimally, a RF antenna of the loop type would be placed with its central axis perpendicular to the quantization axis (as it is done in many cold-atom experiments using glass cells). If the antenna cannot be placed in that way, it needs to be placed off-centre for perpendicular

---

<sup>9</sup>Note that the presented formula is only exact for a constant Rabi frequency and a linearly varying detuning.

components of the magnetic field vector to be present at the place of the atoms. Figure 6.45 illustrates this.

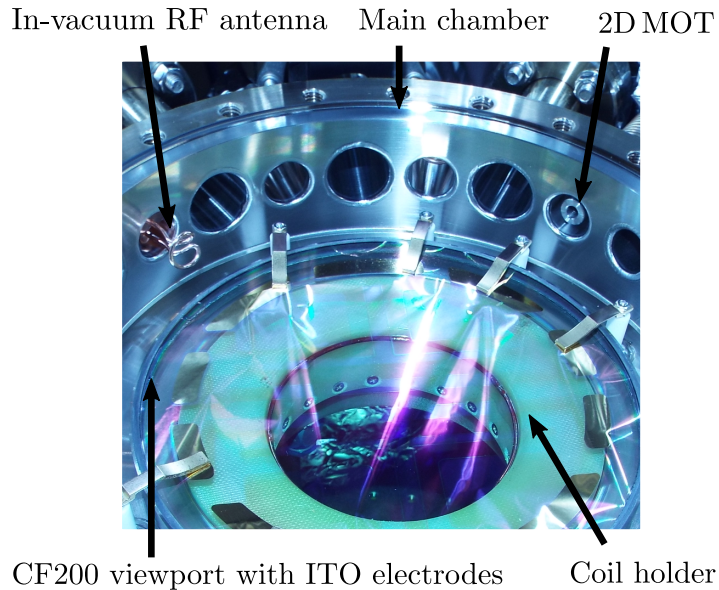


**Figure 6.46: Picture of in-vacuum RF antenna.** The photograph shows the lower CF200 viewport and the metal main chamber. The in-vacuum antenna is attached to a CF16 port. Its distance to the centre of the main chamber is approximately 100 mm. Additionally, the Feshbach coil holder and the differential pumping tube of the 2D MOT are visible.

### Cut-off frequencies of waveguides

Hollow core waveguides can be used to efficiently guide electromagnetic waves over long distances. For frequencies in the MW range (several hundreds of megahertz up to gigahertz), they can be built as rectangular pipes of conducting material.<sup>10</sup> It is important to note in the context of the experimental implementation that these waveguides do possess a cut-off wavelength below which waves cannot propagate inside them any more. It is given by [200]

$$\lambda_c = 2d \quad , \quad (6.42)$$

where  $d$  is the larger of the two dimensions of the cross section of the waveguide.

### Dipole antenna

Dipole antennas emit resonantly at every wavelength with

$$\lambda = \frac{2}{n}L \quad , \quad (6.43)$$

where  $L$  is the length of the dipole and  $n$  is an integer. For a half-wave dipole,  $n = 1$ . When set-up in a feed-line, the impedance of the antenna feedpoint has to match the impedance of the feedline (which in many cases is  $75 \Omega$ ). Since a perfect half-wave dipole has an impedance of  $73 \Omega$ , the only remaining task is to cancel the reactance of the antenna, which is for a perfect

---

<sup>10</sup>A round cross section is also possible, but will lead to different equations for the cut-off frequencies and is not discussed for lucidity.

half-wave dipole antenna  $43\Omega$  [201]. This can be achieved by shortening the antenna by a factor  $k$ , giving a new antenna length of

$$L = \frac{1}{2}k\lambda . \quad (6.44)$$

The factor  $k$  depends on the diameter of the conductor and is between 0.94 for a diameter of  $10^{-5}$  times the wavelength and 0.98 for thick conductors (diameter of  $10^{-3}$  times the wavelength) [202]. For radio frequencies in the range of 100 MHz, having a wavelength of  $\sim 3$  m, the lower value applies normally.

### 6.12.2 Antenna design, characterisation and placement

Because of the inverse-square law, placing the RF antenna as close as possible to the atomic sample reduces the required RF power significantly.

For experiments using glass cells, it is usually possible to place a RF antenna in the vicinity of the experiment region. Additionally, when looking at the emitted radio frequency band of a loop antenna, placed with its central axis perpendicular to the quantization axis, the frequency band is nearly flat over a broad frequency range [203]. These are ideal conditions e.g. for forced evaporation.

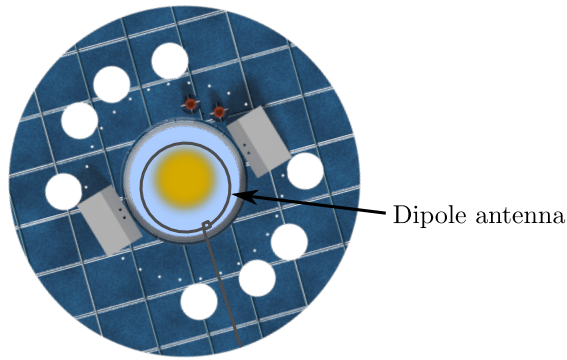


**Figure 6.47: Schematic of the RF-antenna placement on the main chamber.** The RF antenna is placed as off-centre as possible, restricted by the inner diameter of the Feshbach coil holder and the vertical 3D MOT beam (indicated as yellow circle).

In case of experiments performed in large metal chambers, it has to be taken into account that the antennas might be placed farther away from the atoms. This results in a decrease in RF power at the place of the atoms. In some experiments, this problem was mitigated by placing loop antennas in a similar manner to the way they are placed in many glass cell experiments, but inside the vacuum chamber [204]. Where it is technical possible, this will enable a better coupling of the RF field to the atomic sample. In the case of the experiment setup presented in this work, however, the ITO electrodes and the large vertical windows render a similar construction impossible.

An in-vacuum ring antenna has been placed inside the chamber, attached to a CF16 flange, as shown in fig. 6.46 and described in [77]. Both RF and MW evaporation were performed with it, but it was found that very high powers were needed. These high powers led to disturbances in other electronics of the experiment, unlocking the sodium laser lock every time certain RF frequencies were emitted, leading to the necessity of a different solution. The high required powers can be attributed on the one hand to the long distance between the CF16-antenna and the atomic sample of about 100 mm. On the other hand, the cut-off frequency of waveguides (see eq. 6.42) has to be taken into account. When viewed along the horizontal axis of the main chamber, the two vertical windows act like a waveguide due to

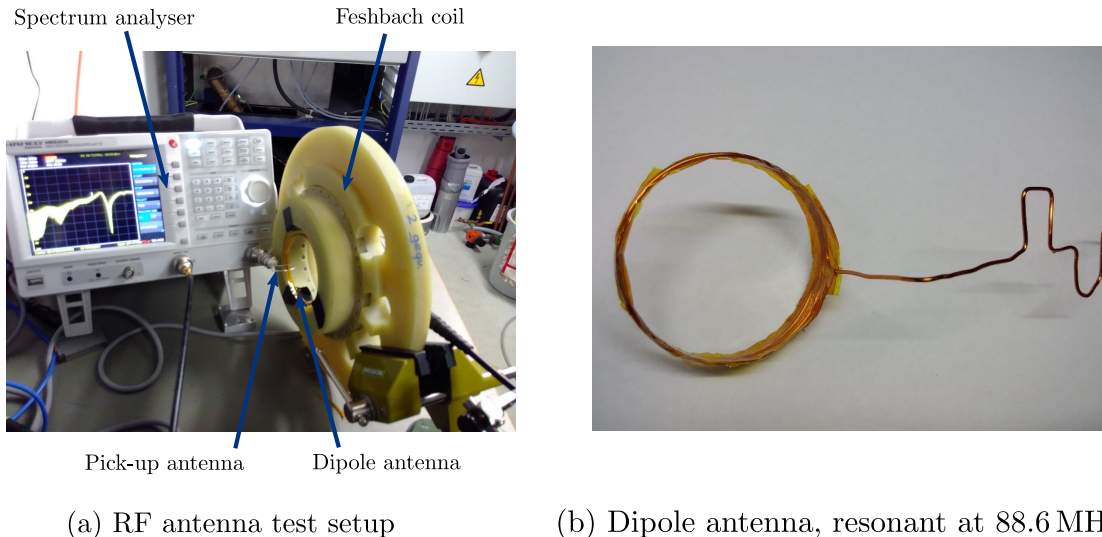


**Figure 6.48: RF antenna test setup.** The test setup to characterize the built RF antenna (a) uses a frequency generator and spectrum analyser to measure the transfer function of the antenna. The antenna is placed inside the housing of a spare Feshbach coil to resemble the final experimental implementation as detailed as possible. The radiation emitted by the antenna is picked up by a small loop antenna which is connected to the spectrum analyser. Important to note is that its central axis has to be aligned perpendicularly to the central axis of the coil housing to mimic the situation experienced by the atoms in the experiment. The photo in (b) shows the final RF antenna design which is used to perform the RF transfers. It has an effective antenna length of 315 mm, manufactured as a spiral with two windings with a diameter of 50 mm.

their stainless steel holder. Their spacing of 22 mm yields a cut-off wavelength of 44 mm. Electromagnetic radiation with a frequency of 100 MHz, having a wavelength of  $\sim 3$  m, will not enter into the region between the two windows (or will be significantly damped). To surpass this problem and to shorten the distance to the atoms, the RF antenna is placed on top of the upper vertical vacuum window.

Due to the restrictions imposed by the experiment setup, several antenna designs have been tested. For the test setup, a small single-loop pick-up antenna (diameter  $\sim 10$  mm) is placed at  $\sim 30$  mm distance from the antenna under investigation. This resembles the distance between antenna and atomic sample as present at the experiment apparatus. The small loop antenna is used since it will not be resonant with any frequency of interest, thereby measuring an unbiased transfer function of the emitted spectrum.<sup>11</sup> To address the possibility of coupling between the RF antenna and the main coils, a spare twin-coil has been used at the test setup. The emitted frequency band in the frequency region of interest is measured by sending a broad frequency output with a constant power for all frequencies (generated by a function generator, *HMS 3010, HAMEG Instruments*) to the antenna under investigation. The signal picked up by the small loop antenna is then measured with a spectrum analyser. The test setup is shown in fig. 6.48. The loop antenna couples to the magnetic field lines of the RF antenna which are parallel to its central axis (compare also fig. 6.45). Thus, this central axis has to be aligned perpendicularly to the central axis of the Feshbach coil housing to mimic the quantization axis experienced by the atoms in the main chamber and the fact that the polarization of the RF has to be perpendicular to that

<sup>11</sup>An even better and cleaner way is to use a circulator for the frequency range of interest and to measure the back reflected power versus the frequency. At the time the RF antenna was set up, such a circulator was not present in the laboratory. This is why the pick-up antenna measurement was performed.

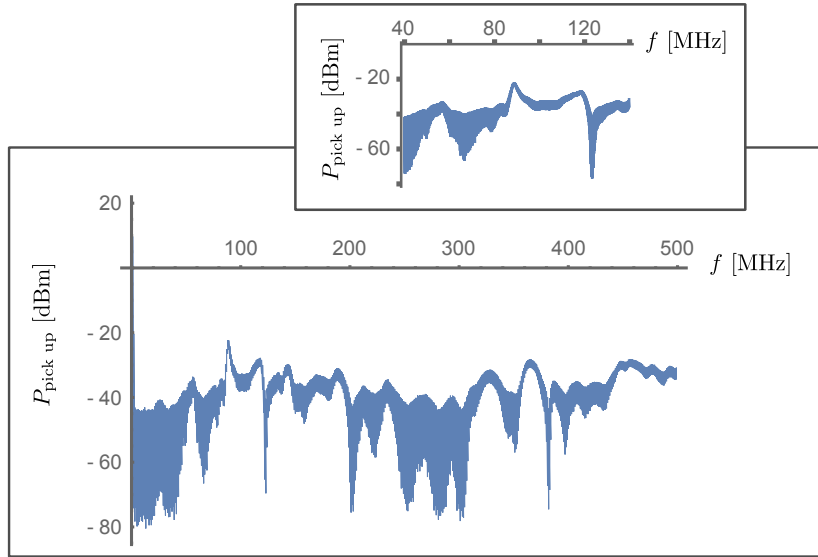


**Figure 6.49: Transfer function of the RF antenna used for the adiabatic passages.** The power is measured using a small ring antenna as pick up. Peaks in the graph are therefore indications for resonances of the RF antenna. The inset shows a zoom to the relevant region and the dominant peak at the frequency of 88.6 MHz. The measurement was taken with the antenna already placed at the experiment. Therefore, all possible interferences with other components of the experiment apparatus are already included. Note that the absolute values of the emitted and picked up power do not give any indication on how much power actually reaches the atoms. It can, however, be used for relative comparison of the performance at different frequencies.

quantization axis.

During the tests, it has been found that the loop antenna design has a broad frequency emission band. However, the radiation only couples to the atoms if the central axis of the loop antenna is perpendicular to the quantization axis. This can be represented in the test setup by turning the loop of the pick-up antenna by  $90^\circ$ . Since in the experiment setup no antenna can be placed with the central axis perpendicular to the quantization axis, loop antennas had to be abandoned.

It has been found that dipole antennas have a better emission for the geometrical restrictions present. The best performance has been achieved for a dipole antenna bent to a ring and placed off-centred inside the coil housing, as depicted in fig. 6.47. As also shown in the figure, the vertical MOT laser beam imposes a restriction on the placement and diameter of the antenna. Dipole antennas emit best on the frequency matched by their length, as can be seen from eq. 6.43. A half-wave dipole antenna would require a  $\sim 1.6$  m long wire for the target frequency of 89 MHz. Such an antenna would, however, be too voluminous. Therefore, during manufacturing the antenna,  $1/4$  of this length was used as starting point. The wire was first cut to the approximate length and the emitted centre frequency was measured with the pick-up antenna. The exact frequency was tuned by carefully reducing the length of the wire.

Fig. 6.48 (b) shows the final antenna design. It consists of a copper wire (diameter 1.0 mm) bent into a spiral of 50 mm diameter with two windings (giving an effective antenna length of 315 mm).

The emitted frequency band in the frequency region of interest is measured by sending a broad frequency output with a constant power for all frequencies (generated by a function generator, *HMS 3010, HAMEG Instruments*) to the dipole antenna and measuring the signal picked up by the small loop antenna. The test setup is shown in fig. 6.48 (a).

The best performance is achieved at the designed main frequency of 89 MHz. Due to impedance matching, this frequency shifted by 0.4 MHz when the antenna was placed at the experiment, which is why the transfer function was remeasured directly at the experiment setup. The RF transfers have been adapted to the measured centre frequency of 88.6 MHz, the measured transfer function is depicted in fig. 6.49. Adding a resistor to the feedline to improve the impedance matching, as sometimes suggested, does not work in the setup. Measuring such a feedline with a circulator can be misleading as the back reflected power is indeed reduced, but only by the amount of power dissipated as heat inside the added resistor. The picked up emitted power does either not change or might even drop. A more sophisticated impedance matching, using capacities and coils, has not been performed.

At the experiment, the frequencies are generated by the same function generator as is used for the MW evaporation. The setup is therefore identical with fig. 6.30.

### 6.12.3 Transfer efficiencies

The power emitted by the antenna proved to be crucial in the experiment. It has been found that, if working at a different than the peak frequency of the antenna, only partial transfers could be realized. Additionally, the sample was significantly heated after the transfers, indicating the necessity for a high emitted RF power.

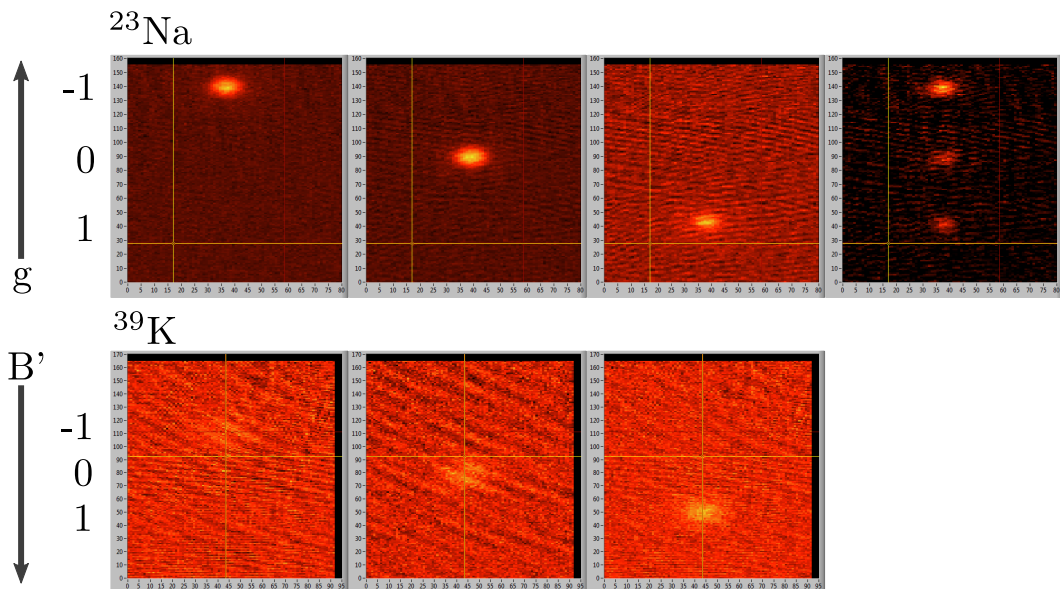


**Figure 6.50: TOF images in a Stern-Gerlach field for  $^{23}\text{Na}$  (top) and  $^{39}\text{K}$  (bottom).** The different images are pictures directly taken from the experiment imaging software. Gravitation  $g$  acts towards the top of the images due to the picture handling of the imaging software. The magnetic field gradient  $B'$  is directed opposite. The different  $m_f$  components are indicated by the numbers on the left side. For  $^{23}\text{Na}$ , also a spin mixture has been prepared (top right image). Due to different TOFs for the two species, the spread in space is different for  $^{23}\text{Na}$  and  $^{39}\text{K}$ .

Due to the dipole design of the RF antenna, only very restricted frequencies are available for the RF transfers. As can be seen in fig. 6.49, the emitted power differs by  $\sim 15$  dB between the peak and the average emitted power. Therefore, the main frequency of the antenna has carefully been chosen to enable transfers to all possible hyperfine Zeeman states. Furthermore, the exact order of the transfers is chosen with the help of preliminary theoretical knowledge of the different Feshbach resonances. Thereby, strong atom losses in between the transfers can be prevented.

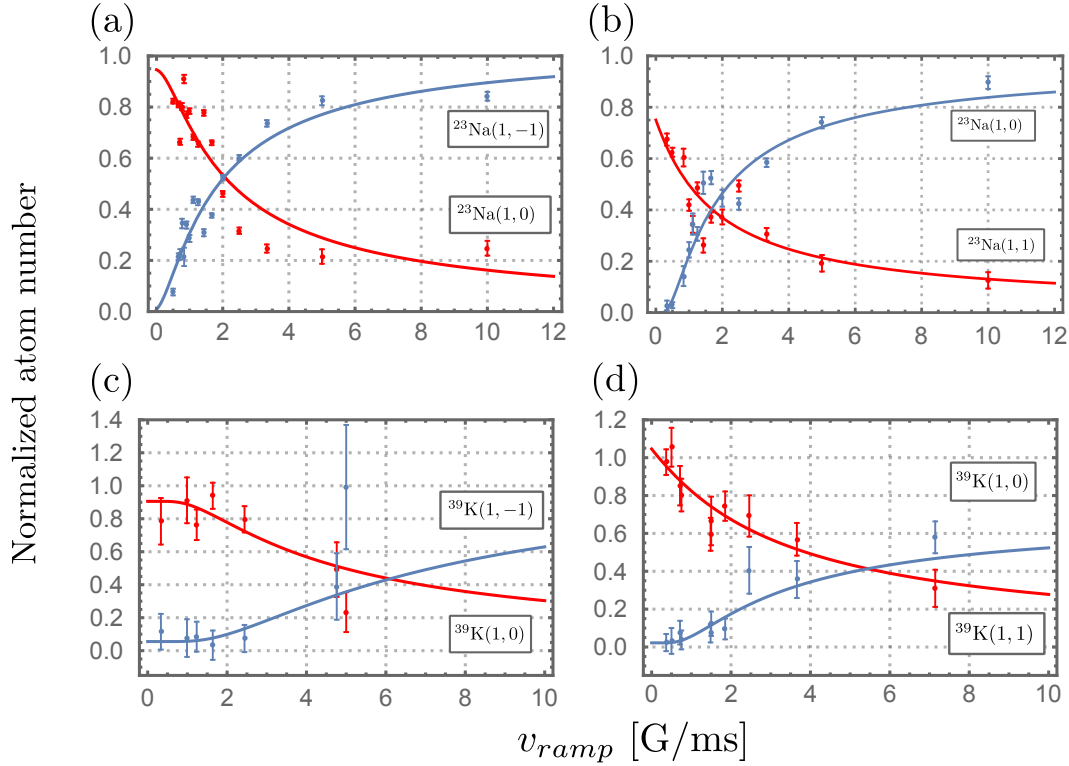


**Figure 6.51: Efficiency measurements for the different adiabatic passages.** In (a) the transfer efficiency versus the transfer speed is shown for  $^{23}\text{Na} \left| f = 1, m_f = -1 \right\rangle \rightarrow \left| f = 1, m_f = 0 \right\rangle$  and in (b) for  $^{23}\text{Na} \left| f = 1, m_f = 0 \right\rangle \rightarrow \left| f = 1, m_f = 1 \right\rangle$ . The pictures (c) and (d) show the transfer efficiencies for  $^{39}\text{K} \left| f = 1, m_f = -1 \right\rangle \rightarrow \left| f = 1, m_f = 0 \right\rangle$  and  $\left| f = 1, m_f = 0 \right\rangle \rightarrow \left| f = 1, m_f = 1 \right\rangle$ , respectively. The transfers have been performed at the maximum output power of the RF amplifier. The red dots in every graph are the transferred atom fraction while the blue ones show the atoms remaining in the Zeeman state from which the transfer started. The Landau-Zener formula is fitted to the data. The atom number is normalized to the maximum atom number given by the fit. In picture (c) and (d), only a cutout region for the slow ramp speeds is shown for lucidity. As can be seen, the transfer efficiency for each transfer well exceeds 90 % for ramp speeds below 1 G/ms. Nevertheless, high powers are needed to guarantee efficient transfers.

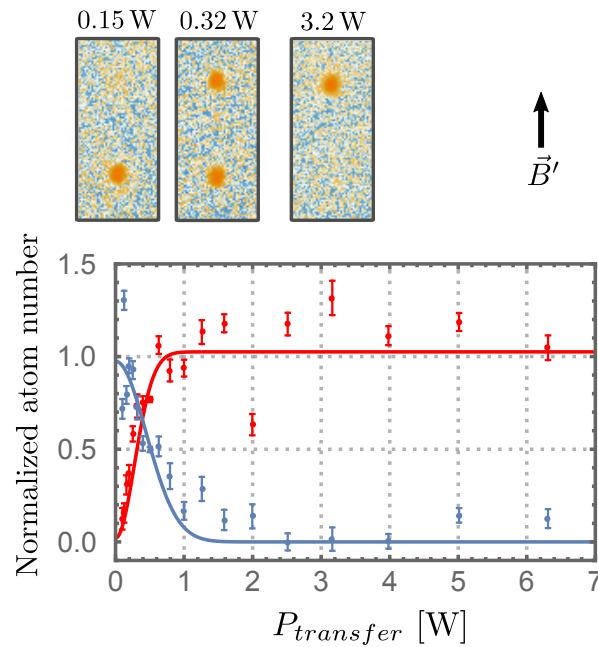
For the state transfers, ARPs are performed in the cODT by applying radio frequency pulses at 88.6 MHz and ramping the magnetic Helmholtz field over the avoided crossings. At the chosen radio frequency, the centre points of the transfers are determined by the Breit-Rabi equation, see eq. 2.11. For  $^{23}\text{Na}$ , they are located at 122.25 G for the  $\left| f = 1, m_f = -1 \right\rangle \rightarrow \left| f = 1, m_f = 0 \right\rangle$  transition and at 135.35 G for the  $\left| f = 1, m_f = 0 \right\rangle \rightarrow \left| f = 1, m_f = 1 \right\rangle$  transition. For  $^{39}\text{K}$ , the transfer points are at 142.88 G for the  $\left| f = 1, m_f = -1 \right\rangle \rightarrow \left| f = 1, m_f = 0 \right\rangle$  and at 258.74 G for the  $\left| f = 1, m_f = 0 \right\rangle \rightarrow \left| f = 1, m_f = 1 \right\rangle$  transition. To determine the efficiencies of the transfers, the magnetic field coils are switched to generate a magnetic gradient field and the atomic sample is released from the trap. In a Stern-Gerlach free fall, the high-field-seeking hyperfine states fall slower than the low-field seekers. Thereby, a separation of the different  $m_f$  components can be detected after TOF in absorption imaging [136]. In fig. 6.50, transfers of  $^{23}\text{Na}$  (top) and  $^{39}\text{K}$  (bottom) are shown as TOF images. It is also possible to prepare spin mixtures by adjusting the ramping times or RF powers, as is shown in fig. 6.50 for a spin mixture in  $^{23}\text{Na}$  with all three  $m_f$  components of the  $f = 1$  hyperfine state. Due

to the fact that only  $^{23}\text{Na}$  was prepared in a BEC for the transfer efficiency measurements, the TOF for the  $^{39}\text{K}$  is reduced to be able to image the thermal clouds. This explains the difference in spacial spread in the images of the two species.

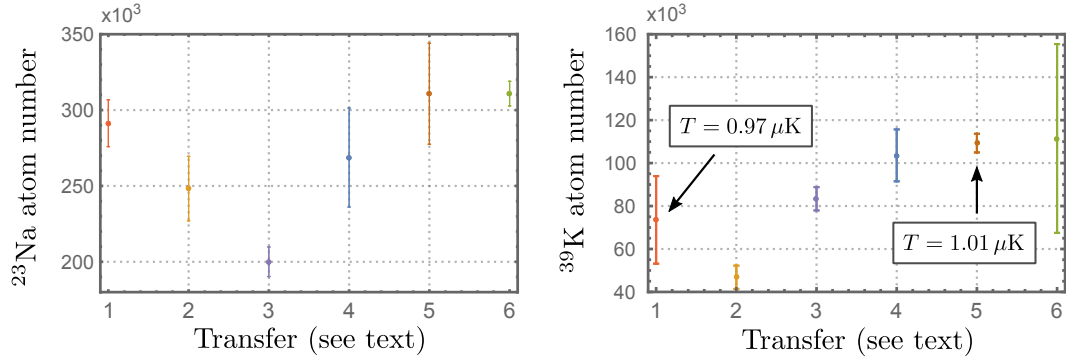
The efficiencies of the transfers are investigated by Stern-Gerlach TOF measurements. In fig. 6.51 (a)-(d), the transfer curves for all transfers in the  $f = 1$  hyperfine states of  $^{39}\text{K}$  and  $^{23}\text{Na}$  are shown. The Landau-Zener formula (eq. 6.40) is fitted to the data for a constant ratio of Rabi frequency to rate of change in detuning. The efficiency for all transfers is close to unity for ramp speeds below 1 G/ms.

Figure 6.52 shows a scan of the emitted RF power for a fixed transfer time of 30 ms for the transfer  $^{23}\text{Na} |f = 1, m_f = 0\rangle \rightarrow |f = 1, m_f = 1\rangle$ . The Landau-Zener formula is fitted to the data, this time for a constant transfer time  $t$ . It can be seen that high powers are required to guarantee efficient transfers, indicating the mentioned sub-optimal placement of the RF antenna.

With the measurements at hand, the RF power for every transfer is set to the maximum possible to reduce the transfer time as much as possible. To guarantee a stable transfer efficiency close to unity in the experiment, the transfer times have been set to 60 ms for all but the transfer  $|f = 1, m_f = 0\rangle \rightarrow |f = 1, m_f = 1\rangle$  of  $^{39}\text{K}$  for which 70 ms have been chosen. The magnetic field is ramped over  $\sim 10$  G for all but the transfer  $|f = 1, m_f = 0\rangle \rightarrow |f = 1, m_f = 1\rangle$  of  $^{39}\text{K}$ , where it is ramped over  $\sim 15$  G instead. The centres of the ramps are given by the respective avoided crossing points (see above). The reason why the latter transfer of  $^{39}\text{K}$  has to be treated differently is because of the relatively high magnetic field with which it has to



**Figure 6.52: Transfer efficiency as function of RF power.** A scan of the output power of the RF amplifier which is fed to the RF antenna is given for the transfer of  $^{23}\text{Na} |f = 1, m_f = 0\rangle \rightarrow |f = 1, m_f = 1\rangle$  (note that the output power of the amplifier saturates at 37 dBm which equals 5 W). The top images show pictures of BECs imaged in TOF in a magnetic field gradient. They are used to determine the transferred fraction. The time of this transfer is set to 30 ms for a ramp over  $\sim 10$  G. The red dots in the graph are the transferred atom fraction while the blue ones show the atoms remaining in the Zeeman state the transfer started from. The Landau-Zener formula is fitted to the data. The atom number is normalized to the maximum atom number given by the fits.



**Figure 6.53: Number of  $^{23}\text{Na}$  and  $^{39}\text{K}$  atoms after transfers.** The atoms are transferred to  $|f = 1, m_f = 1\rangle_{\text{Na}} + |f = 1, m_f = 1\rangle_K$  (data at  $x = 1$ ), to  $|f = 1, m_f = 1\rangle_{\text{Na}} + |f = 1, m_f = 0\rangle_K$  (2), to  $|f = 1, m_f = 1\rangle_{\text{Na}} + |f = 1, m_f = -1\rangle_K$  (3), to  $|f = 1, m_f = 0\rangle_{\text{Na}} + |f = 1, m_f = -1\rangle_K$  (4), no transfer, thereby sample in  $|f = 1, m_f = -1\rangle_{\text{Na}} + |f = 1, m_f = -1\rangle_K$  (5) and finally again to  $|f = 1, m_f = 1\rangle_{\text{Na}} + |f = 1, m_f = 1\rangle_K$  (6). For each transfer, the atom numbers are given as an average over at least three experiment runs. For the transfers (1) and (5), temperatures of the  $^{39}\text{K}$  atoms were measured by a series of TOF expansions. No heating of the sample due to the transfers is observed.

be performed due to the fixed RF frequency of 88.6 MHz. At the required magnetic field, the relative slope of the two Zeeman levels is already quite small, leading to a broad avoided crossing. To start the transfer with defined Zeeman states and also end the adiabatic passage in such, a wider magnetic field range has to be travelled, leading to a longer ramp time.

To perform measurements in the  $|f = 1, m_f = 0\rangle_{\text{Na}} |f = 2, m_f = -2\rangle_K$  channel,  $^{39}\text{K}$  is transferred by applying a microwave frequency of 365.50 MHz while ramping the Helmholtz field from 52.9 G to 49.9 G in 500 ms. The efficiency for this transfer is also well above 90 %.

To confirm that neither heating of the sample nor atom loss occurs due to the transfers, a series of transfers is performed, all starting with a sample in  $|f = 1, m_f = -1\rangle_{\text{Na}} + |f = 1, m_f = -1\rangle_K$ . After every transfer sequence, the atom numbers are measured and the average atom number of at least three experiment runs is calculated. Figure 6.53 shows the measurements. The atom-number variation is within the fluctuations expected from the stability of the experiment. Furthermore, for the different atom number measurements, different resonances have to be crossed to image the atoms at zero field. This can lead to additional artificial losses. To exclude the possibility of heating, the temperature of  $^{39}\text{K}$  was exemplarily measured before and after the complete transfer sequence ( $|f = 1, m_f = -1\rangle_{\text{Na}} + |f = 1, m_f = -1\rangle_K \rightarrow |f = 1, m_f = 1\rangle_{\text{Na}} + |f = 1, m_f = 1\rangle_K$ ) by a series of TOF expansions. The measured temperatures are given as insets in fig. 6.53. No heating is observed.

Taking all the characterisations into account, stable and efficient transfers of the two atomic species to all hyperfine combinations of interest can be performed using the setup presented here.

# Chapter 7

## Feshbach resonance measurements

In this chapter, the experiments performed to investigate the Feshbach resonance spectrum of  $^{23}\text{Na} + ^{39}\text{K}$  are presented. The main results of this chapter have been published in [1] and [2] and figures and tables taken from these publications are marked accordingly.

The chapter first introduces the different methods available to detect Feshbach resonances as well as zero crossings of the scattering length in sec. 7.1. For the single species  $^{23}\text{Na}$  and  $^{39}\text{K}$ , intraspecies Feshbach resonances exist which are summarised. For the preparation of an ultracold mixture in the  $1 \mu\text{K}$  range, the interspecies scattering properties at zero magnetic field become important as they can potentially hinder evaporative cooling. Therefore, they are discussed in sec. 7.2. Section 7.3 investigates the losses in  $(1, -1)_{\text{Na}} + (1, -1)_{\text{K}}$  mixtures at zero magnetic field strength. This is followed in sec. 7.4 by a detailed description of the experiment sequence which is used to measure the resonance features in various scattering channels. Finally, sec. 7.5 presents the results of the measurements. Furthermore, their impact on the known molecular potentials of NaK is discussed.

Locating the different Feshbach resonances can be a tedious task if their positions are largely unknown. To reduce the magnetic field range which has to be sampled to find the resonances, E. Tiemann calculated the positions of resonance features using the data available for the fermionic  $^{23}\text{Na}^{39}\text{K}$  at that time ([74] and [76]). The predicted positions are given in tab. 7.1 and served as a first guidance for the measurements presented here.

### 7.1 Methods to measure Feshbach resonances

As discussed in chap. 4, the scattering rate for elastic collisions is strongly enhanced at a Feshbach resonance and highly suppressed at a zero crossing of the scattering length. Therefore, one possible way of detecting these features is to measure the thermalization rate of the ensemble as a function of magnetic field strength. The enhancement of the two-body elastic scattering rate also leads to significant three-body losses since the three-body loss coefficient scales with  $L_3 \propto a^4$  [205]. Therefore, the resonance positions can also be investigated by measuring the atom loss from a trap.

For the investigation of zero crossings of the scattering length, a simple loss measurement will not yield the correct position of the feature. Although in a simple picture the three-body losses should be minimal at the point of the zero crossing, it has been shown that this is not necessarily the case [206, 207]. Therefore, to directly access the elastic two-body losses, the optical evaporation outlined in sec. 6.11.3 is used. Since  $^{39}\text{K}$  is sympathetically cooled by  $^{23}\text{Na}$ , the losses observed for sodium depend on the scattering rate between  $^{23}\text{Na}$  and  $^{39}\text{K}$  during the optical evaporation. This means that the sodium atom signal after evaporation of a sample consisting of equal amounts of  $^{23}\text{Na}$  and  $^{39}\text{K}$  can be detected as a function of the magnetic field. At the position of the zero crossing, the interspecies elastic two-body scattering rate is lowest and so are the losses in the atom number.

**Table 7.1:** Predictions for Feshbach resonances (" $_{res}$ ") and zero crossings (" $_{ZC}$ ") in  $^{23}\text{Na} + ^{39}\text{K}$ . The values have been calculated by E. Tiemann.

$M$	$(f, m_f)_{^{23}\text{Na}}$	$(f, m_f)_{^{39}\text{K}}$	$B_{res}$ [G]	$B_{ZC}$ [G]
2	1,1	1,1	410	381.5
			508.5	506.5
1	1,1	1,0	6.5	
			329	328.5
			467	442
	1,0	1,1	580.5	577.5
			8.5	
			418.5	
0	1,0	1,0	5.5	
			29.5	
			475.5	
	1,1	1,-1	15	
			393.5	393
			536.5	516.5
-1	1,-1	1,1	522.5	
			12.5	
			245	
	1,0	1,-1	107.5	
			540.5	
			138	
-2	1,1	1,-2	471	
			271.5	
			465.5	
	1,-1	1,-1	33.3	
			247.68	117.32
			650	
1,0	1,0	1,-2	229.5	
			260.5	117.32
			358.5	

### Elastic and inelastic collisions

As already stated, the two-body process of elastic collisions is strongly enhanced at a Feshbach resonance. However, it has to be kept in mind that this collision alone, to which a two-particle scattering rate is assigned, does not lead to a loss feature in a trapped sample of atoms. This is due to the fact that momentum and energy have to be conserved in a two-body scattering process. If loss features are used to investigate Feshbach resonances, the process leading to these losses is a three-body process. On the other hand, also inelastic losses can occur when molecular levels come close to resonance. In this case, already two-particle scattering can lead to direct losses from the trap. Therefore, careful interpretation of loss measurement is necessary. The different stoichiometry of the elastic and inelastic scattering process can lead to much shorter lifetimes for a sample at an inelastic feature than for a sample at an elastic feature, even though the two-particle scattering rate for the inelastic collision is e.g. an order of magnitude smaller than for the elastic feature. This is because the probability that two atoms come close to each other is statistically much higher than for three atoms to meet. Such a behaviour has been observed for the measured inelastic features as is discussed in sec. 7.5.1.

## 7.2 Known Feshbach resonances

For both atomic species used in the experiment, several intraspecies Feshbach resonances have been found already (see [94, 208–210] for  $^{23}\text{Na}$  and [211, 212] for  $^{39}\text{K}$ ). Tab. 7.2 summarises the findings.

Intraspecies Feshbach resonances are of interest as they can interfere with the measurement of interspecies resonances in two ways. First, ramping the magnetic field strength over a resonance to a value at which the actual measurement shall be performed can lead to significant losses even before the actual data is taken. Second, intraspecies resonances can lie at very similar values of the magnetic field strength as interspecies resonances, thereby distorting the measured loss feature.

## 7.3 Three-body losses in $(f=1, m_f=-1)_{\text{Na}} + (f=1, m_f=-1)_K$ mixtures

Theoretical predictions for the interspecies scattering length in the  $(f = 1, m_f = -1)_{\text{Na}} + (f = 1, m_f = -1)_K$  mixture [213] indicated a problematic situation at low magnetic field strengths due to a very high scattering length ( $a(B = 0) \approx -4000 a_0$ ). The observation that forced evaporation of the mixture in a magnetic trap is possible in the experiment setup presented in this thesis (see sec. 6.10) gives first hints that the actual scattering length is much smaller. Recent calculations done by E. Tiemann including the at that time most actual data set [37, 74] have been more consistent with this recent observation (see below).

In a first set of measurements, three-body losses in the  $(f = 1, m_f = -1)_{\text{Na}} + (f = 1, m_f = -1)_K$  mixture at zero magnetic field are investigated in detail. First the single-species losses are measured in the cODT for a  $^{23}\text{Na}$  sample at  $3 \mu\text{K}$ , giving a  $1/e$  lifetime of  $31.7 \text{ s}$  and for a  $^{39}\text{K}$  sample at  $2.7 \mu\text{K}$ , giving a  $1/e$  lifetime of  $37.8 \text{ s}$ . These lifetimes are very similar to the ones measured during the investigation of the vacuum conditions of the main chamber, see sec. 6.2, indicating that in single-species operation the losses are dominated by collisions with the background gas atoms.

Figure 7.1 shows the measurement for a mixture at  $2.6 \mu\text{K}$  where an imbalanced atom number ratio was chosen with  $N_{\text{Na}}/N_K \ll 1$ . The rapid decay of the  $^{39}\text{K}$  fraction indicates three-body losses. The three-body loss coefficient is extracted by fitting the experimentally obtained data to solutions of three coupled differential equations set up to describe the atom number loss dynamics in the mixture. The extracted loss coefficients are  $L_{\text{Na},\text{Na},K} = 1.03(62) \cdot$

**Table 7.2:** Known Feshbach resonances for  $^{39}\text{K}$  and  $^{23}\text{Na}$ . Values in square brackets in the  $B_{exp}$  column indicate a second measurement.

Species	$m_{f_a}, m_{f_b}$	$B_{exp}$ [G]	$B_{th}$ [G]	References
$^{39}\text{K}$	1,1	$25.85 \pm 0.1$	25.9	[211]
		$403.4 \pm 0.7$	402.4	[211]
			745.1	[211]
	0,0	$59.3 \pm 0.6$ [58.92 $\pm$ 0.3]	58.8	[211, 212]
		$66.0 \pm 0.9$ [65.67 $\pm$ 0.5]	65.6	[211, 212]
		$471.0 \pm 0.4$	471	[211, 212]
			490	[211]
		$32.6 \pm 1.5$ [33.64 $\pm$ 0.15]	33.6	[211, 212]
	-1,-1	$162.8 \pm 0.9$ [162.35 $\pm$ 0.18]	162.3	[211, 212]
		$562.2 \pm 1.5$ [560.72 $\pm$ 0.20]	560.7	[211, 212]
$^{23}\text{Na}$	1,1	$493.6 \pm 0.2$	493.4	[94]
		$508.0 \pm 0.2$	507.6	[94]
		$508.8 \pm 0.2$	508.9	[94]
		$510.9 \pm 0.2$	511.2	[94]
		$536.6 \pm 0.2$	535.7	[94]
		$586.3 \pm 0.2$	585.2	[94]
		$644.8 \pm 0.3$	644.1	[94]
		$662.8 \pm 0.3$	663.8	[94]
		$715.6 \pm 0.1$	715.4	[94]
		$727.1 \pm 0.1$	730.3	[94]
	-1,-1	$851.0 \pm 0.2$ [853]	84.82	[94, 208]
		$905.1 \pm 0.4$ [907]	908.1	[94, 208]
		$1590.0 \pm 0.3$	1590.2	[94]
		$2054.2 \pm 0.4$	2054.5	[94]
		1195	$1219.0 \pm 2.2$	[209, 210]
			$1497 \pm 1$	[210]
			$2634 \pm 2$	[210]

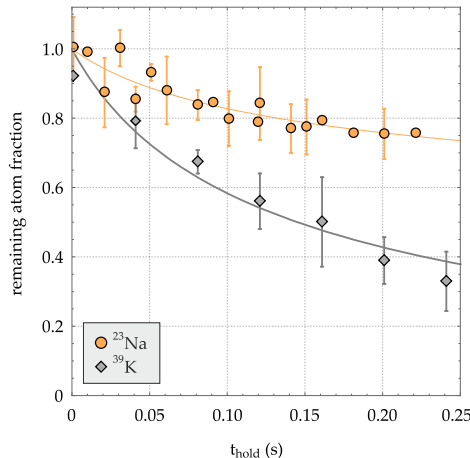


**Figure 7.1: Lifetime measurement in a mixture of  $^{23}\text{Na}$  and  $^{39}\text{K}$ , both in the  $|f = 1, m_f = -1\rangle$  hyperfine state.** An atom-number imbalanced sample is produced for this measurement. The normalised atom numbers for  $t = 0$  correspond to  $3.8 \cdot 10^5$  for  $^{23}\text{Na}$  and to  $1.1 \cdot 10^5$  for  $^{39}\text{K}$ . The measurement is performed at zero magnetic field. The fit gives the 1/e lifetime of 240 ms for  $^{39}\text{K}$  while the sodium atom number is only marginally reduced. Figure taken from [2].

$10^{-25} \text{ cm}^6 \text{s}^{-1}$  and  $L_{\text{Na},\text{K},\text{K}} = 0.5(3) \cdot 10^{-25} \text{ cm}^6 \text{s}^{-1}$ . By comparison with other investigations on loss rate coefficients [214–217], they appear to be compatible with the theoretically calculated scattering length for  $(f = 1, m_f = -1)_{\text{Na}} + (f = 1, m_f = -1)_{\text{K}}$  of  $a(B = 0) = -416 a_0$ . For more details about the calculations see [2, 36]. Although the background scattering length proved to be smaller than first predicted, it nevertheless impedes forced evaporation in the magnetic trap as observed in the experiment (see sec. 6.10.4). Furthermore, evaporative cooling of the mixture in the cODT at zero magnetic field suffers from the high interspecies scattering length. This directly motivates the detailed investigations of the interspecies scattering length over a large range of magnetic field strength.

## 7.4 Sequence for Feshbach measurements

In this section, the experiment sequence is described which is used to perform the Feshbach resonance and zero crossing measurements.

### 7.4.1 Magnetic field calibration

An accurate knowledge of the magnetic field strength is crucial for the investigation of Feshbach resonances. Since the magnetic field strength is only indirectly controlled by the current flowing through the Feshbach coils, a detailed calibration of the dependence of electrical current to actual magnetic field strength is needed.

The magnetic field is calibrated by MW spectroscopy of the  $^{23}\text{Na}$  state-transition from  $|f = 1, m_f = -1\rangle$  to  $|f = 2, m_f = 0\rangle$  at a given electric current. State-selective imaging on the  $f = 1$  to  $f' = 2$  transition is used to measure the atom number in the  $f = 1$  state as a function of the MW frequency for a set coil current. The dependence between current and magnetic field can then be calculated by applying the Breit-Rabi formula, see eq. 2.11. To obtain a high accuracy, several such measurements are performed over the range of magnetic field values of interest. Figure 7.2 shows this principle as well as the obtained calibration.

To account for possible day-to-day drifts in the magnetic field strength on the sub-Gauss level, it is reasonable to perform a field calibration on a smaller scale immediately after a

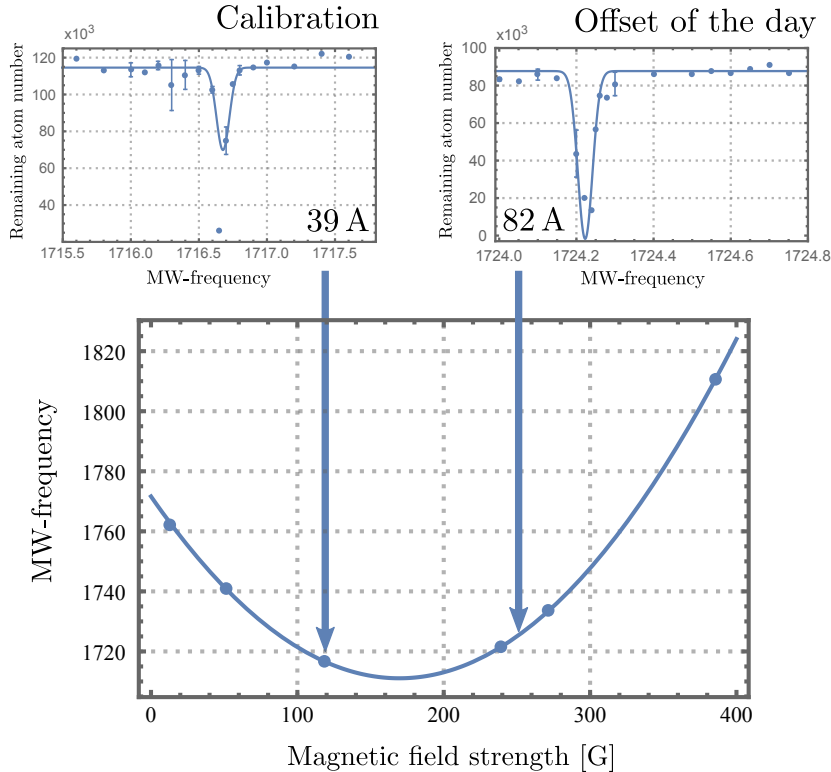


**Figure 7.2: Magnetic field calibration.** For different electric currents flowing through the Feshbach coils, MW spectroscopy measurements are performed (upper left graph shows one representative measurement). Using the Breit-Rabi formula, the magnetic field strength is calculated. Several such measurements yield the magnetic field calibration curve (lower graph). After a resonance measurement, an "offset of the day" is determined by a small set of MW spectroscopy measurements around the magnetic field values of the Feshbach scan (upper right graph shows a representative measurement).

data set related to a Feshbach resonance (or zero crossing) has been collected. It was aimed at recording at least one set of calibration data per measured resonance, containing of one to three MW measurements at field strengths close to the investigated field. This set lead to the "offset of the day" which is used to correct the calibration at the position of the feature.

For some measurements, no "offset of the day" calibration data could be recorded (e.g. due to failures of the experiment apparatus). The magnetic field strengths for such measurements are calculated by using the detailed main calibration given in fig. 7.2 . Additionally, a second field calibration is obtained using "offset of the day" data from previous measurements. The final magnetic field values used in that cases are the average of the two calibrations, performing full error propagation.

#### 7.4.2 Preparation of a cold mixture in the cODT

As has been shown in sec. 7.3, keeping the atomic mixture at zero magnetic field strength leads to undesired losses. Additionally, the intra- and interspecies scattering properties are unfavourable for a combined optical evaporation. That is why for the dual-species optical evaporation, the magnetic field strength has to be adjusted to obtain optimal scattering lengths, according to calculations performed by E. Tiemann.

For all measurements presented in this chapter, the preparation of the atomic samples inside the cODT is to a certain extent the same. First, the dual 3D MOT is loaded as described in sec. 6.7.1. The atoms are then transferred to the magnetic trap in the same way as in sec. 6.8.

After the forced MW evaporation (see sec. 6.10), the pre-cooled sample is transferred to the cODT, following the sequence described in sec. 6.11.2.

After the magnetic fields are ramped down to zero, the H-bridge is used to switch the coil configuration to provide Helmholtz fields. The magnetic Helmholtz field is ramped up to 106.9 G in 5 ms where the sample equilibrates for 170 ms. The chosen field is predicted to be in a region of overall low scattering lengths. This proved to be correct after the measurements presented in this chapter were used to precisely calculate the internuclear scattering length (giving  $a_{\text{NaK}} = 25.3 a_0$  using the data obtained in sec. 7.5 and  $a_{\text{Na}} = 52 a_0, a_{\text{K}} = 7.6 a_0$ ). For the full picture see fig. 8.3 in the next chapter.

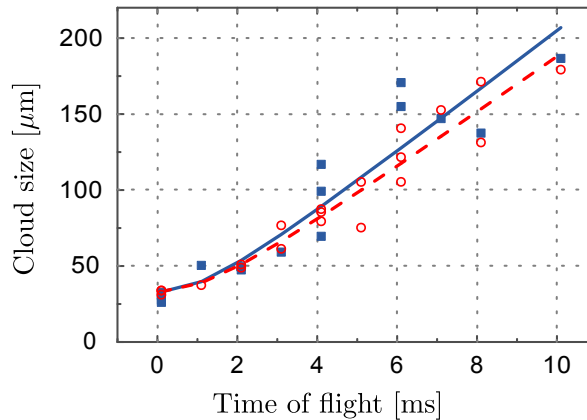


**Figure 7.3: Determination of sample temperature for Feshbach measurements.** A series of TOF measurements is performed on sodium atoms released from the cODT after optical evaporation in a Feshbach resonance-measurement sequence. The dependence on the TOF of the cloud size in  $x$  (blue squares) and  $y$  (red circles), imaged along the horizontal direction of the experiment main chamber, is fitted with eq. 6.27 giving a sample temperature of  $(1.13 \pm 0.14) \mu\text{K}$  in  $x$  and  $(0.95 \pm 0.07) \mu\text{K}$  in  $y$  direction.

For the following optical evaporation, it is intended to use  $^{23}\text{Na}$  as a coolant for  $^{39}\text{K}$  due to the smaller trap depth of  $^{23}\text{Na}$  and its larger atom numbers in the 3D MOT. For this purpose a sufficiently high interspecies scattering rate is needed as otherwise thermalization will not be fast enough. Likewise, the intraspecies scattering lengths should be small to prevent three-body losses of  $^{39}\text{K}$ . A magnetic field strength of  $\sim 83$  G (yielding  $a_{\text{NaK}} = 120 a_0$  using the data obtained in sec. 7.5 and  $a_{\text{Na}} = 52 a_0, a_{\text{K}} = 10.8 a_0$ ) is used which was empirically optimised by observing the performance of the two-species optical evaporation. In an evaporation step of 2.5 s duration, the powers of the cODT beams are reduced to 260 mW for the strong confining beam along  $y$  and 850 mW for the elliptically shaped beam along  $x$ . The obtained temperatures are  $\sim 1 \mu\text{K}$  for both species, as measured by a series of TOF expansions, see fig. 7.3 for a representative measurement on sodium. The time dependence of the cloud expansion is fitted using eq. 6.27, both in  $x$  and  $y$  direction.

#### 7.4.3 Adjusting the initial atom numbers

The initial atom numbers of the two species are varied for the atom loss spectroscopy to prepare one species as the majority fraction and the other one as the minority the losses of which are primarily measured. To adjust the atom numbers, different tuning knobs in the experiment sequence can be used.

The first one is given by the loading times of the atoms into the dual 3D MOT, which influences the initial numbers of atoms in the magnetic trap. This includes both the absolute atom numbers as well as the ratio of both species, depending on how long the two 3D MOTs are operated, see fig. 6.24 for comparison.

The second tuning knob is related to the observation that the repulsion of  $^{39}\text{K}$  by the blue-plug potential is smaller than for  $^{23}\text{Na}$ . This is because for  $^{39}\text{K}$ , the blue-plug laser frequency is farther blue-detuned than for  $^{23}\text{Na}$  (see also eq. 6.34). Hence, a deeper evaporation and thereby a colder atomic sample leads to an increased  $^{39}\text{K}$  density close to the centre of the magnetic trap compared to the density of  $^{23}\text{Na}$ . Thus, the losses for  $^{39}\text{K}$  are enhanced and therefore a deeper evaporation shifts the atom ratio inside the cODT towards  $^{23}\text{Na}$ .

#### 7.4.4 Atom loss measurements

After the optical evaporation in the cODT, the atoms are transferred to the Zeeman spin states of interest by applying the RF-driven adiabatic passages described in sec. 6.12. The order of the transfers is adapted to the preliminary theoretical knowledge of the different Feshbach resonances (see tab. 7.1) to prevent strong atom losses in between the transfers.

To locate resonant loss features, the magnetic field is then ramped to the target value within a few milliseconds. The exact duration depends on the magnetic field strength at which the last state transfer ended and on the magnetic field value which shall be reached. The ramp time is limited by the speed with which the Feshbach coils can be driven. An overshoot in the current, present for very fast ramps (see segment A in fig. 6.20), could lead to a false signal in the measurement, especially when the target value is close to a resonance. To avoid this, the ramp time has to be sufficiently long. Additionally, eddy currents in the experiment chamber can prevent very fast ramps. To still achieve reasonably fast ramp times in the range of a few milliseconds, a pre-ramp is implemented if necessary. The pre-ramp is used to reach a magnetic field close enough to the target magnetic field so that the last actual ramp can be fast. This last magnetic field ramp is on the order of 150 G in 2 - 3 ms.

At the target magnetic field, the atom mixture is held to allow for the three-body losses to deplete the atoms in the cODT. For every investigated mixture the optimal holding time is determined experimentally by ensuring that the minority sample is not depleted completely at the resonance but that the loss feature is well visible. The holding times are between 10 ms and 1000 ms.

After the holding time, the number of remaining atoms is recorded by absorption imaging of the majority component in the cODT and of the minority component after a short TOF. The imaging is performed on the horizontal axis (see sec. 6.9.2 for details). If possible, the magnetic field is ramped down to zero (including the guiding field of the vertical compensation coils) in 5 to 40 ms (depending on the initial magnetic field value). Then the majority component is imaged in trap at zero magnetic field. To remove possibly remaining majority atoms after their detection, resonant light of a few mW is applied for 40 ms. Subsequently the cODT is switched off and the minority probe atoms are imaged after 50  $\mu\text{s}$  of TOF. The short TOF time is chosen to enhance the signal-to-noise ratio and TOF is primarily performed to image the minority component without any confinement. As discussed in sec. 6.9.2, a magnetic or optical confinement leads to an inferior image quality for the imaging system used.

For some spin state combinations, it has been found that low-field Feshbach resonances or high background scattering lengths lead to unwanted losses when both species are imaged at zero magnetic field. To circumvent these losses, the implemented high-field imaging on the  $^{39}\text{K}$  D2 line (see sec. 6.9.2) is used to image  $^{39}\text{K}$  before ramping the magnetic field strength to zero. A magnetic field value in the vicinity of the investigated resonance is chosen, for which no other resonance has to be crossed and for which the scattering rate of the state combination under investigation is low. The image of  $^{39}\text{K}$  is taken at that field in the cODT. Next, all of the remaining  $^{39}\text{K}$  atoms are removed using a resonant light pulse. With only the  $^{23}\text{Na}$  fraction left, the magnetic field is ramped to zero and the  $^{23}\text{Na}$  image is taken after a TOF as explained above. All loss measurements to identify Feshbach resonances were performed following the sequence outlined above.

In case of the investigation of zero crossings of the scattering length, one has to avoid the problems arising from simply searching for a minimal rate of losses when holding the trapped sample at a given magnetic field. Therefore, the state transfer is performed directly after transferring the two species to the cODT. The magnetic field is then scanned already during the optical evaporation (see sec. 6.11.3) which follows the state transfers. With this procedure the elastic two-body losses are directly accessed. The maximum of the atom signal measured in TOF after the evaporation of a sample with equal amounts of  $^{23}\text{Na}$  and  $^{39}\text{K}$  at the beginning of the evaporation is then assigned to the respective zero crossing under investigation.

#### 7.4.5 Image post-processing

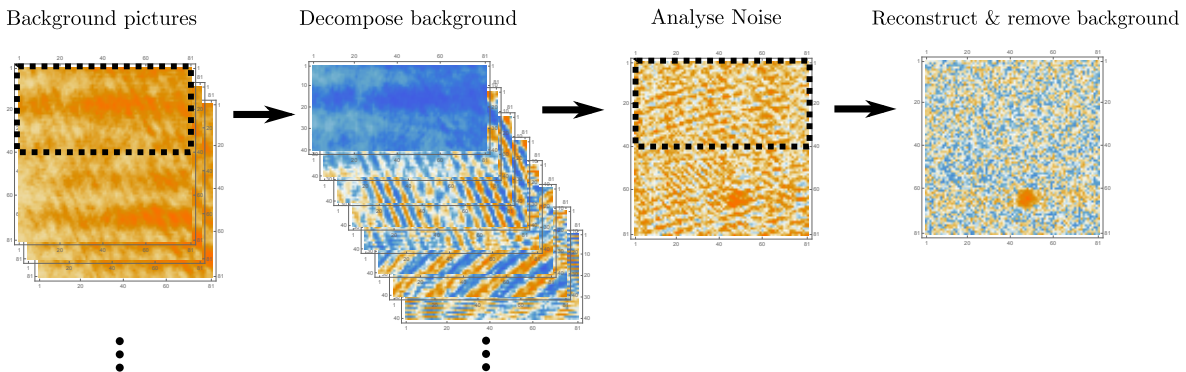


**Figure 7.4: Schematic representation of the principle component analysis procedure.** A set of background pictures (only three shown here for lucidity) is decomposed into the patterns common to most of the background pictures. For every image containing the atomic signal the noise is analysed. The background is reconstructed using combinations of the decomposed patterns and removed from the image. The black dashed box indicates the ROI for the PCA.

The picture processing at the experiment is described in sec. 6.9.1. For most measurements, the described procedure of using a single background picture per image is sufficient to obtain good image quality. However, for the atom loss measurements performed to investigate the Feshbach resonances, it is found that calculating the atom numbers from images of very small numbers of atoms is error-prone. To increase the signal-to-noise ratio, the absorption images of  $^{23}\text{Na}$  and  $^{39}\text{K}$  are therefore post-processed. This post-processing was performed for all measurements presented in this chapter.

The applied procedure is illustrated in fig. 7.4. The background of every picture is reconstructed by involving a principal component analysis (PCA) [218]. The PCA uses the complete set of background pictures taken during the measurement of the loss feature under investigation. Patterns common to many of these background pictures (e.g. diffraction patterns present in every experiment image) are identified by the algorithm and stored as decomposed features. The backgrounds of the pictures which contain the atomic signals are then analysed by selecting a region of interest (ROI) for every picture that does not contain the atomic feature. The section of the background inside the selected ROI is decomposed into contributions of the different background features stored by the PCA. The complete image background is then reconstructed using weighted combinations of the stored decomposed background features according to their contributions in the selected ROI. In fig. 7.4, a representative atom image is shown before and after the PCA. As can be seen, the distorting features, mainly diffraction patterns, are significantly reduced by the PCA.

After post-processing of the pictures from all experiment runs, the pictures recorded at equal magnetic field values are averaged. Typically at least three pictures are taken for every

sampled magnetic field value to reduce shot-to-shot fluctuations of the experiment. The averaged picture is fitted with a two-dimensional Gaussian. From the fit, the atom number is derived in a similar way as described for the picture handling software, see sec. 6.9.2. The error bars on the atom numbers given in every graph in this chapter result from the standard deviation of the two-dimensional Gaussian fit.

## 7.5 Results

Twenty-one loss features have been measured in the course of this thesis. Fourteen belong to Feshbach resonances with three-body losses, three to inelastic losses and four to zero crossings. Additionally, one broad loss feature was observed in the  $|1, -1\rangle_{\text{Na}} |1, 0\rangle_{\text{K}}$  channel which cannot be explained so far. In the following, the experiment results are presented and discussed. Additionally, the calculated resonance positions using the new refined molecular potentials are listed.

### 7.5.1 Experiment results

Intraspecies Feshbach resonances for  ${}^{39}\text{K}$  were measured first, in part to test the experiment setup for its capability to measure such features, in part to cross-check the magnetic field calibration by comparing the extracted resonance positions with their values already published in the literature. Fig. 7.5 exemplarily shows the atom loss measurement of the two Feshbach resonances around 480 G in the  $|1, 0\rangle_{{}^{39}\text{K}} + |1, 0\rangle_{{}^{39}\text{K}}$  channel. A Gaussian fit is performed to extract the position of each resonance. The error bars on the atom numbers originate from the fit procedure to the images described above. The fit is done using the bare coil current values. This means that the resonance position is first derived in Ampere, the error resulting from the standard deviation of the Gaussian fit to the loss feature. The resonance position in Gauss is then obtained by using the magnetic field calibration (see sec. 7.4.1) while ensuring full error propagation. Tab. 7.3 compares the intraspecies Feshbach resonance positions found for  ${}^{39}\text{K}$  with those listed in tab. 7.2. They agree with each other within the respective error bars.

**Table 7.3:** Measured intraspecies Feshbach resonance positions  $B_{\text{exp}}$  with systematic uncertainties ( $\pm$ ) for  ${}^{39}\text{K}$  in  $f = 1$  compared to the values given in tab. 7.2 called  $B_{\text{exp},\text{publ}}$  and  $B_{\text{th}}$  (for the theoretical predictions) in this table.

$m_{f_a}, m_{f_b}$	$B_{\text{exp}}$ [G]	$B_{\text{exp},\text{publ}}$ [G]	$B_{\text{th}}$ [G]
1,1	-	$25.85 \pm 0.1$	25.9
	$401.03 \pm 1.99$	$403.4 \pm 0.7$	402.4
0,0	$58.66 \pm 0.58$	$59.3 \pm 0.6$ [ $58.92 \pm 0.3$ ]	58.8
	-	$66.0 \pm 0.9$ [ $65.67 \pm 0.5$ ]	65.6
	$472.35 \pm 1.58$	$471.0 \pm 0.4$	471
	$492.55 \pm 2.02$	-	490
-1,-1	$32.29 \pm 83$	$32.6 \pm 1.5$ [ $33.64 \pm 0.15$ ]	33.6
	-	$162.8 \pm 0.9$ [ $162.35 \pm 0.18$ ]	162.3

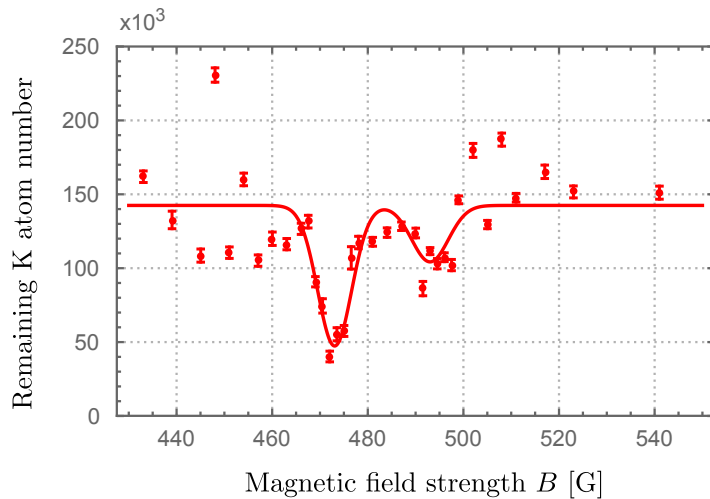


**Figure 7.5:** Remaining potassium atom number in the  $|1, 0\rangle_{^{39}\text{K}} + |1, 0\rangle_{^{39}\text{K}}$  channel as a function of magnetic field strength. Two Feshbach resonances are associated with the two loss features measured.

The measurements of the  $^{39}\text{K}$  resonances have also been necessary, because at several occasions they lie close to a predicted  $^{23}\text{Na}+^{39}\text{K}$  resonance. This is for example the case for the low-field  $^{23}\text{Na}+^{39}\text{K}$  resonance in the  $|1, -1\rangle_{\text{Na}} |1, -1\rangle_{\text{K}}$  channel. To extract the resonance position, only the wings of the measured interspecies feature are used for which the intraspecies  $^{39}\text{K}$  resonance does not disturb the data. This is shown in fig. 7.6.

Fig. 7.7 shows an overview over all  $^{23}\text{Na}+^{39}\text{K}$  features which could be measured and identified over the course of this thesis. In the case that the loss feature was clearly visible both in the majority and in the minority atomic sample, the most representative one is selected for the figure. For each loss feature, the atom number as a function of the magnetic field is fitted to a phenomenological Gaussian with the weight for each field point given by the standard deviation from the evaluation of the atom number. For every measurement,

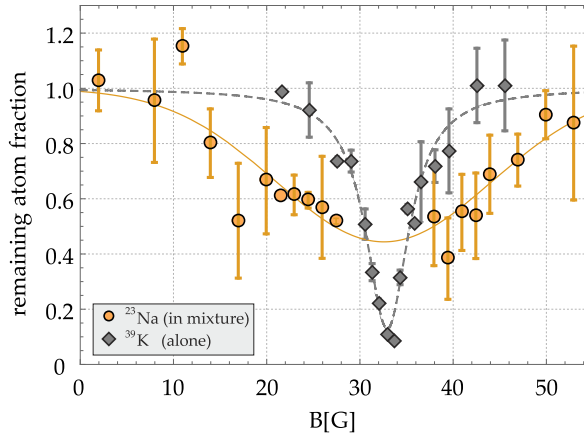


**Figure 7.6:** Remaining atom fraction in the  $|1, -1\rangle_{\text{Na}} |1, -1\rangle_{\text{K}}$  channel as a function of magnetic field strength.  $^{39}\text{K}$  atom number loss in single-species operation (grey diamonds) and  $^{23}\text{Na}$  losses in dual-species operation (yellow dots) unveil two overlaid resonances. The fitted function (dashed line) determines the homonuclear resonance. A Gaussian fit (solid line) to the wings of the  $^{23}\text{Na}$  minority signal determines the heteronuclear resonance location. The absolute atom numbers are  $3 \cdot 10^4$  ( $^{23}\text{Na}$ ) and  $1.5 \cdot 10^5$  ( $^{39}\text{K}$ ). Figure taken from [2].

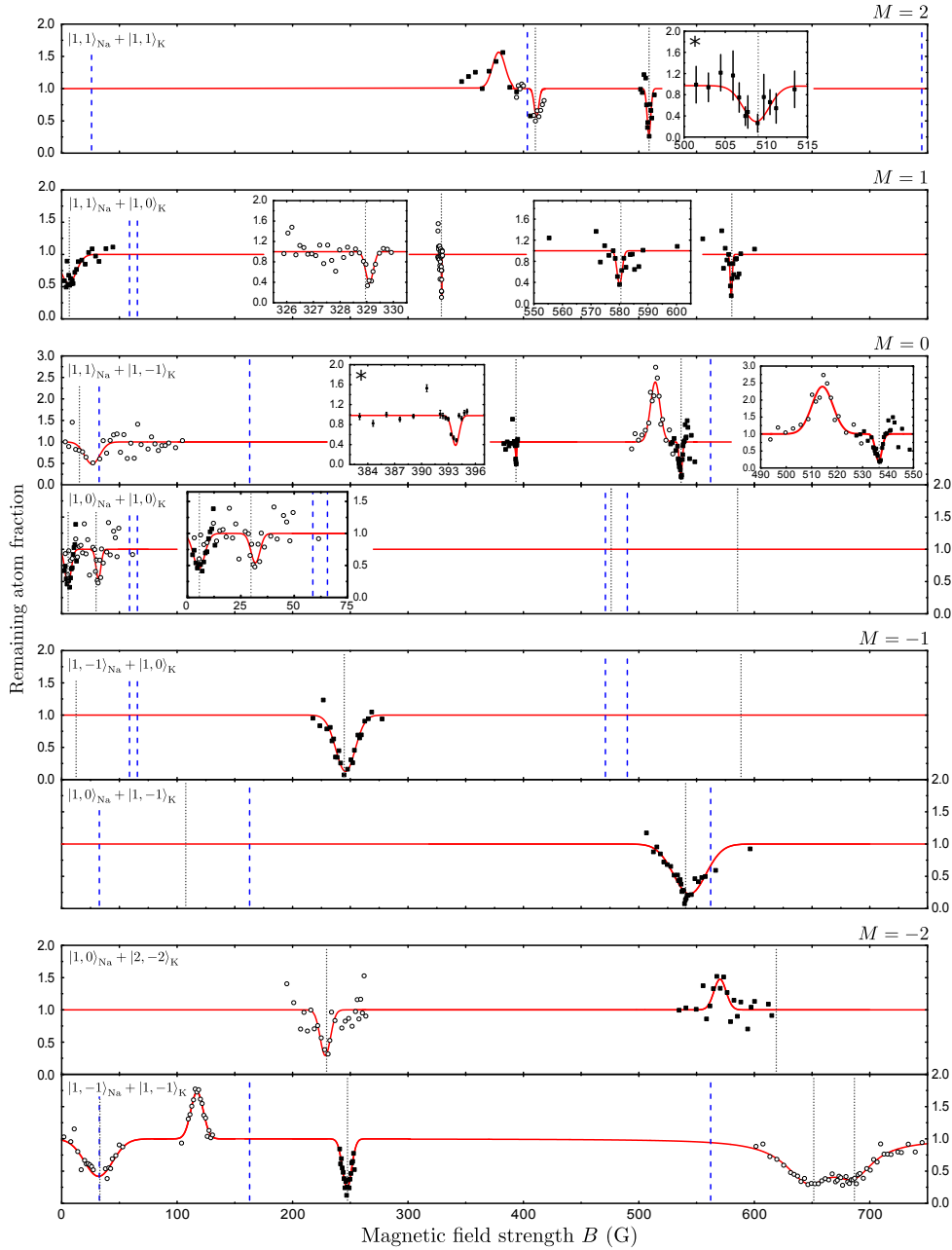


**Figure 7.7: Collection of resonant features in different spin mixtures of  $^{23}\text{Na} + ^{39}\text{K}$ .**  $M$  is the total magnetic quantum number of the pair  $|f, m_f\rangle_{\text{Na}} + |f, m_f\rangle_{\text{K}}$ ,  $f$  is for increasing magnetic field strength  $B$  only an approximate quantum number. Open circles and solid squares correspond to resonances observed by loss of  $^{23}\text{Na}$  and of  $^{39}\text{K}$ , respectively. Insets show zooms to the detected narrow resonance features. For two measurements, in  $|1, 1\rangle_{\text{Na}} + |1, 1\rangle_{\text{K}}$  and  $|1, 1\rangle_{\text{Na}} + |1, -1\rangle_{\text{K}}$  marked with (\*), error bars are given, representing the variation in the errors for different loss measurements. For each recording, the holding time and the initial atom numbers are independently optimized. The data are normalized according to the respective phenomenological Gaussian fit (red solid line) of the feature with a baseline set to one. Zero crossings appear therefore artificially as enhancement of the atom number. Vertical grey dotted lines indicate the calculated positions of  $^{23}\text{Na} + ^{39}\text{K}$  Feshbach resonances as listed in Tab. 7.4. Vertical dashed blue lines mark the positions of  $^{39}\text{K}$  resonances, taken from [211, 212]. The trace for the  $|1, -1\rangle_{\text{Na}} + |1, -1\rangle_{\text{K}}$  mixture corresponds to data from Ref. [2]. Figure taken from [1].

the atom number is normalised to the one measured far away from the resonances. In fig. 7.7, the normalised atom numbers of the different measurements for every channel are set equal. This leads to an artificial increase in the normalized atom number above one in case of a measured zero crossing. The resulting positions of all measured features are collected in Tab. 7.4 at the end of this chapter. In cases of loss features being visible for both species, the position of the resonance is the weighted average of the centre positions from the two fits. The error estimate of the experimentally determined resonance positions given in Tab. 7.4 includes the uncertainty in the profile fit and the uncertainty in the calibration of the magnetic field strength.

As visible in Tab. 7.4, some calculated resonances remain undetected. The main reasons are:

- Some of the state combinations experience a very high background scattering rate over the entire investigated magnetic field range. For these spin mixtures, the resonances are hidden since the atomic samples experienced too high losses already during the state preparation and the ramp to the target magnetic field.
- While pure  $^{23}\text{Na}$  does not exhibit significant loss features in the investigated range of magnetic field,  $^{39}\text{K}$  possesses several Feshbach resonances for the different spin states investigated in this thesis. Some of them are critical to the measurements since they lie very close to the resonance positions predicted for  $^{23}\text{Na}+^{39}\text{K}$ . These cases are mentioned in Tab. 7.4. Additionally, the potassium Feshbach resonances are indicated in Fig. 7.7 as blue vertical dashed lines.

To access more Feshbach resonances than presented in this thesis, the problems of large background scattering lengths and overlapping intraspecies resonances would need to be overcome. Recently, a method was presented that investigates Feshbach resonances in caesium by employing a Mott insulator phase which protects the atomic ensemble from high background three-body losses [219]. This, however, would require loading  $^{23}\text{Na}$  and  $^{39}\text{K}$  to a three-dimensional optical lattice. Such a lattice configuration is planned for the future of this experiment apparatus but was not implemented yet during the course of the measurements presented in this thesis.

### Special features

During the investigations of the scattering properties of  $^{23}\text{Na}+^{39}\text{K}$ , two features were detected that cannot easily be assigned to a Feshbach resonance.

For the first feature, calculations predict a Feshbach resonance at 15 G in the  $|1, 1\rangle_{\text{Na}} |1, -1\rangle_{\text{K}}$  channel. The measurements show a broad loss peak at 26.34 (3.31) G instead, see fig. 7.8 and tab. 7.4 below. The large deviation can be explained by considering both scattering rates, the elastic and the inelastic one. Fig. 7.8 shows the elastic peak at 15.2 G and an enhancement of the inelastic loss rate at 28.4 G. The inelastic part is due to the coupling to the  $|1, 0\rangle_{\text{Na}} |1, 0\rangle_{\text{K}}$  channel and gains a rate boost by a close lying Feshbach molecular state, which is responsible for the Feshbach resonance of the aforementioned entrance channel at 29.5 G. For the detection, the inelastic losses take place on a shorter timescale due to the fact that they are a pure two-body effect. They thereby dominate the losses originating from the elastic part of the scattering rate (losses due to a three-body effect). The elastic peak might be hidden in the shoulder of the profile but could not be resolved in the performed measurement. The strong dominance of the inelastic scattering rate is an interesting effect as it illustrates that careful analysis of the underlying physics is necessary to clearly assign a measured loss feature to its physical origin.

In several channels, the calculations predict maxima of the elastic and inelastic scattering rates to appear close to each other, see tab. 7.4 below. For several measurements of Feshbach resonances shifts and asymmetric broadening of the loss signals have been reported

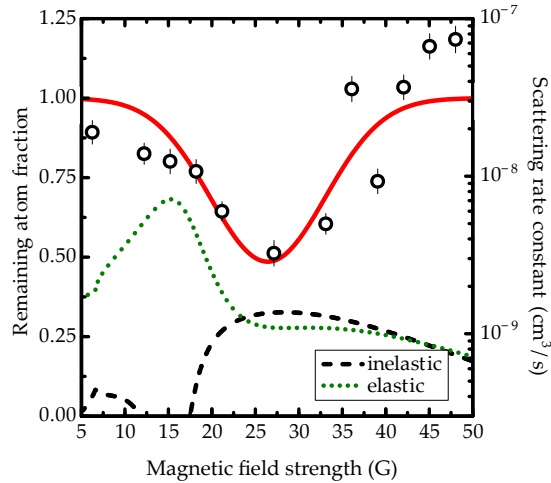


**Figure 7.8: Atom loss measurement in  $|1,1\rangle_{\text{Na}} + |1,-1\rangle_{\text{K}}$ .** Remaining atom fraction of  $^{23}\text{Na}$  (open circles) and Gaussian fit (red curve) as well as elastic (green dotted line) and inelastic (black dashed line) collision rate constants for the  $|1,1\rangle_{\text{Na}} + |1,-1\rangle_{\text{K}}$  channel. The rate constants have been calculated by E. Tiemann for a kinetic energy of  $1\mu\text{K}$ . The peak densities in the cODT for this measurement were  $2.2 \cdot 10^{12} \text{ cm}^{-3}$  for  $^{23}\text{Na}$  and  $4.4 \cdot 10^{13} \text{ cm}^{-3}$  for  $^{39}\text{K}$ . Figure taken from [1].

[220–225]. They have been attributed to processes like weakly-bound dimer formation and subsequent secondary losses. Closely located maxima of elastic and inelastic scattering rates can be an additional reason for the observed discrepancies. To access such Feshbach resonance positions precisely, binding energy measurements can be performed [226].

The second loss feature was detected in the  $|1,-1\rangle_{\text{Na}} |1,0\rangle_{\text{K}}$  channel, see fig. 7.9, without matching any theoretical predictions for possible Feshbach resonant structures, neither in the elastic nor inelastic loss rate calculations up to d-wave contributions. Fig. 7.9 presents the calculations for the channel and an enlarged section of the relevant region showing the different scattering rates of  $|1,0\rangle_{\text{K}} |1,0\rangle_{\text{K}}$ ,  $|1,-1\rangle_{\text{Na}} |1,-1\rangle_{\text{Na}}$  and for  $|1,0\rangle_{\text{Na}} |1,-1\rangle_{\text{K}}$ , revealing only an inelastic feature around 69 G. The reason for the large atom loss at around 90 G remains unknown. The sequence was checked for possible flaws and the measurement was repeated after the upgrade of the apparatus had been performed (see chap. 6), showing the same behaviour. Possible effects from the cODT whose beams are modulated with 80 MHz can be excluded as a molecule association would require different energies. Further future measurements could be performed to exclude technical issues as source of the feature.

### 7.5.2 Theoretical calculations

The calculations for the presented measurements are twofold. The methods used depend upon whether a prediction for the Feshbach resonances is needed or whether experimentally acquired data is used to optimise the knowledge about the involved molecular potentials. This process is iterative. Every new set of experimental data can be used to optimise the molecular potentials and precisely calculated potential energy curves can be used to predict the positions of features such as Feshbach resonances. The goal is a self-consistent model for the molecular potentials which agrees with every new experimental dataset within the respective error bars.

#### Predictions of Feshbach resonance positions

To calculate Feshbach resonance positions (as has been done by E. Tiemann for the predictions aiding the atom loss measurements of this chapter, see tab. 7.1), the Hamiltonian in eq. 4.20

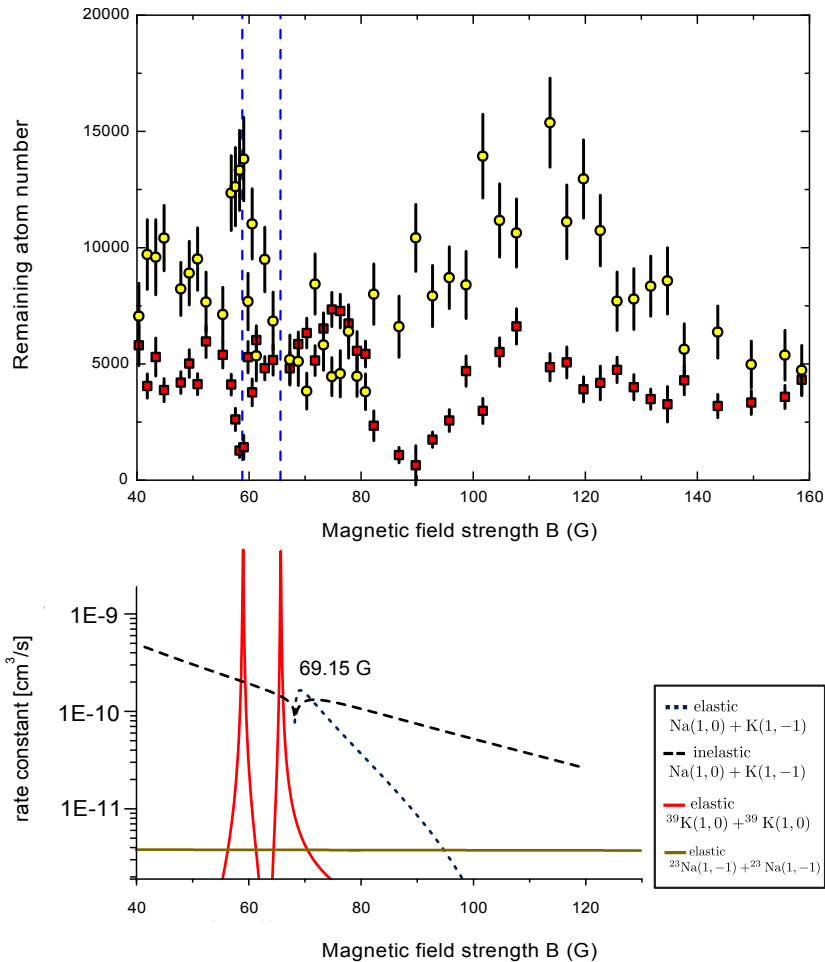


**Figure 7.9: Atom loss measurement in  $|1, -1\rangle_{\text{Na}} |1, 0\rangle_{\text{K}}$ .** The atom signal in the potassium (red squares) and sodium (yellow circles) is shown together with the collision rate constants for the entrance channel calculated by E. Tiemann for a kinetic energy of  $1\mu\text{K}$  at low fields. The elastic as well as the inelastic rate constant is given and, additionally the elastic rate constants for sodium and potassium intraspecies scattering are plotted, see legend in the plot for details. It can be seen that the inelastic interspecies scattering rate constant shows a feature at around 69.15 G but decreases for higher magnetic field strength, leaving the loss feature at about 90 G unexplained.

is used and the best known values are taken for the different fit parameters of the molecular potentials.

A coupled-channel calculation is performed where each channel wave function follows the partial-wave ansatz (see sec. 3.2.1). To reduce calculation time, the partial-wave ansatz is truncated, often already for  $l > 0$ , since higher partial waves experience the centrifugal barrier at the ultracold temperatures at which Feshbach measurements are normally performed.

With the coupled channel equations for a chosen incoming and outgoing channel, the scattering matrix (see sec. 4.2) is calculated on a grid of different magnetic field values, yielding the scattering rate over the investigated magnetic field range. For elastic scattering, the outgoing channel is the same as the incoming one, which is not true in the case of inelastic scattering. Since the total  $M$  as well as the parity are always conserved in the scattering processes under investigation, the number of contributing channels can be constrained. Only those channels with the total  $M$  of the chosen incoming channel can contribute. By allocation of the maxima in the obtained scattering rate to a Feshbach resonance, their positions can be predicted.

### Calculation of molecular potentials

To calculate the potential energy curves and to find all different fit parameters introduced in the other terms of eq. 4.20, assumptions and simplifications have to be made. They are made based on the already existing knowledge about the molecule in question.

For the hyperfine interaction (see eq. 4.21), the starting point is the combined hyperfine structure of the two separate atoms. This is a good approximation for large internuclear distances. For shorter distances, the hyperfine structure will become smaller as the character of the electronic orbitals changes from s to p.

For the Born-Oppenheimer potentials, ab-initio calculations can be used although they usually do not yield very accurate predictions. The representation of the potentials can be significantly optimised if experimental data is available. With the help of spectroscopic data which maps out the potential minimum and other measurements which yield information about the long-range part, as for example Feshbach resonances do, the potentials can be fitted to higher accuracy. The same is also true for the other parameters used in the other terms of the Hamiltonian. In case that no spectroscopic data for a certain atomic isotope exists, a mass rescaling of data from other isotopes can be used to adapt the the potential energy curves to the isotope of interest.

Several methods exists to iteratively optimise the potentials and interaction terms to best explain the experimental data. For the calculations presented in [1], a *MINUIT* algorithm (developed at the CERN) has been used which is a numerical minimisation program written in the *FORTRAN* programming language.

By iteratively adjusting the different fit parameters the theoretical model can be optimised to best describe the measured Feshbach resonances. These adjustments can only be done in a way that they do not impair the already achieved conformity with the other available measurements. For example, the possible adjustment of the long-range part of a molecular potential could be constrained by a large set of highly precise spectroscopic data which fixes the minimum of the potential within tight boundaries.

### Refined molecular potentials and resonance positions

The measurements presented in this chapter are new important data to optimise the fits for the bosonic molecule  $^{23}\text{Na}^{39}\text{K}$ , since only Feshbach resonance data from the fermionic isotope existed up till now. With the measured resonance positions, a new fit of the Born-Oppenheimer potentials has been performed, following the procedure outlined above. The values for the fit parameters can be found in the supplement of [1].

Using the refined potentials, the Feshbach resonance positions for the bosonic  $^{23}\text{Na}+^{39}\text{K}$  mixture are re-calculated. The results are listed in tab 7.4. With this data at hand, the next steps towards double-degenerate ensembles can be taken, as is discussed in the next chapter.

**Table 7.4: Measured magnetic field positions  $B_{\text{exp}}$  and uncertainties ( $\pm$ ) together with calculated positions  $B_{\text{th}}$ , applying the improved potentials.**  $M$  is the total magnetic quantum number of the pair  $|f, m_f\rangle_{\text{Na}} + |f, m_f\rangle_{\text{K}}$ ,  $f$  is in most cases only an approximate quantum number. Subscripts "res" and "zc" stand for resonance and zero crossing, respectively. In some cases, maxima of the elastic (el.) and inelastic (in.) scattering rate are listed respectively. A.1 marks the inelastic loss feature discussed in section 7.5.1. The measurements with (\*) have been previously presented in [2]. Table taken from [1].

$M$	$\text{Na}_{f,m_f}$	$\text{K}_{f,m_f}$	$B_{\text{exp., zC}}$ (G)	$B_{\text{th., zC}}$ (G)	$B_{\text{exp., res.}}$ (G)	$B_{\text{th., res.}}$ (G)
2	1,1	1,1	380.88 (3.83)	381.43	411.33 (1.28)	410.1
			-	507.0	508.73 (0.83)	508.81

1	1,1	1,0		6.72 (2.09)	6.6
		-	328.5	329.12 (0.77)	328.96
		-	442.5	cls. to KK res.	467
		-	577.5	579.94 (0.88)	580.49
1,0		1,1		-	7.5 (in.)
		-	336.0	cls. to KK res.	9.0 (el.)
				-	419.0
				-	508.5 (in.)
				-	512.0 (el.)
0	1,0	1,0	-	4.25	5.47 (1.01)
					31.86 (1.69)
		-	407	cls. to KK res.	475.5 (in.)
					476.0 (el.)
				-	581.5 (in.)
				-	585.5 (el.)
1,1		1,-1		26.34 (3.31)	A.1
		-	393.0	393.61 (0.76)	393.59
		515.85 (1.68)	516.4	536.07 (0.94)	536.67
1,-1		1,1		-	516.0 (el.)
				-	522.5 (in.)
-1	1,-1	1,0		-	13.0
			245.76 (1.45)		244.75
			-		588.5 (el.)
			-		593.0 (in.)
1,0		1,-1		-	107.5
			541.09 (1.50)		540.5
1,1		2,-2		-	88.5 (in.)
			-		134.0 (in.)
			-		138.0 (el.)
			-		471
2,-2		1,1		-	272.5 (in.)
			-		314.5 (in.)
			-		465.5 (in.)
			-		473.5 (el.)
-2	1,-1	1,-1		32.5 (0.8)(*)	33.13
		117.2 (0.2)(*)	117.08	247.1 (0.2)(*)	247.57
				646.6 (1.5)(*)	651.5 (el./in.)
				686.2 (1.5)(*)	686.7 (in.)
1,0		2,-2		228.48 (1.49)	229.5
		570.29 (2.55)	574.3	-	619.0
2,-2		1,0		-	358.5 (in.)
				-	528.0 (in.)
				-	533.0 (el.)



# Chapter 8

## Bose-Einstein condensation

The production of quantum-degenerate samples of  $^{23}\text{Na}$  and  $^{39}\text{K}$  is an important step on the route towards ground-state molecules produced via Feshbach resonances and STIRAP [49, 58, 75]. In this chapter, the experimental realisation of single as well as dual-species BECs of  $^{23}\text{Na}$  and  $^{39}\text{K}$  in the  $|f = 1, m_f = -1\rangle$  Zeeman hyperfine state is presented. Parts of this chapter have been published in [2]. Figures taken from that publication are marked accordingly.

Moreover, investigations of a  $^{23}\text{Na}$  BEC in the  $|f = 1, m_f = 1\rangle$  Zeeman hyperfine state are presented.

### 8.1 Single-species BECs in $|f = 1, m_f = -1\rangle_{\text{Na/K}}$

In the course of this thesis, pure  $^{23}\text{Na}$  BECs in the  $|f = 1, m_f = -1\rangle$  hyperfine state consisting of  $\sim 1.5 \cdot 10^5$  atoms and only with a few percent thermal background have been created on a regular basis. To produce these single-species BECs, the experiment is performed without loading any  $^{39}\text{K}$ . For a fully loaded sodium 3D MOT, the sequential steps of loading the magnetic trap and forced MW-evaporation for 15 s followed by loading the atoms into the cODT are left unchanged from the ones presented in sec. 6.7.1 (dual-species 3D MOT), 6.8.2 (magnetic trap loading), 6.10 (forced MW evaporation in the magnetic trap) and 6.11 (cODT loading). Since the intraspecies scattering length for  $^{23}\text{Na}$  in  $|f = 1, m_f = -1\rangle$  is constant over the magnetic field range used for the experiments presented in this thesis, and especially also at zero field, BECs can be produced at any given magnetic field strength. To enable optimal imaging conditions, the magnetic field is ramped down to zero before the optical evaporation begins. BEC is reached by lowering the powers in the cODT to  $P_{\vec{e}_x} = 3.8\text{ W}$  (elliptically shaped focus trap) and  $P_{\vec{e}_y} = 1.18\text{ W}$  (radially shaped focus trap) in 1.5 s and then to  $P_{\vec{e}_x} = 126\text{ mW}$  and  $P_{\vec{e}_y} = 60\text{ mW}$  within 2.5 s.

Quantum degeneracy can be verified in multiple ways. The first method is the observation of a phase transition from a purely thermal distribution to a bimodal distribution, following the arguments outlined in sec. 5.2.1. Since the onset of BEC depends on the PSD of the atomic sample, one can for example tune the temperature by varying the depth of the optical evaporation. A measurement following this idea is shown in [36].

Imaging a Na BEC on the vertical axis (see sec. 6.9.3) in free fall after a TOF inversion of the aspect ratio will be observed which is another method to verify quantum degeneracy. The theory behind this method is described in sec. 5.2.2. Fig. 8.1 shows the aspect ratio versus the time of free expansion of a  $^{23}\text{Na}$  BEC after it is released from a cODT. The aspect ratio is calculated from the widths of the BEC. These are determined using a two-dimensional fit of a rotated double Gaussian. The fit using eq. 5.23 is in excellent agreement with the data. With the imaging along the z axis and the confinement of the cODT along this axis being the

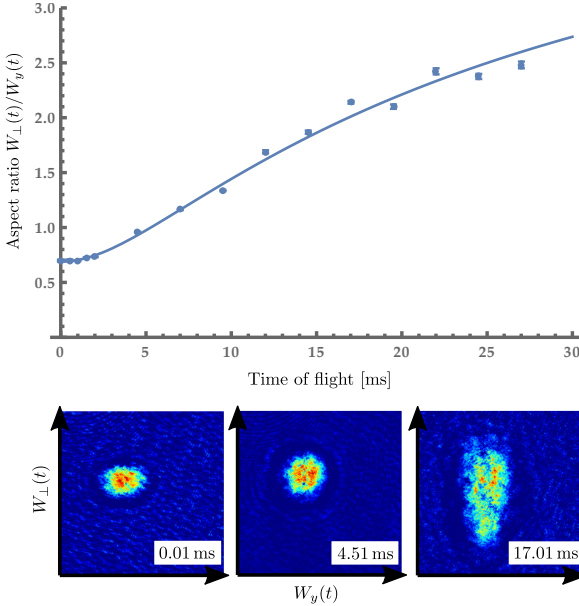


**Figure 8.1: Change of aspect ratio during TOF of a  $^{23}\text{Na}$  BEC in the  $|f = 1, m_f = -1\rangle$  hyperfine state.** The BEC is released from the cODT and recorded using the imaging on the vertical axis, denoted as  $z$  axis. The fit follows eq. 5.23, showing excellent agreement of the experimental data with the theory. The three images show the BEC after different TOFs.

same as along the  $x$  axis, in order to keep the notation of eq. 5.23 the width in  $x$  direction is called  $W_{\perp}$ .

Pure  $^{39}\text{K}$  BECs in the  $|f = 1, m_f = -1\rangle$  state have been produced as well. Fig.8.2 shows a measurement of a K BEC consisting of  $\sim 1.7 \cdot 10^5$  atoms with  $N_{\text{BEC}}/N_{\text{total}} = 0.25$  at  $T \approx 255$  nK. Since  $^{39}\text{K}$  has a negative scattering length at zero magnetic field, a BEC cannot be produced at that field. In other publications, intraspecies Feshbach resonances have been used to overcome this problem and even all-optical condensation of  $^{39}\text{K}$  could be realised at a magnetic field strength of 550 G, yielding a scattering rate of  $a_K = 130a_0$  [227].

Experimentally, the BEC presented here was produced applying a similar experiment sequence as in [228]. In that publication  $^{87}\text{Rb}$  is used as a sympathetic coolant in the forced MW evaporation inside the magnetic trap and also in the subsequent optical evaporation due to the smaller trap depth experienced by  $^{87}\text{Rb}$  in the optical dipole trap (ODT). During the optical evaporation, the scattering lengths are modified using known Feshbach resonances. The last step to quantum degeneracy of  $^{39}\text{K}$  is then achieved by pure  $^{39}\text{K}$  evaporation close to an intraspecies Feshbach resonance.

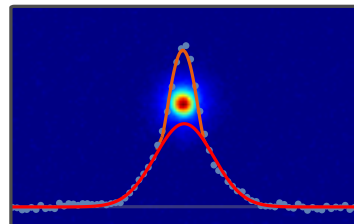


**Figure 8.2: BEC of  $^{39}\text{K}$  in  $|f = 1, m_f = -1\rangle$ .** The image shows the column density distribution as recorded by the imaging system. A bimodal fit to this data (light blue circles) is used to determine the parameters of the BEC (red and orange curve). The sample consists of  $1.7 \cdot 10^5$  atoms with  $N_{\text{BEC}}/N_{\text{total}} = 0.25$  at  $T \approx 255$  nK.

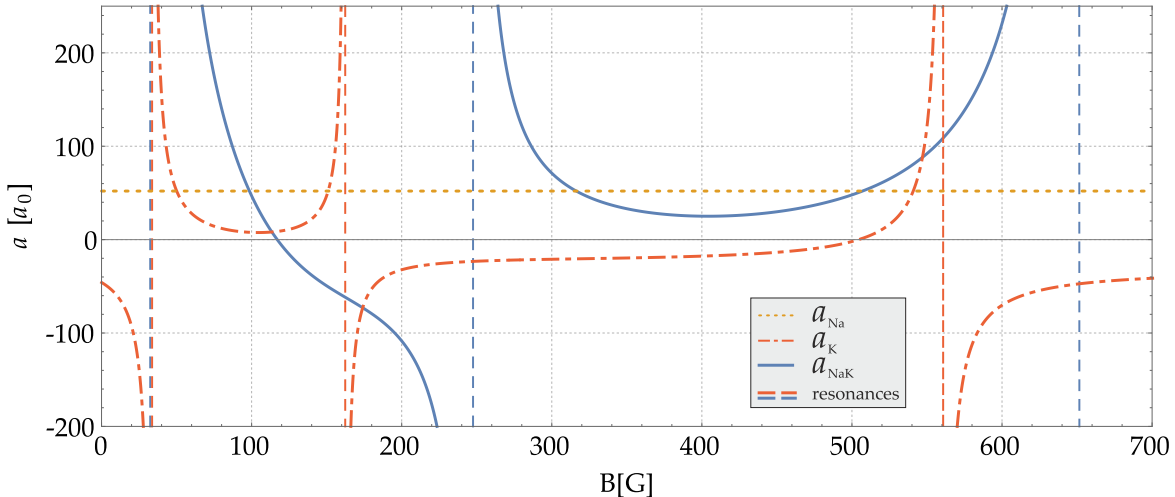


**Figure 8.3:** Scattering length of  $^{23}\text{Na}$ ,  $^{39}\text{K}$  and  $^{23}\text{Na}^{39}\text{K}$ . The dashed red and vertical lines mark the positions of Feshbach resonances in  $^{39}\text{K}$  and  $^{23}\text{Na}^{39}\text{K}$ , respectively. Figure taken from [2].

For the measurement presented here, adapting this sequence for  $^{23}\text{Na} + ^{39}\text{K}$  works well.  $^{23}\text{Na}$  is used as coolant in the magnetic trap as well as in the first cODT evaporation step by lowering the cODT powers to  $P_{\vec{e}_x} = 152 \text{ mW}$  (elliptically shaped focus trap) and  $P_{\vec{e}_y} = 47 \text{ mW}$  and using a magnetic field of 82.9 G to ensure good interspecies scattering length of  $a_{\text{NaK}} = 122.6a_0$  ( $a_K = 10.9a_0$ ). After that, the remaining sodium is removed using a flash of resonant light, the magnetic field is swept to 42.4 G ( $a_K = 108.5a_0$ ) and a last 2 s long evaporation is performed without further reducing the cODT power.

## 8.2 Dual-species BEC using Feshbach resonances

While the creation of single-species BECs has been achieved following experimental steps given in the literature, the dual-species condensation has not been straightforward. It has been found that a simple dual-species evaporation in the cODT at zero magnetic field does not lead to quantum degeneracy as the losses become too large due to an interspecies scattering length of  $a_{\text{NaK}} = -430.2a_0$ .

Because the three-body losses at zero magnetic field prevent an efficient way to dual-species quantum degeneracy, the different scattering lengths in the mixture have to be altered. As has already been shown in chap. 7, Feshbach resonances are an appropriate tool to tune the interaction strength. With the Feshbach resonances measured in the  $|f = 1, m_f = -1\rangle_{\text{Na}} + |f = 1, m_f = -1\rangle_{\text{K}}$  mixture, see sec. 7.5, the scattering length over the investigated magnetic field region can be calculated with high precision.

Figure 8.3 shows a plot of the inter- and intraspecies scattering rates (as published in [2]), where the intraspecies scattering rates are taken from [229] for  $^{23}\text{Na}$  and from [211, 230] for  $^{39}\text{K}$ .

Double BECs are produced on a regular basis in the experiment by using the following sequence: After the forced MW evaporation in the magnetic trap (see sec. 6.10), the atoms are loaded into the cODT (see sec. 6.11.2). The coil configuration is switched to generate Helmholtz fields (see sec. 6.5.2) and the magnetic field strength is ramped up to a value of  $\sim 119.9$  G at which the scattering lengths are small ( $a_{\text{NaK}} = -1a_0$ ,  $a_K = 8.9a_0$ ). The system equilibrates for 700 ms and then the magnetic field strength is ramped to a value of  $\sim 151.4$  G which proved to be optimal for the combined evaporation, giving scattering lengths of

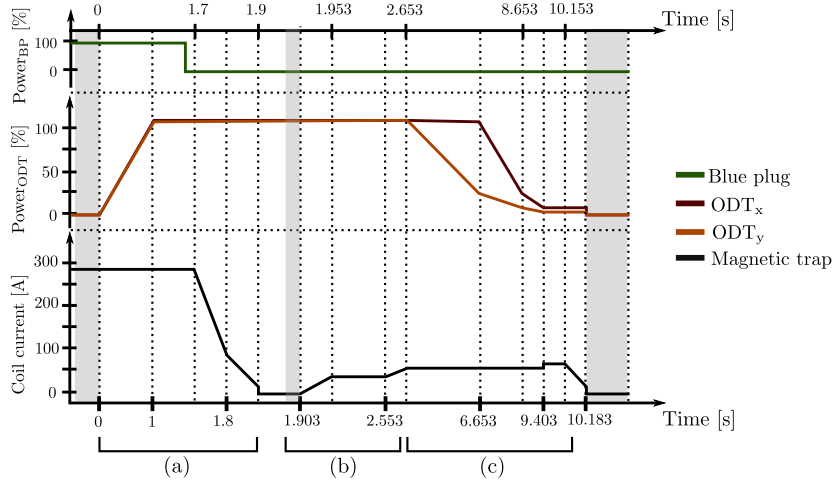


**Figure 8.4: Experiment sequence for double-species BEC production.** After the forced MWevaporation in the magnetic trap (indicated by first grey shaded area), the atoms are loaded into the cODT (segment (a)). The coil configuration is switched to generate Helmholtz fields (second grey shaded area) and the magnetic field strength is ramped up (b). It is then ramped to the field strength used for the combined optical evaporation and the laser intensities of the ODTs are reduced in segmented ramps (c). Finally, the magnetic field is switched off and the atoms are released from the cODT. After a TOF, the BECs are imaged (last grey shaded area).

$a_{NaK} = -47.2a_0$ ,  $a_K = 42.8a_0$ . The laser intensities of the ODTs are reduced in segmented ramps over a time of 7.5 s. For the last segment the magnetic field strength is jumped by  $\sim 4.5$  G to yield  $a_{NaK} = -51.7a_0$ ,  $a_K = 69.3a_0$ . Finally, the magnetic field is switched off and the atoms are released from the cODT. After a TOF, the BECs are imaged on the horizontal axis using the fast-kinetic imaging mode (see sec. 6.9.2). Figure 8.4 gives a schematic overview of the experiment sequence. In the production of the double-species BECs, especially the magnetic field strength during the evaporation in the cODT turned out to be crucial.

Figure 8.5 shows a representative single measurement, at the state of the experiment when also the Feshbach resonance measurements were taken. Both species are imaged in the same experiment run using the fast kinetic imaging technique described in sec. 6.9.2. The figure shows  $N_{C,K} = 17\%$  and  $N_{C,Na} = 42\%$  condensed BEC fraction for  $^{39}\text{K}$  and  $^{23}\text{Na}$ , respectively, with total atom numbers  $N_C + N_{\text{thermal}}$  of  $7 \cdot 10^4$  for  $^{39}\text{K}$  and  $4 \cdot 10^4$  for  $^{23}\text{Na}$ . As

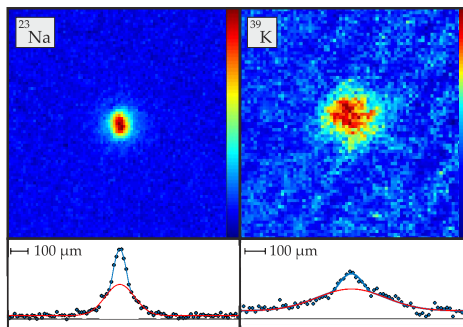


**Figure 8.5: Double BEC of  $^{23}\text{Na}$  (left) and  $^{39}\text{K}$  (right), both in the  $|f = 1, m_f = -1\rangle$  hyperfine state.** The TOF is 11.3 ms ( $^{23}\text{Na}$ ) and 14.4 ms ( $^{39}\text{K}$ ). The bottom panel shows bimodal fits to the thermal (red) and condensed (blue) parts of the integrated column density of the top pictures. Figure taken from [2].

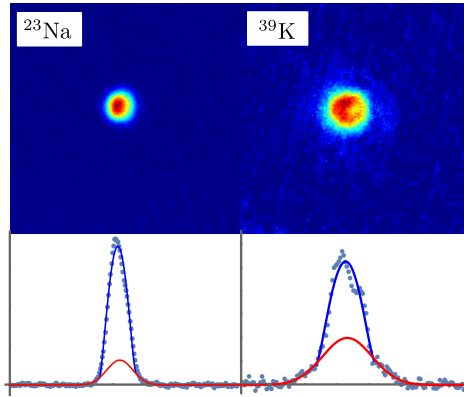


**Figure 8.6: Double BEC of  $^{23}\text{Na}$  (left) and  $^{39}\text{K}$  (right), both in the  $|f = 1, m_f = -1\rangle$  hyperfine state, after optimization of the experiment setup.** The TOF is 19 ms ( $^{23}\text{Na}$ ) and 15 ms ( $^{39}\text{K}$ ). The bottom panel shows bimodal fits to the thermal (red) and condensed (blue) parts of the integrated column density of the top pictures giving  $N_{\text{C},\text{K}} = 53\%$  and  $N_{\text{C},\text{Na}} = 78\%$  condensed BEC fraction for  $^{39}\text{K}$  and  $^{23}\text{Na}$ , respectively, with total atom numbers  $N_{\text{C}} + N_{\text{thermal}}$  of  $3.9 \cdot 10^4$  for  $^{39}\text{K}$  and  $1.8 \cdot 10^4$  for  $^{23}\text{Na}$ . The temperatures of the two BECs deduced from the thermal part of the bimodal distribution are  $T_{\text{K}} = 97\text{nK}$  for  $^{39}\text{K}$  and  $T_{\text{Na}} = 31\text{nK}$  for  $^{23}\text{Na}$ .

described in detail in [2, 36], the magnetic field at which the forced evaporation in the cODT is performed yields  $\delta g(B) = 0.047$  and is therefore in the region where mean field collapse should occur (compare chapter 5.1.2). Due to a relative gravitational sag of  $\delta z = 3.27\text{\mu m}$  which is larger than the extension of the two BECs along the vertical axis in the cODT, a reduced interspecies interaction is expected, thereby altering the exact value of  $\delta g(B)$  (which is calculated for perfectly overlapping samples) for which mean field collapse will start to occur. This explanation is supported by unequal temperatures of the two BECs deduced from the thermal part of the bimodal distribution of  $T_{\text{K}} = 186\text{nK}$  for  $^{39}\text{K}$  and  $T_{\text{K}} = 87\text{nK}$  for  $^{23}\text{Na}$ , indicating that no interspecies thermalization could took place.

After the modifications to the system described in chap. 6 and with an optimized vibration isolation of the cODT optics, the performance of the BEC fraction could be significantly enhanced, leading to dual BECs of  $N_{\text{C},\text{K}} = 53\%$  and  $N_{\text{C},\text{Na}} = 78\%$  condensed BEC fraction for  $^{39}\text{K}$  and  $^{23}\text{Na}$ , respectively, with total atom numbers  $N_{\text{C}} + N_{\text{thermal}}$  of  $3.9 \cdot 10^4$  for  $^{39}\text{K}$  and  $1.8 \cdot 10^4$  for  $^{23}\text{Na}$ . The temperatures of the two BECs deduced from the thermal part of the bimodal distribution are  $T_{\text{K}} = 97\text{nK}$  for  $^{39}\text{K}$  and  $T_{\text{Na}} = 31\text{nK}$  for  $^{23}\text{Na}$ . A picture of these dual BECs imaged with 4 ms in between the images is shown in fig. 8.6. For the picture, 38 images from 38 subsequent experiment runs are averaged per species after each picture is post-processed using the same method of noise reduction with PCA as described in sec. 7.4.5. The observation that the two BECs do not thermalise with each other, discussed already in the context of fig. 8.5, remains for this measurement.

The dual BECs in the  $|f = 1, m_f = -1\rangle_{\text{Na}} + |f = 1, m_f = -1\rangle_{\text{K}}$  mixture are a good starting point for the next experiment steps. It has been shown in recent experiments on  $^{23}\text{Na}^{40}\text{K}$  that a not resolvable hyperfine structure in the intermediate state of the STIRAP process leads to a considerably large drop in the total transfer efficiency [231]. Producing Feshbach molecules by using a resonance at high magnetic field strength can help to mitigate this problem by splitting the hyperfine levels of the excited state and thereby enabling a well defined STIRAP transition. In particular, the resonance at 247 G in the  $|f = 1, m_f = -1\rangle_{\text{Na}} + |f = 1, m_f = -1\rangle_{\text{K}}$  mixture can be used for that purpose.

Moreover, the border of the magnetic field region of  $131.5\text{G} < B < 151.1\text{G}$  has properties making it interesting for the investigation of droplets (see sec. 5.1.2). Droplets have been

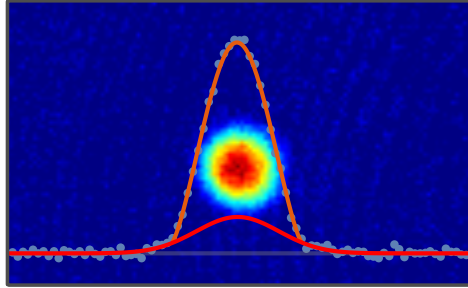


**Figure 8.7: BEC of  $^{23}\text{Na}$  in  $|f = 1, m_f = 1\rangle$ .** The image shows the column density distribution as recorded by the imaging system. A bimodal fit to this data is used to determine the parameters of the BEC (red and orange curve). The sample consists of  $8.4 \cdot 10^4$  atoms with  $N_{\text{BEC}}/N_{\text{total}} = 0.77$  at  $T \approx 89$  nK.

detected in systems of magnetic dipolar atoms [232, 233] and Zeeman state mixtures [234–236] and recently first indications for droplets of photons have been reported [237]. However, in a mixture of two atomic species, droplets have not yet been observed.

### 8.3 BEC of $^{23}\text{Na}$ in $|f = 1, m_f = 1\rangle$

Since mixtures in all spin state combinations can be prepared with the experiment setup, also the state  $|f = 1, m_f = 1\rangle_{\text{Na}} |f = 1, m_f = 1\rangle_K$  was investigated in more detail. First of all, it is the absolute ground state of the atomic system. Furthermore, it does have a Feshbach resonance at even higher magnetic field than the  $|f = 1, m_f = -1\rangle_{\text{Na}} |f = 1, m_f = -1\rangle_K$  state, namely at 508.5 G. Therefore, this state could serve as a starting point for the production of ground-state molecules as well. Pure  $^{23}\text{Na}$  BECs have been created in the  $|f = 1, m_f = 1\rangle$  state, following a similar procedure as for the dual-species BECs (see sec. 8.2). The transfer to the cODT is the same, as shown in fig. 8.4. Before the optical evaporation, the sodium atoms are transferred to the  $|f = 1, m_f = 1\rangle$  state using the RF transfers described in sec. 6.12.3. Optical evaporation is performed at zero magnetic field strength and apart from that in the same way as illustrated in fig. 8.4. No potassium is loaded into the MOT during this sequence. Fig. 8.7 shows a representative measurement. The BEC consists of  $8.4 \cdot 10^4$  atoms with  $N_{\text{BEC}}/N_{\text{total}} = 0.77$  at  $T \approx 89$  nK.

#### 8.3.1 Levitating a BEC of $^{23}\text{Na}$ in $|f = 1, m_f = 1\rangle$

Since the  $|f = 1, m_f = 1\rangle$  state is a high-field seeker, levitation of the atom cloud in a gradient magnetic field is possible [238]. By applying a Stern-Gerlach gradient field, the gravitation can be compensated if in the vertical direction:

$$U_z = 0 = mgz + \mu_B m_f g_f \frac{\partial B}{\partial z} z, \quad (8.1)$$

where  $g$  is the gravitation on earth and  $m$  is the atom mass. Following [239], the magnetic field gradient of the upper coil can be estimated in first order by:

$$\frac{\partial B(z)}{\partial z} = -\frac{3}{2} \frac{\mu_0 N I R^2 z}{\sqrt{(R^2 + z^2)^5}} \quad (8.2)$$

where  $\mu_0$  is the vacuum permeability,  $N$  the number of windings of the coil,  $R$  the radius of the coil and  $I$  the electric current flowing through the coil. With the geometric dimensions

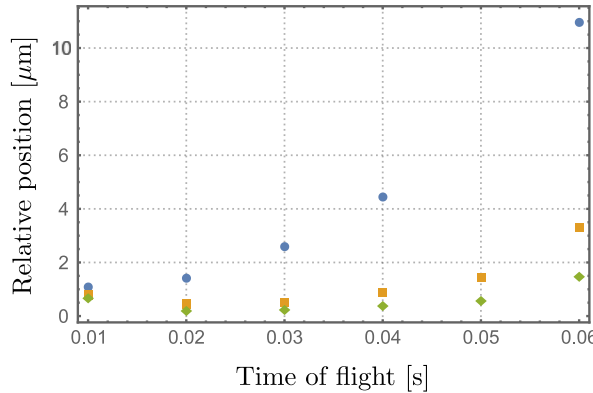


**Figure 8.8: Levitating a BEC of  $^{23}\text{Na}$  in the  $|f = 1, m_f = 1\rangle$  hyperfine state.** The relative position after TOF in a Stern-Gerlach field is recorded for three different coil currents: 17.73 A (blue circles), 18.30 A (orange squares), 18.53 A (green diamonds).

of the upper coil (see [77]) of  $N = 24$ ,  $R = 55$  mm and at a distance of  $z = 34$  mm, this simple equation gives a current of  $I \approx 19.62$  A for compensating the gravitation.

In the experiment, the needed magnetic field has been determined by scanning the current flowing through the upper coil while observing the position of the atoms during TOF. Fig. 8.8 shows this measurement, leading to a required electric current of  $\sim 18.53$  A to achieve levitation. The deviations from the calculation can originate from the simple model used to calculate the magnetic field gradient. As pointed out in [77], the deviations from an ideal coil in the design of the used coils lead to the necessity to include further corrections for eq. 8.2. Furthermore, treating the field gradient homogeneous over the complete sample might become incorrect since the atomic sample is a macroscopic object and subject to expansion during TOF. Although more sophisticated simulations of the magnetic gradient would increase the quality of the calculated required electric current, it is more feasible to access this parameter experimentally.

Levitating the atomic samples could be interesting in terms of increasing spacial overlap by compensating the gravitational sag between two BECs of  $^{23}\text{Na}$  and  $^{39}\text{K}$  both in the  $|f = 1, m_f = 1\rangle$ , e.g. when loading them into an optical lattice. Finding the optimal conditions would, however, require a precise investigation on how to balance the different gravitational sag with the different trap depths in the cODT (which are mass dependent, see eq. 6.36) and the different levitation effect due to the different Zeeman hyperfine level splitting of  $^{23}\text{Na}$  and  $^{39}\text{K}$ .



# Chapter 9

## Conclusion and Outlook

Within the course of this thesis, an experiment apparatus has been developed and set up for the preparation of ultracold dipolar bosonic ground-state  $^{23}\text{Na}^{39}\text{K}$  molecules. The system is capable of producing dual-species 3D MOTs of about  $3 \cdot 10^9$   $^{23}\text{Na}$  atoms and about  $5 \cdot 10^7$   $^{39}\text{K}$  atoms. Using sub-Doppler cooling and optical state transfer, up to  $1 \cdot 10^9$   $^{23}\text{Na}$  and  $1 \cdot 10^7$   $^{39}\text{K}$  atoms are transferred to a magnetic quadrupole trap where they are trapped in their  $|f = 1, m_f = -1\rangle$  Zeeman hyperfine state. Majorana spin flip losses have been identified as one limiting loss channel for the forced microwave evaporation in the magnetic trap. A blue detuned laser has been precisely adjusted to plug the magnetic field zero, thereby significantly reducing the Majorana losses. Three-body losses have been shown to limit dual-species operation for high densities and in the absence of an external magnetic field. A cODT has been installed and the transfer of the mixture into it has been optimized. Using the pure optical trapping potential, the behaviour of the interspecies scattering length of the  $|f = 1, m_f = -1\rangle_{\text{Na}} + |f = 1, m_f = -1\rangle_K$  mixture has been investigated for a magnetic field range of 0 to 750 G. The gathered knowledge of the interspecies scattering length is used to efficiently produce double degenerated samples of  $^{23}\text{Na}$  and  $^{39}\text{K}$  both in a BEC state. The achieved atom numbers and temperatures are on par with other state of the art experiments in the field of ultracold dipolar molecules (compare [76], [231, 240] and [74]).

To better understand the molecular properties of bosonic  $^{23}\text{Na}^{39}\text{K}$ , extensive atom-loss measurements have been performed to investigate the Feshbach resonance spectrum in several different spin state combinations. For that purpose, RF state transfers have been implemented in the setup and their performance has been characterised. The results of the Feshbach resonance study have been used by E. Tiemann to refine the singlet and triplet molecular ground state potentials of NaK. The improved potentials lead to a higher consistency between the experimental data and theoretically predicted resonance features for both the bosonic  $^{23}\text{Na} + ^{39}\text{K}$  mixture and the Bose-Fermi mixture of  $^{23}\text{Na} + ^{40}\text{K}$ . It has also been shown in this thesis how a maximum in the inelastic scattering rate, located close to a Feshbach resonance, can shift the minimum in an atom loss measurement significantly, illustrating the need for further investigations in such cases.

The measurements and refined molecular potentials allow for precise predictions for the other, experimentally still unexplored, bosonic mixture of  $^{23}\text{Na} + ^{41}\text{K}$  and will considerably aid in the realisation of the next experiment steps towards stable  $^{23}\text{Na}^{39}\text{K}$  molecules in their absolute ground state, as will be illustrated in the following sections.

### 9.1 Feshbach molecules

The next step towards ground-state molecules is the production and characterisation of Feshbach molecules in the bulk sample in the cODT. To associate Feshbach molecules, different experimental paths are possible [241]. The first option is to ramp the magnetic field across

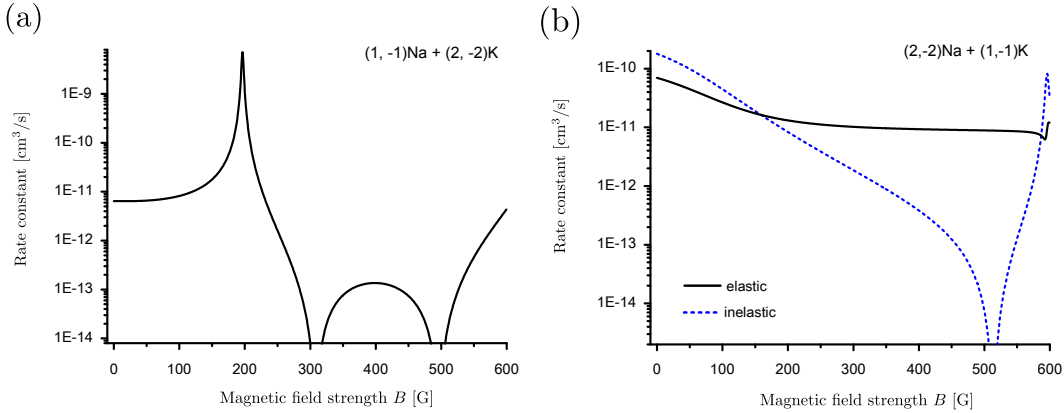


**Figure 9.1: Scattering rate constant of possible starting point state combinations for RF association of Feshbach molecules.** The scattering rates have been calculated by E. Tiemann using the new potential energy curves.

the resonance adiabatically. The second possibility is to modulate the magnetic field close to the resonance with a frequency corresponding to the binding energy of the molecule [242]. The third option is to transfer one atomic species to another (Zeeman-) hyperfine state and then to associate the atoms to molecules at a fixed magnetic field value by shining in a radio frequency resonant with the energy of the molecular state at that field. This RF association of Feshbach molecules is widely used, see e.g. [243] and [244]. The efficiencies of the methods listed here are on the order of 5 to 15 %. It was shown that the transfer efficiency for an association by a magnetic field ramp increases with the PSD of the atomic mixture up to 50 % [245].

With the ultracold mixture of  $|f = 1, m_f = -1\rangle_{\text{Na}} + |f = 1, m_f = -1\rangle_K$  at hand, the method currently pursued in the laboratory is the RF association of the molecules. Starting from a different hyperfine state (e.g. from  $|f = 2, m_f = -2\rangle_{\text{Na}}$ ), Feshbach molecules are produced in the vicinity of the broad Feshbach resonance at 247 G by applying a radio frequency to directly access the bound molecular Feshbach state. The remaining  $^{23}\text{Na}$  atoms can subsequently be removed with light resonant on the  $F = 2 \rightarrow F' = 3$  transition (in the case of  $|f = 2, m_f = -2\rangle$  as a starting point).

In fig. 9.1, the scattering rates for two possible state combinations to start a RF association with are shown. They have been calculated by E. Tiemann using the new potential energy curves. As can be seen, both state combinations are suitable as starting point for the association process. However, care has to be taken, not to spend too much time of the experiment sequence in magnetic field regions where the scattering rate is large. This would significantly reduce the lifetime of the ensemble.

With the detailed study of the numerous Feshbach resonances in different spin state combinations presented in this thesis, a large pool of information exists to tailor the final Feshbach molecular state to the demands of the following experimental step, which is the ground-state transfer.

## 9.2 Ground-state molecule production via STIRAP

The transfer to the absolute ro-vibrational ground state will be performed by a two-photon transition in the STIRAP configuration [246]. A single photon transfer will not be possible as the Feshbach molecular state is triplet dominated whereas the molecular ground state is a singlet state. To achieve a sufficient transition efficiency, an intermediate state needs to be chosen which can mix singlet and triplet wave functions while also having a decent

Franck-Condon overlap integral for both transitions. With the new molecular potentials at hand and theoretical pre-studies already performed (see [4]), the necessary effort to identify a suitable state should be manageable.

The laser systems to perform the STIRAP process need to have a small relative linewidth of  $< 1 \text{ kHz}$  due to the need to be phase stable with respect to each other over the complete time of the transfer [247]. To achieve this task, the lasers need to be locked onto an ultra-stable high-finesse reference cavity ( $F \approx 16000$ ). A laser setup which can perform this task will be presented in an upcoming thesis [142].

With usual transfer efficiencies of about 10 % in the production of Feshbach molecules and of 75 to 92 % for the STIRAP [58, 247, 248], the experiment apparatus presented in this thesis should be able to produce at least  $3 \cdot 10^3$  ground-state molecules in a bulk sample inside the cODT. When this goal is reached, the scattering properties of ground-state bosonic  $^{23}\text{Na}^{39}\text{K}$  molecules can be investigated in detail, as has been done so far only for the fermionic  $^{23}\text{Na}^{40}\text{K}$  [58].

An important result from the investigations of  $^{23}\text{Na}^{39}\text{K}$  molecules in the bulk system will be their lifetime. Even molecules which do not undergo exothermic reactions in their absolute ground state are reported to experience short lifetimes in trap, most likely due to sticky collisions [249]. Different suggestions exist on how to avoid the observed losses. Using microwave radiation to shield the molecules from sticky collisions by influencing the possible scattering states has been proposed [250, 251]. In addition, it has been stated that electric fields could be used for shielding against sticky collisions [252]. For fermionic molecules, recent experiments show a reduction of the loss rate when reaching quantum degeneracy [68]. The effects behind this stabilisation of the sample, however, originate in the fermionic nature of the  $^{40}\text{K}^{87}\text{Rb}$  molecules used in that experiment. The findings will therefore not be applicable to the bosonic  $^{23}\text{Na}^{39}\text{K}$  molecules.

### 9.3 Optical lattice and single-site imaging

Another option to prevent losses due to sticky collisions is to load to or associate the molecules inside an optical lattice, one molecule per lattice site, and thus making contact interactions between the molecules impossible.

The experiment apparatus features optical paths to guide laser beams into the main chamber, forming an optical lattice by overlaying the lattice beams with the MOT laser beams on the horizontal plane and with the blue-plug laser on the vertical axis using dichroic mirrors. The first realisation will most likely be a cubic three-dimensional lattice, but other geometries such as hexagonal [253] and kagome [254] lattices are possible by using different optical ports of the main chamber. The laser light will be generated by the same laser also used for the cODT, see sec. 6.4.3. A phase stabilisation for the lattice beams has already been set up and characterised on a test assembly [255].

A crucial point in the loading of molecules to or their association inside the lattice will be to reach a sufficient filling factor. The optimal case would be a filling factor of unity, which has, however, so far not been realised in an experiment. By optimising the merging of two quantum-degenerate atomic samples and associating the atoms to molecules inside the lattice, low-entropy samples could recently be prepared in the case of KRb [256] and RbCs [257]. To achieve similar results for bosonic  $^{23}\text{Na}^{39}\text{K}$  will be a subject of future investigations.

With the high-resolution objective currently implemented in the experiment setup, investigations can be carried out by recording TOF images on the vertical axis, similar to e.g. [15, 258]. To extend the options to image the physical processes happening when dipolar molecules are placed inside an optical lattice, single-site resolution imaging will be implemented at the experiment apparatus in the future. An objective with single-site resolution on the sodium D2 line wavelength for a lattice spacing of 532 nm has already been developed

and characterised on a test setup using gold nano-particles [77].

### 9.3.1 Inducing electric dipoles

An electric dipole moment of up to 2.72 Debye can be induced in ground-state  $^{23}\text{Na}^{39}\text{K}$  molecules when applying an external electric field. If control over the electric field axis is guaranteed, effects of the dipole alignment can be studied. A key feature of the experiment apparatus are the in-vacuum electrodes, which are described in great detail in [3, 77]. Since they are located inside the vacuum chamber and no glass surface is in between the electrodes and the molecular sample, it is expected that disturbing effects due to the dielectric properties of the glass will not be present. Effects such as mirror-charges are a major problem in experiment setups using electrodes placed outside the vacuum chamber (which is often a glass cell) as they make the generation of a homogeneous and tunable electric field in the region of the molecular sample very difficult [259]. The electrodes implemented in the experiment apparatus presented in this thesis are specifically designed to ensure both, a high homogeneity of the electric field over the region of the molecular sample as well as the possibility to freely tune the electric field strength and direction.

## 9.4 Polarized $^{23}\text{Na}^{39}\text{K}$ molecules in an optical lattice

Ultra-cold ground-state  $^{23}\text{Na}^{39}\text{K}$  molecules trapped in a cODT or in an optical lattice will enable many interesting experiments. This will be on the one hand the investigations in the bulk system, such as BEC of bosonic polar molecules (a BEC of dipolar atoms has been reported in [33]) or ultracold chemistry [260], where the induced and tunable electric dipole interaction will add a further layer of possible processes. On the other hand, the investigation of lattice-based effects promises a large variety of physical phenomena (see e.g. [261] and [262]). A topic currently highly investigated is supersolidity [25]. While first experimental indications for this new phase of matter have been reported recently in [26] and [27], much room is still left for further investigations. As another example, the investigation of thermalization of isolated quantum many-body systems [263] will be a fascinating topic for the future.





# Bibliography

- [1] T. Hartmann, T. A. Schulze, K. K. Voges, P. Gersema, M. W. Gempel, E. Tiemann, A. Zenesini, and S. Ospelkaus, *Feshbach resonances in  $^{23}\text{Na} + ^{39}\text{K}$  mixtures and refined molecular potentials for the NaK molecule*, Phys. Rev. A, 2019, DOI: 10.1103/PhysRevA.99.032711.
- [2] T. A. Schulze, T. Hartmann, K. K. Voges, M. W. Gempel, E. Tiemann, A. Zenesini, and S. Ospelkaus, *Feshbach spectroscopy and dual-species Bose-Einstein condensation of  $^{23}\text{Na}-^{39}\text{K}$  mixtures*, Phys. Rev. A, 2018, DOI: 10.1103/PhysRevA.97.023623.
- [3] M. W. Gempel, T. Hartmann, T. A. Schulze, K. K. Voges, A. Zenesini, and S. Ospelkaus, *Versatile electric fields for the manipulation of ultracold NaK molecules*, New Journal of Physics, 18, 2016.
- [4] T. A. Schulze, I. I. Temelkov, M. W. Gempel, T. Hartmann, H. Knöckel, S. Ospelkaus, and E. Tiemann, *Multichannel modeling and two-photon coherent transfer paths in NaK*, Phys. Rev. A, 2013, DOI: 10.1103/PhysRevA.88.023401.
- [5] P. Verkerk, B. Lounis, C. Salomon, C. Cohen-Tannoudji, J.-Y. Courtois, and G. Grynberg, *Dynamics and spatial order of cold cesium atoms in a periodic optical potential*, Phys. Rev. Lett., 1992, DOI: 10.1103/PhysRevLett.68.3861.
- [6] P. S. Jessen, C. Gerz, P. D. Lett, W. D. Phillips, S. L. Rolston, R. J. C. Spreeuw, and C. I. Westbrook, *Observation of quantized motion of Rb atoms in an optical field*, Phys. Rev. Lett., 1992, DOI: 10.1103/PhysRevLett.69.49.
- [7] A. Hemmerich and T. W. Hänsch, *Two-dimensional atomic crystal bound by light*, Phys. Rev. Lett., 1993, DOI: 10.1103/PhysRevLett.70.410.
- [8] C. C. Bradley, C. A. Sackett, J. J. Tollett, and R. G. Hulet, *Evidence of Bose-Einstein Condensation in an Atomic Gas with Attractive Interactions*, Phys. Rev. Lett., 1995, DOI: 10.1103/PhysRevLett.75.1687.
- [9] K. B. Davis, M. O. Mewes, M. R. Andrews, N. J. van Druten, D. S. Durfee, D. M. Kurn, and W. Ketterle, *Bose-Einstein Condensation in a Gas of Sodium Atoms*, Phys. Rev. Lett., 1995, DOI: 10.1103/PhysRevLett.75.3969.
- [10] M. H. Anderson, J. R. Ensher, M. R. Matthews, C. E. Wieman, and E. A. Cornell, *Observation of Bose-Einstein Condensation in a Dilute Atomic Vapor*, Science, 269, 1995, DOI: 10.1126/science.269.5221.198.
- [11] B. Lücke, J. Peise, G. Vitagliano, J. Arlt, L. Santos, G. Tóth, and C. Klempert, *Detecting Multiparticle Entanglement of Dicke States*, Phys. Rev. Lett., 2014, DOI: 10.1103/PhysRevLett.112.155304.
- [12] J. Peise, B. Lücke, L. Pezze, F. Deuretzbacher, W. Ertmer, J. Arlt, A. Smerzi, L. Santos, and C. Klempert, *Interaction-free measurements by quantum Zeno stabilization of ultracold atoms*, Nature Communications, 6, 2015.

- [13] C. A. Regal, M. Greiner, and D. S. Jin, *Observation of Resonance Condensation of Fermionic Atom Pairs*, Phys. Rev. Lett., 2004, DOI: 10.1103/PhysRevLett.92.040403.
- [14] M. W. Zwierlein, C. A. Stan, C. H. Schunck, S. M. F. Raupach, A. J. Kerman, and W. Ketterle, *Condensation of Pairs of Fermionic Atoms near a Feshbach Resonance*, Phys. Rev. Lett., 2004, DOI: 10.1103/PhysRevLett.92.120403.
- [15] M. Greiner, O. Mandel, T. Esslinger, T. W. Hänsch, and I. Bloch, *Quantum phase transition from a superfluid to a Mott insulator in a gas of ultracold atoms*, Nature, 2002, DOI: 10.1038/415039a.
- [16] W. S Bakr, J. I Gillen, A. Peng, S. Fölling, and M. Greiner, *A Quantum Gas Microscope for Detecting Single Atoms in a Hubbard-regime Optical Lattice*, Nature, 2009.
- [17] W. S. Bakr, A. Peng, M. E. Tai, R. Ma, J. Simon, J. I. Gillen, S. Fölling, L. Pollet, and M. Greiner, *Probing the Superfluid-to-Mott Insulator Transition at the Single-Atom Level*, Science, 329, 2010, DOI: 10.1126/science.1192368.
- [18] J. F. Sherson, C. Weitenberg, M. Endres, M. Cheneau, I. Bloch, and S. Kuhr, *Single-atom-resolved fluorescence imaging of an atomic Mott insulator*, Nature, 2010.
- [19] L. W. Cheuk, M. A. Nichols, M. Okan, T. Gersdorf, V. V. Ramasesh, W. S. Bakr, T. Lompe, and M. W. Zwierlein, *Quantum-Gas Microscope for Fermionic Atoms*, Phys. Rev. Lett., 2015, DOI: 10.1103/PhysRevLett.114.193001.
- [20] E. Haller, J. Hudson, A. Kelly, D. Cotta, B. Peaudecerf, G. Bruce, and S. Kuhr, *Single-atom imaging of fermions in a quantum-gas microscope*, Nature Physics, 2015, DOI: 10.1038/nphys3403.
- [21] M. F. Parsons, F. Huber, A. Mazurenko, C. S. Chiu, W. Setiawan, K. Wooley-Brown, S. Blatt, and M. Greiner, *Site-Resolved Imaging of Fermionic  ${}^6\text{Li}$  in an Optical Lattice*, Phys. Rev. Lett., 2015, DOI: 10.1103/PhysRevLett.114.213002.
- [22] M. Baranov, L. Dobrek, K. Goral, L. Santos, and M. Lewenstein, *Ultracold Dipolar Gases - a Challenge for Experiments and Theory*, pages 74–81.
- [23] T. Lahaye, C. Menotti, L. Santos, M. Lewenstein, and T. Pfau, *The physics of dipolar bosonic quantum gases*, Reports on Progress in Physics, 72, 2009.
- [24] A. Griesmaier, *Generation of a dipolar Bose-Einstein condensate*, Journal of Physics B: Atomic, Molecular and Optical Physics, 40, 2007.
- [25] A. J. Leggett, *Can a Solid Be "Superfluid"?*, Phys. Rev. Lett., 1970, DOI: 10.1103/PhysRevLett.25.1543.
- [26] J. li, J. Lee, W. Huang, S. Burchesky, B. Shteynas, F. Cagri Top, A. O. Jamison, and W. Ketterle, *A stripe phase with supersolid properties in spin-orbit-coupled Bose-Einstein condensates*, Nature, 2017.
- [27] P. Z. T. E. Julian Leonard, Andrea Morales and T. Donner, *Supersolid formation in a quantum gas breaking a continuous translational symmetry*, 2017.
- [28] A. Griesmaier, J. Werner, S. Hensler, J. Stuhler, and T. Pfau, *Bose-Einstein Condensation of Chromium*, Phys. Rev. Lett., 94, 2005.
- [29] M. Lu, N. Q. Burdick, S. H. Youn, and B. L. Lev, *Strongly Dipolar Bose-Einstein Condensate of Dysprosium*, Phys. Rev. Lett., 107, 2011.

- [30] K. Aikawa, A. Frisch, M. Mark, S. Baier, A. Rietzler, R. Grimm, and F. Ferlaino, *Bose-Einstein Condensation of Erbium*, Phys. Rev. Lett., 108, 2012.
- [31] J. Billy, S. Müller, E. Henn, H. Kadau, A. Griesmaier, and T. Pfau, 2011.
- [32] A. de Paz, A. Sharma, A. Chotia, E. Maréchal, J. H. Huckans, P. Pedri, L. Santos, O. Gorceix, L. Vernac, and B. Laburthe-Tolra, *Nonequilibrium Quantum Magnetism in a Dipolar Lattice Gas*, Phys. Rev. Lett., 2013, DOI: 10.1103/PhysRevLett.111.185305.
- [33] H. Kadau, M. Schmitt, M. Wenzel, C. Wink, T. Maier, I. Ferrier-Barbut, and T. Pfau, *Observing the Rosensweig instability of a quantum ferrofluid*, Nature, 530, 2016.
- [34] P. S. Julienne, T. M. Hanna, and Z. Idziaszek, *Universal ultracold collision rates for polar molecules of two alkali-metal atoms*, Phys. Chem. Chem. Phys., 2011.
- [35] V. S. Prasanna, S. Sreerekha, M. Abe, V. M. Bannur, and B. P. Das, *Permanent electric dipole moments of alkaline-earth-metal monofluorides: Interplay of relativistic and correlation effects*, Phys. Rev. A, 2016, DOI: 10.1103/PhysRevA.93.042504.
- [36] T. A. Schulze, *Quantum degenerate mixtures of  $^{23}\text{Na}$ - $^{39}\text{K}$  and coherent transfer paths in NaK molecules*, PhD thesis, Fakultät für Mathematik und Physik der Gottfried Wilhelm Leibniz Universität Hannover, 2018.
- [37] I. Temelkov, H. Knöckel, A. Pashov, and E. Tiemann, *Molecular beam study of the  $a^3\Sigma^+$  state of NaK up to the dissociation limit*, Phys. Rev. A, 2015, DOI: 10.1103/PhysRevA.91.032512.
- [38] J. Gerschmann, E. Schwanke, A. Pashov, H. Knöckel, S. Ospelkaus, and E. Tiemann, *Laser and Fourier-transform spectroscopy of KCa*, Phys. Rev. A, 2017, DOI: 10.1103/PhysRevA.96.032505.
- [39] R. W. Dreyfus, R. Kelly, and R. E. Walkup, *Laser-induced fluorescence studies of excimer laser ablation of  $\text{Al}_2\text{O}_3$* , Applied Physics Letters, 49, 1986, DOI: 10.1063/1.97308.
- [40] S. Chervenkov, X. Wu, J. Bayerl, A. Rohlfes, T. Gantner, M. Zeppenfeld, and G. Rempe, *Continuous Centrifuge Decelerator for Polar Molecules*, Phys. Rev. Lett., 2014, DOI: 10.1103/PhysRevLett.112.013001.
- [41] S. Y. van de Meerakker, N. Vanhaecke, and G. Meijer, *STARK DECELERATION AND TRAPPING OF OH RADICALS*, Annual Review of Physical Chemistry, 57, 2006, DOI: 10.1146/annurev.physchem.55.091602.094337.
- [42] M. Petzold, P. Kaebert, P. Gersema, M. Siercke, and S. Ospelkaus, *A Zeeman slower for diatomic molecules*, New Journal of Physics, 20, 2018.
- [43] J. D. Weinstein, R. Decarvalho, T. Guillet, B. Friedrich, and J. Doyle, *Magnetic trapping of calcium monohydride molecules at millikelvin temperature*, Nature, 1998.
- [44] J. F. Barry, D. McCarron, E. Norrgard, M. H. Steinecker, and D. DeMille, *Magneto-optical trapping of a diatomic molecule*, Nature, 2014.
- [45] L. Anderegg, B. L. Augenbraun, Y. Bao, S. Burchesky, L. W. Cheuk, W. Ketterle, and J. Doyle, *Laser Cooling of Optically Trapped Molecules*, 2018.
- [46] S. Truppe, H. J. Williams, M. Hambach, L. Caldwell, N. Fitch, E. A. Hinds, B. Sauer, and M. Tarbutt, *Molecules cooled below the Doppler limit*, Nature Physics, 2017.
- [47] L. Anderegg, B. L. Augenbraun, E. Chae, B. Hemmerling, N. R. Hutzler, A. Ravi, A. Collopy, J. Ye, W. Ketterle, and J. M. Doyle, *Radio Frequency Magneto-Optical Trapping of CaF with High Density*, Phys. Rev. Lett., 2017, DOI: 10.1103/PhysRevLett.119.103201.

- [48] H.-I. Lu, I. Kozryev, B. Hemmerling, J. Piskorski, and J. M. Doyle, *Magnetic Trapping of Molecules via Optical Loading and Magnetic Slowing*, Phys. Rev. Lett., 2014, DOI: 10.1103/PhysRevLett.112.113006.
- [49] J. J. Zirbel, K.-K. Ni, S. Ospelkaus, T. L. Nicholson, M. L. Olsen, P. S. Julienne, C. E. Wieman, J. Ye, and D. S. Jin, *Heteronuclear molecules in an optical dipole trap*, Phys. Rev. A, 2008, DOI: 10.1103/PhysRevA.78.013416.
- [50] S. Ospelkaus, A. Pe'er, K. Ni, J. Zirbel, B. Neyenhuis, S. Kotochigova, P. Julienne, J. Ye, and D. Jin, *Efficient state transfer in an ultracold dense gas of heteronuclear molecules*, Nature Physics, 2008.
- [51] K.-K. Ni, S. Ospelkaus, M. H. G. de Miranda, A. Pe'er, B. Neyenhuis, J. J. Zirbel, S. Kotochigova, P. S. Julienne, D. S. Jin, and J. Ye, *A High Phase-Space-Density Gas of Polar Molecules*, Science, 322, 2008, DOI: 10.1126/science.1163861.
- [52] J. Deiglmayr, A. Grochola, M. Repp, K. Mörtlbauer, C. Glück, J. Lange, O. Dulieu, R. Wester, and M. Weidemüller, *Formation of Ultracold Polar Molecules in the Rovibrational Ground State*, Phys. Rev. Lett., 2008, DOI: 10.1103/PhysRevLett.101.133004.
- [53] P. Zabawa, A. Wakim, M. Haruza, and N. P. Bigelow, *Formation of ultracold  $X^1\Sigma^+(v'' = 0)$  NaCs molecules via coupled photoassociation channels*, Phys. Rev. A, 2011, DOI: 10.1103/PhysRevA.84.061401.
- [54] M.-S. Heo, T. T. Wang, C. A. Christensen, T. M. Rvachov, D. A. Cotta, J.-H. Choi, Y.-R. Lee, and W. Ketterle, *Formation of ultracold fermionic NaLi Feshbach molecules*, Phys. Rev. A, 2012, DOI: 10.1103/PhysRevA.86.021602.
- [55] T. M. Rvachov, H. Son, A. T. Sommer, S. Ebadi, J. J. Park, M. W. Zwierlein, W. Ketterle, and A. O. Jamison, *Long-Lived Ultracold Molecules with Electric and Magnetic Dipole Moments*, Phys. Rev. Lett., 2017, DOI: 10.1103/PhysRevLett.119.143001.
- [56] T. Takekoshi, L. Reichsöllner, A. Schindewolf, J. M. Hutson, C. R. Le Sueur, O. Dulieu, F. Ferlaino, R. Grimm, and H.-C. Nägerl, *Ultracold Dense Samples of Dipolar RbCs Molecules in the Rovibrational and Hyperfine Ground State*, Phys. Rev. Lett., 2014, DOI: 10.1103/PhysRevLett.113.205301.
- [57] P. K. Molony, P. D. Gregory, Z. Ji, B. Lu, M. P. Köppinger, C. R. Le Sueur, C. L. Blackley, J. M. Hutson, and S. L. Cornish, *Creation of Ultracold  $^{87}\text{Rb}^{133}\text{Cs}$  Molecules in the Rovibrational Ground State*, Phys. Rev. Lett., 2014, DOI: 10.1103/PhysRevLett.113.255301.
- [58] J. W. Park, S. A. Will, and M. W. Zwierlein, *Ultracold Dipolar Gas of Fermionic  $^{23}\text{Na}^{40}\text{K}$  Molecules in Their Absolute Ground State*, Phys. Rev. Lett., 2015, DOI: 10.1103/PhysRevLett.114.205302.
- [59] M. Guo, B. Zhu, B. Lu, X. Ye, F. Wang, R. Vexiau, N. Bouloufa-Maafa, G. Quéméner, O. Dulieu, and D. Wang, *Creation of an Ultracold Gas of Ground-State Dipolar  $\text{Na}_{23}\text{Rb}_{87}$  Molecules*, Physical Review Letters, 2016, DOI: 10.1103/physrevlett.116.205303.
- [60] A. Frisch, M. Mark, K. Aikawa, S. Baier, R. Grimm, A. Petrov, S. Kotochigova, G. Quéméner, M. Lepers, O. Dulieu, and F. Ferlaino, *Ultracold Dipolar Molecules Composed of Strongly Magnetic Atoms*, Phys. Rev. Lett., 2015, DOI: 10.1103/PhysRevLett.115.203201.
- [61] V. Barbe, A. Ciamei, B. Pasquiou, L. Reichsöllner, F. Schreck, P. Zuchowski, and J. M. Hutson, *Observation of Feshbach resonances between alkali and closed-shell atoms*, 2017.

- [62] F. Schäfer, N. Mizukami, P. Yu, S. Koibuchi, A. Bouscal, and Y. Takahashi, *Experimental realization of ultracold  $Yb-^7Li$  mixtures in mixed dimensions*, 2018.
- [63] S. Ospelkaus, K.-K. Ni, D. Wang, M. H. G. de Miranda, B. Neyenhuis, G. Quéméner, P. S. Julienne, J. L. Bohn, D. S. Jin, and J. Ye, *Quantum-State Controlled Chemical Reactions of Ultracold Potassium-Rubidium Molecules*, Science, 327, 2010, DOI: 10.1126/science.1184121.
- [64] J. M. Hutson, *Ultracold Chemistry*, Science, 327, 2010, DOI: 10.1126/science.1186703.
- [65] M. McDonald, B. McGuyer, F. Apfelbeck, C. H. Lee, I. Majewska, R. Moszynski, and T. Zelevinsky, *Photodissociation of ultracold diatomic strontium molecules with quantum state control*, Nature, 2016.
- [66] L. R. Liu, J. D. Hood, Y. Yu, J. T. Zhang, N. R. Hutzler, T. Rosenband, and K.-K. Ni, *Building one molecule from a reservoir of two atoms*, Science, 360, 2018, DOI: 10.1126/science.aar7797.
- [67] A. Chotia, B. Neyenhuis, S. A. Moses, B. Yan, J. P. Covey, M. Foss-Feig, A. M. Rey, D. S. Jin, and J. Ye, *Long-Lived Dipolar Molecules and Feshbach Molecules in a 3D Optical Lattice*, Phys. Rev. Lett., 2012, DOI: 10.1103/PhysRevLett.108.080405.
- [68] L. De Marco, G. Valtolina, K. Matsuda, W. G. Tobias, J. P. Covey, and J. Ye, *A Fermi Degenerate Gas of Polar Molecules*, 2018.
- [69] P. S. Zuchowski and J. M. Hutson, *Reactions of ultracold alkali-metal dimers*, Phys. Rev. A, 81, 2010.
- [70] F. Wang, X. He, X. Li, B. Zhu, J. Chen, and D. Wang, *Formation of ultracold  $NaRb$  Feshbach molecules*, New Journal of Physics, 17, 2015.
- [71] M. Mayle, B. P. Ruzic, and J. L. Bohn, *Statistical aspects of ultracold resonant scattering*, Phys. Rev. A, 2012, DOI: 10.1103/PhysRevA.85.062712.
- [72] M. Mayle, G. Quéméner, B. P. Ruzic, and J. L. Bohn, *Scattering of ultracold molecules in the highly resonant regime*, Phys. Rev. A, 2013, DOI: 10.1103/PhysRevA.87.012709.
- [73] M. Aymar and O. Dulieu, *Calculations of transition and permanent dipole moments of heteronuclear alkali dimers  $NaK$ ,  $NaRb$  and  $NaCs$* , Mol. Phys., 105, 2007.
- [74] M.-J. Zhu, H. Yang, L. Liu, D.-C. Zhang, Y.-X. Liu, J. Nan, J. Rui, B. Zhao, J.-W. Pan, and E. Tiemann, *Feshbach loss spectroscopy in an ultracold  $^{23}Na - ^{40}K$  mixture*, Phys. Rev. A, 2017, DOI: 10.1103/PhysRevA.96.062705.
- [75] F. Seeßelberg, N. Buchheim, Z.-K. Lu, T. Schneider, X.-Y. Luo, E. Tiemann, I. Bloch, and C. Gohle, *Modeling the adiabatic creation of ultracold polar  $^{23}Na^{40}K$  molecules*, Phys. Rev. A, 2018, DOI: 10.1103/PhysRevA.97.013405.
- [76] J. W. Park, C.-H. Wu, I. Santiago, T. G. Tiecke, S. Will, P. Ahmadi, and M. W. Zwierlein, *Quantum degenerate Bose-Fermi mixture of chemically different atomic species with widely tunable interactions*, Phys. Rev. A, 2012, DOI: 10.1103/PhysRevA.85.051602.
- [77] M. W. Gempel, *Towards Ultracold Polar  $NaK$  Molecules and the Investigation of Dipolar Quantum Gases*, PhD thesis, Gottfried Wilhelm Leibniz Universität Hannover Fakultät für Mathematik und Physik, 2016.
- [78] B. H. Bransden and C. J. Joachain, *Physics of Atoms and Molecules*. Pearson Education Limited, 2003.
- [79] M. S. Child, *Molecular Collision Theory*. Dover Publications Inc., 1996.

- [80] A. Marte, *Feshbach-Resonanzen bei Stößen ultrakalter Rubidiumatome*, PhD thesis, Technische Universität München Max-Planck-Institut für Quantenoptik, 2003.
- [81] J. James Patrick Burke, *Theoretical Investigation of Cold Alkali Atom Collisions*, PhD thesis, Faculty of the Graduate School of the University of Colorado, 1999.
- [82] L. Pitaevskii and S. Stringari, *Bose-Einstein Condensation*. Oxford University Press, 2003.
- [83] F. Dalfovo, S. Giorgini, L. P. Pitaevskii, and S. Stringari, *Theory of Bose-Einstein condensation in trapped gases*, Rev. Mod. Phys., 1999, DOI: 10.1103/RevModPhys.71.463.
- [84] T. Mayer-Kuckuk, *Atomphysik*. Teubner, 1985.
- [85] D. A. Steck.  
*Sodium D Line Data*.  
Theoretical Division (T-8), MS B285 Los Alamos National Laboratory Los Alamos, NM 87545, 2000.
- [86] T. G. Tiecke, *Properties of Potassium*, rev. 1.02, 2011.
- [87] G. Breit and I. I. Rabi, *Measurement of Nuclear Spin*, Phys. Rev., 1931, DOI: 10.1103/PhysRev.38.2082.2.
- [88] J. Mauritsson, P. Johnsson, E. Mansten, M. Swoboda, T. Ruchon, A. L'Huillier, and K. J. Schafer, *Coherent Electron Scattering Captured by an Attosecond Quantum Stroboscope*, Phys. Rev. Lett., 2008, DOI: 10.1103/PhysRevLett.100.073003.
- [89] V. Leong, M. Alexander Seidler, M. Steiner, A. Cere, and C. Kurtsiefer, *Time-resolved scattering of a single photon by a single atom*, Nature Communications, 2016.
- [90] E. Tiesinga, B. J. Verhaar, and H. T. C. Stoof, *Threshold and resonance phenomena in ultracold ground-state collisions*, Phys. Rev. A, 1993, DOI: 10.1103/PhysRevA.47.4114.
- [91] A. J. Moerdijk, B. J. Verhaar, and A. Axelsson, *Resonances in ultracold collisions of  $^6\text{Li}$ ,  $^7\text{Li}$ , and  $^{23}\text{Na}$* , Phys. Rev. A, 1995, DOI: 10.1103/PhysRevA.51.4852.
- [92] S. G. Porsev and A. Derevianko, *Accurate relativistic many-body calculations of van der Waals coefficients C8 and C10 for alkali-metal dimers*, The Journal of Chemical Physics, 119, 2003, DOI: 10.1063/1.1578052.
- [93] H. T. C. Stoof, J. M. V. A. Koelman, and B. J. Verhaar, *Spin-exchange and dipole relaxation rates in atomic hydrogen: Rigorous and simplified calculations*, Phys. Rev. B, 1988, DOI: 10.1103/PhysRevB.38.4688.
- [94] S. Knoop, T. Schuster, R. Scelle, A. Trautmann, J. Appmeier, M. K. Oberthaler, E. Tiesinga, and E. Tiemann, *Feshbach spectroscopy and analysis of the interaction potentials of ultracold sodium*, Phys. Rev. A, 2011, DOI: 10.1103/PhysRevA.83.042704.
- [95] B. V. Noumerov, *A Method of Extrapolation of Perturbations*, Monthly Notices of the Royal Astronomical Society, 84, 1924, DOI: 10.1093/mnras/84.8.592.
- [96] R. G. Gordon, *New Method for Constructing Wavefunctions for Bound States and Scattering*, The Journal of Chemical Physics, 51, 1969, DOI: 10.1063/1.1671699.
- [97] L. Erdős, B. Schlein, and H.-T. Yau, *Rigorous Derivation of the Gross-Pitaevskii Equation*, Phys. Rev. Lett., 2007, DOI: 10.1103/PhysRevLett.98.040404.
- [98] L. Erdos, B. Schlein, and H.-T. Yau, *Derivation of the Gross-Pitaevskii Equation for the Dynamics of Bose-Einstein Condensate*, Annals of Mathematics, Second Series, 2010.

- [99] P. Pieri and G. C. Strinati, *Derivation of the Gross-Pitaevskii Equation for Condensed Bosons from the Bogoliubov–de Gennes Equations for Superfluid Fermions*, Phys. Rev. Lett., 2003, DOI: 10.1103/PhysRevLett.91.030401.
- [100] W. Thirring, editor, *The Stability of Matter: From Atoms to Stars*. Springer, Berlin, Heidelberg, 2001.
- [101] J. L. Roberts, N. R. Claussen, S. L. Cornish, E. A. Donley, E. A. Cornell, and C. E. Wieman, *Controlled Collapse of a Bose-Einstein Condensate*, Phys. Rev. Lett., 2001, DOI: 10.1103/PhysRevLett.86.4211.
- [102] D. S. Petrov, *Quantum Mechanical Stabilization of a Collapsing Bose-Bose Mixture*, Phys. Rev. Lett., 2015, DOI: 10.1103/PhysRevLett.115.155302.
- [103] T.-L. Ho and V. B. Shenoy, *Binary Mixtures of Bose Condensates of Alkali Atoms*, Phys. Rev. Lett., 1996, DOI: 10.1103/PhysRevLett.77.3276.
- [104] C. K. Law, H. Pu, N. P. Bigelow, and J. H. Eberly, “*Stability Signature*” in *Two-Species Dilute Bose-Einstein Condensates*, Phys. Rev. Lett., 1997, DOI: 10.1103/PhysRevLett.79.3105.
- [105] H. Pu and N. P. Bigelow, *Properties of Two-Species Bose Condensates*, Phys. Rev. Lett., 1998, DOI: 10.1103/PhysRevLett.80.1130.
- [106] M. R. Andrews, C. G. Townsend, H.-J. Miesner, D. S. Durfee, D. M. Kurn, and W. Ketterle, *Observation of Interference Between Two Bose Condensates*, Science, 275, 1997, DOI: 10.1126/science.275.5300.637.
- [107] C. Kohstall, S. Riedl, E. R. S. Guajardo, L. A. Sidorenkov, J. H. Denschlag, and R. Grimm, *Observation of interference between two molecular Bose-Einstein condensates*, New Journal of Physics, 13, 2011.
- [108] Y. Castin and R. Dum, *Bose-Einstein Condensates in Time Dependent Traps*, Phys. Rev. Lett., 1996, DOI: 10.1103/PhysRevLett.77.5315.
- [109] Y. Kagan, E. L. Surkov, and G. V. Shlyapnikov, *Evolution of a Bose-condensed gas under variations of the confining potential*, Phys. Rev. A, 1996, DOI: 10.1103/PhysRevA.54.R1753.
- [110] F. Dalfovo, C. Minniti, S. Stringari, and L. Pitaevskii, *Nonlinear dynamics of a Bose condensed gas*, Physics Letters A, 227, 1997, DOI: [https://doi.org/10.1016/S0375-9601\(97\)00069-8](https://doi.org/10.1016/S0375-9601(97)00069-8).
- [111] Y. Castin and R. Dum, *Bose-Einstein Condensates in Time Dependent Traps*, Phys. Rev. Lett., 1996, DOI: 10.1103/PhysRevLett.77.5315.
- [112] D. G. Fink and D. Christiansen, *Electronics engineers' handbook*. McGraw-Hill, 1996.
- [113] A. Chambers, *Modern Vacuum Physics*. Chapman & Hall/CRC, 2005.
- [114] G. V. Hans Rottländer, Walter Umrath, Fundamentals of leak detection, Technical report, Leybold GmbH, 2016.
- [115] Vacom product catalog, Technical report, VACOM Vakuum Komponenten & Messtechnik GmbH, 2018.
- [116] Leak detection compendium.  
Pfeiffer Vacuum GmbH, 2013.
- [117] K. Jousten, 1999.

- [118] R. Calder and G. Lewin, *Reduction of stainless-steel outgassing in ultra-high vacuum*, British Journal of Applied Physics, 18, 1967.
- [119] Vacuum technology compendium.  
Pfeiffer Vacuum GmbH, 2010.
- [120] J. H. Moore, C. C. Davis, and M. A. Coplan, *Building Scientific Apparatus*. Cambridge University Press, 4 edition, 2009.
- [121] J. Scherschligt, J. A. Fedchak, D. S. Barker, S. Eckel, N. Klimov, C. Makrides, and E. Tiesinga, *Development of a new UHV/XHV pressure standard (cold atom vacuum standard)*, Metrologia, 54, 2017.
- [122] J. E. Bjorkholm, *Collision-limited lifetimes of atom traps*, Phys. Rev. A, 1988, DOI: 10.1103/PhysRevA.38.1599.
- [123] T. Arporntip, C. A. Sackett, and K. J. Hughes, *Vacuum-pressure measurement using a magneto-optical trap*, Phys. Rev. A, 2012, DOI: 10.1103/PhysRevA.85.033420.
- [124] Pfeiffer Vacuum Technology AG.  
*Compact Cold Cathode Gauge All-metal IKR 270*.
- [125] *Leakage Testing Handbook*. General Electric, 1969.
- [126] K. Zapfe, *Leak detection*, CAS - CERN Accelerator School and ALBA Synchrotron Light Facility : Course on Vacuum in Accelerators, 2006, DOI: 10.5170/CERN-2007-003.227.
- [127] H. Katsuta and K. Furukawa, *Hydrogen and Deuterium Transport through Type 304 Stainless Steel at Elevated Temperatures*, Journal of Nuclear Science and Technology, 1981.
- [128] M. Bernardini, S. Braccini, R. De Salvo, A. Di Virgilio, A. Gaddi, A. Gennai, G. Genuini, A. Giazotto, G. Losurdo, H. B. Pan, A. Pasqualetti, D. Passuello, P. Popolizio, F. Raffaelli, G. Torelli, Z. Zhang, C. Bradaschia, R. Del Fabbro, I. Ferrante, F. Fidecaro, P. La Penna, S. Mancini, R. Poggiani, P. Narducci, A. Solina, and R. Valentini, *Air bake-out to reduce hydrogen outgassing from stainless steel*, Journal of Vacuum Science & Technology A, 16, 1998, DOI: 10.1116/1.580967.
- [129] M. Petzold, *Zeeman Slower und magnetischer Transport zur Präparation einer quantenentarteten Mischung aus  $^{23}\text{Na}$  und  $^{40}\text{K}$* , Master's thesis, Gottfried Wilhelm Leibniz Universität Hannover, Institut für Quantenoptik, 2012.
- [130] M. Lambropoulos and S. E. Moody, *Design of a three-stage alkali beam source*, Review of Scientific Instruments, 48, 1977, DOI: 10.1063/1.1134993.
- [131] R. D. Swenumson and U. Even, *Continuous flow reflux oven as the source of an effusive molecular Cs beam*, Review of Scientific Instruments, 52, 1981, DOI: 10.1063/1.1136639.
- [132] G. A. Beitel, *Adsorption of Carbon Monoxide and Hydrogen on Graphite*, Journal of Vacuum Science and Technology, 9, 1972, DOI: 10.1116/1.1316616.
- [133] H. H. Saeki, J. Ikeda, *Optical window sealed with indium for ultrahigh vacuum*, Vacuum, 39, 1989.
- [134] S. Rutherford, *Ion pump operation & trouble shooting guide*, Technical report, Duniv-way Stockroom Corp., 1997.
- [135] Gamma Vacuum.  
*Ion Pump Users Manual*, pn 900013, rev b edition.

- [136] C. Ospelkaus, *Fermi–Bose mixtures – From mean–field interactions to ultracold chemistry*, PhD thesis, Universität Hamburg Department für Physik, 2006.
- [137] K. Diedrich,  
*Entwurf und Realisierung einer elektronischen Steuerung für einen optischen Shutter*. Bachelor thesis, 2017.
- [138] D. Edler, *Computer assisted data analysis for a polar molecule experiment*, Master’s thesis, Gottfried Wilhelm Leibniz Universität Hannover Fakultät für Mathematik und Physik, 2016.
- [139] G. C. Bjorklund, *Frequency-modulation spectroscopy: a new method for measuring weak absorptions and dispersions*, Opt. Lett., 1980, DOI: 10.1364/OL.5.000015.
- [140] E. A. Donley, T. P. Heavner, F. Levi, M. O. Tataw, and S. R. Jefferts, *Double-pass acousto-optic modulator system*, Review of Scientific Instruments, 76, 2005, DOI: 10.1063/1.1930095.
- [141] D. Schlippert, *Quantum tests of the universality of free fall*, PhD thesis, Gottfried Wilhelm Leibniz Universität Hannover, 2014.
- [142] K. K. Voges, *(Title tba)*, PhD thesis.
- [143] E. Schwanke, *Hyperfeinstruktur des NaK-Grundzustandes und Intensitätsstabilisierung einer Dipolfalle*, Master’s thesis, Leibniz Universität Hannover, 2014.
- [144] E. L. Raab, M. Prentiss, A. Cable, S. Chu, and D. E. Pritchard, *Trapping of Neutral Sodium Atoms with Radiation Pressure*, Phys. Rev. Lett., 1987, DOI: 10.1103/PhysRevLett.59.2631.
- [145] J. Catani, P. Maioli, L. De Sarlo, F. Minardi, and M. Inguscio, *Intense slow beams of bosonic potassium isotopes*, Phys. Rev. A, 2006, DOI: 10.1103/PhysRevA.73.033415.
- [146] S. Ospelkaus–Schwarzer, *Quantum Degenerate Fermi-Bose Mixtures of  $^{40}\text{K}$  and  $^{87}\text{Rb}$  in 3D Optical Lattices*, PhD thesis, Universität Hamburg Department für Physik, 2006.
- [147] L. Marcassa, V. Bagnato, Y. Wang, C. Tsao, J. Weiner, O. Dulieu, Y. B. Band, and P. S. Julienne, *Collisional loss rate in a magneto-optical trap for sodium atoms: Light-intensity dependence*, Phys. Rev. A, 1993, DOI: 10.1103/PhysRevA.47.R4563.
- [148] W. Ketterle, K. B. Davis, M. A. Joffe, A. Martin, and D. E. Pritchard, *High densities of cold atoms in a dark spontaneous-force optical trap*, Phys. Rev. Lett., 1993, DOI: 10.1103/PhysRevLett.70.2253.
- [149] M. Prentiss, A. Cable, J. E. Bjorkholm, S. Chu, E. L. Raab, and D. E. Pritchard, *Atomic-density-dependent losses in an optical trap*, Opt. Lett., 1988, DOI: 10.1364/OL.13.000452.
- [150] T. Walker, D. Sesko, and C. Wieman, *Collective behavior of optically trapped neutral atoms*, Phys. Rev. Lett., 1990, DOI: 10.1103/PhysRevLett.64.408.
- [151] M. M. Nakat.  
*Kohärente Grundzustandsmanipulation von fermionischem Kalium bei hoher Teilchenzahl*. Diplomarbeit, 2004.
- [152] A. Görlitz, T. L. Gustavson, A. E. Leanhardt, R. Löw, A. P. Chikkatur, S. Gupta, S. Inouye, D. E. Pritchard, and W. Ketterle, *Sodium Bose-Einstein Condensates in the  $F = 2$  State in a Large-Volume Optical Trap*, Phys. Rev. Lett., 2003, DOI: 10.1103/PhysRevLett.90.090401.
- [153] K. M. R. van der Stam, E. D. van Ooijen, R. Meppelink, J. M. Vogels, and P. van der Straten, *Large atom number Bose-Einstein condensate of sodium*, Review of Scientific Instruments, 78, 2007, DOI: 10.1063/1.2424439.

- [154] Z. Hadzibabic, S. Gupta, C. A. Stan, C. H. Schunck, M. W. Zwierlein, K. Dieckmann, and W. Ketterle, *Fiftyfold Improvement in the Number of Quantum Degenerate Fermionic Atoms*, Phys. Rev. Lett., 2003, DOI: 10.1103/PhysRevLett.91.160401.
- [155] K. M. R. van der Stam, A. Kuijk, R. Meppelink, J. M. Vogels, and P. van der Straten, *Spin-polarizing cold sodium atoms in a strong magnetic field*, Phys. Rev. A, 2006, DOI: 10.1103/PhysRevA.73.063412.
- [156] M. Landini, S. Roy, G. Roati, A. Simoni, M. Inguscio, G. Modugno, and M. Fattori, *Direct evaporative cooling of  $^{39}\text{K}$  atoms to Bose-Einstein condensation*, Phys. Rev. A, 2012, DOI: 10.1103/PhysRevA.86.033421.
- [157] P. D. Lett, R. N. Watts, C. I. Westbrook, W. D. Phillips, P. L. Gould, and H. J. Metcalf, *Observation of Atoms Laser Cooled below the Doppler Limit*, Phys. Rev. Lett., 1988, DOI: 10.1103/PhysRevLett.61.169.
- [158] J. Dalibard and C. Cohen-Tannoudji, *Laser cooling below the Doppler limit by polarization gradients: simple theoretical models*, J. Opt. Soc. Am. B, 1989, DOI: 10.1364/JOSAB.6.002023.
- [159] Z. Shi, P. Wang, Z. Li, Z. Meng, L. Huang, and J. Zhang, *Sub-Doppler laser cooling of  $^{23}\text{Na}$  in gray molasses on the D2 line*, 2018.
- [160] M. Landini, S. Roy, L. Carcagní, D. Trypogeorgos, M. Fattori, M. Inguscio, and G. Modugno, *Sub-Doppler laser cooling of potassium atoms*, Phys. Rev. A, 2011, DOI: 10.1103/PhysRevA.84.043432.
- [161] D. B. Hume, I. Stroescu, M. Joos, W. Muessel, H. Strobel, and M. K. Oberthaler, *Accurate Atom Counting in Mesoscopic Ensembles*, Phys. Rev. Lett., 2013, DOI: 10.1103/PhysRevLett.111.253001.
- [162] L. W. Cheuk, M. A. Nichols, K. R. Lawrence, M. Okan, H. Zhang, and M. W. Zwierlein, *Observation of 2D Fermionic Mott Insulators of  $^{40}\text{K}$  with Single-Site Resolution*, Phys. Rev. Lett., 2016, DOI: 10.1103/PhysRevLett.116.235301.
- [163] J. Söding, D. Guéry-Odelin, P. Desbiolles, F. Chevy, H. Inamori, and J. Dalibard, *Three-body decay of a rubidium Bose-Einstein condensate*, Applied Physics B, 1999, DOI: 10.1007/s003400050805.
- [164] G. Reinaudi, T. Lahaye, Z. Wang, and D. Guéry-Odelin, *Strong saturation absorption imaging of dense clouds of ultracold atoms*, Opt. Lett., 2007, DOI: 10.1364/OL.32.003143.
- [165] H. J. Lewandowski, D. M. Harber, D. L. Whitaker, and E. A. Cornell, *Simplified System for Creating a Bose-Einstein Condensate*, Journal of Low Temperature Physics, 2003, DOI: 10.1023/A:1024800600621.
- [166] K. Beloy, *Theory of the ac Stark Effect on the Atomic Hyperfine Structure and Applications to Microwave Atomic Clocks*, PhD thesis, University of Nevada, Reno, 2009.
- [167] N. Masuhara, J. M. Doyle, J. C. Sandberg, D. Kleppner, T. J. Greytak, H. F. Hess, and G. P. Kochanski, *Evaporative Cooling of Spin-Polarized Atomic Hydrogen*, Phys. Rev. Lett., 1988, DOI: 10.1103/PhysRevLett.61.935.
- [168] R. van Roijen, J. J. Berkhout, S. Jaakkola, and J. T. M. Walraven, *Experiments with Atomic Hydrogen in a Magnetic Trapping Field*, Phys. Rev. Lett., 1988, DOI: 10.1103/PhysRevLett.61.931.
- [169] H. F. Hess, G. P. Kochanski, J. M. Doyle, N. Masuhara, D. Kleppner, and T. J. Greytak, *Magnetic trapping of spin-polarized atomic hydrogen*, Phys. Rev. Lett., 1987, DOI: 10.1103/PhysRevLett.59.672.

- [170] C. R. Monroe, E. A. Cornell, C. A. Sackett, C. J. Myatt, and C. E. Wieman, *Measurement of Cs-Cs elastic scattering at T=30 μK*, Phys. Rev. Lett., 1993, DOI: 10.1103/PhysRevLett.70.414.
- [171] W. Ketterle and N. V. Druten, Evaporative cooling of trapped atoms, volume 37 of *Advances In Atomic, Molecular, and Optical Physics*, pages 181 – 236. Academic Press, 1996, DOI: [https://doi.org/10.1016/S1049-250X\(08\)60101-9](https://doi.org/10.1016/S1049-250X(08)60101-9).
- [172] O. J. Luiten, M. W. Reynolds, and J. T. M. Walraven, *Kinetic theory of the evaporative cooling of a trapped gas*, Phys. Rev. A, 1996, DOI: 10.1103/PhysRevA.53.381.
- [173] C. Myatt, *Bose-Einstein Condensation Experiments in a Dilute Vapor of Rubidium*, PhD thesis, University of Colorado, 1997.
- [174] M.-S. Heo, J.-y. Choi, and Y.-i. Shin, *Fast production of large <sup>23</sup>Na Bose-Einstein condensates in an optically plugged magnetic quadrupole trap*, Phys. Rev. A, 2011, DOI: 10.1103/PhysRevA.83.013622.
- [175] H. J. Lewandowski, D. M. Harber, D. L. Whitaker, and E. A. Cornell, *Simplified System for Creating a Bose-Einstein Condensate*, Journal of Low Temperature Physics, 2003, DOI: 10.1023/A:1024800600621.
- [176] E. Majorana, *Atomi orientati in campo magnetico variabile*, Il Nuovo Cimento (1924-1942), 1932, DOI: 10.1007/BF02960953.
- [177] R. Dubessy, K. Merloti, L. Longchambon, P.-E. Pottie, T. Liennard, A. Perrin, V. Lorent, and H. Perrin, *Rubidium-87 Bose-Einstein condensate in an optically plugged quadrupole trap*, Phys. Rev. A, 2012, DOI: 10.1103/PhysRevA.85.013643.
- [178] D. E. Pritchard, *Cooling Neutral Atoms in a Magnetic Trap for Precision Spectroscopy*, Phys. Rev. Lett., 1983, DOI: 10.1103/PhysRevLett.51.1336.
- [179] W. Petrich, M. H. Anderson, J. R. Ensher, and E. A. Cornell, *Stable, Tightly Confining Magnetic Trap for Evaporative Cooling of Neutral Atoms*, Phys. Rev. Lett., 1995, DOI: 10.1103/PhysRevLett.74.3352.
- [180] D. S. Naik and C. Raman, *Optically plugged quadrupole trap for Bose-Einstein condensates*, Phys. Rev. A, 2005, DOI: 10.1103/PhysRevA.71.033617.
- [181] J. Kim, B. Friedrich, D. P. Katz, D. Patterson, J. D. Weinstein, R. DeCarvalho, and J. M. Doyle, *Buffer-Gas Loading and Magnetic Trapping of Atomic Europium*, Phys. Rev. Lett., 1997, DOI: 10.1103/PhysRevLett.78.3665.
- [182] F. Schreck, G. Ferrari, K. L. Corwin, J. Cubizolles, L. Khaykovich, M.-O. Mewes, and C. Salomon, *Sympathetic cooling of bosonic and fermionic lithium gases towards quantum degeneracy*, Phys. Rev. A, 2001, DOI: 10.1103/PhysRevA.64.011402.
- [183] F. Schreck, L. Khaykovich, K. L. Corwin, G. Ferrari, T. Bourdel, J. Cubizolles, and C. Salomon, *Quasipure Bose-Einstein Condensate Immersed in a Fermi Sea*, Phys. Rev. Lett., 2001, DOI: 10.1103/PhysRevLett.87.080403.
- [184] G. Roati, F. Riboli, G. Modugno, and M. Inguscio, *Fermi-Bose Quantum Degenerate <sup>40</sup>K–<sup>87</sup>Rb Mixture with Attractive Interaction*, Phys. Rev. Lett., 2002, DOI: 10.1103/PhysRevLett.89.150403.
- [185] B. DeMarco, J. L. Bohn, J. P. Burke, M. Holland, and D. S. Jin, *Measurement of p-Wave Threshold Law Using Evaporatively Cooled Fermionic Atoms*, Phys. Rev. Lett., 1999, DOI: 10.1103/PhysRevLett.82.4208.

- [186] J. Dalibard and C. Cohen-Tannoudji, *Dressed-atom approach to atomic motion in laser light: the dipole force revisited*, J. Opt. Soc. Am. B, 1985, DOI: 10.1364/JOSAB.2.001707.
- [187] R. Grimm, M. Weidemüller, and Y. B. Ovchinnikov, *Optical Dipole Traps for Neutral Atoms*, 42, 2000, DOI: [https://doi.org/10.1016/S1049-250X\(08\)60186-X](https://doi.org/10.1016/S1049-250X(08)60186-X).
- [188] M. S. Safranova, B. Arora, and C. W. Clark, *Frequency-dependent polarizabilities of alkali-metal atoms from ultraviolet through infrared spectral regions*, Phys. Rev. A, 2006, DOI: 10.1103/PhysRevA.73.022505.
- [189] A. H. Hansen, A. Y. Khramov, W. H. Dowd, A. O. Jamison, B. Plotkin-Swing, R. J. Roy, and S. Gupta, *Production of quantum-degenerate mixtures of ytterbium and lithium with controllable interspecies overlap*, Phys. Rev. A, 2013, DOI: 10.1103/PhysRevA.87.013615.
- [190] T. A. Savard, K. M. O'Hara, and J. E. Thomas, *Laser-noise-induced heating in far-off resonance optical traps*, Phys. Rev. A, 1997, DOI: 10.1103/PhysRevA.56.R1095.
- [191] M. E. Gehm, K. M. O'Hara, T. A. Savard, and J. E. Thomas, *Dynamics of noise-induced heating in atom traps*, Phys. Rev. A, 1998, DOI: 10.1103/PhysRevA.58.3914.
- [192] Y.-J. Lin, A. R. Perry, R. L. Compton, I. B. Spielman, and J. V. Porto, *Rapid production of  $^{87}\text{Rb}$  Bose-Einstein condensates in a combined magnetic and optical potential*, Phys. Rev. A, 2009, DOI: 10.1103/PhysRevA.79.063631.
- [193] H. P. Mishra, A. S. Flores, W. Vassen, and S. Knoop, *Efficient production of an  $87\text{Rb}$   $F = 2$ ,  $mF = 2$  Bose-Einstein condensate in a hybrid trap*, The European Physical Journal D, 2015, DOI: 10.1140/epjd/e2015-50843-y.
- [194] T. Weber, J. Herbig, M. Mark, H.-C. Nägerl, and R. Grimm, *Bose-Einstein Condensation of Cesium*, Science, 299, 2003, DOI: 10.1126/science.1079699.
- [195] D. Jacob, E. Mimoun, L. D. Sarlo, M. Weitz, J. Dalibard, and F. Gerbier, *Production of sodium Bose-Einstein condensates in an optical dimple trap*, New Journal of Physics, 13, 2011.
- [196] J.-F. Clément, J.-P. Brantut, M. Robert-de Saint-Vincent, R. A. Nyman, A. Aspect, T. Bourdel, and P. Bouyer, *All-optical runaway evaporation to Bose-Einstein condensation*, Phys. Rev. A, 2009, DOI: 10.1103/PhysRevA.79.061406.
- [197] C.-L. Hung, X. Zhang, N. Gemelke, and C. Chin, Runaway evaporative cooling to bose-einstein condensation of cesium atoms in optical traps, In *Frontiers in Optics 2008 Laser Science XXIV Plasmonics and Metamaterials Optical Fabrication and Testing*, page LTuG4. Optical Society of America, 2008.
- [198] J. C. Camparo and R. P. Frueholz, *A dressed atom interpretation of adiabatic rapid passage*, Journal of Physics B: Atomic and Molecular Physics, 17, 1984.
- [199] N. V. Vitanov, T. Halfmann, B. W. Shore, and K. Bergmann, *LASER-INDUCED POPULATION TRANSFER BY ADIABATIC PASSAGE TECHNIQUES*, Annual Review of Physical Chemistry, 52, 2001, DOI: 10.1146/annurev.physchem.52.1.763.
- [200] I. C. Hunter, *Theory and Design of Microwave Filters*. The Institution of Engineering and Technology, 2001.
- [201] S. J. Orfanidis, *Electromagnetic Waves and Antennas*. Rutgers University, 2016.
- [202] C. J. J. Amlaner and D. W. MacDonald, editors, *A Handbook on Biotelemetry and Radio Tracking*. Pergamon Press, 1979.

- [203] M. Succo, *Degenerate Quantum Gases in Optical Lattice Potentials*. Diploma thesis, 2006. Faculty of Mathematics, Informatics and Natural Sciences.
- [204] C.-H. Wu, *Strongly Interacting Quantum Mixtures of Ultracold Atoms*, PhD thesis, MASSACHUSETTS INSTITUTE OF TECHNOLOGY, 2013.
- [205] T. Weber, J. Herbig, M. Mark, H.-C. Nägerl, and R. Grimm, *Three-Body Recombination at Large Scattering Lengths in an Ultracold Atomic Gas*, Phys. Rev. Lett., 2003, DOI: 10.1103/PhysRevLett.91.123201.
- [206] M. Gustavsson, E. Haller, M. J. Mark, J. G. Danzl, G. Rojas-Kopeinig, and H.-C. Nägerl, *Control of Interaction-Induced Dephasing of Bloch Oscillations*, Phys. Rev. Lett., 2008, DOI: 10.1103/PhysRevLett.100.080404.
- [207] Z. Shotan, O. Machtey, S. Kokkelmans, and L. Khaykovich, *Three-Body Recombination at Vanishing Scattering Lengths in an Ultracold Bose Gas*, Phys. Rev. Lett., 2014, DOI: 10.1103/PhysRevLett.113.053202.
- [208] S. Inouye, M. R. Andrews, J. Stenger, H.-J. Miesner, D. M. Stamper-Kurn, and W. Ketterle, *Observation of Feshbach resonances in a Bose-Einstein condensate*, Nature, 1998.
- [209] J. Stenger, S. Inouye, M. R. Andrews, H.-J. Miesner, D. M. Stamper-Kurn, and W. Ketterle, *Strongly Enhanced Inelastic Collisions in a Bose-Einstein Condensate near Feshbach Resonances*, Phys. Rev. Lett., 1999, DOI: 10.1103/PhysRevLett.82.2422.
- [210] T. Laue, E. Tiesinga, C. Samuelis, H. Knöckel, and E. Tiemann, *Magnetic-field imaging of weakly bound levels of the ground-state Na<sub>2</sub> dimer*, Phys. Rev. A, 2002, DOI: 10.1103/PhysRevA.65.023412.
- [211] C. D'Errico, M. Zaccanti, M. Fattori, G. Roati, M. Inguscio, G. Modugno, and A. Simoni, *Feshbach resonances in ultracold 39 K*, New Journal of Physics, 9, 2007.
- [212] S. Roy, M. Landini, A. Trenkwalder, G. Semeghini, G. Spagnolli, A. Simoni, M. Fattori, M. Inguscio, and G. Modugno, *Test of the Universality of the Three-Body Efimov Parameter at Narrow Feshbach Resonances*, Phys. Rev. Lett., 2013, DOI: 10.1103/PhysRevLett.111.053202.
- [213] A. Viel and A. Simoni, *Feshbach resonances and weakly bound molecular states of boson-boson and boson-fermion NaK pairs*, Phys. Rev. A, 2016, DOI: 10.1103/PhysRevA.93.042701.
- [214] R. S. Bloom, M.-G. Hu, T. D. Cumby, and D. S. Jin, *Tests of Universal Three-Body Physics in an Ultracold Bose-Fermi Mixture*, Phys. Rev. Lett., 2013, DOI: 10.1103/PhysRevLett.111.105301.
- [215] R. Pires, J. Ulmanis, S. Häfner, M. Repp, A. Arias, E. D. Kuhnle, and M. Weidmüller, *Observation of Efimov Resonances in a Mixture with Extreme Mass Imbalance*, Phys. Rev. Lett., 2014, DOI: 10.1103/PhysRevLett.112.250404.
- [216] S.-K. Tung, K. Jiménez-García, J. Johansen, C. V. Parker, and C. Chin, *Geometric Scaling of Efimov States in a <sup>6</sup>Li-<sup>133</sup>Cs Mixture*, Phys. Rev. Lett., 2014, DOI: 10.1103/PhysRevLett.113.240402.
- [217] L. J. Wacker, N. B. Jørgensen, D. Birkmose, N. Winter, M. Mikkelsen, J. Sherson, N. Zinner, and J. J. Arlt, *Universal Three-Body Physics in Ultracold KRb Mixtures*, Phys. Rev. Lett., 2016, DOI: 10.1103/PhysRevLett.117.163201.
- [218] X. Li, M. Ke, B. Yan, and Y. Wang, *Reduction of interference fringes in absorption imaging of cold atom cloud using eigenface method*, Chin. Opt. Lett., 2007.

- [219] M. J. Mark, F. Meinert, K. Lauber, and H.-C. Nägerl, *Mott-Insulator-Aided Detection of Ultra-Narrow Feshbach Resonances*, 2018.
- [220] K. Dieckmann, C. A. Stan, S. Gupta, Z. Hadzibabic, C. H. Schunck, and W. Ketterle, *Decay of an Ultracold Fermionic Lithium Gas near a Feshbach Resonance*, Phys. Rev. Lett., 2002, DOI: 10.1103/PhysRevLett.89.203201.
- [221] T. Bourdel, J. Cubizolles, L. Khaykovich, K. M. F. Magalhães, S. J. J. M. F. Kokkelmans, G. V. Shlyapnikov, and C. Salomon, *Measurement of the Interaction Energy near a Feshbach Resonance in a  ${}^6\text{Li}$  Fermi Gas*, Phys. Rev. Lett., 2003, DOI: 10.1103/PhysRevLett.91.020402.
- [222] C. Weber, G. Barontini, J. Catani, G. Thalhammer, M. Inguscio, and F. Minardi, *Association of ultracold double-species bosonic molecules*, Phys. Rev. A, 2008, DOI: 10.1103/PhysRevA.78.061601.
- [223] O. Machtey, D. A. Kessler, and L. Khaykovich, *Universal Dimer in a Collisionally Opaque Medium: Experimental Observables and Efimov Resonances*, Phys. Rev. Lett., 2012, DOI: 10.1103/PhysRevLett.108.130403.
- [224] S. Zhang and T.-L. Ho, *Atom loss maximum in ultra-cold Fermi gases*, New Journal of Physics, 13, 2011.
- [225] A. Y. Khramov, A. H. Hansen, A. O. Jamison, W. H. Dowd, and S. Gupta, *Dynamics of Feshbach molecules in an ultracold three-component mixture*, Phys. Rev. A, 2012, DOI: 10.1103/PhysRevA.86.032705.
- [226] J. Ulmanis, S. Häfner, R. Pires, E. D. Kuhnle, M. Weidemüller, and E. Tiemann, *Universality of weakly bound dimers and Efimov trimers close to Li-Cs Feshbach resonances*, New Journal of Physics, 17, 2015.
- [227] G. Salomon, L. Fouché, S. Lepoutre, A. Aspect, and T. Bourdel, *All-optical cooling of  ${}^{39}\text{K}$  to Bose-Einstein condensation*, Phys. Rev. A, 2014, DOI: 10.1103/PhysRevA.90.033405.
- [228] G. Roati, M. Zaccanti, C. D'Errico, J. Catani, M. Modugno, A. Simoni, M. Inguscio, and G. Modugno,  *${}^{39}\text{K}$  Bose-Einstein Condensate with Tunable Interactions*, Phys. Rev. Lett., 2007, DOI: 10.1103/PhysRevLett.99.010403.
- [229] E. Tiesinga, C. J. Williams, P. S. Julienne, K. M. Jones, P. D. Lett, and W. D. Phillips, *A Spectroscopic Determination of Scattering Lengths for Sodium Atom Collisions*, Journal of Research of the National Institute of Standards and Technology, 1996.
- [230] A. Simoni, private communication.
- [231] F. Seeßelberg, N. Buchheim, Z.-K. Lu, T. Schneider, X.-Y. Luo, E. Tiemann, I. Bloch, and C. Gohle, *Modeling the adiabatic creation of ultracold polar  ${}^{23}\text{Na}{}^{40}\text{K}$  molecules*, Phys. Rev. A, 2018, DOI: 10.1103/PhysRevA.97.013405.
- [232] M. Schmitt, M. Wenzel, F. Böttcher, I. Ferrier-Barbut, and T. Pfau, *Self-Bound Droplets of a Dilute Magnetic Quantum Liquid*, Nature 539, 259, 2016.
- [233] L. Chomaz, S. Baier, D. Petter, M. J. Mark, F. Wächtler, L. Santos, and F. Ferlaino, *Quantum-Fluctuation-Driven Crossover from a Dilute Bose-Einstein Condensate to a Macro-droplet in a Dipolar Quantum Fluid*, Phys. Rev. X, 2016, DOI: 10.1103/PhysRevX.6.041039.
- [234] C. R. Cabrera, L. Tanzi, J. Sanz, B. Naylor, P. Thomas, P. Cheiney, and L. Tarruell, *Quantum liquid droplets in a mixture of Bose-Einstein condensates*, Science, 359, 2018, DOI: 10.1126/science.aa05686.

- [235] P. Cheiney, C. R. Cabrera, J. Sanz, B. Naylor, L. Tanzi, and L. Tarruell, *Bright Soliton to Quantum Droplet Transition in a Mixture of Bose-Einstein Condensates*, Phys. Rev. Lett., 2018, DOI: 10.1103/PhysRevLett.120.135301.
- [236] G. Semeghini, G. Ferioli, L. Masi, C. Mazzinghi, L. Wolswijk, F. Minardi, M. Modugno, G. Modugno, M. Inguscio, and M. Fattori, *Self-Bound Quantum Droplets of Atomic Mixtures in Free Space*, Phys. Rev. Lett., 2018, DOI: 10.1103/PhysRevLett.120.235301.
- [237] K. E. Wilson, N. Westerberg, M. Valiente, C. W. Duncan, E. M. Wright, P. Öhberg, and D. Faccio, *Observation of photon droplets and their dynamics*, 2018.
- [238] Y. Li, G. Feng, R. Xu, X. Wang, J. Wu, G. Chen, X. Dai, J. Ma, L. Xiao, and S. Jia, *Magnetic levitation for effective loading of cold cesium atoms in a crossed dipole trap*, Phys. Rev. A, 2015, DOI: 10.1103/PhysRevA.91.053604.
- [239] T. Bergeman, G. Erez, and H. J. Metcalf, *Magnetostatic trapping fields for neutral atoms*, Phys. Rev. A, 1987, DOI: 10.1103/PhysRevA.35.1535.
- [240] Z. Lu, *Towards many body physics with ultracold NaK molecules*, PhD thesis, Fakultät für Physik, Ludwig-Maximilians-Universität München, 2016.
- [241] M. W. Z. W. Ketterle, *Making, probing and understanding ultracold Fermi gases*, Proceedings of the International School of Physics "Enrico Fermi", 164, 2008, DOI: 10.3254/978-1-58603-846-5-95.
- [242] S. T. Thompson, E. Hodby, and C. E. Wieman, *Ultracold Molecule Production via a Resonant Oscillating Magnetic Field*, Phys. Rev. Lett., 2005, DOI: 10.1103/PhysRevLett.95.190404.
- [243] C. Ospelkaus, S. Ospelkaus, L. Humbert, P. Ernst, K. Sengstock, and K. Bongs, *Ultracold Heteronuclear Molecules in a 3D Optical Lattice*, Phys. Rev. Lett., 2006, DOI: 10.1103/PhysRevLett.97.120402.
- [244] C.-H. Wu, J. W. Park, P. Ahmadi, S. Will, and M. W. Zwierlein, *Ultracold Fermionic Feshbach Molecules of  $^{23}\text{Na}$ - $^{40}\text{K}$* , Phys. Rev. Lett., 2012, DOI: 10.1103/PhysRevLett.109.085301.
- [245] E. Hodby, S. T. Thompson, C. A. Regal, M. Greiner, A. C. Wilson, D. S. Jin, E. A. Cornell, and C. E. Wieman, *Production Efficiency of Ultracold Feshbach Molecules in Bosonic and Fermionic Systems*, Phys. Rev. Lett., 2005, DOI: 10.1103/PhysRevLett.94.120402.
- [246] K. Bergmann, H. Theuer, and B. W. Shore, *Coherent population transfer among quantum states of atoms and molecules*, Rev. Mod. Phys., 1998, DOI: 10.1103/RevModPhys.70.1003.
- [247] M. Debatin, *Creation of Ultracold RbCs Ground-State Molecules*, PhD thesis, Faculty of Mathematics, Computer Science and Physics of the University of Innsbruck, 2013.
- [248] P. Molony, P. Gregory, A. Kumar, C. Ruth Le Sueur, J. M Hutson, and S. Cornish, *Production of ultracold  $^{87}\text{Rb}$ - $^{133}\text{Cs}$  in the absolute ground state: complete characterisation of the STIRAP transfer*, Chemphyschem : a European journal of chemical physics and physical chemistry, 2016.
- [249] X. Ye, M. Guo, M. L. González-Martínez, G. Quéméner, and D. Wang, *Collisions of ultracold  $^{23}\text{Na}$ - $^{87}\text{Rb}$  molecules with controlled chemical reactivities*, Science Advances, 4, 2018, DOI: 10.1126/sciadv.aaq0083.
- [250] A. Micheli, G. Pupillo, H. P. Büchler, and P. Zoller, *Cold polar molecules in two-dimensional traps: Tailoring interactions with external fields for novel quantum phases*, Phys. Rev. A, 2007, DOI: 10.1103/PhysRevA.76.043604.

- [251] L. Lassablière and G. Quéméner, *Controlling the scattering length of ultracold dipolar molecules*, 2018.
- [252] M. L. González-Martínez, J. L. Bohn, and G. Quéméner, *A dimensional theory of shielding in ultracold collisions of dipolar rotors*, Phys. Rev. A, 2017, DOI: 10.1103/PhysRevA.96.032718.
- [253] L. Tarruell, D. Greif, T. Uehlinger, G. Jotzu, and T. Esslinger, *Creating, moving and merging Dirac points with a Fermi gas in a tunable honeycomb lattice*, Nature, 2012.
- [254] G.-B. Jo, J. Guzman, C. K. Thomas, P. Hosur, A. Vishwanath, and D. M. Stamper-Kurn, *Ultracold Atoms in a Tunable Optical Kagome Lattice*, Phys. Rev. Lett., 2012, DOI: 10.1103/PhysRevLett.108.045305.
- [255] H. P. Nautrup.  
*Phase Stabilization for Optical Lattices*.  
 Bachelor thesis, 2014.
- [256] S. A. Moses, J. P. Covey, M. T. Miecnikowski, B. Yan, B. Gadway, J. Ye, and D. S. Jin, *Creation of a low-entropy quantum gas of polar molecules in an optical lattice*, Science, 350, 2015, DOI: 10.1126/science.aac6400.
- [257] L. Reichsöllner, A. Schindewolf, T. Takekoshi, R. Grimm, and H.-C. Nägerl, *Quantum Engineering of a Low-Entropy Gas of Heteronuclear Bosonic Molecules in an Optical Lattice*, Phys. Rev. Lett., 2017, DOI: 10.1103/PhysRevLett.118.073201.
- [258] S. Taie, H. Ozawa, T. Ichinose, T. Nishio, S. Nakajima, and Y. Takahashi, *Coherent driving and freezing of bosonic matter wave in an optical Lieb lattice*, Science Advances, 1, 2015, DOI: 10.1126/sciadv.1500854.
- [259] M. Viteau, J. Radogostowicz, M. G. Bason, N. Malossi, D. Ciampini, O. Morsch, and E. Arimondo, *Rydberg spectroscopy of a Rb MOT in the presence of applied or ion created electric fields*, Opt. Express, 2011, DOI: 10.1364/OE.19.006007.
- [260] J. L. Bohn, A. M. Rey, and J. Ye, *Cold molecules: Progress in quantum engineering of chemistry and quantum matter*, Science, 357, 2017, DOI: 10.1126/science.aam6299.
- [261] K. Goral, L. Santos, and M. Lewenstein, *Quantum Phases of Dipolar Bosons in Optical Lattices*, Phys. Rev. Lett., 2002, DOI: 10.1103/PhysRevLett.88.170406.
- [262] C. Menotti, C. Trefzger, and M. Lewenstein, *Metastable States of a Gas of Dipolar Bosons in a 2D Optical Lattice*, Phys. Rev. Lett., 2007, DOI: 10.1103/PhysRevLett.98.235301.
- [263] Y. Tang, W. Kao, K.-Y. Li, S. Seo, K. Mallayya, M. Rigol, S. Gopalakrishnan, and B. L. Lev, *Thermalization near Integrability in a Dipolar Quantum Newton's Cradle*, Phys. Rev. X, 2018, DOI: 10.1103/PhysRevX.8.021030.





# Curriculum vitae

## Personal Details

Name                  Torsten Hartmann  
Date of birth        February 19, 1985  
Place of birth        Neustadt am Rübenberge, Germany

## Education

- 12/2011 - 11/2018    Doctoral studies at Institut für Quantenoptik , Leibniz Universität Hannover  
10/2014 - 12/2014    Visiting scientist at University of Strathclyde, Glasgow, UK  
07/2010 - 10/2010    Summer student program at DESY, Hamburg  
10/2009 - 07/2011    Master's studies at Leibniz Universität Hannover  
10/2006 - 07/2009    Bachelor's studies at Leibniz Universität Hannover  
06/2004               Abitur at Gymnasium Stolzenau



# DANKSAGUNG

---

Über die Jahre, in denen ich am Institut gearbeitet und geforscht habe, durfte ich die Bekanntschaft vieler netter und hilfsbereiter Menschen machen. Es war eine spannende, interessante und lehrreiche Zeit. An dieser Stelle möchte ich die Gelegenheit nutzen, mich zu bedanken.

Zuallererst danke ich Silke dafür, dass ich an ihrem Experiment meine Doktorarbeit schreiben durfte. Sie hat viele Freiheiten gelassen und es mir stets ermöglicht, mich fachlich und auch persönlich weiterzuentwickeln.

Milutin danke ich dafür, dass er sich bereit erklärt hat, als Zweitgutachter meiner Arbeit zu fungieren. Er hat mich begleitet, lange bevor ich meine Doktorarbeit begonnen habe. Ich möchte ihm auch für die vielen hilfreichen Ratschläge, die er mir auf den Fluren des Instituts gab, danken.

Mein Dank geht an Herrn Hammerer für die Übernahme des Prüfungsvorsitzes.

Herrn Tiemann danke ich für die angenehme und extrem lehrreiche Zusammenarbeit, die ihren Höhepunkt für mich in der Einreichung unserer gemeinsamen Veröffentlichung gefunden hat.

Ich danke den Sekretärinnen Elke, Katrin, Frau Faber und Frau Ohlendorf, denn ohne sie wäre meine Doktorarbeit schlicht nicht durchführbar gewesen. Egal, mit welchem Anliegen ich bei ihnen vorstellig wurde, mir wurde stets freundlich und mit herausragender Kompetenz und Professionalität geholfen.

Dem Werkstattteam des IQO, Herrn Witzlau, Herrn Dohm, Matthias, Jonas und Alex möchte ich für die vielen Male danken, in denen sie schnellste Hilfe auf exzellentem technischen Niveau geleistet haben. Ich habe durch sie viel lernen dürfen, über Materialeigenschaften, über das richtige Anfertigen technischer Zeichnungen, über verschiedene Fertigungsprozesse und vieles mehr. Für mich war es nie selbstverständlich, mit welcher Geduld mir all diese mir unbekannten Dinge erklärt wurden. Für die Überstunden, die meinentwegen bestimmt notwendig waren, wenn mal wieder dringend ein Bauteil für mich gefertigt werden musste, möchte ich mich entschuldigen und mich bedanken, dass die angefragten Teile dennoch immer rechtzeitig fertig wurden.

Von Kai-Martin habe ich so viel über Elektronik gelernt wie von sonst keinem anderen Menschen. Ich bewundere seinen Einsatz, wenn er als Leiter und derzeit einziger Mitarbeiter unserer Elektronikwerkstatt die Lagerhaltung, Buchhaltung und Instandhaltung stemmt und dennoch nie müde wird, jedem, der seine Werkstatt betritt, den richtigen Umgang mit dem Lötkolben beizubringen oder mit Rat und Tat bei der Umsetzung auch der abwegigsten Elektroniken zur Seite steht.

Ich hatte die Ehre, das Experiment in Gemeinschaftsarbeit mit anderen fähigen Menschen aufzubauen zu dürfen und ihnen möchte ich besonders danken:

- Alessandro, meinem "direkten Vorgesetzten", welcher nicht nur mit Fassung die Bürde trug, als erster diese Arbeit Korrektur lesen zu müssen, sondern auch meine Italienischkenntnisse um wertvolle Redewendungen bereichert hat.
- Von allen Doktoranden der ersten Generation war Matthias der allererste und ohne ihn

gäbe es das Experiment nicht, an dem ich meine Forschung durchführen konnte. Ich war vom ersten Moment der Zusammenarbeit an und bin bis heute extrem beeindruckt von seinen Leistungen. In meiner Vorstellung hat er 80% des gesamten Experiments aufgebaut und jede seiner Baugruppen ist nahe der Perfektion. Gemeinsam mit ihm die Maschine zu errichten, hat mich viel gelehrt und auch im Privaten freue ich mich, ihn kennen zu dürfen.

- Torben danke ich für den theoretischen Hintergrund, den er an das Experiment gebracht hat. Er ist zudem der bestvernetzte Mensch, den ich am Institut kenne und das hat sich häufig als hilfreich erwiesen, wenn dringend ein defektes Bauteil ersetzt werden musste.
- Ich danke Kai für seine massive Unterstützung, insbesondere in den letzten Monaten meiner Laborzeit, in denen viele wichtige Messungen für meine Arbeit durchgeführt wurden. Er war es, der nach Wochen des gemeinsamen Grübelns und Probierens die erste funktionierende Radiofrequenzantenne fertigte. Auch bei vielen langwierigen Messkampagnen saß er neben mir bei arktischen Temperaturen vor den Experiment-steuerrechnern. All das war eine enorme Hilfe für mich.
- Und genauso möchte ich auch Philipp danken, dem (derzeit) jüngsten Doktoranden am POLAR-Experiment, der direkt in seinen ersten Wochen und Monaten eine unschätzbare Unterstützung für mich war, als wir dem System die letzten Daten-punkte meiner Messungen abgerungen haben. Seine positive Art ist sicherlich nicht unschuldig daran, dass er die bisher beindruckendste Statistik von Dingen, die auf Anhieb klappten, in dieser Gruppe besitzt.

Ich danke auch den Kollegen an Silkes anderen Experiment. Den SLOMOS, Mirko, Maurice, Paul und Mariia danke ich für die gute Labornachbarschaft und die angenehme Zeit im gemeinsamen Büro und den Spektroskopikern Horst, Erik und Julia für die netten Gespräche in ihrem Büro direkt unter dem Dach.

Ich danke den IONEN Timko, Malte, Sebastian, Martina, Jojo und Teresa für die gemein-same Zeit als Doktoranden in Arbeitsgruppen, die zeitgleich ihre ersten Experimente in Hannover aufgebaut haben - mit all den spannenden Ereignissen, die dies bringt. Einer IONIN möchte ich im Speziellen danken. AGP, mit der ich die ersten fünf Jahre ein Büro teilen durfte und die die heiterste Person ist, die ich kenne. Diese Heiterkeit ist jedes Mal wieder direkt ansteckend.

Ich bedanke mich bei Wuying für ihre Freundschaft und die vielen Kaffees und Kuchen, die wir verzehrt haben.

Ilka kenne ich seit meinen ersten Tagen als Physikstudent und ich möchte ihr danken, dass sie trotzdem nach wie vor gewillt ist, mit mir Mittagessen zu gehen.

Und auch abseits des Instituts gibt es Menschen, denen ich dankbar bin für so vieles. Für ihre dauerhafte Unterstützung seit ich denken kann, danke ich meiner Familie. Ben ist der Mensch, den ich neben meinen Familienmitgliedern am längsten kenne und ich hoffe, dass unsere Freundschaft stets bestehen bleibt. Eike danke ich für die vielen gemeinsamen Kinoabende und vieles mehr. Für ihre Freundschaft und die vielen lustigen gemeinsamen Stunden bedanke ich mich bei Malte (der mich zu einem besseren Strategen machte), Nils (mit dem ich viele interessante Diskussionen führen durfte), Victoria (bei der ich immer gerne zu Besuch bin), Christian, Jannes und Eike (für die gemeinsamen Abende), Bernhard (mit dem ich ab und an verwechselt wurde) und Kevin (der besser fliegen kann als ich). Und ich danke Carola und ihrer Familie für die viele Hilfe und die vielen tollen gemeinsamen Erlebnisse.



